

Smart Innovation, Systems and Technologies 301

Biplab Das
Ripon Patgiri
Valentina Emilia Balas *Editors*



Advances in Smart Energy Systems

The logo for KES International, featuring the letters 'KES' in a stylized blue font above the word 'International' in a smaller blue font.

The Springer logo, which consists of a stylized chess knight icon followed by the word 'Springer' in a serif font.

Smart Innovation, Systems and Technologies

Volume 301

Series Editors

Robert J. Howlett, Bournemouth University and KES International,
Shoreham-by-Sea, UK

Lakhmi C. Jain, KES International, Shoreham-by-Sea, UK

The Smart Innovation, Systems and Technologies book series encompasses the topics of knowledge, intelligence, innovation and sustainability. The aim of the series is to make available a platform for the publication of books on all aspects of single and multi-disciplinary research on these themes in order to make the latest results available in a readily-accessible form. Volumes on interdisciplinary research combining two or more of these areas is particularly sought.

The series covers systems and paradigms that employ knowledge and intelligence in a broad sense. Its scope is systems having embedded knowledge and intelligence, which may be applied to the solution of world problems in industry, the environment and the community. It also focusses on the knowledge-transfer methodologies and innovation strategies employed to make this happen effectively. The combination of intelligent systems tools and a broad range of applications introduces a need for a synergy of disciplines from science, technology, business and the humanities. The series will include conference proceedings, edited collections, monographs, handbooks, reference books, and other relevant types of book in areas of science and technology where smart systems and technologies can offer innovative solutions.

High quality content is an essential feature for all book proposals accepted for the series. It is expected that editors of all accepted volumes will ensure that contributions are subjected to an appropriate level of reviewing process and adhere to KES quality principles.

Indexed by SCOPUS, EI Compendex, INSPEC, WTI Frankfurt eG, zbMATH, Japanese Science and Technology Agency (JST), SCImago, DBLP.

All books published in the series are submitted for consideration in Web of Science.

Biplab Das · Ripon Patgiri · Valentina Emilia Balas
Editors

Advances in Smart Energy Systems

 Springer

Editors

Biplab Das
Department of Mechanical Engineering
National Institute of Technology Silchar
Silchar, Assam, India

Ripon Patgiri
Department of Computer Science
and Engineering
National Institute of Technology Silchar
Silchar, Assam, India

Valentina Emilia Balas
Department of Automation and Applied
Informatics
Aurel Vlaicu University of Arad
Arad, Romania

ISSN 2190-3018

ISSN 2190-3026 (electronic)

Smart Innovation, Systems and Technologies

ISBN 978-981-19-2411-8

ISBN 978-981-19-2412-5 (eBook)

<https://doi.org/10.1007/978-981-19-2412-5>

© The Editor(s) (if applicable) and The Author(s), under exclusive license to Springer Nature Singapore Pte Ltd. 2023

This work is subject to copyright. All rights are solely and exclusively licensed by the Publisher, whether the whole or part of the material is concerned, specifically the rights of translation, reprinting, reuse of illustrations, recitation, broadcasting, reproduction on microfilms or in any other physical way, and transmission or information storage and retrieval, electronic adaptation, computer software, or by similar or dissimilar methodology now known or hereafter developed.

The use of general descriptive names, registered names, trademarks, service marks, etc. in this publication does not imply, even in the absence of a specific statement, that such names are exempt from the relevant protective laws and regulations and therefore free for general use.

The publisher, the authors, and the editors are safe to assume that the advice and information in this book are believed to be true and accurate at the date of publication. Neither the publisher nor the authors or the editors give a warranty, expressed or implied, with respect to the material contained herein or for any errors or omissions that may have been made. The publisher remains neutral with regard to jurisdictional claims in published maps and institutional affiliations.

This Springer imprint is published by the registered company Springer Nature Singapore Pte Ltd.

The registered company address is: 152 Beach Road, #21-01/04 Gateway East, Singapore 189721, Singapore

Preface

Optimal use of sustainable energy technologies has been attracting researchers, developers, industrialists, etc., in recent years due to the exponential increase in energy crisis and corresponding environmental problems linked with the burning of conventional sources. However, the highly variable and site-specific nature of renewable energy sources has also increased the level of uncertainty in the operation of power systems and the unpredictability of load situations. Smart computing techniques offer an effective solution for investigating and modeling the stochastic behavior of renewable energy generation, operation of grid-connected renewable energy systems, and smart decision-making among alternatives. The application of soft computing techniques to make an intelligent decision for optimum use of suitable alternatives gives an upper hand compared to conventional systems. It includes upgradation of the existing system by embedding of machine intelligence. In the recent era, the combination of use of neural networks, fuzzy systems, and genetic algorithms are illustrated in several applications including forecasting, security, verification, diagnostics of a specific fault, efficiency optimization, etc. Smart energy systems integrate a holistic approach in diverse sectors including electricity, thermal comfort, power industry, transportation. It allows affordable and sustainable solutions to solve the future energy demands with suitable alternatives. Thus, integration of the machine intelligence with the energy system, for efficient collection and effective utilization of the available energy sources, is the need of the hour.

The key objectives of the book are outlined below:

- To disseminate the recent research findings on the intelligent energy system.
- To review the current state-of-the-art solution of the smart energy system.
- To attract broad readership from diverse research domains.
- To unveil the applicability of advanced smart computing techniques for energy harvesting.

Silchar, India
Silchar, India
Arad, Romania

Biplab Das
Ripon Patgiri
Valentina Emilia Balas

Contents

1 Optimization Analysis of a Stand-Alone Hybrid Energy System for the Class Room at RLJIT, Doddaballapur, Southern Part of India	1
Jagannath Reddy, Jagadish, and Biplab Das	
2 A Study of Internet of Things in Smart Grid and Smart Grid Security	15
Kaushik Kalita, Partha Pratim Borah, and Kankan Kishore Pathak	
3 An Overview of Quantum Computing Approach in the Present-Day Energy Systems	39
Chiranjit Biswas, Jayanta Pal, and Swanirbhar Majumder	
4 Symbiotic Organisms Search Algorithm-Based Optimal Allocation and Sizing of Capacitor Bank in Radial Distribution Networks	55
Saubhagya Ranjan Biswal and Gauri Shankar	
5 Optimization of the Mechanical Properties of Energy-Efficient Natural Fiber-Reinforced Polymeric Composites	77
Satadru Kashyap and Jahidul Islam	
6 Extended State Observer-Based Controller Design Application in a Two-Link Robotic Manipulator	101
Piyali Das, Ram Krishna Mehta, and Om Prakash Roy	
7 Optimisation of Energy and Exergy Analysis of 100 W Solar Photovoltaic Module Using ANN Method	125
I. R. Ganesh Kumar, S. Vijay Kumar, Jagannath Reddy, G. Rajendra, Yoga Sainath Reddy, Sai Ranjith Reddy, and Biplab Das	

8	Obstructed Material Classification Using mmWave Radar with Deep Neural Network for Industrial Applications	147
	Yi Sheng Leong, Sukanta Roy, and King Hann Lim	
9	Modeling and Simulation of Plain and Corrugated Shell and Tube Heat Exchanger	163
	A. Bora, A. P. Kalita, M. Bardalai, and Partha P. Dutta	
10	Computational Fluid Dynamics Analysis of Wind Turbine Blades at Various Angles of Attack	175
	Nabanikha Das, Amir Sohail, Rajesh Doley, and Shikha Bhuyan	
11	Computational Analysis of Air Energy Extractors for Guided Flow Exhaust Applications	185
	Enderaaj Singh, Sukanta Roy, Yam Ke San, Ming Chiat Law, and Perumal Kumar	
12	Computational Simulations on the Performance of Savonius Turbines in a Solar Chimney Power Plant	205
	Pavitri Apparavoo, Sukanta Roy, and Yam Ke San	
13	Presentation of Real-Time Lab Analysis for Multiple-Area Renewable Sources-Thermal-Hydro System by Implementation of Cat Swarm Optimization	221
	Arindita Saha, Lalit Chandra Saikia, Naladi Ram Babu, Sanjeev Kumar Bhagat, Manoja Kumar Behera, Satish Kumar Ramoji, and Biswanath Dekaraja	
14	Impact of Electric Vehicles and Wind Turbine in Combined ALFC and AVR Studies Using AFA-Optimized CFPD-PIDN Controller	233
	Biswanath Dekaraja, Lalit Chandra Saikia, Satish Kumar Ramoji, Manoja Kumar Behera, Sanjeev Kumar Bhagat, Arinditi Saha, and Naladi Ram Babu	
15	A QSSA Optimized Fractional-Order Controller for Improving Transient Response in AC Autonomous Microgrid VSC System	255
	Manoja Kumar Behera, Lalit Chandra Saikia, Satish Kumar Ramoji, Biswanath Dekaraja, Arindita Saha, Sanjeev Kumar Bhagat, and Naladi Ram Babu	
16	Conflated Voltage–Frequency Control of Multi-area Multi-source System Using Fuzzy TID Controller and Its Real-Time Validation	277
	Satish Kumar Ramoji, Lalit Chandra Saikia, Biswanath Dekaraja, Manoja Kumar Behera, Sanjeev Kumar Bhagat, Naladi Ram Babu, and Arindita Saha	

Editors and Contributors

About the Editors

Dr. Biplab Das is presently working as Assistant Professor in the Department of Mechanical Engineering, National Institute of Technology Silchar, India. He completed his Ph.D. from NERIST, Itanagar, India, in the year of 2014. Later, he pursued his Postdoctoral Research from University of Idaho, USA. He is the recipient of the prestigious Bhaskara Advance Solar Energy (BASE) Fellowship from IUSSTF and DST, Government of India. He is also awarded with “DBT Associate-ship” by the Department of Biotechnology, Government of India. He has 12+ years of experience in teaching and research and published more than 60 nos. of referred international/national journal/conference papers. Presently, he is actively involved in 8 nos. of ongoing sponsored projects to develop a solar thermal system for North East India, worth 0.268 billion INR, sponsored by SERB, DST, Ministry of Power, and the Ministry of Climate Change, Government of India. He is guiding 6 nos. of Ph.D. scholars. He has ongoing research activities in collaboration with Jadavpur University, India, IIT Guwahati, India, University of Idaho, USA, Ulster University, UK.

Dr. Ripon Patgiri is Assistant Professor in the Department of Computer Science and Engineering, National Institute of Technology Silchar. He received his Bachelor Degree from Institution of Electronics and Telecommunication Engineers, New Delhi, in 2009, M.Tech. degree from Indian Institute of Technology Guwahati in 2012, and Ph.D. from National Institute of Technology Silchar in 2019. After M.Tech. degree, he joined as Assistant Professor in the Department of Computer Science and Engineering, National Institute of Technology Silchar, in 2013. He has published numerous papers in reputed journals, conferences, and books. His research interests include bloom filters, networking, security, privacy, secrecy, and communication. He is a senior member of IEEE. He is a member of ACM and EAI. He is a lifetime member of ACCS, India. Also, he is an associate member of IETE. He was General Chair of 6th International Conference on Advanced Computing, Networking, and

Informatics (ICACNI 2018) and International Conference on Big Data, Machine Learning and Applications (BigDML 2019). He is Organizing Chair of 25th International Symposium on Frontiers of Research in Speech and Music (FRSM 2020) and International Conference on Modeling, Simulations and Applications (CoMSO 2020). He is Convenor, Organizing Chair, and Program Chair of 26th annual International Conference on Advanced Computing and Communications (ADCOM 2020). He is an area editor of the EAI Endorsed Transactions on Internet of Things. He is also an editor in a multi-authored book, titled *Health Informatics: A Computational Perspective in Healthcare*, in the book series of “Studies in Computational Intelligence”, Springer. Also, he is writing a monograph book, titled *Bloom Filter: A Data Structure for Computer Networking, Big Data, Cloud Computing, Internet of Things, Bioinformatics and Beyond*, Elsevier. He is also an editor of contributed volume, *Principles of Big Graph: In-depth Insight*, “Advances in Computers”, Elsevier, and *Principles of Social Networking: The New Horizon and Emerging Challenges*, “Smart Innovation, Systems and Technologies” (SIST), Springer. He serves an editor of several conference proceedings, including Proceedings of International Conference on Big Data, Machine Learning and Applications (LNNS, Springer, 2021), Modeling, Simulation and Optimization (SIST, Springer, 2021), and Big Data, Machine Learning, and Applications (CCIS, Springer, 2020).

Valentina Emilia Balas is currently Full Professor in the Department of Automatics and Applied Software at the Faculty of Engineering, “Aurel Vlaicu” University of Arad, Romania. She holds a Ph.D. Cum Laude, in Applied Electronics and Telecommunications from Polytechnic University of Timisoara. She is the author of more than 350 research papers in refereed journals and International Conferences. Her research interests are in intelligent systems, fuzzy control, soft computing, smart sensors, information fusion, modeling and simulation. She is Editor-in-Chief to *International Journal of Advanced Intelligence Paradigms* (IJAIIP) and to *International Journal of Computational Systems Engineering* (IJCSysE), the member in Editorial Board member of several national and international journals and is evaluator expert for national, international projects and Ph.D. Thesis. She is Director of Intelligent Systems Research Centre in Aurel Vlaicu University of Arad and Director of the Department of International Relations, Programs and Projects in the same university. She served as General Chair of the International Workshop Soft Computing and Applications (SOFA) in nine editions organized in the interval 2005–2020 and held in Romania and Hungary. She participated in many international conferences as organizer, honorary chair, session chair, member in steering, advisory or international program committees, and keynote speaker. Now she is working in a national project with EU funding support: BioCell-NanoART = Novel Bio-inspired Cellular Nano-Architectures—For Digital Integrated Circuits, 3M Euro from National Authority for Scientific Research and Innovation. She is a member of European Society for Fuzzy Logic and Technology (EUSFLAT), member of Society for Industrial and Applied Mathematics (SIAM) and a senior member IEEE, member in Technical Committee—Fuzzy Systems (IEEE Computational Intelligence Society), chair of the Task Force 14 in Technical Committee—Emergent Technologies (IEEE CIS), member in Technical

Committee—Soft Computing (IEEE SMCS). She was past Vice-president (responsible with Awards) of IFSA, International Fuzzy Systems Association Council (2013–2015), is Joint Secretary of the Governing Council of Forum for Interdisciplinary Mathematics (FIM), A Multidisciplinary Academic Body, India, and Recipient of the “Tudor Tanasescu” Prize from the Romanian Academy for contributions in the field of soft computing methods (2019).

Contributors

Apparavoo Pavitri Faculty of Engineering and Science, Curtin University Malaysia, Miri, Malaysia

Babu Naladi Ram Department of Electrical Engineering, National Institute of Technology Silchar, Silchar, Assam, India;
Department of Electrical and Electronics Engineering, Aditya Engineering College, East-Godavari, Andhra Pradesh, India

Bardalai M. Tezpur University, Assam, India

Behera Manoja Kumar Department of Electrical Engineering, National Institute of Technology Silchar, Silchar, Assam, India

Bhagat Sanjeev Kumar Department of Electrical Engineering, National Institute of Technology Silchar, Silchar, Assam, India

Bhuyan Shikha Department of Mechanical Engineering, Tezpur University, Tezpur, Assam, India

Biswal Saubhagya Ranjan Department of Electrical Engineering, Indian Institute of Technology (ISM), Dhanbad, Jharkhand, India

Biswas Chiranjit Department of Information Technology, Tripura University, Tripura, India

Bora A. Tezpur University, Assam, India

Borah Partha Pratim Department of Mechanical Engineering, Girijananda Chowdhury Institute of Management and Technology, Guwahati, Assam, India

Das Biplab Department of Mechanical Engineering, National Institute of Technology Silchar, Silchar, Assam, India;
Department of Mechanical Engineering, National Institute of Technology Raipur, Raipur, Chhattisgarh, India

Das Nabanikha Department of Mechanical Engineering, Tezpur University, Tezpur, Assam, India

Das Piyali NERIST, Nirjuli, Andhra Pradesh, India

Dekaraja Biswanath Department of Electrical Engineering, National Institute of Technology Silchar, Silchar, Assam, India

Doley Rajesh Department of Mechanical Engineering, Tezpur University, Tezpur, Assam, India

Dutta Partha P. Tezpur University, Assam, India

Ganesh Kumar I. R. Department of Mechanical Engineering, R L Jalappa Institute of Technology, Doddaballapura, Karnataka, India

Islam Jahidul Department of Mechanical Engineering, Tezpur University, Sonitpur, Assam, India

Jagadish Department of Mechanical Engineering, University of Idaho, Moscow, ID, USA

Kalita A. P. Tezpur University, Assam, India

Kalita Kaushik Department of Electronics and Communication Engineering, Girijananda Chowdhury Institute of Management and Technology, Guwahati, Assam, India

Kashyap Satadru Department of Mechanical Engineering, Tezpur University, Sonitpur, Assam, India

Ke San Yam Faculty of Engineering and Science, Curtin University Malaysia, Miri, Malaysia

Kumar Perumal Faculty of Engineering and Science, Curtin University Malaysia, Miri, Malaysia

Law Ming Chiat Faculty of Engineering and Science, Curtin University Malaysia, Miri, Malaysia

Leong Yi Sheng Faculty of Engineering and Science, Curtin University Malaysia, Miri, Malaysia

Lim King Hann Faculty of Engineering and Science, Curtin University Malaysia, Miri, Malaysia

Majumder Swanirbhar Department of Information Technology, Tripura University, Tripura, India

Mehta Ram Krishna NERIST, Nirjuli, Andhra Pradesh, India

Pal Jayanta Department of Information Technology, Tripura University, Tripura, India

Pathak Kankan Kishore Department of Mechanical Engineering, Girijananda Chowdhury Institute of Management and Technology, Guwahati, Assam, India

Rajendra G. Department of Mechanical Engineering, R L Jalappa Institute of Technology, Doddaballapura, Karnataka, India

Ramoji Satish Kumar Department of Electrical Engineering, National Institute of Technology Silchar, Silchar, Assam, India

Reddy Jagannath Department of Mechanical Engineering, National Institute of Technology Silchar, Silchar, Assam, India;
Department of Mechanical Engineering, R L Jalappa Institute of Technology, Doddaballapura, Karnataka, India

Reddy Sai Ranjith Department of Mechanical Engineering, R L Jalappa Institute of Technology, Doddaballapura, Karnataka, India

Reddy Yoga Sainath Department of Mechanical Engineering, R L Jalappa Institute of Technology, Doddaballapura, Karnataka, India

Roy Om Prakash NERIST, Nirjuli, Andhra Pradesh, India

Roy Sukanta Faculty of Engineering and Science, Curtin University Malaysia, Miri, Malaysia

Saha Arindita Department of Electrical Engineering, Regent Education and Research Foundation Group of Institutions, Kolkata, India;
Department of Electrical Engineering, National Institute of Technology Silchar, Silchar, Assam, India

Saha Arinditi Department of Electrical Engineering, National Institute of Technology, Silchar, Assam, India

Saikia Lalit Chandra Department of Electrical Engineering, National Institute of Technology Silchar, Silchar, Assam, India

Shankar Gauri Department of Electrical Engineering, Indian Institute of Technology (ISM), Dhanbad, Jharkhand, India

Singh Enderaaj Faculty of Engineering and Science, Curtin University Malaysia, Miri, Malaysia

Sohail Amir Department of Mechanical Engineering, Tezpur University, Tezpur, Assam, India

Vijay Kumar S. Department of Mechanical Engineering, R L Jalappa Institute of Technology, Doddaballapura, Karnataka, India;
Department of Mechanical Engineering, Nitte Meenakshi Institute of Technology, Yelahanka, Karnataka, India

Chapter 1

Optimization Analysis of a Stand-Alone Hybrid Energy System for the Class Room at RLJIT, Doddaballapur, Southern Part of India



Jagannath Reddy, Jagadish, and Biplab Das

Abstract In this present work, the hybrid energy systems are used for replacing power grid electricity that is presently used for electrifying the lecture halls, in mechanical department of RLJIT, Doddaballapur, Bengaluru. There is lack of energy resources day by day and also increase in energy demand. This is where hybrid energy systems come into picture. A hybrid energy system is a combination of two or more renewable or non-renewable energy resources used for generation of electricity. The depletion of conventional energies leads to usage of hybrid systems to meet the growing energy needs and generation of electricity. In this study, a hybrid system of solar–wind–battery–diesel energy system is used as substitute for the grid power supply. The average monthly power required for lecture halls is calculated using respective methods. Solar irradiance and wind speed data have been collected from NASA’s POWER Data Access Viewer. The battery bank is used to store the energy produced from the renewable energy sources. Diesel generator is used for power generation when all other sources are at rest. This paper focuses on the usage of technique for order of preference by similarity to ideal solution (TOPSIS) method for getting the enhanced energy resource among the combination of these energy resources. Various combinations of hybrid energy systems are compared and analyzed with TOPSIS. Different criteria like capital cost, maintenance cost, availability, emission, etc., are also studied in this TOPSIS method, and also many alternatives are considered to get accurate results. The results show that the combination of solar–battery–diesel hybrid energy system is optimal combination for power supply to the lecture halls.

J. Reddy (✉) · B. Das

Department of Mechanical Engineering, National Institute of Technology Silchar, Silchar, Assam 788010, India

e-mail: jreddy.mech@gmail.com

Jagadish

Department of Mechanical Engineering, University of Idaho, Moscow, ID 83844-0902, USA

B. Das

Department of Mechanical Engineering, National Institute of Technology Raipur, Raipur, Chhattisgarh 492010, India

1.1 Introduction

Self-sustainable buildings are in huge demand in the present scenario due to depletion of energy supply resources day by day. Hence, optimisation analysis finds a significant usage in evaluating the optimal configuration with least cost of energy and emissions. Research has been carried out on optimisations for large-scale harvesting technologies, design of rocket motors, flow channels, etc., and have attained acceptable results from obtained models. The both renewable and non-renewable energies used in this TOPSIS method are solar energy for photovoltaic system, wind for wind conversion system, battery bank, and diesel generator. Photovoltaic system which consists of PV cells uses solar radiation for generation of electricity. Wind conversion system uses the high-speed wind in the atmosphere and produce electricity. Battery banks are used for storing the energy produced by the HES(s). Diesel generator uses diesel as fuel and generates power. This paper gives the most optimal set of process parameter and configuration of energy systems for high power output by reducing emissions and cost. The goal of this study is increase environmental, technical, and economic benefits and reduce various objective functions such as the annual cost, power loss, and fuel cost.

Various research investigations are performed in the field of optimisation of renewable energy sources. Researchers have formulated the size optimization of grid-independent hybrid wind–photovoltaic–biodiesel–battery systems (WT/PV/BDG/BAT) proposing a hybrid algorithm on this optimization problem. The variables considered include number of batteries, photovoltaic area, etc. The major goal in this investigation is to reduce life cycle cost. Out of all the examined optimisation procedures, hybrid harmony search-simulated annealing algorithm successfully predicts the most optimal results [1]. Optimisation techniques have also been applied for achieving the optimal design of a solar ground source heat pump. After modeling, it is observed that higher borehole heat exchanger length and collector area can lead to lower emissions and reduced costs [2]. Similarly, optimisation schemes are also applied to solar hybrid conventional combined cooling heating power (CCHP) systems for design and achieving optimal performance [3]. Optimisation techniques have also been utilized for predicting the most optimal output of an HES consisting of reverse osmosis desalination system [4]. Even conceptual and sophisticated designs such as hybrid solar power airships find extensive use of optimisation techniques for achieving the highest theoretical efficiency [5]. At an industrial level, large solar district heating plants, customized power systems, etc., have been modeled and optimized using several algorithms for the highest power output, least cost of energy [6–9]. Self-sustainable buildings in the present scenario are in huge demand because of depletion of existing sources of energy supply. Hence, optimisation schemes also find a significant usage in evaluating the optimal configuration with the lease cost of energy and emissions [10]. Researchers have also carried out optimizations for macro-scale harvesting technologies, design of rocket motors, flow channels, etc., and have obtained acceptable results from the developed models [11–15]. On the premise of the available literature, the present study is carried out with the aim of

electrifying the lecture hall of RLJIT, Doddaballapur, southern part of Bangalore, India, with an optimal combination of renewable energy sources. In this work, authors have plotted the monthly energy consumption curve of the case study building.

1.2 Materials and Methodology

1.2.1 Materials

In the case study of lecture halls in the mechanical department of R. L. Jalappa Institute of Technology, Doddaballapur, Karnataka, India, the monthly energy demand is evaluated. The solar irradiance data and wind speed data for that particular reason are collected from NASA power data access viewer, respectively, and presented in Table 1.1.

The following assumptions have been considered for drawing the monthly energy demand of lectures halls:

- Summer months: March to October.
- Winter months: November to February.
- In a month, there are four Sundays and four Saturdays.
- The nonoperational months when lecture halls are not in use are January, July, and the first fifteen days of February and August.

Table 1.1 Solar irradiance and wind speed data

Month	Average insolation (KWh/m ²)	Wind speed (m/s)
Jan	5.36	4.1
Feb	6.06	4.5
Mar	6.56	3.5
Apr	6.38	2.6
May	6.03	3.3
June	4.84	6.9
July	4.5	7.2
Aug	4.47	6.9
Sep	5.03	5.6
Oct	4.63	3.5
Nov	4.5	3.9
Dec	4.74	3.7

1.2.2 Photovoltaic System

System which uses the solar radiation for the generation of electricity or power is termed as photovoltaic system or PV systems or solar energy system. Here, intensity of solar radiation plays a vital role in determining the power output. The type of solar panels considered for this case study is monocrystalline, polycrystalline, and amorphous silicon solar panels.

1.2.3 Wind Energy Conversion System (WECS)

Vertical axis wind turbines are those energy systems which have a transverse arrangement of blades with respect to the direction of the wind. The major components of the system are placed at the bottom of the turbine. With the presence of gearbox and generator at the base, diagnostic and maintenance jobs are simplified. These turbines are usually preferred in regions with low wind speed. Power range of the turbines considered is 400–600 W.

1.2.4 Battery Bank

Battery banks are storage devices which store surplus energy from the HES(s). Their relative arrangement may be parallel; series are combination of both, based on need. The battery bank system allows one to store electrical power generated by another system at any point of time. The battery bank capacities considered for this investigation range from 50 to 400 ah.

1.2.5 Diesel Generator

Diesel generators use diesel as an energy source for power generation. They are some of the widely used energy systems for quick power generation. However, with their usage, emissions and costs remain a huge drawback. In this investigation, diesel generator is kept as a backup for energy supply when the rest of the renewable energy sources are not able to meet the energy demand. The power range of diesel generators considered is 16–200 kve.

1.2.6 Biomass Gasifier

Biomass gasification includes burning of biomass in a limited supply of air to give biogas. The gas is cleaned to make it useful in boilers, engines, and turbines to produce heat and power. Biowastes are used broadly due to their ability to produce low toxic emissions. The power output of considered biomass gasifier is 5–65KW.

1.2.7 Methodology

Technique for order of preference by similarity to ideal solution or TOPSIS is a widely used decision analysis methodology for evaluating the optimal solution from a system. It was initially developed in 1981 with modifications in 1987. TOPSIS allows the user to evaluate the most optimal solution based on geometric distances (GD) from ideal solutions. The optimal solution needs to have the lowest GD from the positive ideal solution and the highest GD from the negative ideal solution. Platforms such as MATLAB and Python are widely used for TOPSIS calculations. Examples such as nuclear power plants require TOPSIS for evaluating the highest power output. HES(s) can also be evaluated using this methodology as it allows each individual and combination of systems to be ranked on several criteria, with a specific weightage to each of them. This method thus reduces time consumption and provides results with high accuracy.

The following are the steps used to perform the TOPSIS methodology:

Step 1. Normalize the decision matrix:

$$r_{ij} = \frac{x_{ij}}{\sqrt{\sum_{k=1}^m x_{kj}^2}} \quad (1.1)$$

$$i = 1, \dots, m; j = 1, \dots, n$$

where r_{ij} denotes the normalized value of the j th criterion for the i th alternative A_i .

Step 2. Calculate the weighted normalized decision matrix:

$$v_{ij} = w_j r_{ij}, i = 1, \dots, m; j = 1, \dots, n \quad (1.2)$$

where w_j is the weight of the j th attribute or criterion.

Step 3. Determine the positive ideal and negative ideal solution:

$$A^+ = \{v_1^+, \dots, v_n^+\} \quad (1.3)$$

$$A^- = \{V_1^-, \dots, V_n^-\} \quad (1.4)$$

where A^+ denotes the positive ideal solution and A^- denotes the negative ideal solution. If the j th criterion is a beneficial criterion, then

$$v_j^+ = \max\{v_{ij}, i = 1 \dots m\} \text{ and } v_j^- = \min\{v_{ij}, i = 1 \dots m\}.$$

In contrast, if the j th criterion is a cost criterion, then $v_j^+ = \min\{v_{ij}, i = 1 \dots m\}$ and $v_j^- = \max\{v_{ij}, i = 1 \dots m\}$.

Step 4. Calculate the distances from each alternative to a positive ideal solution and a negative ideal solution:

$$D_i^+ = \sqrt{\sum_{j=1}^n (v_{ij} - v_j^+)^2}, i = 1, \dots, m \quad (1.5)$$

$$D_i^- = \sqrt{\sum_{j=1}^n (v_{ij} - v_j^-)^2}, i = 1, \dots, m \quad (1.6)$$

where D_i^+ denotes the distance between the i th alternative and the positive ideal solution and D_i^- denotes the distance between the i th alternative and the negative ideal solution.

Step 5. Calculate relative closeness to the ideal solution:

$$C_i = \frac{D_i^-}{D_i^+ + D_i^-} \quad (1.7)$$

Step 6. Rank the alternatives, sorting by the value C_i in decreasing order.

1.3 Results and Discussions

The optimization using TOPSIS method has been carried for each of the energy sources and five combinations of energy sources. The five combinations have been taken based on the rankings obtained from the TOPSIS analysis of the individual sources, and they are solar–diesel–battery configuration, solar–wind–battery configuration, solar–wind–diesel configuration and solar–diesel–biomass configuration, solar–wind–battery configuration.

While carrying out the TOPSIS analysis, six criteria or attributes have been considered, and they are capital cost, maintenance cost, availability, emission, fuel cost, and energy generated. Each of the attributes is given a weightage of except energy generated, which is given a weightage of 0.5 because it is give more emphasis. The decision matrix for the individual source configurations has been given in Tables 1.2 and 1.3, respectively. The normalized decision matrices are shown in Tables 1.4 and 1.5. The weighted normalized decision matrix is found by multiplying the normalized magnitude of each criterion for each energy system with the weightage of that criterion. Tables 1.6 and 1.8 give the weighted normalized decision matrix for the individual

Table 1.2 Decision matrix for individual source configurations

Weightage	0.1	0.1	0.1	0.1	0.1	0.5
	Capital cost (Rs.)	Maintenance cost (Rs.)	Availability (%)	Emission (on a scale of 5)	Fuel cost (on a scale of 5)	Energy generated (kWh)
Solar	98,750	1896.428571	36.33	1	1	1941.666667
Wind	131,000	5625	9.66	1	1	402.2222222
Diesel	66,055.5556	7600	15.33	4	4	1540
Biomass	165,500	9575	36.66	3	1	760
Battery	33,083.33333	3805.555556	15.33	1	3	1440

Table 1.3 Decision matrix for combined source consideration

Weightage	0.1	0.1	0.1	0.1	0.1	0.5
	Capital cost (Rs.)	Maintenance cost (Rs.)	Availability (%)	Emission (on a scale of 15)	Fuel cost (on a scale of 15)	Energy generated (kWh)
Solar + Diesel + Battery	187,500	12,775	70	6	9	4680
Solar + Wind + Battery	250,000	10,950	55.33	3	5	3510
Solar + Wind + Diesel	281,250	14,600	55.33	6	7	3900
Solar + Diesel + Biomass	332,500	18,250	75.33	8	7	4290
Solar + Wind + Biomass	375,000	16,425	64.67	5	3	3120

Table 1.4 Normalized decision matrix for individual source configurations

Weightage	0.1	0.1	0.1	0.1	0.1	0.5
	Capital cost	Maintenance cost	Availability	Emission	Fuel cost	Power generated
Solar	0.403951687	0.134380264	0.639521707	0.188982237	0.188982237	0.648858973
Wind	0.53587515	0.39858553	0.170046234	0.188982237	0.188982237	0.134413132
Diesel	0.270210158	0.538533339	0.26985598	0.755928946	0.755928946	0.514631494
Biomass	0.677002575	0.678481147	0.64533074	0.56694671	0.188982237	0.253973984
Battery	0.135332337	0.269660334	0.26985598	0.188982237	0.56694671	0.481213865

Table 1.5 Normalized decision matrix for combined source configurations

Weightage	0.1	0.1	0.1	0.1	0.1	0.5
	Capital cost	Maintenance cost	Availability	Emission	Fuel cost	Power generated
Solar + Diesel + Battery	0.286622518	0.385337318	0.484436193	0.460178993	0.616669839	0.531368931
Solar + Wind + Battery	0.382163357	0.33028913	0.382912208	0.230089497	0.342594355	0.398526698
Solar + Wind + Diesel	0.429933777	0.440385506	0.382912208	0.460178993	0.479632097	0.442807443
Solar + Diesel + Biomass	0.508277265	0.550481883	0.521322549	0.613571991	0.479632097	0.487088187
Solar + Wind + Biomass	0.573245035	0.495433694	0.447549837	0.383482494	0.205556613	0.354245954

Table 1.6 Weighted normalized decision matrix for individual source configurations

Weightage	0.1	0.1	0.1	0.1	0.1	0.5
	Capital cost	Maintenance cost	Availability	Emission	Fuel cost	Power generated
Solar	0.040395169	0.013438026	0.063952171	0.018898224	0.018898224	0.324429486
Wind	0.053587515	0.039858553	0.017004623	0.018898224	0.018898224	0.067206566
Diesel	0.027021016	0.053853334	0.026985598	0.075592895	0.075592895	0.257315747
Biomass	0.067700257	0.067848115	0.064533074	0.056694671	0.018898224	0.126986992
Battery	0.013533234	0.026966033	0.026985598	0.018898224	0.056694671	0.240606932
A+	0.013533234	0.013438026	0.063952171	0.018898224	0.018898224	0.324429486
A-	0.067700257	0.067848115	0.017004623	0.075592895	0.075592895	0.067206566

Table 1.7 Allocated rank to the each individual configuration

Energy source	D+	D-	C	Rank
Solar	0.026862	0.280183	0.912515	1
Wind	0.265838	0.086088	0.244619	5
Diesel	0.118805	0.195171	0.621611	2
Biomass	0.215191	0.096975	0.310652	4
Battery	0.100022	0.195817	0.661904	3

sources and the combination configuration, respectively. From the relative distance to the ideal solution, the energy systems have been ranked, as shown in Tables 1.7 and 1.9. Among the individual energy sources, the solar configuration is found to be the most optimal, while the solar–diesel–battery configuration is chosen to be the best for the case study.

Feasibility of the solar–diesel–battery energy system opted for the present investigation is verified from TOPSIS analysis. The variation of each combination of energy source configuration with energy generated, capital cost, maintenance cost, availability, emission, and fuel cost have been presented in Figs. 1.2, 1.3, 1.4, 1.5, 1.6 and 1.7, respectively.

From Fig. 1.2, it is evident that the highest ranked energy system combination, solar–diesel–battery, has the least capital requirement as compared to another configuration.

Table 1.8 Weighted normalized decision matrix for combination source configurations

Weightage	0.1	0.1	0.1	0.1	0.1	0.5
	Capital cost	Maintenance cost	Availability	Emission	Fuel cost	Power generated
Solar + Diesel + Battery	0.028662252	0.038533732	0.048443619	0.046017899	0.061666984	0.265684466
Solar + Wind + Battery	0.038216336	0.033028913	0.038291221	0.02300895	0.034259435	0.199263349
Solar + Wind + Diesel	0.042993378	0.044038551	0.038291221	0.046017899	0.04796321	0.221403721
Solar + Diesel + Biomass	0.050827726	0.055048188	0.052132255	0.061357199	0.04796321	0.243544094
Solar + Wind + Biomass	0.057324504	0.049543369	0.044754984	0.038348249	0.020555661	0.177122977
A+	0.057324504	0.038533732	0.048443619	0.046017899	0.04796321	0.265684466
A-	0.050827726	0.055048188	0.038291221	0.046017899	0.04796321	0.199263349

Table 1.9 Allocated rank to each combination configuration

Energy source	D+	D–	C	Rank
Solar + Diesel + Battery	0.03177	0.073937	0.699454	1
Solar + Wind + Battery	0.075016	0.036893	0.329669	4
Solar + Wind + Diesel	0.047954	0.025938	0.351029	3
Solar + Diesel + Biomass	0.032466	0.048864	0.600811	2
Solar + Wind + Biomass	0.093744	0.03761	0.286323	5

Similarly, Figs. 1.2, 1.3, and 1.4 show that the solar–diesel–battery configuration is near to the ideal best configuration, though Fig. 1.7 shows that solar–diesel battery configuration has the highest fuel cost which is not favorable. Figure 1.1 represents the flowchart of TOPSIS optimization scheme.

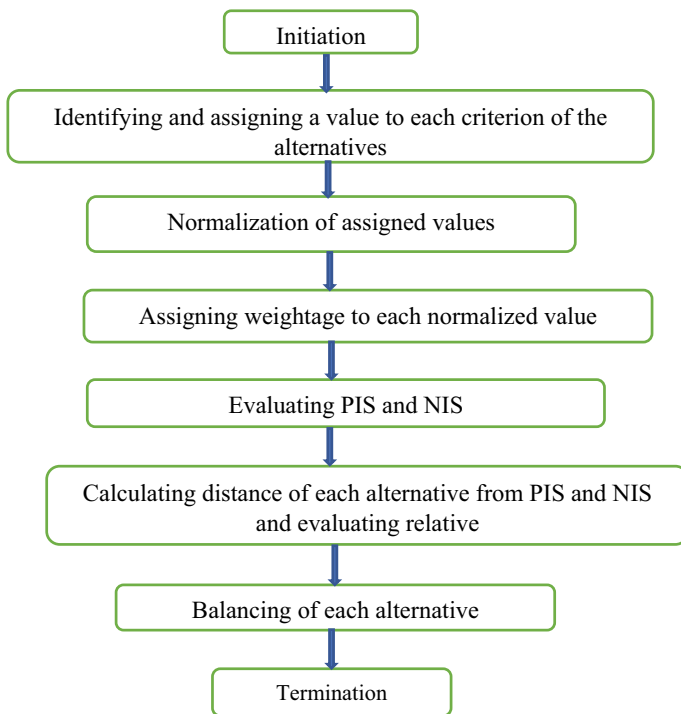


Fig. 1.1 Flowchart of TOPSIS optimization method

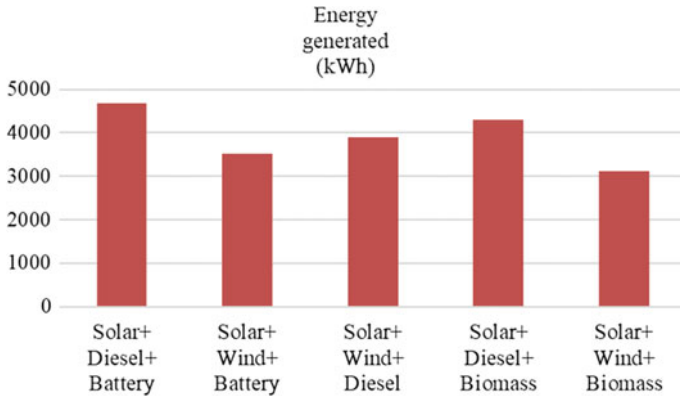


Fig. 1.2 Combination configuration versus energy generated

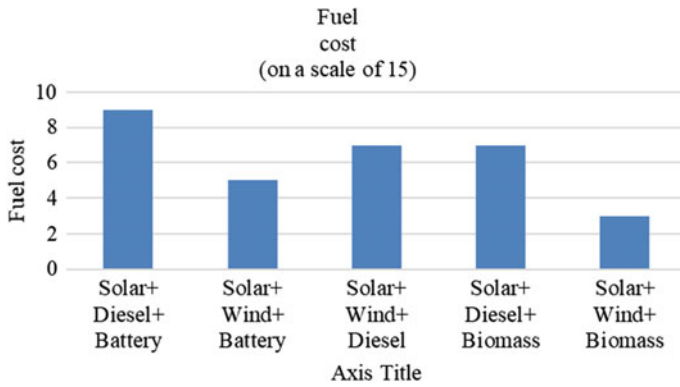


Fig. 1.3 Combination configuration versus fuel cost

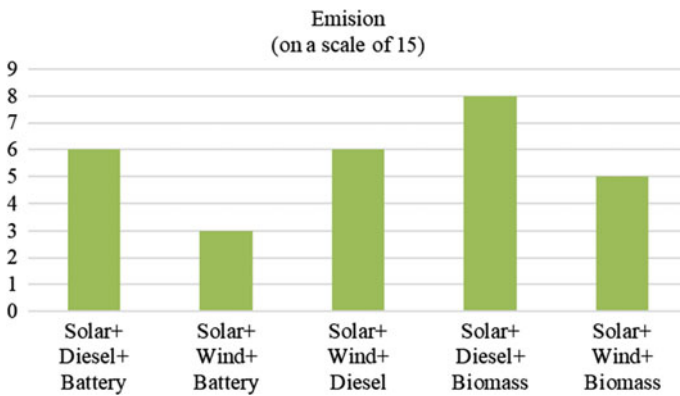


Fig. 1.4 Combination configuration versus emission

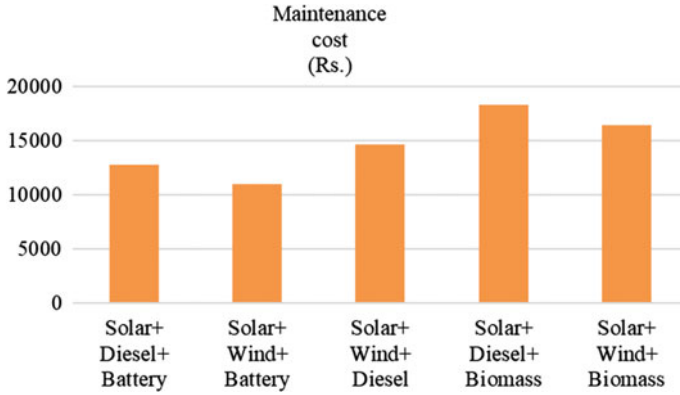


Fig. 1.5 Combination configuration versus maintenance cost

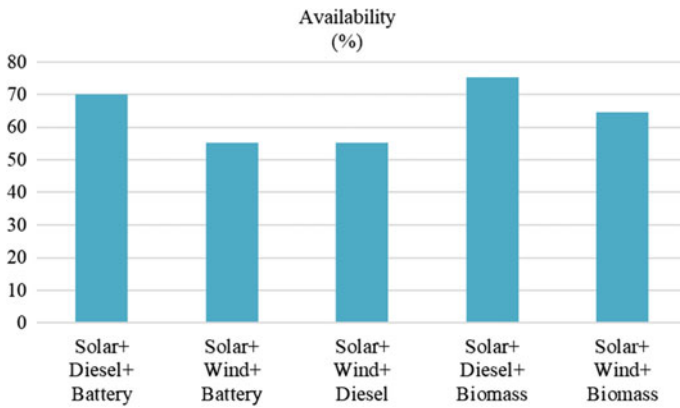


Fig. 1.6 Combination configuration versus availability

1.4 Conclusions

The present investigation aims to present an optimisation analysis of HES as a substitute for meeting the electrical energy requirements of the lecture halls in the mechanical department, RLJIT, Doddaballapur, Bengaluru. A multicriteria decision making is used for evaluating the optimal combination of energy systems. The present study has used TOPSIS method, and results show that solar–diesel–battery is the best combination among all other alternatives. Major conclusions drawn from the present investigation is as follows:

- The present case study site has a very low wind speed, so WES(s) are inadequate for energy generation.

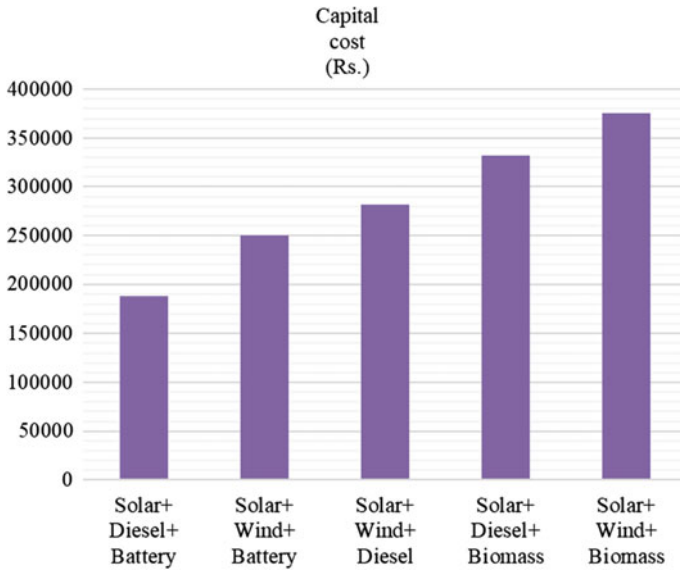


Fig. 1.7 Combination configuration versus capital cost

- The biomass energy is also inadequate due to lot of constraints like low calorific value, time taken for fermentation, low efficiency, and also capital cost, etc.
- Solar–diesel–battery secures the highest rank on the basis of TOPSIS methodology and hence is obtained to be the most optimal combination for the present scenario.
- The findings of this research work can be utilized for further investigations and evaluation of better energy configurations to achieve a higher efficiency in power generation and supply.

Although there are many applications of hybrid energy systems already in use and also various research works have been carried out in the field of optimization of renewable energy sources, there is still much research to continue. The main reason of the research work in this field is to achieve better efficiency at reduced costs and emissions. There are many future scopes of research on optimization of renewable energy sources. As in today’s world, it is needed to find different sources of renewable energy, and this alone forms a major area of research. Waste energy-converting devices like biomass gasifiers can be studied. Also, different optimization techniques can be used to find the optimal combination for the power generation.

Acknowledgements Authors are thankful to the Department of Mechanical Engineering, RLJIT, Doddaballpur, for providing the opportunity to carry out this research work.

References

1. Guangqian, D., Bekhrad, K., Azarikhah, P., Maleki, A.: A hybrid algorithm based optimization on modeling of grid independent biodiesel-based hybrid solar/wind systems. *Renew. Energ.* **122**, 551–560 (2018)
2. Miglania, S., Orehouniga, K., Carmeliet, J.: Design and optimization of a hybrid solar ground source heat pump with seasonal regeneration. *Energ. Procedia* **122**, 1015–1020 (2017)
3. Yang, G., Zhai, X.: Optimization and performance analysis of solar hybrid CCHP systems under 7 different operation strategies. *Appl. Therm. Eng.* **133**, 327–340 (2018)
4. Penga, W., Malekic, A., Rosend, M.A., Azarikhah, P.: Optimization of a hybrid system for solar-wind-based water desalination by reverse osmosis: comparison of approaches. *Desalination* **442**, 16–31 (2018)
5. Zhang, L., Lv, M., Meng, J., Du, H.: Optimization of solar-powered hybrid airship conceptual design. *Aerosp. Sci. Technol.* **65**, 54–61 (2017)
6. Tian, Z., Perers, B., Furbo, S., Fan, J.: Thermo-economic optimization of a hybrid solar district heating plant with flat plate collectors and parabolic trough collectors in series. *Energ. Convers. Manage.* **165**, 92–101 (2018)
7. Wang, F.C., Chen, H.C.: The development and optimization of customized hybrid power systems. *Int. J. Hydrogen Energ.* **41**, 12261–12272 (2016)
8. Eteibaa, M.B., Barakat, S., Samy, M.M., Wahba, W.I.: Optimization of an off-grid PV/Biomass hybrid system with different battery technologies. *Sustain. Cities Soc.* **40**, 713–727 (2018)
9. Wang, H., Cai, W., Wang, Y.: Optimization of a hybrid ejector air conditioning system with PSOGA. *Appl. Therm. Eng.* **112**, 1474–1486 (2017)
10. Ariyoa, B.O., Akoredea, M.F., Omeizaa, I.O.A., Amudaa, S.A.Y., Oladeji, S.A.: Optimisation analysis of a stand-alone hybrid energy system for the senate building, university of Ilorin, Nigeria. *J. Build. Eng.* **19**, 285–294 (2018)
11. Hao, Z., Hui, T., Guobiao, C.: Hybrid uncertainty-based design optimization and its application to hybrid rocket motors for manned lunar landing. *Chin. J. Aeronaut.* **30**(2), 719–725 (2017)
12. Saini, P.K., Biswas, A., Bhanja, D.: Performance evaluation and simulation of solar panel, wind mill, fuel cell hybrid system for Small scale energy harvesting. *J. Clean Energ. Technol.* **3**, 417–421 (2015)
13. Tao, M., Guo, K., Huang, Z., Liu, H., Liu, C.: A hybrid optimization method to design shapes of three-dimensional flow channels. *Chem. Eng. Res. Des.* **114**, 190–201 (2016)
14. Cornejo-Bueno, L., Garrido-Merchán, E.C., Hernández-Lobato, D., Salcedo-Sanz, S.: Bayesian optimization of a hybrid system for robust ocean wave features prediction. *Neurocomputing* **275**, 818–828 (2018)
15. Biswas, A., Kumar, A.: Techno-economic optimization of a stand-alone PV/PHS/battery systems for very low load situation. *7*(2), 844–856 (2017)
16. Baruah, M., Sarma, L., Saikia, D., Sarma, S.: Average monthly solar radiations at various places of north east India. *Int. J. Innov. Res. Dev.* **1**(7) (2012)

Chapter 2

A Study of Internet of Things in Smart Grid and Smart Grid Security



Kaushik Kalita, Partha Pratim Borah, and Kankan Kishore Pathak

Abstract The Internet of Things (IoT) may be demarcated as any kind of network that is embedded with sensors, interlinked with software, and other technologies for communication or connectivity of devices over the Internet. IoT is a massive lively global network infrastructure and plays a chief role in smart grid growth and enhances intelligent grid information and communication. Smart grid (SG) is usually a data communication network that is consolidated with a power grid to collect data and information from the substation, consumers, and transmission lines. With IoT, it is like an upgraded version of the network. In this chapter, an attempt has been made to study various applications, communication infrastructures, protocols, and security services of IoT in SG. The importance of securities in the SG for secure communications and prevention of all possible failures or threats is to be discussed thoroughly. Moreover, an attempt has been made to give an idea of cyber security for the SG and its privacy is also to be addressed in this chapter.

2.1 Introduction

A power grid has to be promoted so that it may adjust to variations during growing power outages, demands, and new requirements equipped with the grid and can undergo self-healing. The grid configuration is upgraded for this purpose with the assist of IoT vision. This change is termed as smart grid (SG) which can adjust to changes and self-assist ones. IoT provides SG better and sustainable power and it has proved to be more reliable than the traditional ones. For this purpose, many power companies are taking attempts to initiate the concept of IoT as a futuristic technology, which lead to connection of each device in the grid. It can be implemented

K. Kalita

Department of Electronics and Communication Engineering, Girijananda Chowdhury Institute of Management and Technology, Guwahati, Assam 781017, India

P. P. Borah · K. K. Pathak (✉)

Department of Mechanical Engineering, Girijananda Chowdhury Institute of Management and Technology, Guwahati, Assam 781017, India

e-mail: kankan_me@gimt-guwahati.ac.in

along with supervisory control and data acquisition (SCADA) and digital subscriber line (DSL) which enables rapid response from the distribution side also. Wired and wireless technologies are available for communication in the smart grid. Wired technology like fiber optics, power line communication (PLC), DSL, and wireless technology involving WLAN and WiMAX are employed presently [33]. IoT-based SG uses as a combination of efficient energy utilization and monitoring and controlling all grid devices and the challenges like security, no connection faults, noises during communication, cost, and information privacy are dealt mostly by software approaches [32].

In IoT-based SG architecture, the equipment shares data with each other through the Internet cloud. In the wireless nodes, resource constraints and shortage of spectrum are major problems. Deployment of SGs has developed the intelligence of grid system interoperation by multi-directional data flow provision between any two or more devices in the networking to achieve a power industry that can revolutionize the industry of power generation, thus, providing adequate data from metering to substation, distributions, transmission, and generation, for increasing security, reliability, and effective control and monitoring of all aspects related to service systems. Ghasempour [15] highlighted that the most crucial application of IoT in SG is data exchanging network which is combined with the power grid to gather and examine data that are acquired from different grid components. Smart grids (SG) have proven protections which are not present in the central control system or the protection schemes for the infrastructure related to power from its value and for smart or advanced homes [34]. The smart grids were introduced for controlling the shortcoming of standard electrical grids using computerized equipment [14]. Since the existence of communication nodes, it has cause to be the expose to attack in the energy sectors, hence, there is a need of a reliable working intelligence of interconnected components for upgraded security protocols, load estimation, demand side management (DSM), cost information, and sustainable use of non-conventional energy systems. There are many challenging issues needed to be addressed and both technology and social knots have to be united before IoT technology being extensively accepted. SGs are a critical infrastructure which attracts cyber-attacks, since monitoring and control can be done over standard Internet-based procedures and solutions relies on public communication infrastructure [16]. This may result in economical losses to the unity and can affect the electric assets, by breaking the real-time balance between energy consumption and production, through operating data produced by smart object or directed from the utility [7].

In this chapter, IoT and its properties in different aspect are described in Sect. 2.2; Sect. 2.3 covers detailed explanation of smart grid, its goals, and challenges. Section 2.4 covers about the applications and services of IoT in SG. In the latter part of this chapter, Sects. 2.5 and 2.6 discuss about the security and cyber security challenges for SG.

2.2 Internet of Things

IoT is the latest upgradation in computer system and electronic engineering which results in enhancing the reliability of the grid that has been the greatest challenge for the technical designers. For enhancing the existing standard grid's utmost reliability and its quick reaction time, the present standard grid with IoT could be introduced. Wortmann and Fluchter [43] have discussed the origin of IoT dated back to more than 15 years. Their work has attributed to the work of the Auto-ID Labs at the Massachusetts Institute of Technology (MIT) on radio-frequency identification (RFID) infrastructure. Assembly manufacturing plot of Intel uses IoT to constantly record the huge amount of data from devices and other framework connected to the grid system for fast leadership action, directed reaction, and insightful results by technically improved hardware operation at minimal cost [28].

2.2.1 Definition

IoT may be stated as the networked interaction of smart devices infrastructure and are embedded with ubiquitous intelligence. IoT may increase the ubiquity of the Internet by assimilating every object for communication via embedded system, which leads to an extremely dispersed network of device communicating with human beings as well as other devices [44]. IoT makes possible the development of a massive number of applications, of which only a very minor part is currently available to the society. IoT application can be assembled under the mention domains:

- *Logistics and transportation domain*—buses, trains, advanced cars, as well as bicycles along with roads and/or rails are mostly embedded with sensors, actuators, and processing power [18]. Real-time data processing technology based on RFID and NFC may realize real-time monitoring of nearly every link of the supply chain, ranging from commodity design [42]. Assisted driving, mobile ticketing, and monitoring environmental parameters like temperature, humidity, and shock during the transportation; the conservation status is monitored, and augmented maps for tourists can be equipped with tags [10] that allow NFC-equipped phones to browse it and provide information about various aspects.
- *Healthcare domain*—IoT technologies in these domain can be grouped mostly into tracking of an individual in motion, this involves both real-time position tracking, and for location and material tracking to prevent left-ins, identification, and authentication for security procedure, and data collection related to integrating RFID technology with other health information, sensing devices enable function centered on patients [42].
- *Smart environment domain*—sensors and actuators associated with the network system in houses and offices can make life comfortable and smarter in several aspects. Industrial plants are automated with maximum employment of RFID

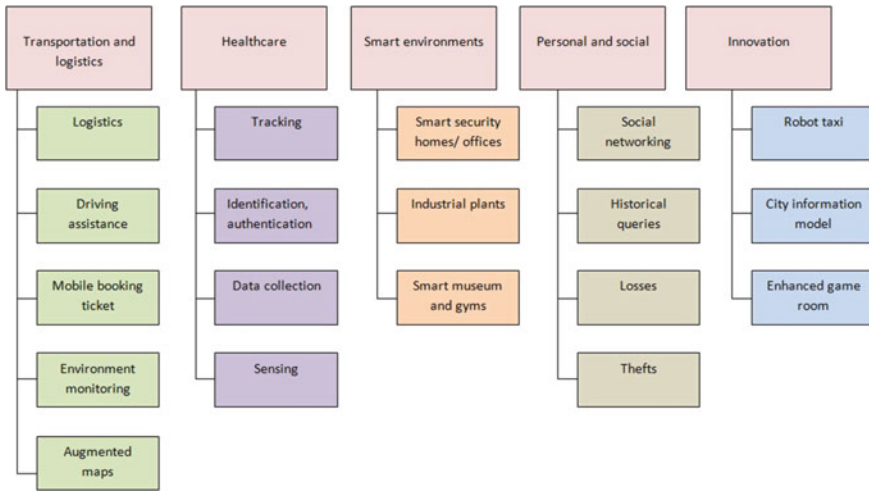


Fig. 2.1 Application domains and relevant major scenarios

tags associated with the production parts [10]. Health parameters are monitored during training session in gyms.

- *Individual and social domain*—the application under this domain is that enable the user to interact with other person to maintain and build social relationship. Historical inquiries about objects and events data let operators study drifts in their activities over time. Search engine for things is been used for searching any object which we cannot remember [22]. For locating the last recorded location of a tagged object a simple web based RFID system is used which act as a search engine for things that we want to locate.
- *Futuristic application domain*—in the future cities, robot taxis swarm together, moving in flocks, providing service where it is needed in a timely and efficient manner. A city information model (CIM) is an idea that keeps the track or monitors the statics and performance of each buildings and urban fabrics by the city government [5] (Fig. 2.1).

2.2.2 Identification of Radio Frequency

Radio signal helps in the identification of a particular target and support in acquiring the data for communication purpose. Establishing mechanical or specific optical contact in the specific target is done by RFID technology techniques. The corresponding electronic data can be identified by the electronic reader in the electronic tag by detecting items specific maker information. The most common use of electronic tags is; it is bundled to goods that are to be taken track off. For example, in the shopping mall, electronic mark is often seen. The special communication protocol

realizes reading and writing data between the electronic reader and electronic tag [11]. Generally, the electronic reader sends the desired instructions or data to the electronic tag. And when the instructions are received, the electronic tag returns the coded data in memory to the sender [10]. This is a widely used method of communication so far as it uses electromagnetic changes and it does not need contact.

2.2.3 Infrared Sensor Technology

Infrared transducer uses infrared rays to measure temperature sensitive physical properties. Infrared light includes physical properties like reflection, interference, refraction, absorption, and scattering. Anything with temperature above absolute zero, radiation infrared can be applied in it [25]. There is no friction in infrared sensor measurement, since it is done without direct contact with the measured object and therefore has high sensitivity and fast response. The infrared sensor is a combination of optical sensing system, detecting circuit, and a switching circuit [12].

2.2.4 Global Position System

GPS is associated with a space satellite, user signal receiving device, and a ground signal connecting point. It provides the consumer with speed, information, and high precious position in all types of weather condition in real-time application. Application of GPS in power system is advantageous because of its positioning function [29]. We need accurate time standard to acquire accurate synchronization purposes for monitoring and protection system in electrical power system such as microcomputer protection and security automatic equipment monitoring system, dispatching automation system, wave recorder that detects faults. With the expansion and upgradation of power grids, it requires higher standards of accuracy and convenience [25].

2.2.5 Machine/Man to Machine/Mobile

Recent development of communication technologies is gradually advancing toward integration from the upgraded mode of independent parallel. Well known examples of summing of mobile communication infrastructure and IP computer network, TV network, computer network, signal network, power network, satellite communication network are all moving toward integration. Transfer of information from one terminal to another terminal is done in M2M, which can be termed as data exchange between the machines [43]. Generally, M can represent machine or person which can

be represented as man and mobile device can be represented as mobile, which represents, M2M as the connection and communication between people or machines and mobile devices [25]. The integration of RFID, M2M, sensing network, and industrial evolution is four major technologies of IoT.

2.3 Smart Grid System

SG technologies all contribute to efficient IoT energy management solution that are currently lacking in the existing framework. What makes the IoT SG better is two-way communication between connected devices and hardware that can sense and respond to user demands. These technologies mean that a SG is more resilient and less costly than the current power infrastructure.

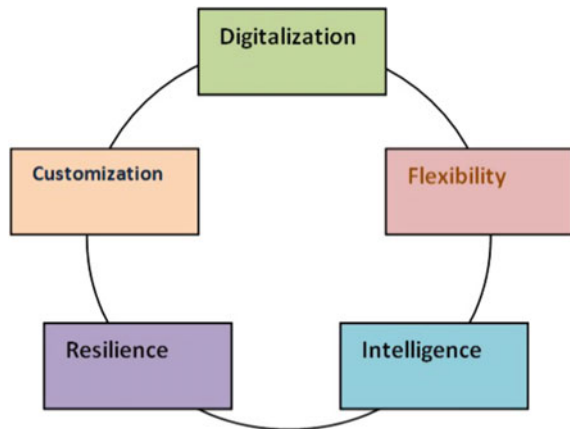
2.3.1 Definition of Smart Grid

SGs are high efficient, reliable, excessive quality, short responsive, and self-sustainable. SGs play a vital position for the improvement of contemporary day towns which is termed as smart cities. Not simply being efficient in transmitting the electricity, however, additionally reduces the carbon emission from electricity saver, which in turn improves the financial condition [33]. Utilization of the assets efficiently to boom the performance of the grid and manages the allotted era efficiently to optimize the electricity intake and offers two-way communication among the grid and the consumer [19] (Fig. 2.2).

Few important features are listed below:

- Real-time monitoring

Fig. 2.2 Smart Grid properties



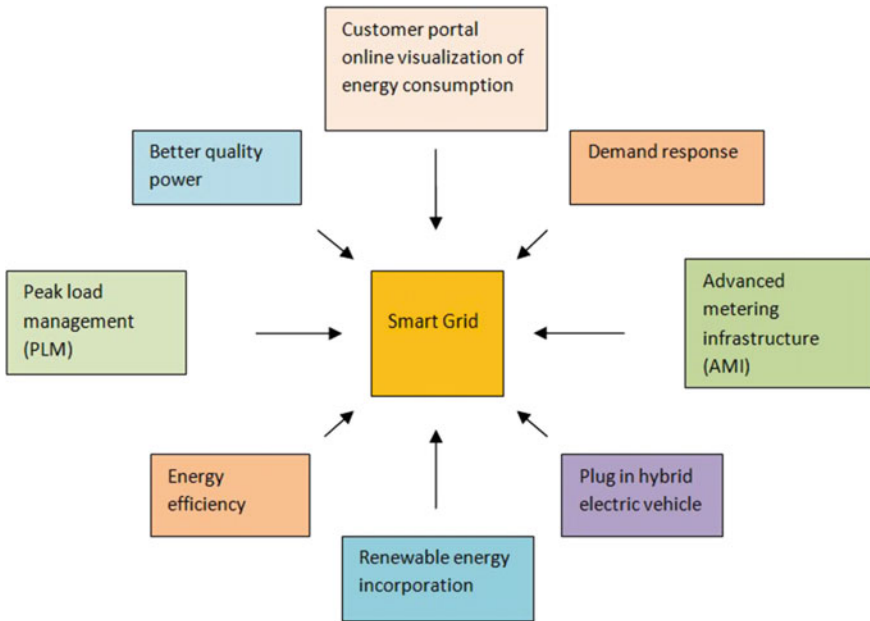


Fig. 2.3 Smart grid benefits

- Quick restoration and automatic outage management
- Energy management
- Tracking and managing of energy usage.

Advantage of smart grid consists of maximal load management, improves device reliability, integration of renewable strength and simplicity of get entry to electricity, and self-sustained grids [33] (Fig. 2.3).

2.3.2 Smart Grid Architecture

The strength shipping community essentially includes subsystems, a transmission system and a distribution system. The grid consists of a tracking gadget and a smart meter which maintains a track of the strength consumed. It consists of superconductive transmission lines which assist to lessen the resistive losses and additionally in like-minded to different asserts of strength like wind, solar, and so forth. The three practical additives of a SG are smart manage centers, advance transmission networks, and intelligent substations. The recent control center plays tracking primarily based totally at the statistics amassed through SCADA and remote terminal units (RTUs). Destiny statistics can be acquired from state management module, which is higher than the prevailing module in phrases of application time and robustness additionally

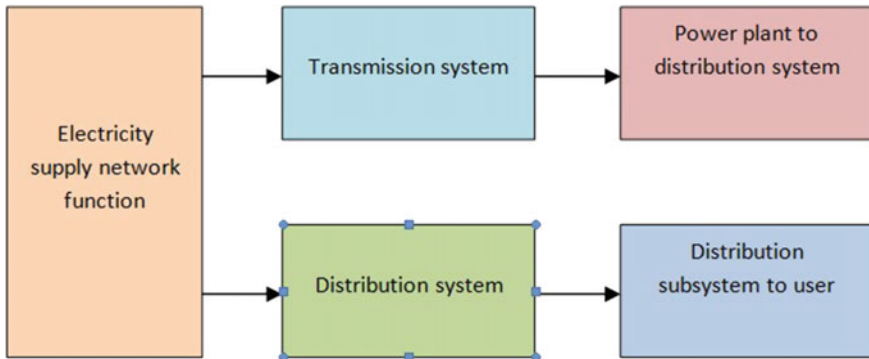


Fig. 2.4 A general model of smart grid

the final results can be blended with a extensive place GIS, and a visible show can be provided [24]. Future is predicted to have online time domain-primarily based totally analysis. These might consist of voltage balance and temporary angular balance. In the future, proactive and adaptive tactic scan be used and there can be coordination so that it will advance a higher manage. There are new functions which is associated with SG, which includes signal processing, sensing, superior materials, electricity electronics, verbal exchange, and computing. For long distance transmission, high-temperature composite conductors and high-temperature superconducting cables are used for electric powered transmission, considering that they have a better present day wearing capacity, low voltage drop, decreased line losses, mild in weight, and higher controllability. Six and twelve section transmission strains are used which offer more electricity transmission with decreased electromagnetic discipline and phase section cancellation. Intelligent sensors are used with superior signal processing to degree the value of line parameters and display the fame with the sensor location. In smart substation, equipments have to be greater dependable and known for capabilities like tracking, controlling, operating, shielding and maintaining [19] (Fig. 2.4).

2.3.3 The Smart Grid Goals and Challenges

2.3.3.1 Goals

The modern power grid of the present time consists of more than 9200 power production units, more than 10 lakh MWs of production capacity, which are linked via 3 lakh miles of transmission lines [39]. The one vital requirement of electricity is its immediate utilization just after its generation which results in blackouts and burnouts. Moreover, efficiency is also an important aspect of the modern power grid. Another cause of major concern is the grid security. The centralized architecture of the present

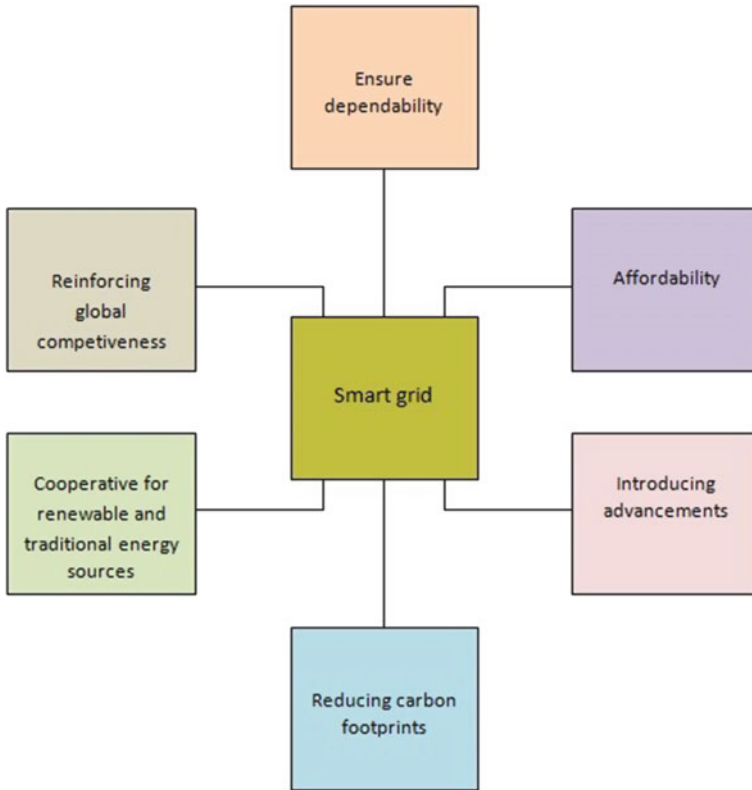


Fig. 2.5 Smart grids goals

power grid makes it more susceptible to attacks. Thus, the smart grid system is introduced which integrates power, communication, as well as computer control. It aims in the efficient control of power supply with reduction in the carbon emission [16]. Digital platform is the basic necessity of a smart grid for a fast and reliable system. A SG should be adaptable, compatible, and expandable because of its flexibility. It should inherit intelligent technology which can be reliable and the system should be customizable by the customer [19] (Fig. 2.5).

2.3.3.2 Challenges

Apart from IoT being a promising technology in the smart grid framework, it has certain disadvantages too. It sometimes leads to disaster. Our lifestyle is completely dependent on the energy market, but the present day infrastructure of SG is very complex which is a major challenge. Monitoring and control of the SG is done over the Internet and few are dependent on public communication technologies, so SGs are

vulnerable to cyber-attacks. Modification in power industry is directed by the penetration of distributed generation and non-conventional energy sources [3]. Because of the growing electricity demand, electricity should be generated and managed carefully. This results in entrepreneurs and local electric industries at distribution level which is a challenge for the reliability and system efficiency. Some of the challenges of smart grid include:

- Infrastructure of the grid
- Concern over storage and stability
- Communication issues
- Cyber security
- Energy management
- Data management [34].

2.4 IoT Application and Services in Smart Grids

IoT has a large and complicated communication infrastructure. The system is primarily based on transmission, acquiring, processing, and storing of statistics in a dependable or stable and reliable manner. In contrast, SG is related to many technologies on generation, distribution, transmission, and consumption in addition to IoT. Our society has to realize the current state of any era associated with the development in their private existence, and manages their very own micro grid supplies, domestic appliance, EVs, and to manipulate and screen the day by day technical updates on offerings which includes electricity, gas, and water [35]. ICT technologies are regularly utilized by the carrier issuer for management and detection of the fault, monitoring, and goals for troubleshooting the fault. The communication shape is being upgraded with the aid of using the use of IoT era in SG equipments. The networking is related to low-price and low-strength microprocessors, virtual communication infrastructure which has safety and reliability supports, and a smart communication layer which has the ability to evolve and protocol systems to have interaction with diverse software program technology and hardware. Some communication technology which incorporates LTE-A, UMTS, LTE, LPWAN, and slender band IOT (NB-IOT) has been advanced further to BLE for personal area networks and Zigbee within side the use of HEMS [21]. Long-range communication is supplied with the aid of using the stepped forward technology within side the unlicensed bands for SG and IoT programs. The functions of evolving LPWAN permit end-consumer IoT programs that require excessive battery existence, low-price equipments, information transmission, and it is able to be utilized in each subject wherein the cell technology is not always feasible. The IoT and SG infrastructure have a main function in software grid system and generation-transmission-distribution cycles and additionally improves day by day existence elements together with smart metropolis and smart constructing infrastructure [17]. For protection protocols, IoT frameworks which

have been proposed with the aid of using many institutes are Arrowhead Framework, Industrial Internet Reference Architecture (IIRA), ETSI structure for M2M, Model Industrie 4.0 (RAMI 4.0), IoT-A, ISO/IEC WD 30141 IoT reference structure (IoT RA), Reference Architecture and the IEEE well-known for an Architecture Framework for IoT [21].

2.4.1 Driving Factors of IoT for Smart Grid

The wireless controlling and monitoring ability of SG networking, which increases the abilities of power plants for more robust DSM and distributed generation (DG) with minimal losses. Hence, demand forecasting (DF) and automatic generation control (AGC) in SG are some control structure required for power generation cycle [23]. The load and supply range as a result of extensive utilization of EVs, non-conventional energy source, strength garage device, and smart clients with their personal distributed energy resources (DERs) adversely have an effect on the not unusual place call for control approaches. The goal of a smart control device may be indexed as strength exceptional and DSM, strength manages, sustainability and fee control, and DG manage. The sluggish and growing integration of supply load to the energy grid calls for strong DF to control the periodic cycle. Another manage technique is AGC which is likewise referred to as secondary frequency manage technique. It addresses troubles reason via means of penetration of intermittent RESs [23]. These manage techniques have been powerful on gradual and restrained modified in load profile. Therefore, they turn out to be insufficient toward the current integration of RESs and distributed generation supply drawing nonlinear dynamics. The AGC manages the strength call by means of monitoring and compensating the frequency of whole structures seeing that a fluctuation at the load reasons equal adjustments at the device frequency, and the weight call is compensated via means of stabilizing the device frequency again [21]. The riding technology of IOT within side the context of SG may be essentially grouped into 3 categories:

- Technologies of data acquisition which produces appropriate information from “things.”
- Data processing, ICT and management technologies.
- Security and privacy awareness technologies.

2.4.2 Communication Infrastructure of IoT

Communication technologies were advanced for distinctive utility planes and requirements. Some of those technologies are not unusual place for unique utility planes which includes Bluetooth in private networks and Zigbee in domestic and tool automations, and the other communication technology offers huge utility regions which includes LPWAN, Wi-Fi, and mobile technology. The communication and

insurance plans of SG may be categorized into three corporations as NAN, HAN, and WAN. The HAN is important for residential devices with smart appliances, power control systems, electricity manipulate tools, ESSs, PV panels, small-scale wind turbines, electric powered motors, and smart meters [2]. NAN offers with distribution degree of SG in which a set of residential or business masses were aggregated in a substation or transformer while WAN friends numerous NAN regions for control. IEEE 802.11 or IEEE 802.15.4 primarily based totally on communication technology may be good enough for HAN and NANs, while WANs require fiber optic, UMTS, LTE, LTE-A kind large insurance communication technology [37]. The maximum good sized improvement were visible within-side the closing decade with Bluetooth low power, IEEE 802.11 primarily based total community technology, IEEE 802.15.fourprimarily based total superior modems, and cellular communication which includes UMTS, LTE-A, LTE and 5G [21].

Software-defined network (SDN) presents development to decorate flexibility, reliability, scalability, and interoperability of IoT-primarily based totally SG communication infrastructure. SDN gives an open structure version in three ranges with the aid of using isolating manipulate and facts planes, allowing centralized logical manipulate and incorporating community programming capability [29]. Thus, SDN copes with verbal exchange issues came about in traditional structure combining safety manipulating, billing, and tracking facts transmission. Its allows communicating machine for keeping apart decided on gadgets upon detection and safety approach, intrusion detection, reducing excessive visitors, and denial of carrier attacks and far flung manipulate sensors and smart meters.

2.4.3 IoT Protocols

There are main IoT protocol type proposed one is primarily based on records trade protocols as bus-primarily based totally and broker-primarily based totally even as the alternative one lists the protocol into three sections as utility protocol, provider discovery protocol and infrastructure protocol. The bus-primarily based totally protocol allows the customer to transmit a specific message to the assigned developer of that message. The provider discovery protocol consists of Data Distribution Service (DDS), Extensible Messaging and Presence Protocol (XMPP), and Representational State Transfer (REST). The distinguished broker-primarily based on IoT protocols are superior message queuing protocol (AMQP), CoAP, Java messaging provider API (JMS), and MQTT protocols. Another type for those protocols is via means of identifying that if they're message-centric or records-centric. Constrained Application Protocol (CoAP) is a web-primarily based on customer and server version protocol is primarily based on REST structure on HTTP and operates within side the utility layer (APP) [1]. The constrain gadgets inclusive of sensors or sensor nodes are applied as servers for IoT applications. AMQP is likewise a APP protocol as CoAP this is primarily based on message-centric structure. AMQP makes use of TCP and it guarantees the hit message shipping thanks to its

authentication and encryption strategies primarily based on SSL/TLS control. The DDS is a latest post/subscribe protocol utilized in M2M communication to allow real-time, excessive overall performance and interoperable records transmission [27]. The protocol consists of records-centric post and subscribes (DCPS) version, and DDS interoperability Wire Protocol (DDSI) that DCPS identifies the DDS structure, and DDSI defines interoperability structure. XMPP is a message-orientated middleware to transmit voice and video records in decentralized customer-subscriber structure. XMPP allows consumer to talk via means of immediate messages on web-primarily based on platform no matter any OS [21].

2.4.4 Future Research Direction

Despite considerable researches for the transformation of traditional software grid to SG had been finished as much as date, there none the less main demanding situations exist to be solved for improving, interoperability, connectivity, reliability and safety of SG CPS [45]. Since the SG infrastructure encompasses complete interplay of energy era, transmission, distribution, and intake environments, it calls for a massive and dependable communication interface to manipulate, control, and reveal this machine. The complexity and heterogeneity of energy and communication structures comprising the SG infrastructure poses demanding situations on interoperability of devices, cyber-architectural safety, resiliency, and statistics control problems. Although the massive operation place of SG attracts a heterogeneous ecosystem, the main demanding situations may be labeled into threefold as manipulate, communication and safety of machine [20]. The demanding situations on manipulate problems are met at era, transmission, distribution, and intake degree that consist of DER integration, far flung tracking, transmission line tracking, PMU and PQ analysis, RES integration, DSM, DR, load control, interoperability, and rising EV programs. It is broadly widespread that maximum of those demanding situations regarding manipulate problems had been solved, and current research have proposed diverse manipulate techniques to conquer energy community deficiencies. However, use of communication machine primarily based on big quantity of various technology and protocols poses numerous demanding situations on interoperability and safety problems.

While the communication networks are essential to enhance the improvement of SG, numerous demanding situations are addressed for robust, secure, resilient, and operational SG communication community. The two-directional communication infrastructure of smart meters is enabled via means of diverse Wi-Fi technology which includes IEEE 802.15.4, IEEE 802.11, cellular, and place community. Therefore, the variety of communication technology running within side the equal infrastructure calls for standardized protocol and alertness interfaces to make certain interoperability of whole machine. To this case, well-known APIs and middleware traits are required to address main demanding situations of heterogeneous infrastructure of communication technology. The particular protocol-primarily based on

programs are any other rising studies place within side the context of SG and IoT integration wherein CoAP, AMQP, MQTT, and JMS are the distinguished ones [8]. The safety and privacy researches are also anticipated to be emerge because of numerous special communication protocol, and framework which are applied in IoT, and SG interplays with precise coding and encryption infrastructure. Some researchers surveyed in this subject matter have remarked that public key infrastructure (PKI) utilization might also additionally address the safety problems. The safety problems have additionally expanded the researches on PHY and MAC layer safety, community layer, IEEE802.15.4 cease-to-cess safety, IP and six LoWPAN safety, and routing safety [21]. The studies on energy-efficient IoT architectures are modern day to control sources and communication infrastructure with low-energy intake and surprisingly green. The subtle structure which can be composed via means of sensing and manipulate layers, statistics processing layers, and alertness layers are being broadly researched within side the context of subsequent era IoT architectures. Micro grid control, equipment manipulate, EV manipulate and tracking researches also are ever-evolving structures within side the context of IoT-primarily based totally SG programs [8]. The sensible manipulate capabilities are described as one of the studies guidelines within side the smart constructing control topics.

2.5 Smart Grid Security and Protocol

Three criteria defined by The National Institute of Standards and Technology (NIST) for the maintenance of security of data or information in the SG for its protection are described below [31]:

- *Confidentiality* can be defined as the preservation of authorized restrictions for the disclosure and access of information. It is essential for the protection of both personal and registered information from being disclosed and accessed by individuals, authorized entities, or processes.
- *Availability* can be defined as the assurance of reliable and timely access to information. It is an important security criterion in the SG because the loss of availability creates trouble to access information in a SG.
- *Integrity* in SG can be defined as the protection against destruction or inappropriate modification of data.
- *Accountability* assures system manageability and records every task performed by a device, person, or a public authority and ensures that everyone can acknowledge his/her action. The recorded data is accessible and can be used for determining the attacker [31].

2.5.1 Smart Grid Security Threats Classification by Source

The different challenges and threats experienced by SG are identified. It is necessary that the threats are well-defined. A complete approach for the effective security requirements must be established and followed. Hence, a study of the threats' sources is important.

2.5.1.1 Technical Sources of Smart Grid Threats

It is classified based on the diagnosed threats which may be traced to the technical elements of SGs. Three key elements of the technical reasserts of those threats are diagnosed and those are infrastructure safety, technical operation safety and systems' statistics control safety.

- *The infrastructure security*—SGs infrastructure could be very complicated structures which can be geographically, logically, and economically distributed, interconnecting users, electricity plants, utilities, transmission, distribution, substations, transformers, etc. As properly as advanced metering infrastructure (AMI), the related conversation, and ICT gadgets along with aggregate of wireless, fiber optic, power line carrier (PLC), and conventional cable or Ethernet, hence, making SGs, a noticeably smart gadget and as such, the safety of the infrastructure turns into critical [38]. The AMI is extra inclined as it's far important to SG operation. AMI safety (AMI-SEC) project pressure changed into pronounced to have evolved a few constant and preferred safety guidelines, through final replace given that 2009, for implementation of AMI answer consisting of meter statistics control gadget (MDMS) down until smart meter interface [34].
- *Technical operational security*—The complexity of the grid necessitates secured operational schemes. This is due to the fact that disasters might also additionally have extra impact given that essential infrastructure rely upon secured and dependable power operations and components for electricity and manipulation. Some of the coordination within side the operation of the device is below manipulate, however, a few part of the operations additionally require on-subject interest of operators on the software manipulate centers, particularly for the duration of emergencies in a few cases. In a resilient grid device, well timed reputation and analysis of trouble situations are key elements for stopping unfold of disturbances [26]. Since faults may also arise because of failure of protecting devices, there may be want to layout the device to be self-recovery with the aid of making sure perfect fault tolerance degree and provision of considered necessary redundancy to accomplishing a dependable operational security [4].
- *Systems' data management security*—It covers actual time recording, tracking and storing of vital information and information, safety of information toward assaults, guidelines and guidelines guiding information policy, privacy adherence with the aid of using running personnel, customers' delight in phrases of privacy assurance, etc. The developing issues over the opportunities of privateness

breach with the aid of using the application organizations in probable revealing customers' information are predominant challenge for customers. Although SMS have but modified the character of SM information frauds or assaults, compromising the meter with the aid of using far flung penetration and manipulate of recorded and saved information can be a supply of very state-of-the-art assaults able to permitting vague modifications to customer's utilization and falsely indict cantered sufferers or relying on their intention, release large-scale assaults on the principle grid [34].

2.5.1.2 Non-technical Sources of Smart Grids Threats

The non-technical reassets of SGs threats offers with the ones elements that may counter in opposition to the deployment or operation. Such elements encompass herbal or guy initiated additionally surroundings risks inclusive of earthquakes, floods, falling of trees, bush burning, etc. Government regulatory policies, making plans and implementation or maybe marketplace operations and personal zone mobilizations, etc. Although, thinking about the causative mode, a few elements are taken into consideration. Non-technical, however, might also additionally require technical method in tackling it.

- *Environment security*—It could be very crucial in SGs implementation because it enables management and keep away from capable catastrophic results at the infrastructure because of any of the herbal or synthetic inflicted surroundings dangers which include flood, tremors, earthquakes, landslides, falling of trees, burning of bushes, etc. with the aim of using articulating smart reaction. Smart reaction, primarily based on environmental attention, is essentially executed with the aim of using sending suitable hazard alert primarily based on acquired records and imparting change feeder for essential infrastructure in such emergencies. GIS, primarily based on instant records, is fundamental on this evaluation specially in terms of herbal screw ups forecast and evaluation, that is utilized in figuring out environmental threats alert [6].
- *Government regulatory policies and implementation*—As there are opportunities in SGs technologies and services; the conventional utility is facing challenges all due to the requirement of new technologies, policies, increasing demands, and business models involved in upgrading to SGs era. Therefore, governments' collaboration in providing requisite regulatory policies to aid smooth market operations and private sector mobilizations is the key for achieving the set objective of SG deployment. Government has a deep role to play in the areas of investing in research and development [34].

2.5.2 Attack Detection and Counter-Measures

The power grid due to complexity community is at risk of physical attacks. With the smart grid, greater infrastructures are needed for safety in opposition to attackers. Physical safety of power plants, equipment, and community is needed, inclusive of barriers, locks, and video surveillance. Working non-public safety awareness, screening, and schooling also are required measures to save assaults. The worst type of assaults to the SG is the denial of service (DoS) assault, due the impossibility to get right of entry to the gadgets and systems. To come across this assault, four techniques may be used: packet-primarily based, sign-primarily based, proactive, and hybrid. The sign-primarily based detection approach includes measuring the sign strength, evaluating it to a threshold value and elevating an alarm while deviations occur. Packet-primarily based detection approach measures the transmission consequences of every packet. It works by assuming that overall performance degradation is resulting from packet transmission failure, indicating a DoS assault.

The proactive approach tries to become aware of DoS assaults by sending probing packets to check or degree the repute of capacity attackers. Lastly, the hybrid approach combines specific thoughts to enhance assault detection accuracy. For instance, sign-primarily based and packet-primarily based techniques may be utilized in Wi-Fi community to become aware of flooding or jamming assaults. To keep away from cyber assaults on SG there also are cryptographic approach to reap steady communication and statistics safety for any statistics system. Several stages of encryption are preferred because of the restricted computational sources in SG layers. All SG gadgets require an authentication manner to keep away from impersonation assaults. Lastly, key control is primarily based totally on cryptographic primitives and makes use of a public key infrastructure (PKI) to manage strength substations community or AMI community. Key control the usage of a PKI is mentioned as one of the handiest answer for securing the SG communications infrastructure [34].

2.6 Cyber Security a Challenge for Smart Grid

The SG system is a complex system for exchanging the information of an electrical infrastructure. To establish an uninterrupted and secure operation, the understanding of security requirements before providing a complete analysis of cyber security in the context of managing and distributing energy. Here, the need of cyber security in SG is described [41].

2.6.1 Cyber Security Model

Cyber security infrastructure has three main objectives: availability, integrity, and confidentiality, i.e., power availability with information integrity and customer's information confidentiality [39].

Availability: It is the most important basis for SG system. It aims to provide an uninterrupted power supply to the consumer for matching the requirements of the customer.

Confidentiality: The grid infrastructure is responsible for the security of users' data. If the data is not secured, enough informative data will be available for the attacker.

Integrity: The data or information received from the user end should be validated. The network ensures that the data is not altered. Also, authenticity of source is ensured [19].

2.6.2 SCADA System

The cyber communications of SG include communication systems, the electronic information, and services along with the data enclosed in these systems, infrastructure. This involves hardware and software systems information. It basically process, store, and communicate data. SCADA is used for this purpose acts as a control system. The SCADA is also a neutral system [19].

The main blocks of SCADA system are: Human machine interface (HMI) for presenting the processed data, a supervisory computer for collecting the data and using it for the function of processing, remote terminal units (RTUs), programmable logic controller, communication infrastructure [9].

By using the power system communication in the smart grid, the SCADA system connects to other systems like the Internet or by certain dedicated lines. The vendors are using off the shelf products as element of the SCADA systems. These products are similar to the personal computers, and thus are vulnerable to different threats [36].

A SCADA system is an essential element in the grid communications. It is used for two purposes; first the public transport system and second the public control system [19].

2.6.3 Cryptograph

Cryptography is used to secure information for the purpose of cyber-security. It is one of the most trusted and secures exchange of data. In the methodology of cryptography, the design should be robust and the algorithm should be error free.

2.6.4 Constraints

2.6.4.1 Computational Constraints

Residential meters have a few boundaries on the subject of computational strength and the cap potential to shop cryptographic materials. The destiny gadgets should have the fundamental cryptographic abilities such as the cap potential to aid symmetric ciphers for authentication. The use of low-cost hardware with embedded cryptography is vital, however, now no longer good enough for the success of excessive availability, integrity, and secrecy within side the SG.

2.6.4.2 Channel Bandwidth

The SG communications take place over different channels having different bandwidths. Advanced encryption standard (AES) is a cipher, which produces the equal number of output bits as input bits. These bits cannot be compressed, since they are random in nature and is encrypted. For compressing this data, we have to compress before encryption. Another factor of concern is the cipher-based message authentication code (CMAC), which is added as a fixed overhead to a message and is usually 64 bits or 96 bits. These overheads are considered important when we are dealing with short messages, since they need large channel bandwidth [19].

2.6.4.3 Connectivity

Standard public key infrastructure-primarily based on peer-to-peer key status quo version, where in any peer may also want to talk with another, is not always applicable from safety factor of view for components. Many gadgets do now no longer incorporate with key server connectivity, online certificates status, certificates authorities, and protocol servers. Many connections among SG gadgets may have longer length than ordinary net connection [19].

2.6.5 General Cryptographic Issues

Entropy. An excellent source of entropy is necessary to generate cryptographic solution for creating randomness that is not available for many devices. It is solved by seeding a deterministic random bit generator (RBG) before distributing any key.

Cipher Suite. It is open and is important to establish a secure network connection via transport layer security (TLS). It ensures a secure communication between users and servers by using different algorithms and protocols.

Key Management Issues. Security protocols are dependent on security relations. There are two types for the authentication of security:

- Using secret key
- Using certificate authority

For using secret keys, it is necessary that the keys are transported from one device to another. For the transportation of these keys, a kind key is required for all the communicating devices that should be well coordinated.

Elliptic Curve Cryptography. A Cryptographic interoperability strategy (CIS) is started by National Security Agency (NSA) for government organization by selecting standard cryptography methodology. It incorporates with AES for encryption with 128 or 256 bits. A periodic upgradation of the protection modules is very necessary [19].

2.7 Conclusions

This paper has described about various aspect of IoT in SG and various SG security protocols and challenges. IoT can be considered as the main part of the existing Internet and its future direction relies on its upgradation and improvement. The application of the IoT in grid system includes power equipment installation surveillance, parking and charging of electric vehicles, application of dynamic scheduling for adjustment of home consumption, management of supply and demand of power, equipment maintenance, failure and fault detection. With the application of suitable models, proper verification, analytic stimulation and optimization tools, the network system can adapt to different challenges and it is important that proper care is taken in both operational stage as well as planning for a secured, robust and flexible grid optimization. So that it could respond to threats, source of such threats, also the nature of the threats for proper preventive response, monitoring and control, even before the threat is manifested. The development of SG infrastructure has resulted to reconciling targets for climate change, energy, and safety of the grid. Cyber security is an important aspect in grid security point of view. As the grid develops the number of nodes that will be not susceptible to cyber-attacks. Domain architecture for explaining these challenges has been described in one of the section. Cryptography and key management techniques are used for a secure system against cyber-attacks. We have covered the constraints for cryptography.

Future work may deal in providing models for tracking SG security threats by source classification for the desired resiliency as well as developing a robust simulation tool for threats sensing and response, for a stabilized system. Also researcher will focus on addressing challenges like energy acquisition, congestion, data communication, identify spoofing, and so on.

References

1. Al-Fuqaha, A., Guizani, M., Mohammadi, M., Aledhari, M., Ayyash, M.: Internet of things: a survey on enabling technologies, protocols and applications. *IEEE Commun. Surveys Tutorials* **17**(4), 2347–2376 (2015)
2. Ali, Q., Montenegro, S.: Explicit model following distributed control scheme for formation flying of mini UAVs. *Dig. Object Identifier* **4**, 397–406 (2016)
3. Amin, S.M., Wollenberg, B.F.: Toward a smart grid. *IEEE Power Energ. Mag.* 34–41 (2005)
4. Arefifar, S.A., Mohamed, Y.A.I., EL-Fouly, T.H.M.: Comprehensive operational planning framework for self-healing control actions in smart distribution grids. *IEEE Trans. Power Syst.* **28**(4), 4192–4200 (2013)
5. Atzori, L., Iera, A., Morabito, G.: The internet of things: a survey. *Comput. Netw.* **54**, 2787–2805 (2010)
6. AyyoobSharifi, A., Yoshiki Yamagata, Y.: Principles and criteria for assessing urban energy resilience: a literature review. *Renew. Sustain. Energ. Rev.* **60**, 1654–1677 (2016)
7. Bekara, C.: Security issues and challenges for the IoT-based smart grid. In: *International Workshop on Communicating Objects and Machine to Machine for Mission Critical Applications (COMMCA-2104)*. *Procedia Comput. Sci.* **34**, 532–537 (2014)
8. Bibri, S.E.: The IoT for smart sustainable cities of the future: an analytical framework for sensor-based big data applications for environmental sustainability. *Sustain. Cities Soc.* **38**, 230–253 (2018)
9. Boroomand, F., Fereidunian, A., Zamani, M.A., Amozegar, M., Jamalabadi, H.R., Nasrollahi, H., Moghimi, M., Lesani, H., Lucas, C.: Cyber security for smart grid: a human-automation interaction framework. In: *Paper published in IEEE PES Innovative Smart Grid Technologies Conference, Europe, 11–13 October 2010*
10. Broll, G., Paolucci, M., Wagner, M., Rukzio, E., Schmidt, A., Hubmann, H.: Perci: pervasive service interaction with the internet of things. *Internet Things Track* **13**(6), 74–81 (2009)
11. Coenen, S., Tenbohlen, S.: Location of PD sources in power transformers by UHF and acoustic measurements. *IEEE Trans. Dielectr. Electr. Insul.* **19**(6), 1934–1940 (2012)
12. Dada, A., Thiesse, F.: Sensor applications in the supply chain: the example of quality-based issuing of perishables. In: *The Internet of Things Lecture Notes in Computer Science*, vol. 4952, pp. 140–154
13. Delgado-Gomes, V., Martins, J.F., Lima, C., Borza, P.N.: Smart grid security issues. In: *Published in 9th International Conference on Compatibility and Power Electronics, 24–26 June 2015*
14. Divakar, P.P., Lakshmi, G.V., Devi, L.: Applications of internet of things on smart grid. *IOP Conf. Ser. Mater. Sci. Eng.* (2020)
15. Ghasempour, A.: Internet of things in smart grid: architecture, applications, services, key technologies, and challenges. *Inventions* **4**(1), 22–33 (2019)
16. Goel, S., Hong, Y.: Security challenges in smart grid implementation. In: *Smart Grid Security*, pp. 1–39. *Springer Briefs in Cyber Security* (2015)
17. Guan, Z., Li, J., Wu, L., Zhang, Y., Wu, J.: Achieving efficient and secure data acquisition for cloud-supported internet of things in smart grid. *IEEE Internet Things J.* **4**(6), 1934–1944 (2015)
18. Ilic, A., Staake, T., Fleisch, E.: Using sensor information to reduce the carbon footprint of perishable goods. *IEEE Pervasive Comput.* **8**(1), 22–29 (2009)
19. Iyer, S.: Cyber security for smart grid, cryptography, and privacy. *Int. J. Dig. Multimedia Broadcast.* (2011)
20. Jaradat, M., Jarrah, M., Bousselham, A., Jararweh, Y., Al-Ayyoub, M.: The internet of energy: smart sensor networks and big data management for smart grid. *Procedia Comput. Sci.* **56**, 592–597 (2015)
21. Kabalci, E., Kabalci, Y.: Internet of things for smart grid application. In: *From Smart Grid to Internet of Things*, pp. 249–307 (2019)

22. Karpischek, S., Michahelles, F., Resatsch, F., Fleisch, E.: Mobile sales assistant an NFC-based product information system for retailers. In: First International Workshop on Near Field Communication, 24–24 February 2009, pp. 20–23
23. Keyhani, A., Chatterjee, A.: Automatic generation control structure for smart power grids. *IEEE Trans. Smart Grid* **3**(3), 1310–1316 (2012)
24. Lee, A., Brewer, T.: Smart grid cyber security strategy and requirements. In: Advanced Security Acceleration Project—Smart Grid (2009)
25. Li, B., Lv, S., Pan, Q.: The internet of things and smart grid. In: Published in 3rd International Conference on Advances in Energy Resources and Environmental Engineering, Harbin, China, 8–10 December 2013
26. Li, F., Luo, B., Liu, P.: Secure and privacy-preserving information aggregation for smart grids. *Int. J. Sec. Netw.* **6**(1), 28–39 (2011)
27. Lin, J., Yu, W., Zhang, N., Yang, X., Zhang, H., Zhao, W.: A Survey on internet of things: architecture, enabling technologies, security and privacy, and applications. *IEEE Internet Things J.* **4**(5), 1125–1142 (2017)
28. Manoj, P., Kumar, Y.B., Gowtham, M., Vishwas, D.B., Ajay, A.V.: Internet of Things for smart grid applications. In: Advances in Smart Grid Power System Network, Control and Society, pp. 159–190 (2021)
29. Mattern, F., Floerkemeier, C.: From the internet of computers to the internet of things. In: Active Data Management to Event-based Systems and More, vol. 6462, pp. 242–259 (2010)
30. Mehrtash, A., Wang, P., Goel, L.: Reliability evaluation of power systems considering restructuring and renewable generators. *IEEE Trans. Power Syst.* **27**(1), 243–250 (2012)
31. Mrabet, Z.E., Kaabouch, N., Ghazi, H.E., Ghazi, H.E.: Cyber-security in smart grid: survey and challenges. *Comput. Electr. Eng.* **67**, 469–482 (2018)
32. Mugunthan, S.R., Vijayakumar, T.: Review on IoT based smart grid architecture implementations. *J. Electr. Eng. Autom. (EEA)* **1**(1), 12–20 (2019)
33. Nandish, B.M., Pushparajesh, V., Girish, V.: Review of internet of things in smart grid. *Int. J. Adv. Sci. Technol.* **29**(08), 2301–2306 (2020)
34. Otuoze, A.O., Mustafa, M.W., Larik, R.M.: Smart grids security challenges: classification by sources of threats. *J. Electr. Syst. Inform. Technol.* **5**, 468–483 (2018)
35. Ou, Q., Zhen, Y., Li, X., Zhang, Y., Zeng, L.: Application of internet of things in smart grid power transmission. In: Published in 2012 Third FTRA International Conference on Mobile, Ubiquitous, and Intelligent Computing, 26–28 June 2012
36. Rawat, D.B., Bajracharya, C.: Cyber security for smart grid systems: status, challenges and perspectives. In: Paper published in Proceedings of the IEEE Southeast Conference, 9–12 April 2015
37. Ray, P.P.: A survey on internet of things architectures. *J. King Saud Univ. Comput. Inform. Sci.* **30**(3), 291–319 (2018)
38. Ribeiro, I.C.G., Albuquerque, C., de Rocha, A.A.A., Passos, D.: THOR: a framework to build an advanced metering infrastructure resilient to DAP failures in smart grids. *Future Gener. Comput. Syst.* **99**, 11–26 (2019)
39. Shafiullah, G.M., Oo, M.T., Amanullah, A., Shawkat, A.B.M., Wolfs, P.: Smart grid for a sustainable future. *Smart Grid Renew. Energ.* **4**(1), 23–34 (2013)
40. Tsolakis, A.C., Moschos, I., Votis, K., Ioannidis, D., Dimitrios, T., Pandey, P., Katsikas, S., Kotsakis, E., García-Castro, R.: A secured and trusted demand response system based on blockchain technologies. In: Published in Innovations in Intelligent Systems and Applications (INISTA), 3–5 July 2018
41. Wang, W., Lu, Z.: Cyber security in the smart grid: survey and challenges. *Comput. Netw.* **57**, 1344–1371 (2013)
42. Welbourne, E., Battle, L., Cole, G., Gould, K., Rector, K., Raymer, S., Balazinska, M., Borriello, G.: Building the internet of things using RFID the RFID ecosystem experience. *Internet Things Track* **13**(3), 48–55 (2009)
43. Wortmann, F., Fluchter, K.: Internet of things technology and value added. *Bus. Inform. Syst. Eng.* **57**, 221–224 (2015)

44. Xia, F., Yang, L.T., Wang, L., Vinel, A.: Internet of things. *Int. J. Commun. Syst.* **25**, 1101–1102 (2012)
45. Zanella, A., Vangelista, L.: Internet of things for smart cities. *IEEE Internet Things J.* **1**(1), 22–32 (2014)
46. Zhang, P., Li, W., Li, S., Wang, Y., Xiao, W.: Reliability assessment of photovoltaic power systems: review of current status and future perspectives. *Appl. Energ.* **104**, 822–833 (2013)

Chapter 3

An Overview of Quantum Computing Approach in the Present-Day Energy Systems



Chiranjit Biswas, Jayanta Pal, and Swanirbhar Majumder

Abstract With the increase in global population and global heating, energy demand is also constantly increasing. The uprising demand to be fulfilled by taking care of environmental conditions' protection to keep global warming in check. Significant efforts have been put into designing, controlling, handling, planning, and managing energy systems. In this regard, bio-inspired or nature-inspired evolutionary optimization schemes in the existing energy systems and innovative energy sources are inducted into the available resources. On the other hand, quantum computing has changed the classical computational approach with speed and efficiency. The assurance of quantum computing in the optimization of energy systems also gained a research attraction. The optimization techniques employed with the quantum advantage by quantum computers supersede classical approaches. This study explores the viability of quantum computing in energy system optimization and various challenges to tackle. This work will help the readers to plan for applying this approach in sustainability energy harvesting, intelligent power and energy systems, distribution network, and renewable energy. Security of the smart grid, intelligent energy systems, evaluation of the energy production process, and other similar or related applications may also be explored.

3.1 Introduction

Quantum computing is the system used for next-generation computing solutions. Quantum computing is described with the characteristics of entanglement superposition and photonics. The development of quantum computing is increasing day by day. The system of quantum computing is applicable in machine learning, quantum cryptography, quantum neuroscience, quantum finance, error correction, and quantum

C. Biswas · J. Pal · S. Majumder (✉)
Department of Information Technology, Tripura University, Tripura, India
e-mail: swanirbhar@ieee.org

J. Pal
e-mail: jayantapal@tripurauniv.ac.in

finance. Earlier computers were number crunching machines deals with 0's and 1's, whereas the computers used for quantum computing use quantum bits or qubits. The advantage of the qubits over the classical bits is the presence of the 'superposition' state or the third state which can represent either '0' or '1' at the same time. This 'superposition' unlike the normal computer's sequential analysis of '0' and '1' helps two qubits to represent four states at the same time. This in turn helps in reducing data crunching time significantly less and being very good for NP-Hard problems.

An energy system basically designs for service of energy supply to end customers. The economical area of energy includes treats and energy markets system of energy as the economic and technical systems which satisfy the demand of customers for energy in fuels, electricity, and heat forms. An energy system concept is developing as new technology, regulations, and entering into service through practices—for example, trading of emission, smart grid development, and use of demand management of energy, respectively. There is no end of energy use in itself nevertheless is always aimed to solve human desires and needs. Earlier days, the energy demand of the end users is satisfied from the conventional energy sources like coal, diesel, fossil fuels, etc. In the present day, use of conventional energy sources for producing the energy is decreasing day by day because conventional energy producing units are emitting the greenhouse gasses which are cause of environmental pollution. So, renewable energy sources are trending for producing the energy to supply end customers. In the present day, there are many types of renewable energy sources like biomass energy, hydro power energy, geothermal energy, wind energy, solar energy, ocean power energy, etc.

Optimization has been being carried out in both Non-Renewable energy as well as Renewable energy sectors. But with Non-Renewable sources depleting, gradually with time, as well as the cry to increasing the usage of environment friendly renewable energy, there has been fast market progression for them. There have been calls for usage of combined version of hybrid renewable energy system (HRES). These are hybrid systems that can overcome local limitations and develop technologies in terms of their fuel efficiency, economics, reliability, and flexibility. But renewable sources of energy have their own issues to be taken care of. There is availability of solar during the day only. That too, when there are no disturbances of clouds or rain along with the stochastic character of the photovoltaic (PV) energy. Similarly, for the wind energy, there are some statistical parameters to be taken care of, based on its load patterns. These kinds of cases have popularized the Hybrid energy systems consisting of renewable and non-renewable energy sources. A large number of random variables or parameters need to be optimized for economic, technical, and designing targets.

3.2 Basic Concept

3.2.1 *Quantum Computing*

Quantum computers can be used as both classical computers (when qubits are ‘0’ and ‘1’) as well as for quantum computing on inclusion of the superposition. Big shots like IBM, Google, Honeywell, etc., are already in this race investing a lot on research in this kind of area. Startups too are focusing on this area with their novel ideas. Companies like D-Wave Systems, Rigetti, and IonQ along with many other newbie companies are looking to develop novel hardware and software stacks to give them the competitive edge to lead this new industry. D-Wave Systems have developed a Quantum Annealer, hardware to solve combinatorial optimization problems. Many companies are into building universal computers which are based on fundamental gate operations similar to the function of the NAND gate traditional computers. As simulations of quantum computing systems are like molecules aligning naturally to their individuality of dealing with this novel computing idea.

Mitsubishi were among the pioneers to have used quantum computers for designing the advanced battery technology. In the energy industry, to understand the properties of hydrocarbons or usage in the oil and gas processing/production or transportation advanced study and analysis of materials and chemicals are very important. So for the analysis of such data and predicting time and solutions to corrosion, element degradation or solid formations those disturb the flow assurance quantum computers may be very helpful. They provide better safety along with reduction of cost in the energy industry. High precision simulations of these elements and their parameter optimization can help in providing solutions immediately compared to experimental explorations in research. The same can be used in other research areas like decision making, planning, and logistics.

Quantum Annealing was also used for solving optimization problems of combinatorial type due to their edge over the classical computers. This accordingly led to the rise of quantum-inspired computing or optimization (QIO) by researchers of classical algorithms who have now included the problem-specific patterns which were being exploited by the quantum algorithms. Thus, these hybrid optimization techniques, provide better results based on both performance and in terms of robustness in all research sectors including the energy sector.

3.2.2 *Energy System*

Biomass Energy: Using the animal or plant material to produce the heat or electricity is called biomass energy. The biomass energy sources are collected from the environment and its processing to produce the heat and electricity. The main processes are direct burning (combustion) to heat producing, for solid, liquid, and gaseous fuels

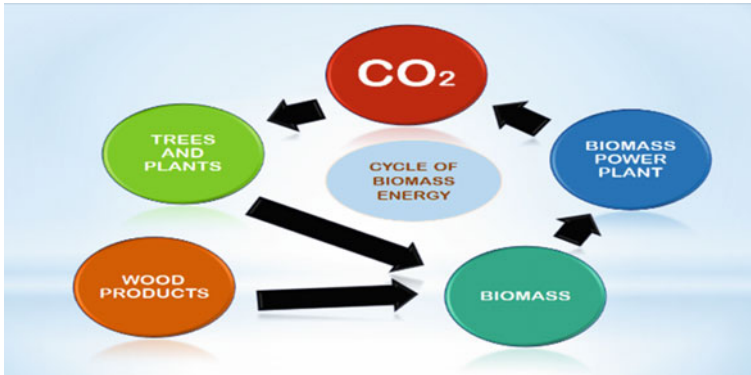
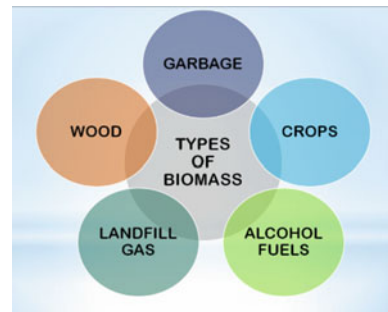


Fig. 3.1 Cycle of biomass energy

Fig. 3.2 Types of biomass sources



thermo-chemical conversion process, for liquid fuels chemical conversion is used. Direct combustion or burning processes is the common method for producing energy. The pyrolysis method is closed heating process of biomass without oxygen. It is used for producing bio-oil, charcoal, methane, renewable diesel, and hydrogen fuels. The hydro heating process is used for producing gasoline, jet fuels with hydrogen. Gasi-fication method is used for heating the organic material with the presence of free oxygen and producing syngas or synthesis gas which consists of hydrogen-rich gas and co gas, and this syngas used for separating hydrogen from the gas. The process of chemical conversion is used for producing FAME (Fatty Acid Methyl Ester) from the vegetable oil and animal fats, which is used for producing biodiesel. The conversion of biological method includes fermentation, fermentation used to produce anaerobic, and ethanol from biomass for producing natural gas for vehicle fuel [9]. Biomass cycle is shown in Fig. 3.1.

There are many types of biomass like plant materials (non-fossilized), municipal waste, and biogas (solid waste, papers, food scraps, grass clippings, cardboard, leaves, leather product, combustible materials, and commercial and industrial waste), etc. 50% of the waste come from renewable sources, biofuels, wood and wood waste, etc. Types of biomass sources are pictured in Fig. 3.2. Modern bioenergy supplies the

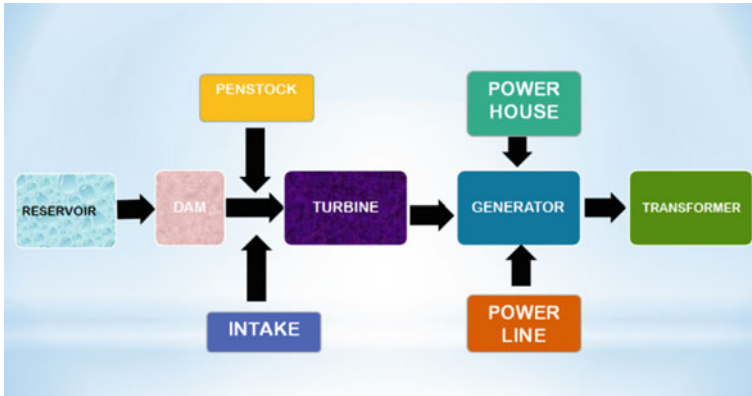


Fig. 3.3 Block diagram of hydropower plant

energy to domestic and small industries and commercial buildings. Biogas is used directly in boiler or stove. The biogas like methane is used in distribution system of natural gas [6].

Hydropower Energy: The kinetic energy or gravitational potential of water source is used for producing the power. Use of flowing water is the main source of producing hydropower, as shown in Fig. 3.3. Conventional hydropower generation units use streams of rivers and dam water to generate electricity through turbine spin. It is a production method of sustainable energy. In the present day, the hydropower is used for generation of hydroelectric power and it is also applied in pumped storage hydroelectricity. Hydropower is the alternative of fossil fuels and does not produce air pollution or carbon directly. The river ecosystem is impact due to the hydropower reservoirs and dams, this type of plants captures the large land areas which cause the emission of greenhouse gasses, and the plant construction impacts the characters of some species [10, 23]. Several challenges faced by the hydropower plant such as technical factors, social acceptability, environmental issue, electricity price, infrastructure, and production [6].

Geothermal Energy: Using the earth surface heat to stream the water and supply it to the stream turbine to generate the electricity, depicted in Fig. 3.4. The origin of geothermal energy is earth crust. The main motive of this energy system is to create a new technology which includes the new process of recovery techniques of resources and also improve the economy of geothermal resources development. The heat extraction by the geothermal energy is smaller than the content of earth heat; because of this, it is called renewable energy source.

The emission of carbon and greenhouse gases is less than the other sources of energy. The forms of geothermal energy are either liquid dominated or vapor dominated. Liquid-dominated plants include LDR (Liquid-dominated reservoirs), which are common for the greater temperature than 200 °C. In EGS (Enhanced geothermal

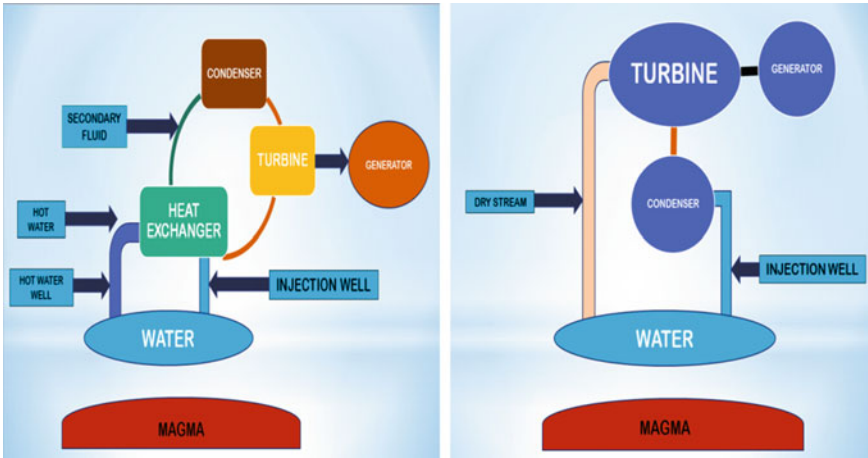


Fig. 3.4 Binary cycle geothermal power plant energy and dry stream geothermal power plant

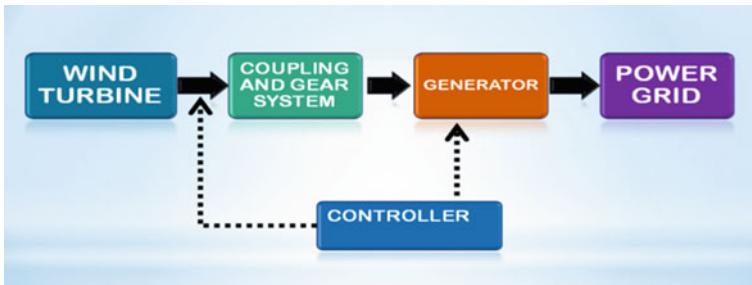


Fig. 3.5 Wind turbine

systems), the water supplies into wells for heating and pumped [10]. The curious advantage of the geothermal energy is lowered developing risk [6].

Wind Energy: Using the kinetic energy of wind to lift the blades of wind turbine. Blades of turbine are connected to the electric generator through a drive train. When blades are turned on because of wind flow, the electric generator generates the electricity. Firstly, wind hit the blade of the turbine, then the blades of turbine start rotating, and then kinetic energy is produced out of rotational energy. The shaft is connected to the generator, and generator produces the electricity. The generating power depends on the turbine size and blade length. The process is shown in Fig. 3.5. There are several problems faced by the wind energy mills like worst weather, low speed of wind, environmental issue, and limitation of land space, maintenance cost of the windmills. But the wind energy systems are eco-friendly to the environment [6, 26, 27].

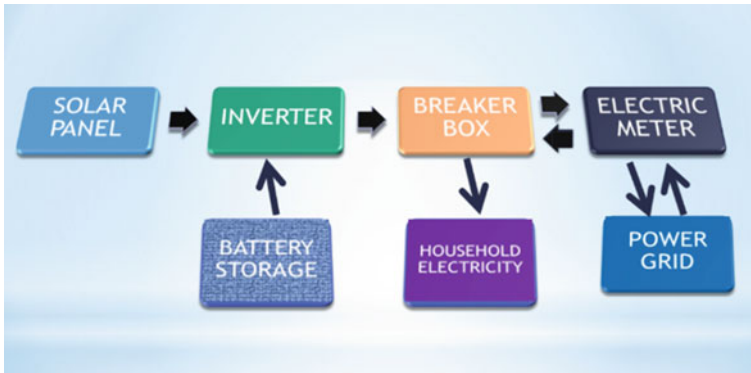


Fig. 3.6 Solar power plant

Solar Energy: The radiation of the sun is used to produce the heat and electricity, as shown in Fig. 3.6. There are many types of solar energy generation system like solar thermal energy systems, solar thermal power plants energy system, and PV (photovoltaic) energy system. During the nighttime, the radiation of the solar is less; because of this, the energy production is less [28, 54]. There are many problems faced by the solar PV systems—the installation of PV module is difficult when the solar irradiation is not same in all areas then it gives the lower power supply; because of this, the demand of the users is not satisfied from this energy sources [31, 32]. Sometimes, battery storage system of the PV module is not sufficient for the supply [61, 62]. But it is no doubt that the solar PV module is better than the conventional energy sources [6, 29, 57, 59, 60].

Ocean power: There are two types of energy systems we get from the ocean: thermal energy (sun heats) and mechanical energy (waves and tides). 70% of the earth surface is covering by the ocean. Thermal energy of ocean is used in generation of electricity, as shown in Fig. 3.7.

In ocean thermal energy, there are three types conversion system of electricity: Open-cycle energy system, Closed cycle energy system, and Hybrid energy system [33]. It is totally different from the ocean mechanical energy. The ocean thermal energy is the cause of sun rays' effects and the ocean mechanical energy is the cause of moon attraction and wind. In the present day, the channel system, floating system, and the column system of oscillating water are used to generating electricity. In mechanical energy system, the tides of water are used to produce the electricity through the generators and also use the wave power of water to produce the electricity through turbine [6].



Fig. 3.7 Ocean energy system

3.3 Related Works

Akshay Ajagekar, Fengqi You, and Travis Humble have proposed a hybrid methods and models that effectively leverage the complementary strengths of deterministic algorithms and for solving the problems of large-scale mixed-integer programming using quantum computing (QC) Techniques [1]. They find some problems like molecular conformation, job-shop scheduling, manufacturing cell formation, and vehicle routing. Hybrid QC partitioning algorithm was used to solve the problem of molecular conformation. For the problem of large-scale job-shop scheduling hybrid QC–MILP (Mixed-integer Linear Program), decomposition method was used. For manufacturing cell formation, hybrid QC–MIQP (Mixed-integer Quadratic Program) step-wise decomposition method was utilized. Lastly, hybrid QC–IQFP (Integer Quadratic Fractional Program) parametric method was used to solve vehicle routing issue. The result shows that all the algorithms are outperforming over the problems and it is exact solver for these problems.

Fengqi You and Akshay Ajagekar have discussed the emerging and new field of quantum computing, and also discussed the applications of optimization of energy systems [2]. They discussed about the quantum algorithm and quantum hardware-related problems which are useful for optimization. There are many problems faced by the quantum computing like error mitigation and precision, and hardware architecture. But, quantum computer has the capability to be compared with matured classical counterpart. Finally, for large scale and complex system, increase in the power of quantum computing is needed, because the quantum computing has the capability to handle those types of problems.

Lim Eng Aik, Ahmad Kadri Junoh, and Tan Wei Hong intend to describe about the application and theory of quantum computing [3]. It also discussed about the optimization algorithms superiority. For improving accuracy and speed up learning in prediction of results, they proposed I-RBFN (Improved Radial Basis Function

Networks) which is combination of quantum computing and cloning operator. They also discussed the demonstration of the search ability and optimization of this algorithm. They compared both RBFN and I-RBFN algorithm through the RMSE (root mean squared error) algorithm. After eight studies, it was shown that the I-RBFN is better than the RBFN algorithm in network architecture and accuracy of prediction. Due to choosing the best value of the center number through clustering method, it is possible to improve the accuracy of this network. Finally, it was made clear that the I-RBFN is more superior to the RBFN algorithm.

Zachary Eldredge and Annarita Giani identified the problems of renewable energy through the quantum computing [4]. Crossover research of theoretical computer science and operations research was easily identified by the nature of optimization problems which are economically useful and translatable into computer science algorithm. The main aim was theoretical separation between quantum and classical complex classes. There exist polynomial and constant improvement benefits if it is realized on near-term quantum hardware. The detail study of this algorithm to help evolving the performance benchmarks of quantum was made. For characterize quantum computer performance, the work is needed in optimization problem.

Therefore, the devices related to the near quantum require deploying algorithms of variation quantum. For calculating the molecule's properties of electrostatic variety and energies, classical-quantum simulators were used. Using IBM quantum computer, it is easy to calculate the energy of ground state and dissociation pathway. This is the first example of calculation of dipole movement actually quantum hardware performance [19].

Navier–Stokes nonlinear differential equation is followed for the solution, which is essential for weather forecasting, aerospace industry, and astrophysics and plasma magneto-hydrodynamics. This algorithm in [20] can be used to find the invisible and compressible flow of static state under the presence of shockwave. The speedup is possible when comparison between classical algorithms and the algorithm's computational cost are deterministic.

3.4 Optimization in Present-Day Energy Systems

Quantum computers are based on the series of research done by the big shots of the industry, i.e., Google, IBM, Microsoft, Intel, and Honeywell as well as several 32+ startups. They are able to deal with a few qubits (Q-bits) that are hard to couple as well as fall under the Universal computing. In the present day, Quantum Computing Landscape is shown in Fig. 3.8. This phase deals with the Quantum annealers like D-wave A5000 (Hybrid-20) and a few startups. These have many qubits (Q-bits) compared to the GATE-based quantum computers but still hard to couple. They fall under Adiabatic Annealing, and to gather with the Universal computing, this whole combined two states are dealing with the Quantum Advantage—Superposition Entanglement. The final stage is the mixed stage of Quantum-Inspired Computing that clubs the Quantum physics to popular classical methods so falling under the

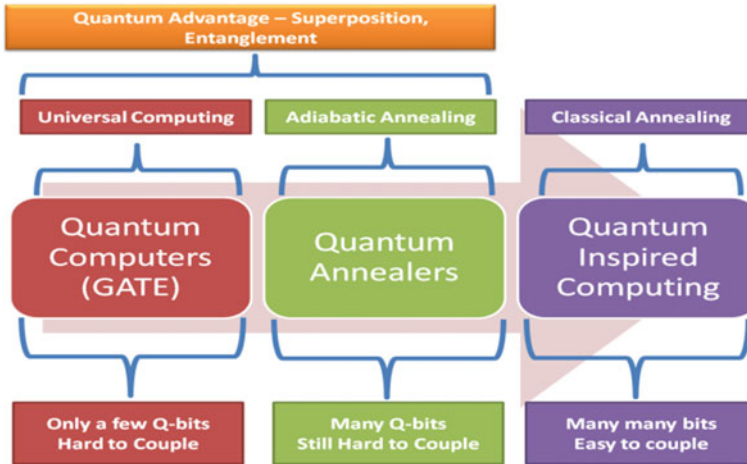


Fig. 3.8 Present day quantum computing landscape

classical annealing process and having the ability to handle much more number of bits than the earlier two stages. Popular variants being the Fujitsu’s Digital Annealer and Toshiba’s Simulated bifurcation machine.

Optimization tries to search best solution from all the available possibilities. Optimization methods try to find the lowest combination between all power generators. The common problem of the quantum chemistry is electronic structure; because of scaling problem, it is complex to find the exact solution of Schrodinger equation. Hamiltonian is the starting approach of this solution and for wave function of system find the suitable approximations in the many electron Hilbert space. This calculation executes either first quantization or second quantization formalism. For first quantization, all integrals are evaluated into a quantum computer [22]. Because of this second quantization, approaches are comfortable for the first-generation quantum devices. For this case, all integrals executed in advance on a classical computer. The Hilbert space sampling is executed in the path of configuration space, which is spanned by determinants of molecular Slater [17].

Nonlinear problems and nonlinear partial differential equations are solved by the variation quantum computing. To achieve this solution, the different duplicates of variational quantum conditions are used to handle nonlinearities efficiently and introduce the networks of tensor as for programming paradigm [21]. The algorithm concepts for the equation of nonlinear Schrodinger can be used as an example for any canonical case. From other numerical experiment, it is proved that the variational quantum ansatz is more efficient than the other matrix product conditions [34]. The methods are ready to modify with two-dimensional and three-dimensional problems, and also applied to the differential operators and nonlinear terms [35]. Grid-side nonlinear problems can be solved using quantum computing through instant scaling of quantum computers [18].

There are many obstructions for developing a hybrid quantum computing model for optimization problem. Solving the problem of discrete continuous optimization is more complex than the continuous optimization problems [36]. There are many optimization problems like (BQP) binary quadratic programming, mixed-integer quadratic programming (MIQP), mixed-integer linear programming (MILP), and integer quadratic fractional programming (IQFP) problem. All these optimization problems are softly tackled by using the quantum computing-based algorithms [1]. In the current technological advancement state, the classical algorithms dominated in quantum algorithms about the gate system with more less expectations and, but on the way, explicitly developed of quantum annealers for better optimization perform in other some cases [25]. Practical problems are not always belonging to the binary quadratic model class; sometimes, it also belongs to the problems of mixed-integer optimization [45–47]. Under uncertainty, the presence for energy system required the online adaptation for ensuring that the system operated optimally [2].

For the solution of low energy optimization problems, algorithm of annealing tries the quantum process [38, 45]. It can be possible to code as QUBO (Quadratic Unconstraint Binary Optimization) problems; these algorithms are included QAOA (quantum adiabatic optimization algorithm) type hybrid quantum classical technique [41, 42]. The process of the state of this algorithm is easy to create; this process easily encodes the optimization problems [4].

3.5 Impact of Quantum Computing on Energy and Utilities

Earlier, we all know the fossil fuels like coal, petrol, and natural gas were the popular options in the energy sector. But now, the mixture of the sources has begun and there are changes coming up. Thus, solar, hydro power, wind, and in some cases geothermal renewable energy alternatives are taking the front seat. If the climate changes issues need to be tackled efficiently, then we need to replace all fossil fuels with their renewable counterparts. In India, Ministry of New and Renewable Energy (MNRE), Government of India, is doing a lot of work in this area by providing support for these kinds of initiatives. But going for these changes never comes easy anywhere. They tend to pose complex challenges for both suppliers and operators. Many a times establishing these cost-effective energy sources tend to have huge initial cost involved. Cost-effective energy sources, processes of systematic distribution, and proper awareness among the population need to be developed. In many countries, the grid that was once unidirectional has upgraded to be smart grids with end customers integrated to it.

The distributed energy sources like solar panels and batteries like many homes, offices, and airports in India like Kochi Airport, which in morning generates more power than required and supply the excess to the grid and in return get power from the grid at night, thereby cutting costs of power by huge margins. These renewable energy sources are un-predictable, and the supply to the grids is decentralized. Therefore, the problem of optimization of various parameters unlike earlier systems has

become more complex and tougher to implement. The usage of quantum computers in this area has aided in obtaining solutions to complex optimization problems along with aiding the process of material development and chemical analysis. The performance appears to be better than present day super computers for material science and chemistry. Batteries have been developed with better capacity and longer life duration by proper optimization in the different parameters of chemicals or materials in it.

Scaling of exponential and optimization are the main concept of quantum which are making better than the classical computer. In quantum grid, the qubits are used instead of solar cell in advanced research technology. Quantum batteries are made using quantum dot [39]. The connection between quantum communication and quantum computing is used for decoding and encoding the information of physical system, eliminated losses of energy, and achieving higher renewable energy goals. Grid cyber-security: in the present day, the infrastructure of power grid is risk for security [24]. If the utilities do not use quantum encryption for grid, then it will be hacked by others easily. Quantum computing is useful for encryption in security. Pattern monitoring of quantum load, quantum computing is more useful for energy consumption. Use of quantum computing calculation is used for calculating the pinpoint accuracy of consumption of smart meter and also providing harmonic spectrum and load analysis for the improving of the spot inefficiencies and power consumption efficiency. Customer analytics use the explosion data of digital channel, smart meter, and smart homes quantum computing working on crunching of intense number. When the CAR++ (entire customer analytical record) of machine learning implemented on quantum computer, then the customer analytics enter into a new phase. Utilities can increase their prediction accuracy by more than 20–30%. If the artificial intelligence is implemented with quantum computing, it is helpful for complex mathematical models [43, 44].

Because of quantum computing, it is easy to handle the large and complex chemical species, balance between chemical insights, and hardware efficiency [48–50]. It is possible that the (LiH) lithium hydride is introducing with 4 qubits on quantum hardware. It is the good idea to characterize the Li–S compound structure for understanding the lithium sulfur battery [51, 52]. Due to quantum computing, it is easy to calculate the polyunsaturated particles formed after discharging the Li–S battery [19, 30, 55].

The main importance of the Navier–Stoke algorithm is that it lies with economically important problems, whose main work is designing the Navier–Stoke equation, designing the supersonic fight engine and flights, and forecasting of weather and magneto-hydrodynamics [53]. For quantum computing, it is easy to solve the hyperbolic algorithms and it is the cause of chemical reaction in hypersonic flow. Quantum computing is significant for more energy producing process [20].

Quantum computing also helps to solve the problem more efficiently. Quantum computing included an increase in computing speed and processing, low data storage cost, for processing the data, developing the algorithms, and big data handling. All these quantum computing applications attracting to research interest. All applications are impacted by the whole energy system [63].

Superconductive qubits are used by the D-wave quantum annealers as the building block. These qubits are creating a connection topology named as chimera graph, which limits the problem topology. A cryogenic environment is needed for quantum annealing. D-wave quantum annealer provides a schedule of fixed annealing. Quantum annealers are leading examples of which machines that are drawn interest from the physics community [64].

Optimization of the power grid and simulation of carbon-absorbing structures are also done by the new quantum computing. The optimization of the power grid included generation, transmission, and distribution; all complex things are easily managed by quantum computing. Quantum computing is good for small-scale issues like the location of the facility, heart exchange network, and unit commitment. Quantum computing helps to solve the machine learning problems, performance of finance, problems of encryptions, defense problems, communication security, data optimization problems, use of energy sources, treatment of patients, climate, and agriculture change problems. Quantum computing is more useful in the energy sector to control energy loss and generation. Quantum cryptography is the advance application of quantum computing because it will break the modern security systems. All applications of quantum computing have enhanced the ability of utilities [65].

3.6 Conclusion

This paper gives a simple overview of quantum computing approaches in present day energy systems. The importance optimization of energy system was brought to the notice of the reader. The problem facing during the optimization like problem of molecular conformation, problem of job-shop scheduling, problem of manufacturing cell formation and vehicle routing problem, accuracy and speed of result prediction, etc., were discussed. The algorithms to solve these problems like Mixed-integer Linear Program, Mixed-integer Quadratic Program, Integer Quadratic Fractional Program, and Improved Radial Basis Function Networks exist. Some of the problems faced by the modified classical computers and some problems faced by quantum computer were reported. Quantum computer is found to be more realistic for result prediction problems. It is evident that increasing the power of quantum computing system will help in solving the large-scale problems and optimization problems of energy system. Overall, quantum computing provides more efficient algorithms for problem-solving mechanisms.

References

1. Ajagekar, A., Humble, T., You, F.: Quantum computing based hybrid solution strategies for large-scale discrete-continuous optimization problems. *Comput. Chem. Eng.* **4**(132), 106630 (2020)

2. Ajagekar, A., You, F.: Quantum computing for energy systems optimization: challenges and opportunities. *Energy* **15**(179), 76–89 (2019)
3. Lim, E.A., Tan, W.H., Junoh, A.K.: An improved radial basis function networks based on quantum evolutionary algorithm for training nonlinear datasets. *IAES Int. J. Artif. Intell.* **8**(2), 120 (2019)
4. Giani, A., Eldredge, Z.: Quantum computing opportunities in renewable energy. *SN Comput. Sci.* **2**(5), 1–5 (2021)
5. <https://www.renewableenergyworld.com/types-of-renewable-energy/ocean-energy-tech/#gref>
6. Murdock, H.E., Gibb, D., André, T., Sawin, J.L., Brown, A., Ranalder, L., Collier, U., Dent, C., Epp, B., Hareesh Kumar, C., Joubert, F.: Renewables 2021-Global status report
7. <https://www.eia.gov/energyexplained/renewable-sources/types-and-usage.php>
8. https://en.wikipedia.org/wiki/Renewable_energy
9. <https://www.eia.gov/energyexplained/biomass/>
10. <https://en.wikipedia.org/wiki/Hydropower>
11. https://en.wikipedia.org/wiki/Geothermal_energy
12. <https://www.irena.org/wind>
13. https://en.wikipedia.org/wiki/Wind_power
14. https://en.wikipedia.org/wiki/Solar_energy
15. <https://www.accenture.com/us-en/blogs/accenture-utilities-blog/quantum-computing-utilities>
16. <https://medium.com/qtft/use-cases-of-quantum-computing-in-the-energy-industry-2974705d379a>
17. Moll, N., Barkoutsos, P., Bishop, L.S., et al.: Quantum optimization using variational algorithms on near-term quantum devices. *Quant. Sci. Technol.* **3**, 3 (2018)
18. Lubash, M., Joo, J., Moinier, P., et al.: Variational quantum algorithms for nonlinear problems. *Phys. Rev. A* **101**, 1 (2020)
19. .Rice, J., Gujarati, T., Takeshita, T., et al.: Quantum chemistry simulations of dominant products in lithium-sulfur batteries (2020)
20. Gaitan, F.: Finding flows of a Navier-Stokes fluid through quantum computing. *NPJ Quant. Inf.* **6**, 61 (2019)
21. Nielsen, M.A., Chuang, I.L.: *Quantum Computation and Quantum Information*. Cambridge University Press, Cambridge (2000)
22. Preskill, J.: Quantum computing in the NISQ era and beyond. *Quantum*. **2**, 79 (2018). US Energy Information Administration (2019)
23. Federal Energy Regulatory Commission, Optimal power flow and formulation papers accessed 06-21-2021 (2021)
24. Brown, K.L., Munro, W.J., Kendon, V.M.: Using quantum computers for quantum simulation. *Entropy* **12**(11), 2268–2307 (2010)
25. Bian, T., Murphy, D., Xia, R., et al.: Quantum computing methods for electronic states of the water molecule. *Mol. Phys.* **117**(15–16), 2069–2082 (2019)
26. NERC: Planning resource adequacy analysis, assessment and documentation (2021)
27. US Global Change Research Program. Fourth National Climate Assessment (2018)
28. The Intergovernmental Panel on Climate Change. *Climate Change* (2014)
29. International Renewable Energy Agency. *Renewable Power Generation Costs in 2018* (2021)
30. NREL: Emerging issues and challenges in integrating high levels of solar into the electrical generation and transmission system (2016)
31. DOE SETO: The SunShot Initiative (2021)
32. Feldman, D., Vignesh, R., Ran, F., Ashwin, R., Jal, D., Robert, M.: US solar photovoltaic system cost benchmark: Q1 2020. National Renewable Energy Laboratory, Golden, CO. NREL/TP-6A20-77324 (2021)
33. US Energy Information Administration. In: *Annual Energy Outlook 2019 with Projections to 2050* (2021)
34. IEEE Spectrum How much power will quantum computing need? (2015)
35. Niedenzu, W., Mukherjee, V., Ghosh, A., et al.: Quantum engine efficiency bound beyond the second law of thermodynamics. *Nat. Commun.* **9**, 165 (2018)

36. Humble, T.S., Thapliyal, H., Muñoz-Coreas, E., Mohiyaddin, F.A., Bennink, R.S.: Quantum computing circuits and devices. *IEEE Des. Test.* **36**(3), 69–94 (2019)
37. Krantz, P., Kjaergaard, M., Yan, F., et al.: A quantum engineer's guide to superconducting qubits. *Appl. Phys. Rev.* **6**, 021318 (2019)
38. Kjaergaard, M., Schwartz, M., Braumüller, J., et al.: Superconducting qubits: current state of play. *Annu. Rev. Condens. Matter Phys.* **11**, 369–395 (2020)
39. Bruzewicz, C., Chiaverini, J., McConnell, R., et al.: Trapped-ion quantum computing: progress and challenges. *Appl. Phys. Rev.* **6**, 021314 (2019)
40. Ville, L., Jiannis, K.P.: A short introduction to topological quantum computation. *Sci. Post Phys.* **3**, 021 (2017)
41. Munoz-Coreas, E., Thapliyal, H.: Quantum circuit design of A T count optimized integer multiplier. *IEEE Trans. Comput.* **68**(5), 729–739 (2019)
42. Thapliyal, H., Munoz-Coreas, E., Varun, T.S.S., Humble, T.S.: Quantum circuit designs of integer division optimizing T count and T depth. *IEEE Trans. Emerg. Top. Comput.* **9**(2), 1045–1056 (2021)
43. Thapliyal, H., Munoz-Coreas, E., Khalus, V.: Quantum circuit designs of carry lookahead adder optimized for T count and qubits. *Sustain. Comput. Inf. Syst.* **29**, 100457 (2021)
44. Major Quantum Computing Advance Made Obsolete by Teenager (2019)
45. Tang, E.: A quantum-inspired classical algorithm for recommendation systems. In: *Proceedings of the 51st Annual ACM SIGACT Symposium on Theory of Computing* (2019)
46. Giovannetti, V., Lloyd, S., Maccone, L.: Quantum random access memory. *Phys. Rev. Lett.* **100**, 160501 (2008)
47. Matteo, O.D., Gheorghiu, V., Mosca, M.: Fault-tolerant resource estimation of quantum random-access memories. *IEEE Trans. Quant. Eng.* **1**, 1–13 (2020)
48. National Academies of Sciences, Engineering, and Medicine: In: *Quantum Computing: Progress and Prospects*, chapter 5. The National Academies Press, Washington, DC (2019)
49. Cirac, J., Zoller, P., Kimble, H., et al.: Quantum state transfer and entanglement distribution among distant nodes in a quantum network. *Phys. Rev. Lett.* **78**, 16–21 (1997)
50. Valivarthi, R., Puigibert, M., Zhou, Q., et al.: Quantum teleportation across a metropolitan fibre network. *Nat. Photonics* **10**, 676–680 (2016)
51. Djidjev, H.N., Chapuis, G., Georg Hahn, G., et al.: Efficient combinatorial optimization using quantum annealing (2016)
52. Ajagekar, A., Humble, T., You, F.: Quantum computing based hybrid solution strategies for large-scale discrete-continuous optimization problems. *Comput. Chem. Eng.* **132**, 106630 (2020)
53. Nigg, S.E., Lörch, N., Tiwari, R.: Robust quantum optimizer with full connectivity. *Sci. Adv.* **3**, 4 (2017)
54. Almosni, S., Delamarre, A., Jehl, Z., et al.: Material challenges for solar cells in the twenty-first century: directions in emerging technologies. *Sci. Technol. Adv. Mater.* **19**(1), 336–369 (2018)
55. Daochen, W., Higgott, O., Brierley, S.: Accelerated variational quantum eigensolver. *Phys. Rev. Lett.* **122**(14), 140504 (2019)
56. DiAdamo, S., Ghibaudi, M., Cruise, J.: Distributed quantum computing and network control for accelerated VQE. *IEEE Trans. Quant. Eng.* **2**, 1–21 (2021)
57. Soliman, A.-H.S., Ahmad, M.A.-K.: *Electrical load forecasting* (2010). ISBN 9780123815439
58. Vivas, E., Allende-Cid, H., Salas, R.: *Entropy* **22**, 1412 (2020)
59. Kleissl, J.: *Solar energy forecasting advances and impacts on grid integration* (2019)
60. Wan, C., Zhao, J., Song, Y., et al.: Photovoltaic and solar power forecasting for smart grid energy management. *CSEE J. Power Eng. Syst.* **1**(4), 38–46 (2015)
61. Hamann, H.F.: *A Multi-scale, multi-model, machine-learning solar forecasting technology*. Technical Report (2021)
62. Marquis, M.: *A public-private-academic partnership to advance solar power for casting* (2021)
63. Elijah, O., Ling, P.A., Rahim, S.K., Geok, T.K., Arsad, A., Kadir, E.A., Abdurrahman, M., Junin, R., Agi, A., Abdulfatah, M.Y.: A survey on Industry 4.0 for the oil and gas industry: upstream sector. *IEEE Access* **9**, 144438–68 (2021)

64. Afoakwa, R., Zhang, Y., Vengalam, U.K., Ignjatovic, Z., Huang, M.: BRIM: bistable resistively-coupled using machine. In: 2021 IEEE International Symposium on High-Performance Computer Architecture (HPCA), 1 February 2021, pp. 749–760. IEEE
65. Ahmad, T., Zhang, D.: Using the internet of things in smart energy systems and networks. *Sustain. Cities Soc.* **19**, 102783 (2021)

Chapter 4

Symbiotic Organisms Search Algorithm-Based Optimal Allocation and Sizing of Capacitor Bank in Radial Distribution Networks



Saubhagya Ranjan Biswal and Gauri Shankar

Abstract Increased line losses in distribution networks is a result of rapid growth in load demand. Aside from that, maintaining voltage stability of the grid in a healthy state becomes a problem for the utility sectors due to fluctuating loads. This paper investigates optimal capacitor placement (OCP) in radial distribution system (RDS) using optimization techniques to solve the above issues. The current work solves the OCP problem using a simple and efficient symbiotic organisms search algorithm. The most desirable buses for the installation of the capacitor are discovered first using a sensitivity index study, minimizing the searching space for the optimization phase. The optimum size and position of the capacitor banks are then determined, with the goal of minimizing system losses and optimizing net annual profit. To demonstrate its effectiveness, the studied approach is applied on 69-, 85-, and 118 bus standard RDSs. Switchable capacitor banks are considered to deal with variable loading condition. Furthermore, the suggested method's performance under maximum load and variable load situations is compared to that achieved using existing cutting-edge methods to determine its utility.

4.1 Introduction

Being the final connection between the main feeder and the end user, the distribution system is an important field of research. Load demands are constantly growing as a result of rapid industrialization and population growth, pushing the line current to its limit. As a consequence, the line losses increase and the bus voltage drops at the customer's location. By satisfying operational constraints, the indeterminate nature of the load makes it difficult to maintain a stable supply voltage and power

S. R. Biswal (✉) · G. Shankar

Department of Electrical Engineering, Indian Institute of Technology (ISM), Dhanbad, Jharkhand, India

e-mail: srbiswal267@gmail.com

G. Shankar

e-mail: gaurishankar@iitism.ac.in

flow, affecting power quality and network stability of system. As a result, distribution companies have a significant difficulty in lowering line losses and maintaining the system's proper voltage profile [1]. Compensation of reactive power demand is a method of achieving these goals in this regard. One of the most frequent types of reactive power compensating equipment is shunt capacitors. In a radial distribution system (RDS), capacitor placement reduces line losses, preserves a healthy voltage profile throughout, and increases power factor and system stability. Shunt capacitor banks must be appropriately placed in order to reap the greatest benefits. The term 'appropriately' corresponds to the best allocation of capacitor banks with regards to its number, location, and size. Selecting the optimal position decreases losses by keeping other constraints within their permissible limits, resulting in a net profit rise [2].

Numerous researchers have recently suggested many optimization methods focused on conventional as well as artificial intelligence approaches. Many researchers suggested analytical methods to solve capacitor allocation problems at first because advanced computational techniques were high priced and not readily accessible at those periods. Neagle in [3] suggested an analytical approach in which in order to have the maximum loss reduction in case of uniformly dispersed load, the capacitors need to be located at a place where load kVAr is twice the capacitor bank kVAr. Schmill in [4] has proposed an approach using 2/3 rule for capacitor placement at its optimal location. These methods consider uniform distribution of load which is an unrealistic assumption. Therefore, using the basic principles of the equal area criterion, the optimal capacitor placement (OCP) problem is solved by Grainger and Lee in [5] non-uniformly distributed load environment by optimizing the net saving. Although analytical approaches are considered as simple methods, however, due to the unrealistic assumptions like neglecting load variation and considering variables as continuous, the obtained value in relation to size and location of the capacitor banks may need to be rounded off. This might result in overvoltage issues and a higher power loss than calculated.

Various numerical programming approaches have been used to resolve OCP problems due to the simple availability of inexpensive computing resources. Iterative techniques for optimizing an objective function by considering number of constraints are known as numerical programming methods. Duran uses a dynamic programming approach for solving OCP by considering discrete capacitor size and loss reduction as the objective function [6]. Later on, Baran and Wu in [7] have utilized a two-stage master and slave approach for solving the OCP issue. In master stage, capacitor location is obtained, whereas, type and size of the capacitor are decided under slave stage. According to the literature review, numerical methods take longer to compute than analytical approaches, and they can often converge to local optima. On the other hand, heuristic approaches are considered as better than the numerical programming-based approach for finding solution nearer to optimal solution for capacitor placement. Abdel-Salam et al. have investigated a heuristic approach-based allocation of capacitor by selecting sensitive nodes in terms of reactive power line losses [8]. Thereafter, the capacitor size is obtained by maximizing power loss reduction. Silva et al. have studied a nonlinear mixed integer method, in which the

OCP issue is fixed by using bus bar sensitivity index and a sigmoid function [9]. In [10], the authors utilize a heuristic search-based node stability indices for solving OCP problem by optimizing power loss and net savings.

In recent decades, numerous nature-inspired intelligent optimization algorithms have been introduced to address the OCP issue. These nature-inspired heuristic techniques are less sensitive to initial solution and easily escapes local optima. In [11], the authors have applied a combination of fuzzy differential evolution and multi agent particle swarm optimization algorithm for OCP problem by maximizing the cost function which involves both energy and capacitor price. While in [12], authors include capacitor installation, maintenance and capacitor reactive power cost in overall cost calculation and minimized the objective function using cuckoo search algorithm (CSA). El-Fergany in [13] incorporates voltage sensitivity index along with energy loss and capacitor cost in objective function for its minimization utilizing artificial bee colony (ABC) algorithm. An attempt in [14] has been made by considering the minimization of multi-objective function using fuzzy-genetic algorithm, which includes different membership function like bus voltage limit, branch current capacity, and line losses in its objective. The vortex search algorithm (DVSA) is utilized to discover the optimal solution for OCP in [15], which employs a Gaussian distribution to help converge the solution to a global optima value with the aim of minimizing the system cost. In [16], the OCP issue is framed as a nonlinear mixed integer programming problem and is solved using the Chu and Beasley genetic algorithm.

According to the ‘no free lunch’ theorem, no optimization strategy is perfectly suited for evaluating an optimization problem. As a result, several researchers have proposed a variety of state-of-the-art optimization methods for address OCP issue such as genetic algorithm [17], teaching learning-based optimization (TLBO) [18], penalty free genetic algorithm (PFGA) [19], bacterial foraging optimization algorithm (BFA) [2], mixed integer programming (MIP) [20], evolution algorithm (EA) [21], modified cultural algorithm [22], modified monkey search optimization technique (MMS) [23], particle swarm optimization approach [24], improved harmony algorithm (IHA) [25], crow search algorithm [26], flower pollination algorithm (FPA) [27], and so on. Symbiotic organisms search (SOS) algorithm, a simple and effective nature-inspired metaheuristic method introduced by Cheng and Prayogo, has been employed by various authors in the past [28]. Many researchers have used SOS algorithm in the past to deal with a variety of complicated real-world issues. This inspires the authors for applying SOS algorithm for OCP problem.

In line with the above, as evidenced by recent literatures, most of the researchers follow a two-step approach for solving OCP problem. At first, the weak and more deserving locations for capacitor allocation are detected utilizing different sensitivity analysis methods. In the second stage, among the identified deserving buses, the optimized size and position of capacitor banks are obtained utilizing optimization techniques. The sensitivity analysis lessens the computational complexity for the optimization process and also decreases the chance of being converged to local optima. Rao et al. use loss sensitivity factor (LSF) for selecting candidate buses for optimization method [29]. Whereas, in [12], power loss index (PLI) has been

utilized for finding potentially weak buses for OCP using CSA. A comparative study between LSF and PLI has been carried out in [21]. However, in [1], two loss sensitivity indices have been used for selecting weak buses for further treatment using ant colony optimization (ACO) approach. Combining two indices based on loss sensitivity and voltage sensitivity, a new sensitivity analysis is proposed in [14].

In this paper, a sensitivity analysis is adopted for selecting weak and deserving candidate buses for OCP problem in studied standard IEEE standard test systems. The sensitivity index is constituted considering both PLI and voltage deviation index (VDI) by giving equal priority to both of them and sort the buses in terms of suitability for the capacitor placement. Following which, the above selected bus locations are considered for the studied SOS optimization method to determine the suitable capacitor bank position and size. Further, discrete and switchable capacitor banks are considered for various loading scenarios. The output yielded for different adopted test systems is compared with results listed in earlier literatures.

The remainder of the paper is laid out as follows. Section 4.2 describes how to create an objective function while evaluating constraint variables. The sensitivity index study that is carried out is depicted in Sect. 4.3. The load flow approach is described in Sect. 4.4. Section 4.5 delves into the SOS algorithm. Section 4.6 evaluates and provides the simulated results, followed by Sect. 4.7's conclusion.

4.2 Problem Formulation

The presented method's objective function is formulated aiming to lessen the line losses by keeping bus voltages within acceptable range, which in turn contributes to a high net annual profit. The prime objective of the studied method is stated as (4.1)

$$\text{minimize} \left(\frac{\text{cost}_a}{\text{cost}_b} * w_1 + \frac{\text{APL}_a}{\text{APL}_b} * w_2 + \frac{\text{RPL}_a}{\text{RPL}_b} * w_3 + \frac{\text{LC}_a}{\text{LC}_b} * w_4 \right) \quad (4.1)$$

where cost_a and cost_b are the total cost per year, APL_a and APL_b are the active power line losses, RPL_a and RPL_b are the reactive power line losses, and LC_a and LC_b are sum of line currents of the distribution system. Here, suffix 'a' and 'b' represent before and after compensation, respectively. The weightage factors are selected by trial-and-error method and finalized as $w_1 = 0.55$, $w_2 = 0.15$, $w_3 = 0.15$ and $w_4 = 0.15$. For calculating the cost of the system, the following formula has been used and is presented by (4.2)

$$\text{Cost} = K_p * \text{APL} * T + D \left(K_I * \text{NC} + K_C * \sum_i^{\text{NC}} Q_{C_i} \right) + K_O * \text{NC} \quad (4.2)$$

Table 4.1 Details of parameters utilized in economic computation of the system [30]

S. No	Variables	Value
1	Depreciation factor (D)	20%
2	Duration per year (T)	8760 h
3	Price of energy (K_P)	\$0.06/kWh
4	Purchase price (K_C)	\$25/kVAr
5	Installation price (K_I)	\$1600/location
6	Operation price (K_O)	\$300/year/location

where NC is denoted as capacitor banks quantity in terms of number. Table 4.1 shows the values of various notations, which are obtained from the study of [30].

4.2.1 Constraints

While addressing the OCP issue, the value of some parameters needed to be held inside a permissible range in order to make the solution feasible. The constraints that were considered in this study are listed below.

4.2.1.1 Voltage Constraint

All the bus voltages should be held inside its lower and upper bounds while executing the optimization method, as stated in (4.3)

$$V_{\min} \leq V_i \leq V_{\max} \tag{4.3}$$

Here, V_i , V_{\min} and V_{\max} , respectively, refer to i th bus voltage, the lowest, and the highest acceptable voltage bounds.

4.2.1.2 Capacitor Bank Constraint

The reactive power compensation provided by the capacitors should kept inside the suitable lower and the upper bounds as shown in (4.4)

$$Q_{C_{\min}} \leq Q_{C_j} \leq Q_{C_{\max}} \tag{4.4}$$

where Q_{C_j} is the j th bus reactive power compensation, and $Q_{C_{\min}}$ and $Q_{C_{\max}}$ represent the lower and the upper kVAr range of capacitive reactive power compensation of a single bus, respectively.

4.3 Determining the Potential Locations

The main aim of identifying potential locations is that it significantly cuts the searching dimensions for the optimization method. In this work, a sensitivity index has been adopted for identifying potentially vulnerable locations that are more sensitive towards capacitor allocation than the other buses. This selection reduces overall system losses and notably enhances systems voltage profile. Here, in this analysis, equal preference is given to both reduction of line losses and bus voltage deviation. Separately, PLI and VDI are calculated for each bus and, finally, sensitivity index for all buses is calculated by giving equal weightage to both. The adopted sensitivity index (SI) is given by (4.5)

$$SI = PLI * 0.5 + VDI * 0.5 \quad (4.5)$$

where PLI and VDI are expressed by (4.6) and (4.7), respectively

$$PLI = \frac{LLR(i) - LLR_{\min}}{LLR_{\max} - LLR_{\min}} \quad (4.6)$$

For calculating the line loss reduction (LLR) of a particular bus (except the slack bus), reactive power load demand of that particular bus is considered to be completely compensated, and thereafter, the reduction in total system line loss from the base value is taken as LLR. LLR_{\min} and LLR_{\max} refer to the minimum and the maximum system line loss reduction, respectively. After calculating LLR, PLI for every bus has been calculated by using (4.6). The VDI component of (4.5) is given by (4.7).

$$VDI = \frac{CVD(i) - CVD_{\min}}{CVD_{\max} - CVD_{\min}} \quad (4.7)$$

Excluding the slack bus, VDI is determined for all other buses. CVD_{\min} and CVD_{\max} are the minimum and the maximum cumulative voltage deviation (CVD) within the system, respectively. The CVD is defined by (4.8)

$$CVD = \begin{cases} 0, & \text{if } 0.95 \leq V_i \leq 1.05 \\ \sum_{i=1}^{NB} 1 - V_i, & \text{else} \end{cases} \quad (4.8)$$

Here, NB refers to the systems number of buses. It is presumed that the reactive power demand of a particular bus is completely compensated, and afterwards, the CVD of that bus is calculated using (4.8). Thereafter, VDI is obtained for each bus using (4.7).

4.4 Load Flow

Many conventional load flow approaches, like the Newton–Raphson method, Gauss–Seidel method, and others, are stated to be inadequate for radial structured distribution systems because of high resistance (R) to reactance (X) value. As a result, a direct approach reported in [31] is taken in this work for load flow calculation. The adopted method utilizes bus injection to branch current (BIBC) matrix and the branch current to bus voltage (BCBV) matrix for calculating the required parameters. The steps of the load flow approach are described thoroughly using a 6-bus RDS (Fig. 4.1) as an example.

With respect to Fig. 4.1, the branch currents (IB_i) may be obtained from the bus load currents (IL_i) as shown in (4.9),

$$\begin{bmatrix} IB_1 \\ IB_2 \\ IB_3 \\ IB_4 \\ IB_5 \end{bmatrix} = \begin{bmatrix} 1 & 1 & 1 & 1 & 1 \\ 0 & 1 & 1 & 1 & 1 \\ 0 & 0 & 1 & 1 & 0 \\ 0 & 0 & 0 & 1 & 0 \\ 0 & 0 & 0 & 0 & 1 \end{bmatrix} \begin{bmatrix} IL_2 \\ IL_3 \\ IL_4 \\ IL_5 \\ IL_6 \end{bmatrix} \tag{4.9}$$

In generalized form, (4.9) may be written as (4.10).

$$[IB] = [BIBC][IL] \tag{4.10}$$

The branch current may be related with the bus voltage in a matrix form as stated in (4.11).

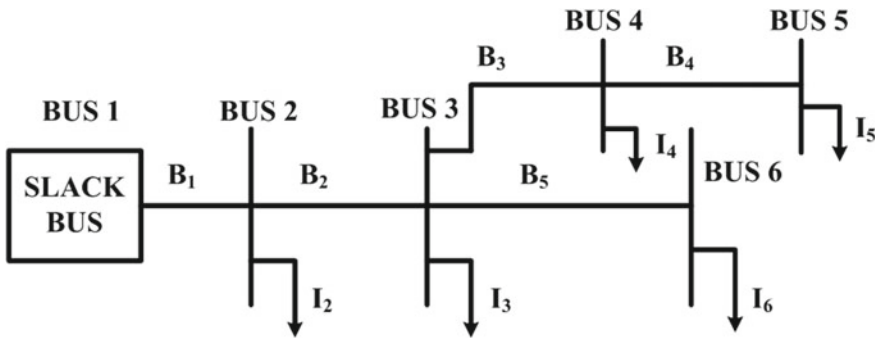


Fig. 4.1 Single-line diagram of a 6-bus RDS

$$\begin{bmatrix} V_1 \\ V_1 \\ V_1 \\ V_1 \\ V_1 \end{bmatrix} - \begin{bmatrix} V_2 \\ V_3 \\ V_4 \\ V_5 \\ V_6 \end{bmatrix} = \begin{bmatrix} Z_{12} & 0 & 0 & 0 & 0 \\ Z_{12} & Z_{23} & 0 & 0 & 0 \\ Z_{12} & Z_{23} & Z_{34} & 0 & 0 \\ Z_{12} & Z_{23} & Z_{34} & Z_{45} & 0 \\ Z_{12} & Z_{23} & 0 & 0 & Z_{36} \end{bmatrix} \begin{bmatrix} \text{IB}_1 \\ \text{IB}_2 \\ \text{IB}_3 \\ \text{IB}_4 \\ \text{IB}_5 \end{bmatrix} \quad (4.11)$$

In generalized form, (4.11) may be written as (4.12).

$$[\Delta V] = [\text{BCBV}][\text{IB}] \quad (4.12)$$

Using (4.10), we may write (4.12) as

$$[\Delta V] = [\text{BCBV}][\text{BIBC}][\text{IL}] = [\text{DLF}][\text{IL}] \quad (4.13)$$

The load flow is continued to run recursively using (4.14) and (4.15) until the total change in bus voltages is not less than 10^{-8} .

$$\text{IL}_i^k = \left(\frac{P_i + Q_i}{V_i^k} \right)^* \quad (4.14)$$

$$V^{k+1} = V^O + [\text{DLF}][\text{IL}^k] \quad (4.15)$$

The total line losses of a system are calculated using (4.16) and (4.17)

$$\text{APL} = \sum_{i=1}^{\text{NB}-1} \text{IB}_i^2 R_i \quad (4.16)$$

$$\text{RPL} = \sum_{i=1}^{\text{NB}-1} \text{IB}_i^2 X_i \quad (4.17)$$

4.5 SOS Algorithm and Capacitor Placement

The SOS algorithm, proposed by Cheng and Prayogo, mimicked the collaborative behaviour of different species in nature [28]. The reliance-based relationship between organisms for sustenance and survival is known as symbiosis. The most frequent symbiotic relations observed are mutualism, commensalism and parasitism. The connection between two separate organisms that favours both of them is known as mutualism. In commensalism, the symbiotic interaction between two different organisms benefits one participant and has no influence on other one. A relationship established between two different species in which one is benefited while the

other one gets harmed is known as parasitism. These three relationships are briefly discussed in subsequent subsections.

4.5.1 Mutualism Phase

The symbiotic relation between a zebra and an oxpecker (a species of bird) in which both get benefitted is a classic example of mutualism phenomenon. Oxpecker sits on zebra's back and eats ticks and other parasites that live on the skin of zebra. Also, when there is danger, the oxpecker flies up into the air and warn through screaming, which helps symbiont to know about imminent danger. The first step in implementing the concept of mutualism for solving OCP problem requires the initialization of population matrix of decision variables, created randomly considering their maximum and minimum limits. The fitness value of every generated outcome inside the population matrix is obtained utilizing the proposed objective function as given in (4.1) and the best fitness solution is selected as Z_{best} . Two solutions Z_i and Z_j are chosen randomly from the population matrix and (4.18)–(4.20) are employed for calculating new candidate solution for Z_i and Z_j by performing the mutualism operation [28].

$$Z_{i\text{new}} = Z_i + \text{rand}(0, 1) * (Z_{\text{best}} - \text{mutual vector} * \text{BF}_1) \quad (4.18)$$

$$Z_{j\text{new}} = Z_j + \text{rand}(0, 1) * (Z_{\text{best}} - \text{mutual vector} * \text{BF}_2) \quad (4.19)$$

$$\text{mutual vector} = \frac{Z_i + Z_j}{2} \quad (4.20)$$

where BF_1 and BF_2 refers to the benefit factors. As stated earlier that in mutualism, both of the participants get benefitted, it may happen that one of them might get more benefit than the other one. Here, the benefit factor signifies the degree of benefit of both organisms in mutualism stage. The newly generated solutions are compared with the old one in terms of fitness function and replaces the old solution, only if it has the higher fitness value. In other words, the fittest one is considered for the next phase of optimization process.

Algorithm 1: Pseudo Code of SOS Algorithm

Step 1 Set the parameters: V_{min} , V_{max} , $Q_{C_{\text{min}}}$, $Q_{C_{\text{max}}}$, number of iteration, population size.

Step 2 Initialize population matrix by generating random capacitor size within allowable range at the bus location obtained by sensitivity analysis index.

Step 3**while** ($t < \text{maximum iteration}$)**for** $i = 1 : n$ % n refers to number of organism find Z_{best}

% Start of mutualism stage

 arbitrarily choose Z_j , here $i \neq j$ mutual vector = $\frac{Z_i + Z_j}{2}$ $Z_{i\text{new}} = Z_i + \text{rand}(0, 1) * (Z_{\text{best}} - \text{mutual vector} * \text{BF}_1)$ % $\text{BF}_1 = \text{random number either 1 or 2}$ $Z_{j\text{new}} = Z_j + \text{rand}(0, 1) * (Z_{\text{best}} - \text{mutual vector} * \text{BF}_2)$ % $\text{BF}_2 = \text{random number either 1 or 2}$ **if** $f(Z_{i\text{new}} > Z_i)$ $Z_i = Z_{i\text{new}}$; **end** **if** $f(Z_{j\text{new}} > Z_j)$ $Z_j = Z_{j\text{new}}$; **end**

% Start of commensalism stage

 arbitrarily choose Z_j , here $i \neq j$ $Z_{i\text{new}} = Z_i + \text{rand}(-1, 1) * (Z_{\text{best}} - Z_j)$ **if** $f(Z_{i\text{new}} > Z_i)$ $Z_i = Z_{i\text{new}}$; **end**

% Start of parasitism stage

 arbitrarily choose Z_j , here $i \neq j$ Produce parasite vector by mutating Z_j **if** $f(\text{parasite vector} > Z_j)$ $Z_j = \text{parasite vector}$; **end****end****end****Step 4** Obtained the current best organism as the best solution.

4.5.2 Commensalism Phase

In commensalism phase, only one party gets benefit while the other one is unaffected by the relation. The commensalism interaction often happens between a larger host and a smaller commensal, in which the smaller one gets benefit from the relation. One of the classic examples of commensalism is the interaction among remora fish

with shark. The remora attaches itself with shark and gets carried along on shark's power throughout the ocean, as well as gets protection from other species. It also gets food from the remaining of the meals of the larger fish. Shark is totally unaffected by this relationship. In order to incorporate commensalism into OCP problem, a random solution Z_j is chosen from the population for interacting with another solution Z_i . In this interaction, Z_i gets sole benefit while Z_j remains unaffected. A new candidate solution is found using (4.21) [28].

$$Z_{i\text{new}} = Z_i + \text{rand}(-1, 1) * (Z_{\text{best}} - Z_j) \quad (4.21)$$

The term $(Z_{\text{best}} - Z_j)$ represents the advantage gained by Z_i from Z_j .

4.5.3 Parasitism Phase

In parasitism relationship, one organism got benefited through harming the other one. An example of parasitism is the relation between aphid (a small green insect) and plant, in which aphid eats the sap of plants for their sustenance. Initially, a parasite vector is created by duplicating an organism Z_i . Then, at least one of the components of parasite vector is modified and interacted with another organism Z_j (randomly chosen from the population matrix). When the parasite vector obtained improved fitness value, then it replaces Z_j and the same is considered for the following iteration.

The pseudocode of the studied SOS algorithm is presented as Algorithm 1.

4.6 Results and Discussion

Using various standard radial distribution test systems (IEEE standard 69-, 85- and 118-RDS), the effectiveness and supremacy of the adopted SOS algorithm in solving OCP issues are examined with variable loading scenarios. As reactive power compensation varies with different loading conditions, switchable capacitor banks are considered for the placement at right location. The search space for optimization process has been reduced significantly by finding the vulnerable locations using the sensitivity analysis. The bus locations are listed in decreasing order according to their corresponding calculated sensitivity index value, and a fixed number of buses (user defined) from the top are selected as an input to the studied optimization process for OCP. The values of the parameters taken for the economic computation are stated in Table 4.1. Within 0.9 and 1.1 p.u., the bus voltage is considered to be allowable. Capacitor banks at a single site are expected to provide reactive power support inside the range of 0–1500 kVAr, with variations of 50 kVAr. The results (presented by the other authors of the published literatures) of the various compared algorithms are computed using the adopted load flow technique and are displayed for avoiding unnecessary incongruities. The studied algorithm has been realized using

MATLAB^R. The value of variables taken during optimization process is: population size = 50, number of iterations = 100. The important outcomes are emphasized in bold in their respective tables associated with each of the studied cases and the symbol ‘—’ for each table indicates that it is not applicable.

4.6.1 Case Study 1: IEEE 69 Bus RDS

The data of 69 bus RDS are considered as specified in [7]. The base case total system load is found to be $(3802.1 + j2694.6)$ kVA. 12.66 kV (voltage) and 10 MVA (power) are taken to be the base value for the load flow calculation. Figure 4.2 illustrates the one-line figure for 69 bus RDS. By executing the base case simulation on this system, the respective APL and RPL are found to be 225 kW and 102.165 kVAr, before the placement of capacitor banks. After performing sensitivity analysis, the buses are sorted (based on calculated index value) in their preference order for capacitor placement as 61, 64, 59, 65, 12, 21, 11, 62, 18, 17, 8, and so on. Eight buses from the starting point are nominated as possible locations for the OCP, and these participate as input to the studied algorithm while finding the optimized result. For this test system, only 100% loading scenario is considered, and the results are compared using the most recent algorithms. Figure 4.3a shows the converging fitness value with respect to the iterations. Figure 4.3b shows the betterment of system bus voltage with OCP as compared to the uncompensated value. The outcome of the studied algorithm results in two different locations for OCP at bus 18 and 61. The capacitor size on these two locations is found as 300 kVAr and 1200 kVAr, respectively. With the obtained outcomes of the OCP, the corresponding APL and RPL of the RDS come down to 146.88 kW and 68.51 kVAr as given in Table 4.2. The minimum value of voltage among all the buses got better from 0.909 to 0.930 p.u., which is observed at bus location 65. The net annual savings is obtained using cost formula as \$32,319.87, which is the better in comparison to other reported optimization algorithms. Table 4.2 also presents the comparison between different parameters obtained using the studied SOS and the other adopted cutting-edge algorithms.

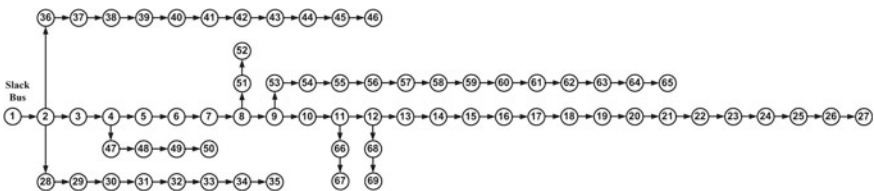


Fig. 4.2 One-line diagram of 69 bus RDS

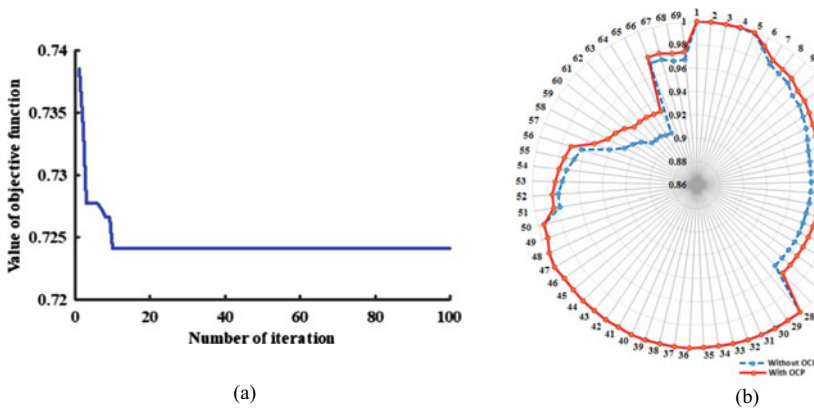


Fig. 4.3 Results found for 69 bus RDS **a** convergence plot of fitness value, **b** value of bus voltage before and after OCP

4.6.2 Case Study 2: IEEE 85 Bus RDS

For this case, the data are considered as available in [32]. Figure 4.4 illustrate the one-line figure for 85 bus RDS. The base case system total load of this studied case is found to be $(2570.28 + j2622.2)$ kVA. The base parameters for the load flow simulation are taken as 11 kV (voltage) and 100 MVA (power), respectively, during simulation. After performing the load flow simulation, the APL and the RPL values are found to be 316.135 kW and 198.613 kVAr, correspondingly. Further, sensitivity analysis is carried out, and the buses are sorted (based on calculated index value) in their preference order for capacitor placement as 54, 55, 51, 76, 69, 74, 39, 72, 66, 28, 62, 38, 61, 60, 82, 80, and so on. From the results found, the top 16 locations are nominated as potential locations for the OCP. Among these suitable buses, the optimum site and size of capacitors are obtained utilizing the studied SOS algorithm. For this present case study, three different loading conditions (represented through load factor in Table 4.4) have been considered, and a relative study of the outcomes is shown compare to the latest literatures. The converging fitness value with respect to the iterations is displayed in Fig. 4.5a. Figure 4.5b shows the betterment of system bus voltage with OCP with respect to the base case value. Table 4.3 presents the comparison between different parameters obtained using the studied SOS and the other adopted algorithms. For full load condition, the SOS algorithm finds six best locations (at the bus number 28, 51, 55, 60, 69, and 82) for OCP with a total compensation of 2100 kVAr. With the obtained outcomes of the OCP, the active and reactive power line losses of the system come down to 147.933 kW and 92.106 kVAr, correspondingly. The lowest value of voltage among all the buses of the system (associated with the bus number 54) got better from 0.871 to 0.921 p.u. The net annual profit is obtained using cost formula as \$74,187.032, which is better among other compared methodology and, thus, proves the superiority of the studied algorithm over the others. Comparison of output results obtained utilizing the studied and other

Table 4.2 Summaries and comparative results pertaining to 69 bus RDS

Items	Uncompensated		Compensated						
	FPA [27]	PFGA [19]	IHA [25]	TLBO [18]	CSA [12]	EA [21]	SOS		
Capacitor location and size	–	18(150) 21(150) 61(1500) 64(300)	61(1350) 21(350)	12(600) 61(1050) 64(150)	21(250) 62(1200)	57(150) 58(50) 61(1000) 60(150) 59(100)	18(300) 61(1200)		
Total kVA _r	–	2100	1700	1800	1450	1450	1500		
APL (kW)	225	156.56	146.88	146.38	148.02	151.46	146.88		
% Loss reduction		30.42	34.72	34.94	34.21	32.68	34.72		
RPL (kVA _r)	102.165	72.12	68.37	68.06	69.07	70.16	68.51		
V_{\min} (p.u.)	0.909	0.940	0.932	0.931	0.930	0.931	0.930		
Net savings (\$)	–	22,992.06	31,319.87	30,462.67	31,970.69	28,302.62	32,319.87		
% saving	–	19.44	26.48	25.76	27.03	23.93	27.33		

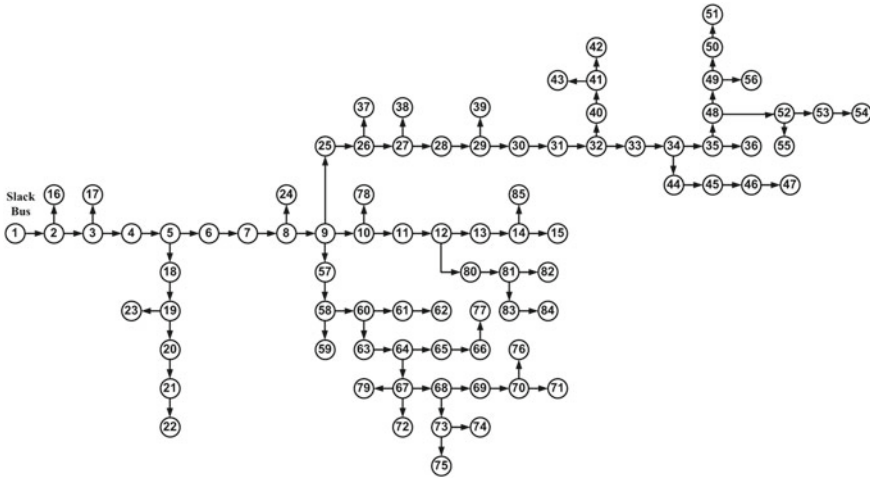


Fig. 4.4 One-line diagram of 85 bus RDS

studied algorithms (as adopted by authors of earlier published works) under different loading conditions is presented in Table 4.4.

Table 4.3 Summaries and comparative results pertaining to 85 bus RDS

Items	Uncompensated	Compensated					
		IHA [33]	BFA [2]	MMS [23]	MIP [20]	ACO [1]	SOS
Capacitor location and size	—	8 (250) 29(350) 34(400) 54(150) 58(350) 64(500) 83(250)	9 (840) 34(660) 60(650)	10,17, 28, 32, 45, 68, 73, 84 (150) 14, 20, 26, 49(300) 60(450)	7 (300) 8(700) 29(900) 58(500)	7(150) 8(300) 19(300) 27(300) 32(300) 48(300) 61(300) 68(300) 80(300)	28(600) 51(200) 55(200) 60(550) 69(250) 82(300)
Total kVAr	—	2250	2150	2850	2400	2550	2100
APL (kW)	316.135	147.605	152.903	145.231	159.410	143.89	147.933
% Loss reduction	—	53.31	51.63	54.06	49.58	54.49	53.21
RPL (kVAr)	198.613	91.833	94.728	90.981	97.431	89.94	92.106
V_{min} (p.u.)	0.871	0.924	0.919	0.927	0.918	0.922	0.921
Net savings (\$)	—	72,989.37	73,184.74	67,517.14	67,894.66	72,201.97	74,187.03
% saving	—	43.93	44.04	40.63	40.86	43.45	44.65

Table 4.4 Summaries and comparative results pertaining to IEEE 85 bus test system for different loading conditions

Load factor	Items	Uncompensated	Compensated			
			SOS	Installed kVAr	IHA [33]	Installed kVAr
1	APL (kW)	316.135	147.933	6 locations (Total capacity = 2100)	147.605	7 Locations (Total capacity = 2250)
	RPL (kVAr)	198.613	92.106		91.832	
	V_{min} (p.u.)	0.871	0.921		0.924	
	Net savings (\$)	—	74,187.032		72,989.368	
0.75	APL (kW)	166.967	81.23	28(450) 55(250) 60(400) 69(200) 82(200) Total = 1500	88.620	8(250) 29(350) 58(350) 64(500) Total = 1450
	RPL (kVAr)	104.953	50.53		54.110	
	V_{min} (p.u.)	0.907	0.941		0.933	
	Net savings (\$)	—	34,463.006		31,449.183	
0.5	APL (kW)	70.099	36.414	28(350) 55(150) 60(450) Total = 950	38.075	8(200) 29(350) 58(350) Total = 900
	RPL (kVAr)	44.083	22.539		23.363	
	V_{min} (p.u.)	0.940	0.960		0.999	
	Net savings (\$)	—	11,095.026		10,471.814	
Net injected kVAr	Fixed (location, kVAr)	(28, 350), (55, 150), (60, 400)				
	Switched (location, kVAr)	(28, 250), (51, 200), (55, 100), (60, 150), (69, 250), (82, 300)				

4.6.3 Case Study 3: IEEE 118 Bus RDS

The data of standard 118-bus RDS are available from [34] with the total load demand of $(22,709.71 + j17040.97)$ kVA. Uncompensated value of voltage and power is taken similar to that of Case Study 2. The one-line diagram for the present case study is shown as Fig. 4.6. After applying the studied load flow approach, the base case APL and RPL is found to be 1297.413 kW and 978.715 kVAr, correspondingly. In this case study as well, as an outcome of sensitivity analysis, the buses are ranked in their preference order for capacitor placement as 39, 118, 74, 70, 109, 86, 71, 107, 43, 111, 32, 110, 91, and so on. Out of these, top 18 bus locations are chosen for participating in the studied SOS algorithm for finding OCP. Three different loading conditions are considered for this case study as well. The results obtained for different loading conditions are analysed by comparing it with recently

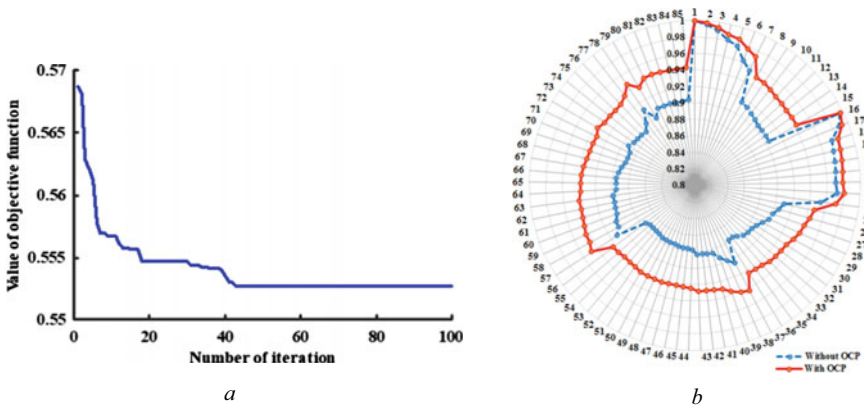


Fig. 4.5 Results found for 85 bus RDS **a** convergence plot of fitness value, **b** value of bus voltage before and after OCP

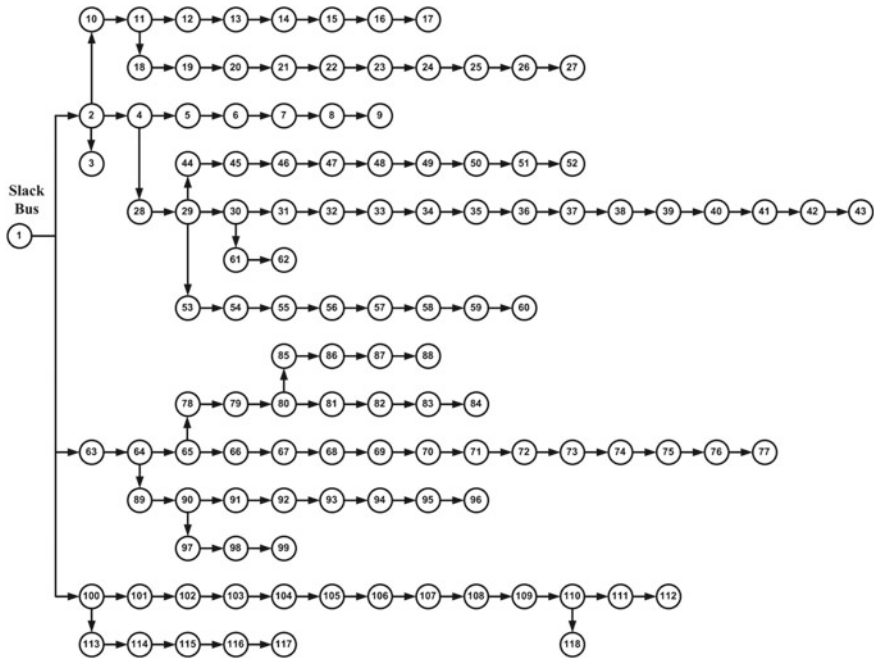


Fig. 4.6 One-line diagram of 118 bus RDS

published literatures. The convergence of fitness function with respect to iterations is displayed in Fig. 4.7a. Figure 4.7b displays the improvement of system bus voltage with OCP in comparison to the base case value. Table 4.5 shows the assessment

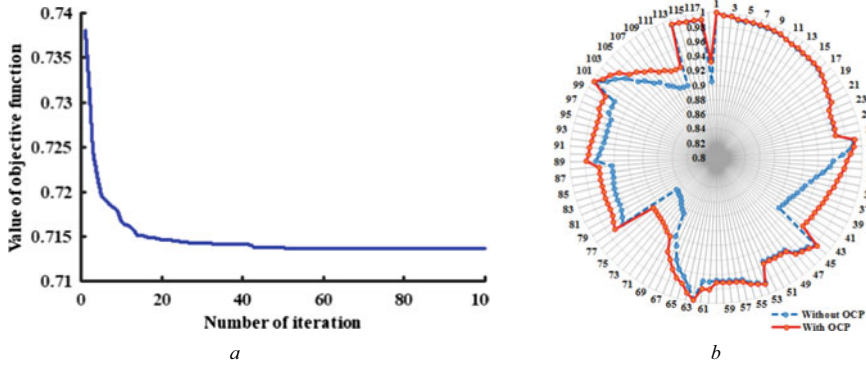


Fig. 4.7 Results found for 118 bus RDS **a** convergence plot of fitness value, **b** value of bus voltage before and after OCP

Table 4.5 Summaries and comparative results pertaining to 118 bus RDS

Items	Uncompensated	Compensated				
		IHA [33]	FPA [35]	ABC [30]	CSA [12]	SOS
Capacitor location and size	—	32(1500)	39(1500)	32(850)	32(1500)	32(1500)
		40(1500)	43(600)	35(1050)	39(1500)	39(1500)
		70(900)	70(500)	40(1300)	40(550)	43(450)
		74(1100)	74(1050)	50(800)	70(950)	70(850)
		89(1500)	86(900)	70(550)	74(750)	74(900)
		104(300)	91(1500)	73(1300)	86(1050)	86(850)
		106(900)	107(700)	79(1200)	108(1500)	91(1400)
		112(400)	109(500)	105(700)	118(1200)	107(800)
	118(1300)	118(1050)	106(250)		109(450)	
			109(800)		110(450)	
			110(1200)		118(900)	
Total kVAR		9400	8300	10,000	9000	10,050
APL (kW)	1297.413	864.797	855.690	856.548	862.031	832.662
% Loss reduction	—	33.34	34.05	33.98	33.56	35.82
RPL (kVAR)	978.715	645.697	646.636	641.96	647.969	624.726
V_{min} (p.u.)	0.869	0.912	0.907	0.909	0.906	0.910
Net savings (\$)	—	174,802.97	185,089.61	174,898.64	178,876.78	187,203.24
% saving	—	25.63	27.14	25.65	26.23	27.45

of different parameters obtained using the studied SOS and the other adopted algorithms. After performing the optimization process for full load condition, the SOS algorithm obtains 11 best locations for OCP with a total compensation of 10,050 kVAR. After applying the studied load flow approach, the base case APL and RPL

is obtained as 832.662 kW and 624.726 kVAr, respectively (refer Table 4.5). Also, the minimum value of voltage among all the buses (i.e. for the bus number 77) is improved from 0.869 to 0.910 p.u. The net annual savings is calculated using cost formula and obtained as \$187,203.242, which is better with respect to other methodologies. Comparison of output results obtained utilizing the studied and other cutting-edge algorithms (as reported in published literatures) under various loading scenarios is presented in Table 4.6.

Table 4.6 Summaries and comparative results pertaining to IEEE 118 bus test system for different loading conditions

Load factor	Items	Uncompensated	Compensated			
			SOS	Installed kVAr	IHA [33]	Installed kVAr
1	APL (kW)	1297.413	832.662	11 Locations (Total capacity = 10,050)	864.797	9 Locations (Total capacity = 9400)
	RPL (kVAr)	978.715	624.726		645.697	
	V _{min} (p.u.)	0.869	0.910		0.912	
	Net savings (\$)	—	187,203.242		174,802.970	
0.75	APL (kW)	696.994	456.575	32(950) 39(1250) 43(250) 70(550) 74(700)	496.393	32(1200) 40(900) 70(900) 89(1200) 118(1300) Total = 5500
	RPL (kVAr)	527.256	343.612		370.143	
	V _{min} (p.u.)	0.905	0.933		0.923	
	Net savings (\$)	—	84,414.32		74,835.886	
0.5	APL (kW)	297.017	203.625	39(1150) 74(700) 86(350) 91(550) 109(550)	213.350	40(900) 70(900) 89(900) 118(900) Total = 3600
	RPL (kVAr)	225.233	154.208		160.302	
	V _{min} (p.u.)	0.939	0.955		0.955	
	Net savings (\$)	—	26,116.92		23,495.375	
Net injected kVAR	Fixed (location, kVAr)	(39, 1150), (74, 700), (86, 350), (91, 550), (109, 450), (118, 550)				
	Switched (location, kVAr)	(32, 1500), (39, 350), (43, 450), (70, 850), (74, 200), (86, 500), (91, 850), (107, 800), (109, 100), (110, 450), (118, 350)				

4.7 Conclusion

The SOS algorithm is utilized in the presented study to decide the best site and size for capacitor banks with an objective function that comprises of net annual expense, active and reactive power line losses, and line currents. The total annual expense contains the total energy cost, the capacitor bank purchase cost, as well as the cost of installation and maintenance. A sensitivity index analysis is adopted for reducing the search space for optimization algorithm. The SOS algorithm is evaluated on 69-, 85-, and 118 RDSs. The dominance of the studied algorithm was demonstrated by comparing the performance of the outcomes obtained under various loading scenarios with those obtained using cutting-edge algorithms as stated in the earlier reported works. Furthermore, the net annual benefit gained by reducing line losses and improving system's voltage profile is very promising and superior to other methodologies.

References

1. Abou El-Ela, A.A., El-Sehiemy, R.A., Kinawy, A.M., Mouwafi, M.T.: Optimal capacitor placement in distribution systems for power loss reduction and voltage profile improvement. *IET Gener. Trans. Distrib.* **10**(5), 1209–1221 (2016)
2. Devabalaji, K.R., Ravi, K., Kothari, D.P.: Optimal location and sizing of capacitor placement in radial distribution system using bacterial foraging optimization algorithm. *Int. J. Electr. Power Energ. Syst.* **1**(71), 383–390 (2015)
3. Neagle, N.M., Samson, D.R.: Loss reduction from capacitors installed on primary feeders. *AIEE Trans.* **75**(3), 950–959 (1956)
4. Schmill, J.V.: Optimum size and location of shunt capacitors on distribution feeders. *IEEE Trans. Power Appar. Syst.* **84**(9), 825–832 (1965)
5. Grainger, J.J., Lee, S.H.: Optimum size and location of shunt capacitors for reduction of losses on distribution feeders. *IEEE Trans. Power Appar. Syst.* (3), 1105–1118 (1981)
6. Dura, H.: Optimum number, location, and size of shunt capacitors in radial distribution feeders a dynamic programming approach. *IEEE Trans. Power Appar. Syst.* **9**, 1769–1774 (1968)
7. Baran, M.E., Wu, F.F.: Optimal capacitor placement on radial distribution systems. *IEEE Trans. Power Deliv.* **4**(1), 725–734 (1989)
8. Abdel-Salam, T.S., Chikhani, A.Y., Hackam, R.: A new technique for loss reduction using compensating capacitors applied to distribution systems with varying load condition. *IEEE Trans. Power Deliv.* **9**(2), 819–827 (1994)
9. da Silva, I.C., Carneiro, S., de Oliveira, E.J., de Souza, C.J., Pereira, J.L., Garcia, P.A.: A heuristic constructive algorithm for capacitor placement on distribution systems. *IEEE Trans. Power Syst.* **23**(4), 1619–1626 (2008)
10. Hamouda, A., Sayah, S.: Optimal capacitors sizing in distribution feeders using heuristic search based node stability-indices. *Int. J. Electr. Power Energ. Syst.* **1**(46), 56–64 (2013)
11. Kannan, S.M., Renuga, P., Kalyani, S., Muthukumaran, E.: Optimal capacitor placement and sizing using Fuzzy-DE and Fuzzy-MAPSO methods. *Appl. Soft Comput.* **11**(8), 4997–5005 (2011)
12. El-Fergany, A.A., Abdelaziz, A.Y.: Capacitor allocations in radial distribution networks using cuckoo search algorithm. *IET Gener. Trans. Distrib.* **8**(2), 223–232 (2014)
13. El-Fergany, A.A.: Involvement of cost savings and voltage stability indices in optimal capacitor allocation in radial distribution networks using artificial bee colony algorithm. *Int. J. Electr. Power Energ. Syst.* **1**(62), 608–616 (2014)

14. Gampa, S.R., Das, D.: Optimum placement of shunt capacitors in a radial distribution system for substation power factor improvement using fuzzy GA method. *Int. J. Electr. Power Energ. Syst.* **1**(77), 314–326 (2016)
15. Gil-González, W., Montoya, O.D., Rajagopalan, A., Grisales-Noreña, L.F., Hernández, J.C.: Optimal selection and location of fixed-step capacitor banks in distribution networks using a discrete version of the vortex search algorithm. *Energies* **13**(18), 4914 (2020)
16. Riaño, F.E., Cruz, J.F., Montoya, O.D., Chamorro, H.R., Alvarado-Barrios, L.: Reduction of losses and operating costs in distribution networks using a genetic algorithm and mathematical optimization. *Electronics* **10**(4), 419 (2021)
17. Moradian, S., Homaei, O., Jadid, S., Siano, P.: Optimal placement of switched capacitors equipped with stand-alone voltage control systems in radial distribution networks. *Int. Trans. Electr. Energ. Syst.* **29**(3), e2753 (2019)
18. Sultana, S., Roy, P.K.: Optimal capacitor placement in radial distribution systems using teaching learning based optimization. *Int. J. Electr. Power Energ. Syst.* **1**(54), 387–398 (2014)
19. Vuletic, J., Todorovski, M.: Optimal capacitor placement in distorted distribution networks with different load models using Penalty Free Genetic Algorithm. *Int. J. Electr. Power Energ. Syst.* **1**(78), 174–182 (2016)
20. Nojavan, S., Jalali, M., Zare, K.: Optimal allocation of capacitors in radial/mesh distribution systems using mixed integer nonlinear programming approach. *Electr. Power Syst. Res.* **1**(107), 119–124 (2014)
21. El-Fergany, A.A.: Optimal capacitor allocations using evolutionary algorithms. *IET Gener. Trans. Distrib.* **7**(6), 593–601 (2013)
22. Halder, V., Chakraborty, N.: Power loss minimization by optimal capacitor placement in radial distribution system using modified cultural algorithm. *Int. Trans. Electr. Energ. Syst.* **25**(1), 54–71 (2015)
23. Duque, F.G., de Oliveira, L.W., de Oliveira, E.J., Marcato, A.L., Silva, I.C., Jr.: Allocation of capacitor banks in distribution systems through a modified monkey search optimization technique. *Int. J. Electr. Power Energ. Syst.* **1**(73), 420–432 (2015)
24. Lee, C.S., Ayala, H.V., dos Santos, C.L.: Capacitor placement of distribution systems using particle swarm optimization approaches. *Int. J. Electr. Power Energ. Syst.* **1**(64), 839–851 (2015)
25. Ali, E.S., Abd Elazim, S.M., Abdelaziz, A.Y.: Improved harmony algorithm and power loss index for optimal locations and sizing of capacitors in radial distribution systems. *Int. J. Electr. Power Energ. Syst.* **1**(80), 252–263 (2016)
26. Montazeri, M., Askarzadeh, A.: Capacitor placement in radial distribution networks based on identification of high potential busses. *Int. Trans. Electr. Energ. Syst.* **29**(3), e2754 (2019)
27. Abdelaziz, A.Y., Ali, E.S., Abd Elazim, S.M.: Flower pollination algorithm and loss sensitivity factors for optimal sizing and placement of capacitors in radial distribution systems. *Int. J. Electr. Power Energ. Syst.* **1**(78), 207–214 (2016)
28. Cheng, M.Y., Prayogo, D.: Symbiotic organisms search: a new metaheuristic optimization algorithm. *Comput. Struct.* **15**(139), 98–112 (2014)
29. Rao, R.S., Narasimham, S.V., Ramalingaraju, M.: Optimal capacitor placement in a radial distribution system using plant growth simulation algorithm. *Int. J. Electr. Power Energ. Syst.* **33**(5), 1133–1139 (2011)
30. El-Fergany, A.A., Abdelaziz, A.Y.: Artificial bee colony algorithm to allocate fixed and switched static shunt capacitors in radial distribution networks. *Electr. Power Comp. Syst.* **42**(5), 427–438 (2014)
31. Teng, J.H.: A direct approach for distribution system load flow solutions. *IEEE Trans. Power Deliv.* **18**(3), 882–887 (2003)
32. Das, D., Kothari, D.P., Kalam, A.: Simple and efficient method for load flow solution of radial distribution networks. *Int. J. Electr. Power Energ. Syst.* **17**(5), 335–346 (1995)
33. Ali, E.S., Abd Elazim, S.M., Abdelaziz, A.Y.: Improved Harmony Algorithm for optimal locations and sizing of capacitors in radial distribution systems. *Int. J. Electr. Power Energ. Syst.* **1**(79), 275–284 (2016)

34. Zhang, D., Fu, Z., Zhang, L.: An improved TS algorithm for loss-minimum reconfiguration in large-scale distribution systems. *Electr. Power Syst. Res.* **77**(5–6), 685–694 (2007)
35. Abdelaziz, A.Y., Ali, E.S., Abd Elazim, S.M.: Optimal sizing and locations of capacitors in radial distribution systems via flower pollination optimization algorithm and power loss index. *Int. J. Eng. Sci. Technol.* **19**(1), 610–618 (2016)

Chapter 5

Optimization of the Mechanical Properties of Energy-Efficient Natural Fiber-Reinforced Polymeric Composites



Satadru Kashyap and Jahidul Islam

Abstract An incredible attempt has been made to study natural fiber-based composites over the last two decades due to their rising demand in the industry as materials with good mechanical properties, lower cost, renewable, eco-friendly, and energy-efficient characteristics. Natural fiber composites are energy efficient and environmentally advanced than synthetic composites in most cases due to: (1) better energy efficiency due to the presence of lightweight natural fibers resulting in lower emissions and better fuel efficiency (energy-efficient automotive applications); (2) replacement of polluting base polymers with biodegradable natural fibers; (3) lower environmental shocks than synthetic composites; and (4) incineration of natural fibers composites upon disposal provides in recovered energy and carbon credits. Additionally, usage of industrial waste such as lime sludge in composite fabrications offers two-pronged advantages—(1) reuse of an industrial waste that otherwise causes pollution and (2) addition of a particulate reinforcement which would add to the properties of the composite. Hence, in this study, natural coir fiber and industrial lime sludge waste are used as reinforcement in an epoxy matrix to study the composites' mechanical properties (tensile and flexural strength). However, it is paramount to know the optimum values of parameters (fiber length, fiber content, and lime sludge content) in order to produce the composite with the best mechanical parameters. Additionally, the influence of these three parameters on the mechanical properties of lime sludge-filled coir fiber-reinforced composites is also important. Hence, Taguchi's L16 orthogonal array with three factors and four levels is used to determine the optimum process parameter values within the chosen levels in order to obtain the best mechanical properties. Moreover, analysis of variance (ANOVA) is also used to examine the effect of each process parameter on the end results. Regression models are also developed for each mechanical property studied as a function of the three input parameters. Overall, it was observed that increasing the fiber length plays the most dominant role in improving the mechanical properties of the energy-efficient lime sludge-filled coir fiber-reinforced polymeric composites.

S. Kashyap (✉) · J. Islam

Department of Mechanical Engineering, Tezpur University, Napam, Sonitpur, Assam 784028, India

e-mail: satadru@tezu.ernet.in

5.1 Introduction

A composite consists of two or more combined constituents with different physical and chemical properties, but each of them retains their own identity in the composite. Composites consist of two phases—(1) the reinforcing phase consisting of either particulates, flakes, or fiber and (2) matrix phase consisting of a continuous part usually the major chunk of material. Herein, the fibers and matrix are bound with each other, but they maintain their own identity and characteristics in the composite [1]. The fibers provide the reinforcement by taking most of the load, while the matrix being ductile in nature provides for the toughness of the composite. Additionally, the matrix encompasses all the reinforcing phase thus protecting them from external damage due to environment or during preprocessing, during fabrication and during service. Thus, composite materials are a combination of two constituents where the role of the reinforcing phase withstands external stresses and makes the material stiff, while the matrix phase grips the fibers together in place by acting as a binding agent [2].

It is evident that the applications of composite materials are far and wide employing them in the manufacture of complex machineries and machine parts as well as objects of our daily lives. They possess numerous advantages over traditional structural materials, viz. light in weight, low density, cheap, versatile and inexpensive fabrication techniques and possess comparable properties with the contemporary structural materials [3]. Mechanically, they are superior than conventional metals by possessing superior properties, viz. high specific strengths (flexural, tensile, and impact). This finds them applications in the fields of aviation, marine, and space where weight of the equipment is a major constraint. They also possess good thermal and electrical properties when used in conjunction with other insulating materials. However, the main advantage is their ability of being tailor made for a specific applications by changing the compositions of the two constituents. In the last few years, polymeric composites have paved their way toward being the major engineering materials in numerous applications. While the domain of composite materials has been continuously increasing with new avenues, owing their various advantages, but the present challenge is to make them more energy efficient, eco-friendly, cheaper, and environmentally stable in hazardous environment in order to substitute contemporary materials [4].

Natural fibers, viz. coir, sisal, jute, flax, bamboo, hemp, etc., have been employed as the reinforcing phase in various polymeric over the last few years. Natural fibers are renewable materials which are abundantly available, are biodegradable, and possess good mechanical properties with low costs and reduced energy utilization. It has been a proven fact that they possess comparable specific mechanical properties with other synthetic fibers used in composites [5]. An incredible attempt has been made to study natural fiber-based composites over the last two decades due to their rising demand in the industry as materials with good mechanical properties, lower-cost, renewable, eco-friendly, and energy-efficient characteristics. Natural fiber composites are energy efficient and environmentally advanced than synthetic composites in most cases due

to: (1) better energy efficiency due to the presence of lightweight natural fibers resulting in lower emissions and better fuel efficiency (energy-efficient automotive applications); (2) replacement of polluting base polymers with biodegradable natural fibers; (3) lower environmental shocks than synthetic composites; and (4) burning of natural fiber composites upon disposal provides in recovered energy and carbon credits.

Natural fibers are usually 50% lighter and cheaper than synthetic fibers such as glass and have specific properties, viz. stiffness comparable with glass fibers although there are absolute values less than glass. Sudhakara et al. [6] illustrated in their work about the numerous applications of natural fibers, viz. coir, jute, and sisal. They reported that these fibers have comparable (moderate) tensile and flexural properties along with high impact strength when compared with other natural fibers. Rao et al. [7] investigated the comparable wear performance of coir dust-reinforced epoxy composites which were untreated and surface treated using Taguchi method to minimize the experimental time and cost. It was observed that the surface treated coir dust epoxy composites demonstrated superior abrasion resistance when compared with untreated composites. With increasing coir loading in the composite, the wear characteristics improved. It was also illustrated that the mechanical properties of composites, viz. tensile, flexural, and impact properties, were hugely influenced by the fiber length of the reinforcing agent. Natarajan et al. [8] reported the properties of hybrid glass and woven coir-reinforced polyester composites based on their stacking sequence. It was observed that the composites demonstrated the advantages of both the reinforcing fibers. The interfacial bonding at the fiber–matrix interface was also studied with scanning electron microscopy. However, it is paramount to mention that there may be variations in the characteristics of natural fibers based on certain parameters such as type of fiber, environment of their growth, how they are extracted, when they are harvested, and how they are surface treated and stored [9, 10]. It has been observed in case of flax fibers that manual extraction leads to 20% more strength in fibers when compared with mechanical extraction, while the strength seems to decline by 15% in just 5 days if fibers are harvest beyond their optimum time period [11].

Additionally, an important parameter which hugely affects the properties of composites is bonding at the fiber–matrix interface. Upon loading, the matrix transfers the load from itself to the fibers via the interface. If the interface is weak, then it will lead to cracks at the interface and fiber pullout leading to low mechanical properties. Hence, a good interfacial bonding along with optimum reinforcing agent is vital for the properties of a composite. It has been observed that insufficient matrix due to high fiber loading can lead to inadequate wetting of fibers which in turn causes low interfacial bonding, defects, and voids at the interface [12]. Since the wetting of fibers is important for interfacial bonding, hence, researchers have put forward many surface treatment (physical and chemical) techniques for fibers in order to enhance the wettability of fibers [13]. It has been observed that chemical treatment of the natural fibers with an alkali leads to the removal of lignin, hemicelluloses, wax, and fat which subsequently increases the surface area or area of wettability by exposing the cellulosic portion of the fibers, thus improving the bonding at the interface [14]. One

more parameter influencing composite properties is dispersion of fibers/particulates in the matrix in case of short fiber-reinforced or particulate composites. A major challenge posed is that natural fibers are inherently hydrophilic while the matrices are hydrophobic in nature. This may lead to agglomeration of fibers (instead of uniform dispersion) especially at high fiber loading and longer fiber lengths. It is obvious that uniform dispersion encourages proper interfacial adhesion and void reduction by allowing the matrix to fully wet the fibers. Moreover, good dispersion also promotes uniform properties all throughout the composites. It has been observed that dispersion is affected by processing parameters such as mixing, pressure, and temperature; and by addition of additives such as stearic acid (to modify dispersion in PE and PP) and MAPP (to increase interfacial bonding) [15].

Li et al. [16] conducted a comparative investigation between untreated and two types of fiber lengths (20 and 40 mm) of coconut fibers treated with alkali as the reinforcing phase in polymeric composites. Additionally, they also included mortar mixed with cement, sand, water, and super plasticizer in ratio of 1: 3: 0.43: 0.01. It was observed that mechanical properties such as flexural strength and ductility improved along with the ability to withstand energy. Thus, the addition of treated coconut fibers and the mortar mix yielded superior material than the original ones. Harish et al. [17] fabricated coir polymer composites in order to study their mechanical properties. They found that coir fiber has enormous potential to be employed as a reinforcing agent in composites designed for low loads. Among natural fibers, coir has enormous potential to emerge as a substitute for traditional plastics or metals for making any product or structural component. Coir fiber is abundantly available, is renewable, recyclable, cheap, environmentally sustainable, biodegradable, and possesses good mechanical properties, viz. lightweight, low density (1.0 to 1.3 g/cm³), comparable specific strengths, high strain up to failure (40%), and good toughness (due to high strain to failure property) [18].

Hybrid composites consist of a combination of two or more reinforcing phases or one reinforcing phase and a filler in the matrix or a reinforcing phase with multiple matrices or a combination of two or more reinforcing and matrix phases. Hybrid composites are more sought after nowadays because of the fact that they offer the advantages of either the reinforcing phases or matrix phases in the composites toward the betterment of their properties, e.g., if the composite contains one fiber with high modulus and one with lower modulus, then the higher modulus fiber can account for higher stiffness and main stress bearing roles. Moreover, there is more leeway with hybrid composites in changing the stacking sequences, fiber loading, and fiber orientation [19]. In today's world, environmental sustainability is given prime importance through reuse and recycling of all hazardous substances than can harm the environment. Industrial wastes disposed off in landfills have created huge amounts of pollution (air, water, and land), and currently, efforts are being made to reuse or recycle these wastes in a bid to reduce pollution. Use of household and industrial wastes in composites as fillers and reinforcing agents provides a huge opportunity for managing these wastes. Thus, these composites can be employed as a sink for carbon credits through use of industrial wastes in addition to renewable and biodegradable natural fibers as reinforcing phases in them.

Many investigations have been conducted over the past few years that have revealed that addition of fillers tends to enhance the properties of composites along with lowering the product cost, thus improving the business viability and reliability [20–22]. This property enhancing quality would expand their range of applications in engineering and also help in mitigating pollution. Off late as a part of sustainable waste management, abundant researches have been carried out in recycling industrial waste as reinforcements/fillers in polymeric composites. Industrial wastes, viz. electronic wastes [23], post-consumer recycled wood [24], biochar [25], industrial fly ash cenospheres [26], non-metals recycled from waste printed circuit boards [27], red mud wastes [28], Thal silica [29], etc., have been used as the reinforcing phase in polymeric composites so that to improve their structural functionality and also recycle the wastes. Usage of industrial waste such as lime sludge in composite fabrications offers two-pronged advantages—(1) reuse of an industrial waste that otherwise causes pollution and (2) addition of a particulate reinforcement which would add to the properties of the composite. In this regard, industrial lime sludge waste is an inert material mostly composed of calcium carbonate and generated from various industries, viz. paper and pulp, fertilizer, acetylene, soda ash, sugar, etc. It mainly consists of calcium carbonate (CaCO_3) in the form of lime as the main component, which showed a composition of 40–50% calcium oxide, along with minute quantities of SiO_2 , Al_2O_3 , Fe_2O_3 and traces of alkali oxides after a loss on ignition of 35–40 upon heating. Utilization of this waste as a filler in composites would serve the dual purpose of pollution abatement as well as reducing the amount of polymer in the composite leading to cost savings. Hence in this investigation, lime sludge waste was used as additional filler with coir fibers in an epoxy matrix with the intention of improving their properties as well as cost reduction (due to addition of a waste) and energy efficiency (recycling of a waste that causes environmental pollution).

However, the main challenge of using natural fibers is moisture/water absorption by the fibers during service and low bonding at the interface. The main objective of using the chemical treatments for the natural fibers is to enhance the interfacial adhesion at the fiber–matrix boundary. The increased bonding helps to improve the stress transfer between the fibers to matrix and to withstand for higher strength. The various chemical treatments reviewed are NaOH, silane, stearic acid, benzylation, fatty acid derivative, sodium chlorite, etc. Rout et al. [30] investigated the characteristics of surface treated coir fiber-reinforced polyester composites. The composites treated with 5% alkali (NaOH) fibers showed enhancement in the flexural and impact strength. Nam et al. [31] reported the mechanical characteristics of the alkali treated coir fiber-reinforced polybutylene succinate composites. They fabricated various fiber loading percentages of coir composites after treating the fibers with 5% NaOH. Upon comparative analysis with non-treated fiber composites, they reported a significant enhancement in the mechanical properties and interfacial shear strength (IFSS) alkali treated coir fiber composites.

Mitigation of the rising environmental pollutions with energy efficiency (lightweight and low carbon credit), low environmental shocks (biodegradable), and development of low cost composites are three very important points to be considered in today's industrial and societal world. Moreover, natural fiber-based composites

have been studied in great advantage largely in recent times due to their sustainability, renewability, and the unique properties they offer in composites materials. Hence, the motivating factors for this research are as follows:

- Limited research has been conducted based on the combined effects of fiber length (short fiber and long fiber) along with different fiber loading related to the mechanical properties of hybrid coir fiber-reinforced lime sludge waste filled composites.
- Utilization of industrial lime sludge waste as filler in polymer composites will hopefully serve the dual purpose of pollution abatement as well as reducing the amount of polymer in the composite leading to cost savings.
- Taguchi analysis of coir fiber-reinforced epoxy composites will provide the advantages of studying the effect of three parameters (fiber length, fiber wt.%, and lime sludge wt.%) together as a collective effort with reduced number of experiments, and ANOVA analysis would show the most important affecting composite properties.

Hence in this study, characteristics of lime sludge waste filled coir fiber-reinforced epoxy composites were studied as a function of fiber length, fiber weight fraction, and lime sludge weight fraction. Determination of tensile and flexural properties of these composites, along with the thermal and water absorption characteristics, was also done to study additional composite characteristics. Subsequently, optimization of their properties was studied using L_{16} design of experiment, ANOVA, and regression analysis.

5.2 Methodology

5.2.1 Materials

Coir fiber was obtained locally for its use as a reinforcing material. Epoxy resin and hardener are supplied by the Perfect Trading Company Ltd. The fibers were then cut in to 5, 8, and 12 mm length to be used as short fibers and 120 mm length as long fibers.

5.2.2 Surface Treatment of Fibers

In order to improve the mechanical properties of composites, to reduce the moisture absorption, and to enhance the fiber–matrix bonding, the fiber surfaces are chemically treated for fabricating the composites. In the present work, chemical treatment is carried out, namely alkali (NaOH) for surface treatment of fibers. Alkali treatment is used for surface treatment of coir fibers. Fibers were rinsed 3 times with water

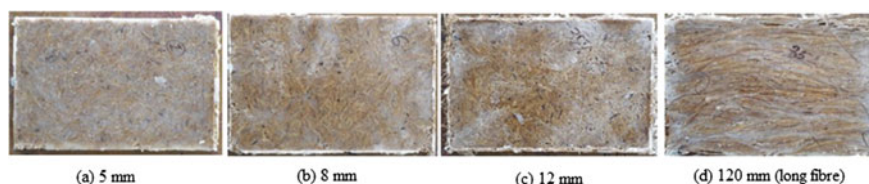


Fig. 5.1 Composites plates of lime sludge-filled coir fiber-reinforced epoxy composites

to eliminate waste remains, contaminants, and dusts. They were then dried for 48 h at room temperature. The surface treatment technique involved dipping 200 g coir fibers in a 5% (W/V) NaOH solution (2L) for 1 h at room temperature. Subsequently, it was washed 10 times with distilled water so as to remove the absorbed alkali from the fibers. Finally, they were dried naturally for 48 h and dried at 500 °C for 8 h in an oven. The dried fibers were preserved in a container before being used in the fabrication process so as to eliminate any atmospheric contamination [32].

5.2.3 Fabrication of Composites

The randomly oriented coir fiber is taken as reinforcement, and lime sludge was employed as the filler constituent while epoxy resin was used as matrix. The epoxy and hardener were mixed in 10:1 ratio by weight and cured at room temperature. The chopped fibers and lime sludge are thoroughly mixed with epoxy resin. The composites were fabricated in a compression molding machine (Make: SANTEC). Three randomly dispersed short coir fiber composites (fiber length 5, 8, 12 mm) and one long fiber composite (full length of the composite, i.e., 120 mm) were taken into consideration for this study. The composites were prepared with four different fiber loadings (10, 20, 30, and 35) wt.%, four different fiber lengths (5, 8, 12, and 120) mm, and four different lime sludge loadings (3, 6, 9, and 12) wt.%. The each composite was pressed with a weight of about 10 kg/cm² for 24 h, following which it was taken out of the mold cavity. The specimens were cured in air for an additional 24 h subsequent to their ejection from mold cavity. Finally, specimens were cut from original compression molded samples as per ISO standards for mechanical tests. Figure 5.1 shows the different lime sludge-filled coir fiber epoxy composite.

5.2.4 Testing of Mechanical Properties

The tensile strength of composites was determined using a Universal Testing Machine (Make: Zwick, Model—Z010). The test was conducted on the composite samples as per ISO 527 standards using a uniaxial loading applied at the ends. The strain rate

Table 5.1 Control factors and their levels

Parameters	Levels			
	Short fiber		Long fiber	
	I	II	III	IV
Fiber length (mm)	5	8	12	120
Fiber weight (%)	10	20	30	35
Lime sludge (%)	3	6	9	12

was taken as 2 mm/min. The rectangular sample size for tensile testing was $100 \times 10 \times 4$ mm.

Three point bending test was also conducted using a Universal Testing Machine (Make: Zwick, Model—Z010) in accordance with ISO 178 to determine the flexural strength of the composites. The rectangular sample size for tensile testing was $80 \times 10 \times 4$ mm. A span of 64 mm was employed maintaining a cross-head speed of 2 mm/min.

5.2.5 Selection of Process Parameters

The selection of process parameters and their levels was one of the major steps for parametric analysis using the Taguchi method. In this research, three parameters selected were fiber length, fiber weight %, and lime sludge content in order to investigate the influence of material compositions on tensile behavior of the composites. Table 5.1 shows the control factors and their corresponding levels. Taguchi design of experiments was used in this investigation to plan and perform the experiments. Based on the input parameters and their chosen levels (refer Table 5.1), Taguchi L_{16} orthogonal array was employed in this study.

5.2.6 Taguchi Analysis

Dr. Genichi Taguchi developed the Taguchi method with an objective to enhance the quality of a fabricated product with the help of different process parameters and, simultaneously, save assets to augment profitability [33]. For design of experiments, Taguchi method uses orthogonal arrays which study a large number of parameters and reduce them to a small number of experiments. Depending upon each process parameter (control factors and their levels), the orthogonal arrays are balanced and provide the best set of experiments for chosen factors and their levels that finally reduces the amount of experiments when judged against a full factorial design. For analysis, the results obtained experimentally are converted into signal-to-noise (S/N) ratios. These S/N ratios are logarithmic functions employed in determining the preferred

output characteristic and are also used as objective functions for optimization. S/N ratio values assist in data analysis and calculation of optimum output values. Taguchi modeling utilizes the signal-to-noise (S/N) ratios, for the quality characteristics and then evaluated the optimum control factor and their levels. S/N ratio reduces the variability by lowering the uncontrollable factors (i.e., noise factors) [33]. Although three types of S/N ratios can be used, viz. larger the better, smaller the better, and nominal the best—the S/N ratio ‘larger the better’ (refer equation 5.1) is used in this research as it was required to maximize the strength properties of the composites.

$$S/N \text{ ratio} = -10 \log_{10} \frac{1}{n} \sum_{i=1}^n \frac{1}{y^2} \quad (5.1)$$

5.2.7 Analysis of Variance and Regression Analysis

Analysis of variance (ANOVA) was first proposed by R.A. Fisher as a statistical model in order to determine which control factor appreciably influences the output characteristics [34]. ANOVA assists in determining the most significant group that primarily influences the response. It forecasts the optimal grouping of the input parameters by providing the main effect plots. P -value < 0.05 shows differences amidst the means at 0.05 significance.

In regression analysis, R^2 (r -square) or coefficient of determination offers a gauge of how good the experiential outputs are simulated by the model as a function of the amount of total variation of outputs given by the model. Additionally, the normal probability plot is a graphical method of testing the normality. The role is to measure if a data set is approximately normally distributed [34]. In the present study, MINITAB 16 trial version software was used for ANOVA and regression analysis.

5.2.8 Water Absorption Test

The consequence of water absorption on lime sludge-filled coir fiber epoxy composites was calculated as per ISO 62:2008. All the composite samples were air dried in a hot air oven before weighing in order to eliminate any debris, lubricant, or moisture on them. The weight taken subsequent to hot air drying was taken as the initial weight of the composites. The composite specimens were immersed in distilled water at 25 °C. After every 24 h of time interval, the specimens were taken out of water, cleaned with a dry cloth, and weighed to note the water absorption in them. These measurements of weight were taken periodically at time intervals of 24 h for up to 600 h. This measurement is continued till it was confirmed that a saturation limit was reached in terms of water absorption. The water absorbed in percentage by the

composites was calculated using Eq. (5.2)

$$W(\%) = \frac{W_t - W_o}{W_o} \times 100\% \quad (5.2)$$

where W is percentage water absorption, W_o is the oven dry weight, and W_t the weight of the sample after time t , respectively.

5.2.9 Thermal Analysis

The thermal stability analysis of the lime sludge-filled epoxy composites is carried out using thermogravimetric analyses (Model: TGA-50 and DSC-60, Make: SHIMADZU) with temperature set between room temperature to 600 °C. The analyzer identifies the loss of mass with a resolution of 0.1 gm as a function of temperature.

5.2.10 Morphological Analysis

Scanning electron microscope (Model: JSM 6390LV, Make: JEOL) was used for the morphological characterization of the composite surface. The surfaces of the specimen were Pt coated before their morphological analysis. Morphological analysis was conducted on the fractured surface of the tensile testing sample using SEM.

5.3 Results and Discussions

5.3.1 Tensile Characterization of Composites

The characterization of the tensile properties of the composites was conducted by studying the tensile strengths of the specimens as per the chosen level using the Taguchi L_{16} array.

5.3.1.1 Effect of Coir Fiber (Weight Fraction) on the Tensile Strength

At first, the effect of fiber weight fraction on the tensile strength of coir fiber-reinforced epoxy composites was found out. Four composites samples with 10, 20, 30, and 35 wt.% coir fiber were tested without any lime sludge content and at constant fiber length of 8 mm.

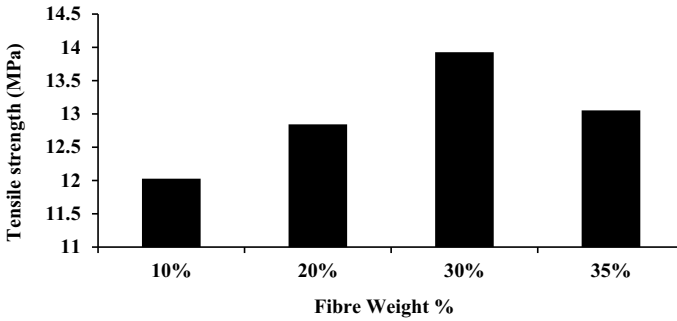


Fig. 5.2 Effect of coir fiber weight (%) on the tensile strength

From Fig. 5.2, it was found that the tensile strength of composite increased as the fiber concentration increases up to 30 wt.% and thereafter further increases in fiber concentration, decreased the tensile strength. Upon loading, the coir fibers work as the main load bearers, while the matrix uniformly transmits the stress to the fibers, which results in superior properties of composites. At 30 wt % fiber loading, the composites show superior tensile strength values because of the presence of sufficient fibers which bear the load. Beyond 30 wt.% amount of fibers increase and matrix decrease, there may be insufficient matrix to transfer the load to the fiber, which tend to increase stress concentration, brittleness, and thus decrease tensile strength.

However, in order to study the effects of two additional parameters (fiber length and lime sludge weight fraction) along with fiber weight fraction, Taguchi design of experiments L_{16} orthogonal array was employed to determine the optimum set of parameters (among the chosen set of parameters) in order to obtain the maximum values of output parameters (tensile and bending strength).

5.3.1.2 Taguchi Design of Experiments (L_{16} Array) for Tensile Property

Tensile values obtained experimentally are given in Table 5.2 that shows the values of tensile strength along with their signal-to-noise (S/N) ratios corresponding to L_{16} Taguchi method. The S/N ratio of all the performance parameters (tensile strength values) is calculated by using Eq. (5.1), i.e., larger-the-better criteria.

Table 5.3 shows the response table for the means of tensile strength that differentiates the influence of each input factor at different levels. This identifies the optimum level of each input factor for specific output characteristics. The response for fiber length at level 1 was determined using the averages of the four responses corresponding to the same level. In the same way, responses for levels 2, 3, and 4 were determined. Similarly, responses for fiber weight and lime sludge are also determined. Table 5.4 shows the response tables for tensile strength with respect to S/N ratios of the composites.

Table 5.2 Taguchi analysis of tensile strength of coir-lime sludge-epoxy composites

Exp. No.	Fiber length (mm)	Fiber weight (%)	Lime sludge (%)	Tensile strength (MPa)	S/N Ratio
1	5	10	3	12.65	22.71
2	5	20	6	13.36	21.84
3	5	30	9	13.76	22.17
4	5	35	12	9.071	19.15
5	8	10	6	12.10	23.58
6	8	20	3	12.11	22.99
7	8	30	12	14.90	22.21
8	8	35	9	10.80	20.67
9	12	10	9	12.21	20.99
10	12	20	12	13.31	21.071
11	12	30	3	14.33	21.82
12	12	35	6	13.39	23.16
13	120	10	12	19.44	25.90
14	120	20	9	23.57	27.21
15	120	30	6	25.73	28.10
16	120	35	3	28.16	30.11

Table 5.3 Response table for means of tensile strength

Level	Fiber length (FL)	Fiber weight (FW)	Lime sludge (LS)
1	11.96	14.18	17.79
2	12.48	15.19	15.82
3	13.31	17.10	14.93
4	25.03	16.33	14.25
Δ	13.07	2.93	3.53
Rank	1	3	2

Δ = (largest value – smallest value) of the corresponding parameter

From Tables 5.3 and 5.4, it is observed that the optimal combination for maximizing the tensile strength according to the rank obtained is FL₄ FW₃ LS₁, i.e., fiber length—120 mm, fiber weight—30 wt%, and lime sludge—3 wt%. Corresponding to the mean values of tensile strength %, the main effects plot is shown in Fig. 5.3. From this, the tensile strength characteristics show a steady improvement with increasing fiber length, i.e., 5 to 12 mm; and in the same way, tensile strength increases for long fiber composites, i.e., 120 mm continuous fiber composite. Two reasons may be attributed to this increase in the tensile properties—(1) increase in the fiber length

Table 5.4 Response table for S/N ratio of tensile strength

Level	Fiber length (FL)	Fiber weight (FW)	Lime sludge (LS)
1	21.45	22.84	24.24
2	21.87	23.30	23.54
3	22.47	24.37	23.10
4	27.83	23.12	22.75
Δ	6.38	1.53	1.49
Rank	1	2	3

Δ = (largest value – smallest value) of the corresponding parameter

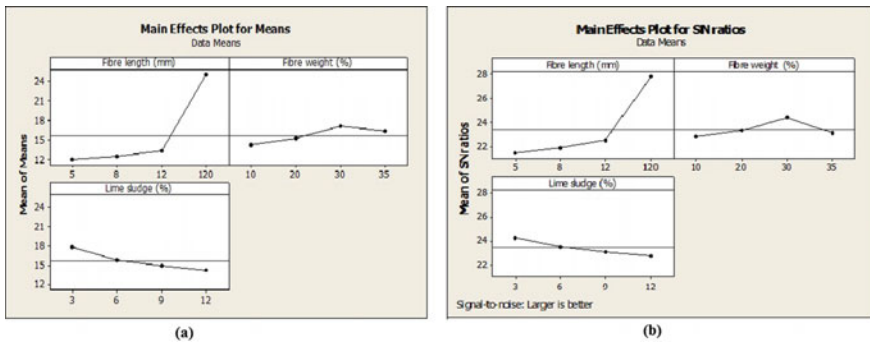


Fig. 5.3 Main effects plot for **a** means and **b** S/N ratios of tensile strength

may improve the load carrying capacity of the fibers in the composite and (2) improvement in the adhesion at the fiber–matrix boundary due to surface treatment of fibers which improves the transmission of the load from the matrix to fibers. Moreover, it is a well-known fact that long fiber composites have better mechanical properties than short fiber composites due to their ability to withstand higher load. Hence, the increase in the tensile properties of the long fiber composites (120 mm fiber length) when compared with short fiber composites in this case is very obvious. Also, it is observed that the tensile strength of composite increases as the fiber concentration increases up to 30 wt.%. Further increase in fiber concentration decreases the tensile strength due to the fact that the amount of matrix required to hold the fibers may be insufficient (due to the increase in fiber concentration) which may lead to voids in the composites and inefficient transmission of stress to the fibers via the matrix.

5.3.1.3 ANOVA Analysis for Tensile Properties

ANOVA analysis is very significant in order to calculate the amount of involvement of each input factor on the output characteristics. MINITAB 16 (trial version) was

Table 5.5 ANOVA data for *S/N* ratio of tensile strength

Source	DOF	Seq SS	Adj SS	Adj MS	F	P	% C
Fiber length (mm)	3	106.61	106.61	35.53	18.27	0.002	63.37
Fiber weight %	3	5.36	5.36	1.78	0.92	0.486	9.82
Lime sludge %	3	4.93	4.93	1.64	0.85	0.517	8.23
Error	6	11.66	11.66	1.94			16.42
Total	15	128.583					100

S (mean square error) = 1.39455 $R^2 = 90.93\%$ R^2 (adjusted) = 77.31%

employed to conduct ANOVA with 95% confidence level and 5% significance level. ANOVA results are given in Table 5.5 which shows the results based on *S/N* ratios of tensile values of the composites. The result of ANOVA for tensile strength reveals that fiber length has the maximum amount of contribution (63.37%) followed by fiber weight (9.82%) and lime sludge (8.23%). This shows that fiber length is largely significant in maximizing the tensile strength.

5.3.2 Flexural Characteristics of Composites

The characterization of the bending characteristics of the composites was conducted by studying the flexural strengths of the specimens as per the chosen level using the Taguchi L_{16} array.

5.3.2.1 Taguchi Design of Experiments (L16 Array) for Flexural Property

The results derived experimentally are provided in Table 5.6 that presents the values of flexural strength along with their signal-to-noise (*S/N*) ratios corresponding to L_{16} Taguchi method. The *S/N* ratio of all the performance parameters (flexural strength values) is calculated by using Eq. (5.1), i.e., larger-the-better criteria.

Tables 5.7 and 5.8 show the response tables for the means and *S/N* ratios of the composites based on flexural strength. From the response tables, it was found that the optimal combination for maximizing the flexural strength is $FL_4 LS_2 FW_3$, i.e., fiber length—120 mm, lime sludge—6%, and fiber weight—20%. The means of flexural strength were illustratively described by the main effects plot shown in Fig. 5.4.

It can be seen from Fig. 5.4 that the bending strength showed gradual improvement as fiber length increased from 5 to 12 mm and in the same way, the flexural strength increased to maximum values for continuous fiber composites (long fiber, 120 mm). Similar to the trend in tensile strength values, the improvement in the bending strength with increasing fiber length can be attributed to the fact that the longer the fibers, the better is their load carrying capacity, especially for long fiber composites where

Table 5.6 Taguchi analysis of flexural strength of coir-lime sludge-epoxy composites

Exp. No.	Fiber length (mm)	Fiber weight (%)	Lime sludge (%)	Flexural strength (MPa)	S/N ratios
1	5	10	3	31.22	29.89
2	5	20	6	36.57	31.26
3	5	30	9	33.30	30.45
4	5	35	12	25.83	28.24
5	8	10	6	38.56	31.72
6	8	20	3	41.29	32.32
7	8	30	12	35.30	30.96
8	8	35	9	36.33	31.21
9	12	10	9	38.32	31.67
10	12	20	12	41.88	32.44
11	12	30	3	36.06	31.14
12	12	35	6	38.48	31.71
13	120	10	12	44.45	32.96
14	120	20	9	51.69	34.27
15	120	30	6	65.42	36.31
16	120	35	3	57.54	35.20

Table 5.7 Response table for means

Level	Fiber length (FL)	Fiber weight (FW)	Lime sludge (LS)
1	31.73	38.14	41.53
2	37.87	42.86	44.76
3	38.69	42.52	39.91
4	54.78	39.55	36.87
Δ	23.04	4.72	7.89
Rank	1	3	2

Δ = (Largest value – Smallest value) of the corresponding parameter

the fibers are continuous in length and offer more load carrying capacity to the composite. Additionally, better transfer of load from matrix to fibers due to high interfacial adhesion owing to surface treatment of fibers may also lead to the increase in strength with fiber length.

It was also revealed that the strength increases initially with rising fiber loading from 10 to 20 wt%. But, beyond 20 wt.% fiber concentration, a slight decrease in bending strength was noticed. This decline in the bending strength beyond 20 wt% fiber loading can be attributed to the shortage of the resin matrix that led to the insufficient wetting of the fibers and subsequently leading to voids or low interfacial

Table 5.8 Response table for *S/N* ratios (larger the better)

Level	Fiber length (FL)	Fiber weight (FW)	Lime sludge (LS)
1	29.96	31.56	32.14
2	31.55	32.57	33.05
3	31.74	32.22	31.31
4	34.68	31.59	30.85
Δ	4.72	1.01	2.20
Rank	1	3	2

Δ = (largest value – smallest value) of the corresponding parameter

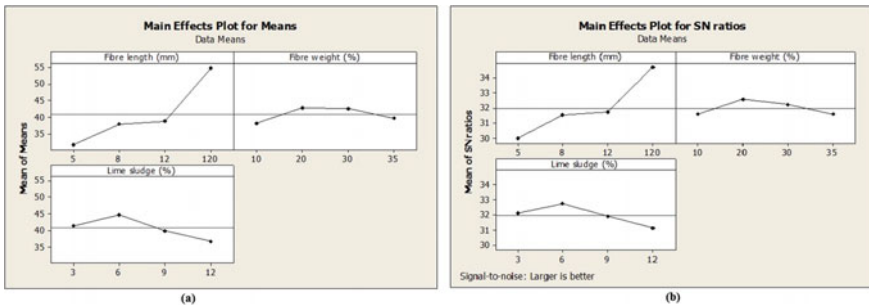


Fig. 5.4 Main effects plot for **a** means and **b** *S/N* ratios of flexural strength

adhesion. Proper fiber mixing and lay up of fibers also create a huge problem during fabrication if the fiber content is very high—may also be a significant cause [35]. Contrary to tensile strength values, it was observed that the optimal contribution of lime sludge weight fraction was 6 wt% which was improvement over the tensile strength values of 3 wt%. This shows that lime sludge being particulate in nature increases the flexural properties of the composites making it more suitable for bending stresses.

5.3.2.2 ANOVA Analysis for Tensile Properties

The ANOVA analysis for the flexural strength values is given in Table 5.9 which illustrates the ANOVA calculations with respect to *S/N* ratios of flexural strength. The result of ANOVA for flexural strength revealed that fiber length showed the maximum contribution (60.15%) which was followed by lime sludge (16.05%) and fiber weight (10.11%). This demonstrated that fiber length was the most influential parameter in maximizing the flexural strength.

Table 5.9 ANOVA data for *S/N* ratio of flexural strength

Source	DOF	Adj SS	Adj MS	F	P	%C
Fiber length (mm)	3	46.5427	15.5142	19.783	0.002	60.15
Fiber weight %	3	2.9472	0.9824	1.251	0.371	10.11
Lime sludge %	3	5.2678	1.7559	2.244	0.184	16.05
Error	6	4.7052	0.7842			13.69
Total	15	59.4629				1000

S (mean square error) = 0.885549 $R^2 = 92.09\%$ $R^2(\text{adj}) = 80.22\%$

5.3.3 Regression Analysis

In order to estimate the relationship between the composite constituents and the strength characteristics affecting composite properties and for prediction of properties, regression analysis was used. Herein, interrelationships were established between the input and output characteristics by modeling the relations using multiple linear regression.

The regression equation for tensile strength (TS) and flexural strength (FS) is as follows:

$$TS = 22.0 + 0.0531(FL) + 0.0299(FW) - 0.163(LS), R^2 = 88.25\% \quad (5.3)$$

$$FS = 35.9 + 0.186(FL) + 0.107(FW) - 0.620(LS), R^2 = 89.06\% \quad (5.4)$$

where FL = fiber length (mm), FW = fiber weight (%), and LS = lime sludge (%).

Equations (5.3) and (5.4) derived from regression analysis may be used for predicting the tensile strength and flexural strength values for any combination of fiber length, fiber weight, and lime sludge. The normal probability plots for tensile and bending strengths (shown in Fig. 5.5) reveal that the error being normally distributed and approximately all the residuals follow a straight line model.

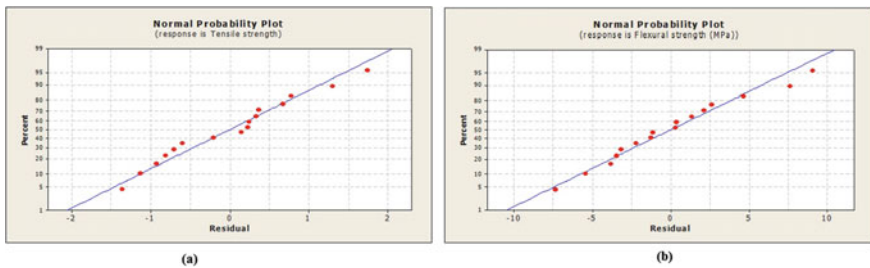


Fig. 5.5 Normal probability plots of residuals for **a** tensile strength and **b** flexural strength

5.3.4 Test for Water Absorption by the Composites

The rate of water absorption depending on the fiber concentration (10, 20, 30, and 35 wt%) along with fiber length (5, 8, 12, and 120 mm) of lime sludge-filled coir-epoxy composites is shown in Fig. 5.6. The time of immersion was studied (up to 600 h). It was revealed from the water absorption studies that the rate of water absorption is steep initially, but it slowly steadies ahead after sometime, until it reaches a saturation level.

From Fig. 5.6, it is clear that with rising fiber content, the water absorption rates increase. It was observed that the 35 wt % fiber composites demonstrated the maximum water absorption irrespective of the fiber length. This may be attributed to the fact that cellulosic fibers (natural fibers) are inherently hydrophilic [36]. Additionally, cellulosic coir fibers exhibit a hollow central region called the lumen. This permits high content of water retention inside it through capillary effect [37]. Again, with rising fiber amounts in the composites, the interfacial area also increases leading to more absorption of water.

This study also revealed that amount of water absorption amplified as fiber length increased. Composites containing longer cellulosic fibers have more hollow section in them and higher interfacial area at the fiber–matrix boundary leading to more water retention. Surface erosion increases with rising fiber length leading to more surface area for natural fibers to absorb water. Hence, greater the fiber length, more is the rate of water absorption. The maximum weight gain was observed for 120-mm-long fiber, i.e., 18.85%. Thus, it was revealed that the fiber content and fiber length were two factors that hugely influenced the water absorption characteristics.

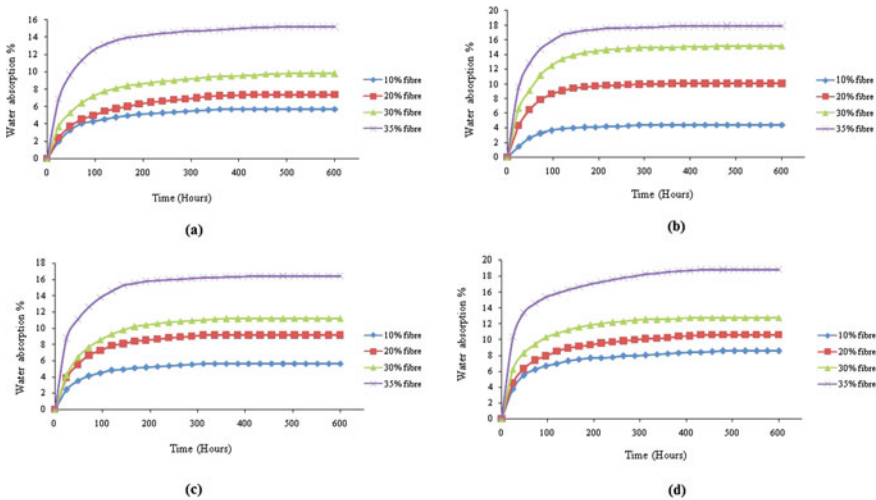


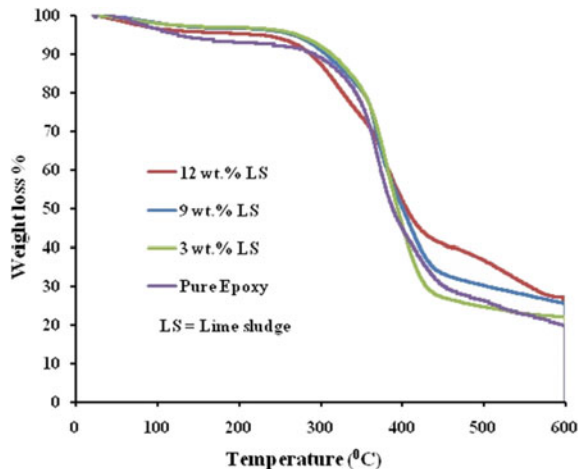
Fig. 5.6 Water absorption rate based on fiber loading and **a** 5 mm, **b** 8 mm, **c** 12 mm, and **d** 120 mm (long) fiber length composites

Another factor of high water absorption may be due to the lime sludge addition, because of the calcium carbonate present in it, it absorbed more water. Therefore, as the lime sludge wt.% increases, the water absorption increases. Thus, it was revealed that fiber loading and fiber length are two important factors that hugely influence the water absorption characteristics.

5.3.5 Thermal Property—Thermogravimetric Analysis (TGA)

The thermal decomposition event of 3 and 12% lime sludge–coir–epoxy composites had been studied for pure epoxy, 3, 9, and 12 wt% lime sludge infused coir–epoxy composites. As observed from Fig. 5.7, three junctures of thermal decomposition were noticed. First juncture (20–250 °C) may be attributed to the water/moisture release from the fibers. Second juncture (250–425 °C) was owing to the fact the hemicelluloses and cellulose (cellulosic substances in natural fibers) were decomposed. Third juncture (425–600 °C) was because of decomposition of non-cellulosic substances in the fibers. It was observed that at lower temperature weight, loss occurs slightly higher in case of 12% lime sludge compared to 3% lime sludge at initial stages (≈ 20 –250 °C) due to excess moisture removal from lime sludge. However, at elevated temperatures, the amount of weight loss in case of 3 wt% lime sludge composite was observed to be higher than that of 12 wt% lime sludge infused coir composite revealing that lime sludge waste has enhanced the decomposition temperature of the coir composites, thus improving the thermal properties.

Fig. 5.7 TGA curves of lime sludge-filled coir fiber-reinforced epoxy composites



5.3.6 Morphological Analysis

Morphological analysis was carried out using scanning electron microscopy. Figure 5.8 presents the topology of the fractured surfaces of lime sludge–coir–epoxy composites after tensile testing. Figure 5.8a shows the fractured surface of the specimen with 35 wt% fiber content with short fiber length of 12 mm. It was revealed through the micrograph that as a result of low interfacial adhesion at the fiber matrix boundary, the fibers get drawn out of the matrix creating voids and loose fibers. It must be noted that the SEM micrographs were taken after tensile testing when sufficient stresses have been applied to deform and break the composites. At higher fibers weight fraction of 35 wt%, the matrix becomes insufficient to hold and wet all the fibers completely creating voids. Subsequently, upon loading, the matrix cannot transfer the applied load to the fibers, thus causing premature failure due to interfacial debonding or fiber pullout. This causes a reduction in the properties of the composites. However, as observed in Fig. 5.8b, it shows topology on the fractured face of composites specimen reinforced with 120 mm continuous fiber at 30 w.% fiber content. It can be observed from the figure that the fiber has broken upon tensile testing without getting pulled out from the matrix (good interfacial adhesion). This means that the matrix can transfer sufficient stresses to the fibers so that the fibers can take the entire load until their fracture. This paves the way for improved mechanical properties in case of continuous fiber composites when compared with short and randomly dispersed fiber composites.

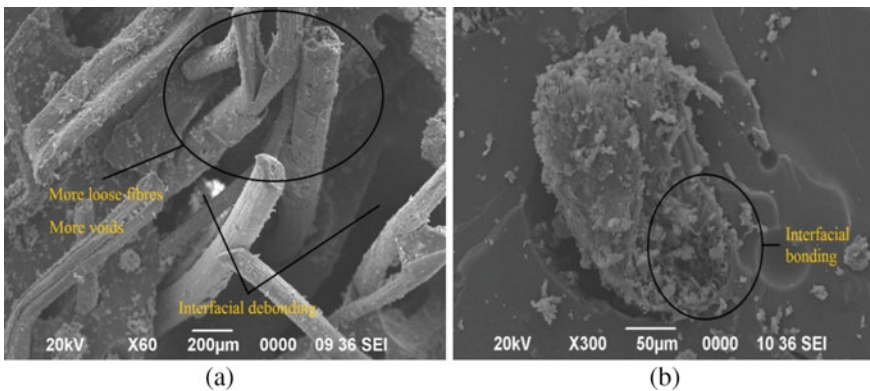


Fig. 5.8 SEM micrographs at the fractured surfaces of tensile testing specimens

5.4 Conclusions

Incorporation of renewable materials such as natural fibers as reinforcement in a composites serves purposes—(1) better energy efficiency as lightweight components can be made out of it, (2) replacement of synthetic fibers with biodegradable materials, (3) eco-friendly material, and (4) recovered energy upon incineration. This investigation presents the role of natural fibers (coir) on the strength characteristics of energy-efficient hybrid lime sludge–coir–epoxy composites as a function of the input parameters—fiber length, fiber weight, and lime sludge using Taguchi method. ANOVA analysis was employed to examine the most influential parameter affecting the performance characteristics in composites. Regression models were developed based on the experimental results to predict the performance at various process parameters. Water absorption behavior as well as thermal and morphological studies was also conducted on the composites. The conclusion derived from this investigation can be summarized under the following points.

- The optimal combination of process parameters among the chosen levels for maximizing the tensile strength was FL₄ FW₃ LS₁ (fiber length—120 mm, fiber weight—30% and lime sludge—3%). For maximizing the flexural strength, the optimal combination among the chosen levels was FL₄ LS₂ FW₃, i.e., fiber length—120 mm, lime sludge—6%, and fiber weight—20%.
- ANOVA analysis revealed that fiber length is the most significant factor influencing tensile strength (contribution 63.37%) followed by fiber weight (9.82%) and lime sludge (8.23%). For flexural strength also, fiber length is largely the significant factor (contribution 60.15%) followed by lime sludge (16.05%) and fiber weight (10.11%).
- The regression models derived in order to forecast the strengths (tensile and bending) of composites are in good accord or and high-order regression analysis.
- The degree of water absorption was affected significantly by the fiber length and fiber loading. Enhancing the fiber length or fiber content leads to higher rate of water absorption.
- Thermal stability of lime sludge–coir–epoxy composites increases as the amount of lime sludge increased.
- During morphological study on the fractured surface of the composites, it was revealed that good interfacial bonding is responsible to improve mechanical properties. The low strength can be associated due to the fiber pullout and void present in the composites due to insufficient matrix and low interfacial bonding.

References

1. Jesson, D.A., Watts, J.F.: The interface and interphase in polymer matrix composites: effect on mechanical properties and methods for identification. *Poly. Rev.* **52**(3), 321–354 (2012)

2. Reddy, B.P., Satish, S., Renald, C.J.T.: Investigation on tensile and flexural properties of coir fiber reinforced isophthalic polyester composites. *Compos. Part B: Engg.* **42**(6), 1648–1656 (2007)
3. Sgriccia, N., Hawley, M.C., Misra, M.: Characterization of natural fibre surfaces and natural fibre composites. *Compos. Part A App. Sci. Manuf.* **39**(10), 1632–37 (2008)
4. Das, S.: Fabrication and characterization of raw and bleached treatment coir fiber reinforced polymer composite. *Compos. Sci. Tech.* **63**(2), 283–293 (2005)
5. Wambua, P., Ivens, J., Verpoest, I.: Natural fibres: can they replace glass in fibre reinforced plastics? *Compos. Sci. Tech.* **63**(9), 1259–1264 (2003)
6. Sudhakara, P., Jagadeesh, D., Wang, Y.Q., et al.: Fabrication of Borassus fruit lignocellulose fiber/PP composites and comparison with jute, sisal and coir fibers. *Carbohydrate Poly.* **98**(1), 1002–1010 (2013)
7. Rao, C.H.C., Madhusudan, S., Raghavendra, G., et al.: Investigation into wear behavior of coir fiber reinforced epoxy composites with Taguchi method. *J. Engg. Res. App.* **2**(5), 371–374 (2012)
8. Jayabal, S., Natarajan, U., Sathiyamurthy, S.: Effect of glass hybridization and staking sequence on mechanical behaviour of interply coir–glass hybrid laminate. *Bull. Mat. Sci.* **34**(2), 293–298 (2011)
9. Ferreira, D.P., Cruz, J., Figueiro, R.: Surface modification of natural fibers in polymer composites. In: *Green Composites for Automotive Applications*, pp. 3–41. Woodhead Publishing, UK p (2019)
10. Imran, S., Adelbert, T.: Effect of alkali treatments of physical and mechanical properties of coir fibre. *Chem. Mat. Engg.* **3**(2), 23–28 (2015)
11. Doan, T.T.L., Gao, S.L., Mader, E.: Jute/polypropylene composites I. Effect of matrix modification. *Compos. Sci. Tech.* **66**(7), 952–963 (2006)
12. Matthews, F.L., Rawlings, R.D.: *Composite Materials: Engineering and Science*. Woodhead Publishing, Cambridge, England (1999)
13. Benard, Q., Fois, M., Grisel, M.: Roughness and fibre reinforcement effect onto wettability of composite surfaces. *Appl. Surf. Sci.* **253**(10), 4753–4758 (2007)
14. Mustafa, A., Abdollah, M.F., Shuhimi, F.F., et al.: Selection and verification of kenaf fibres as an alternative friction material using weighted decision matrix method. *Mat. Des.* **67**(1), 577–582 (2015)
15. Sanadi, A.R., Caulfield, D.F., Jacobson, R.E.: Agro-fiber thermoplastic composites. In: *Paper and Composites from Agro-Based Resources*, pp. 377–401. CRC, Boca Raton, Florida (USA) (1997)
16. Li, Z., Wang, L., Wang, X.: Flexural characteristics of coir fibre reinforced cementitious composites. *Fiber. Poly.* **7**(3), 286–294 (2006)
17. Harish, S., Mihael, P.D., Bensely, A.: Mechanical properties evaluation of natural fibre coir composites. *Mat. Character* **60**(1), 44–49 (2009)
18. Tran, L.Q.N., Fuentes, C.A., Dupont, C.: Wetting analysis and surface characterisation of coir fibres used as reinforcement for composites. *Colloids Surf.: Physicochem. Engg. Aspects* **377**(1–3), 251–260 (2011)
19. Swolfs, Y., Verpoest, I., Gorbatikh, L.: Recent advances in fibre-hybrid composites: materials selection, opportunities and applications. *Int. Mat. Rev.* **64**(4), 181–215 (2019)
20. Bartczak, Z., Argon, A., Cohen, R., et al.: Toughness mechanism in semi-crystalline polymer blends: II. High-density polyethylene toughened with calcium carbonate filler particles. *Polymer* **40**(9), 2347–2365 (1999)
21. Fu, Q., Wang, G., Shen, J.: Polyethylene toughened by CaCO₃ particle: Brittle-ductile transition of CaCO₃-toughened HDPE. *J. App. Poly. Sci.* **49**(4), 673–677 (1993)
22. Kwon, S., Kim, K.J., Kim, H., et al.: Tensile property and interfacial dewetting in the calcite filled HDPE, LDPE, and LLDPE composites. *Polymer* **43**(25), 6901–6909 (2002)
23. Sommerhuber, P.F., Wang, T., Krause, A.: Wood-plastic composites as potential applications of recycled plastics of electronic waste and recycled particle board. *J. Clean. Prod.* **121**, 176–185 (2016)

24. Sommerhuber, P.F., Welling, J., Krause, A.: Substitution potentials of recycled HDPE and wood particles from post-consumer packaging waste in Wood-plastic composites. *Waste Manage.* **46**, 76–85 (2015)
25. Das, O., Sarmah, A.K., Bhattacharyya, D.: A novel approach in organic waste utilization through biochar addition in wood/polypropylene composites. *Waste Manage.* **38**, 132–140 (2015)
26. Deepthi, M., Sharma, M., Sailaja, R., et al.: Mechanical and thermal characteristics of high density polyethylene fly ash Cenospheres composites. *Mater. Des.* **31**(4), 2051–2060 (2010)
27. Yang, S., Bai, S., Wang, Q.: Morphology, mechanical and thermal oxidative aging properties of HDPE composites reinforced by non-metals recycled from waste printed circuit boards. *Waste Manage.* **57**, 168–175 (2016)
28. Rachchh, N.V., Misra, R.K., Roychowdhary, D.G.: Effect of red mud filler on mechanical and buckling characteristics of coir fibre-reinforced polymer composite. *Iranian Poly. J.* **24**(3), 253–265 (2015)
29. Ahmad, T., Ahmad, R., Kamran, M.: Effect of Thal silica sand nanoparticles and glass fiber reinforcements on epoxy-based hybrid composite. *Iranian Poly. J.* **24**(1), 21–27 (2015)
30. Rout, J., Misra, M., Tripathy, S.S., et al.: The influence of fibre treatment on the performance of coir-polyester composites. *Compos. Sci. Tech.* **61**(9), 1303–1310 (2001)
31. Nam, T.H., Ogihara, S., Tung, N.H., et al.: Effect of alkali treatment on interfacial and mechanical properties of coir fiber reinforced poly (butylene succinate) biodegradable composites. *Compos. Part B: Appl. Sci. Manuf.* **42**(6), 1648–1656 (2011)
32. Jayabal, S., Sathiyamurthy, S., Loganathan, K.T.: Effect of soaking time and concentration of NaOH solution on mechanical properties of coir–polyester composites. *Bull. Mater. Sci.* **35**(4), 567–574 (2012)
33. Freddi, A., Salmon, M.: Introduction to the Taguchi method. In: *Design Principles and Methodologies*, pp. 159–180. Springer, Cham, Switzerland (2019)
34. Muthukrishnan, N., Davim, J.P.: Optimization of machining parameters of Al/SiC-MMC with ANOVA and ANN analysis. *J. Mater. Process. Technol.* **209**(1), 225–232 (2009)
35. Joseph, P.V., Joseph, K., Thomas, S.: The thermal and crystallisation studies of short sisal fibre reinforced polypropylene composites. *Compos. Part A: App. Sci. Manuf.* **34**(3), 253–266 (2003)
36. Dhakal, H.N., Zhang, Z.Y., Richardson, M.O.W.: Effect of water absorption on the mechanical properties of hemp fibre reinforced unsaturated polyester composites. *Compos. Sci Tech.* **67**, 1674–1683 (2007)
37. Kim, H.J., Seo, D.W.: Effect of water absorption fatigue on mechanical properties of sisal textile-reinforced composites. *Int. J. Fatigue* **28**, 1307–1314 (2006)

Chapter 6

Extended State Observer-Based Controller Design Application in a Two-Link Robotic Manipulator



Piyali Das , Ram Krishna Mehta , and Om Prakash Roy 

Abstract This work illustrates about an extended state observer (ESO)-based optimal controller for controlling a two-link robotic manipulator. A full state observer was designed with the help of extending the states using control law. Minimizing the quadratic cost functions, control law was designed for the multiple input multiple output (MIMO) plant. An algorithm has been set for tuning the controller parameters whether the best optimized results were compared. This two-link robotic manipulator is very rigid and to design a perfect controller is complex task although in this work it has been tried to construct an effective linear quadratic regulator (LQR)-based extended full state observer. The unknown state was observed by the EFSO which was fed to the controller including an external disturbance. The disturbance was discarded by the controller observer pair, and a stable response was established.

6.1 Introduction

6.1.1 A Subsection Sample

The robotic manipulator is highly nonlinear and consists of un-modelled dynamics along with frictional and other effects. It is a cross-coupled system with two-link manipulators or 2-DOF which may be applied in various engineering as well as medicinal works. Designing a cost-effective controller is a big challenge for researchers. Due to the insufficient parameter for linearization, some assumption of model parameters may be done by the researchers. The prime concern of robotic manipulator is to use for refined tasks such as in medical unit, aerospace or welding which requires precision in response as well accurate trajectory tracking. Performing the complete task of a motion controller is a very complex and obscure work.

In [1], Al-Saggaf et al have proved the effective tracking and robust controller defending the parameter uncertainties using fractional controller. A state feedback

P. Das (✉) · R. K. Mehta · O. P. Roy
NERIST, Nirjuli, Arunachal Pradesh 791109, India
e-mail: pd@nerist.ac.in; das.piyalinee@gmail.com

control is also provided to compare the fractional control. A double-layer feedback control is proposed in [2] for the flexible arms, where inner loop is controlling the motor and outer loop is controlling tip position. The single link of 2-DOF robotic manipulator (2-DOF RM) model is controlled by plain feed forward path control logic. Kim and Oh have presented a new technique of robust controller for the robotic flexible manipulator in [3]. The methodology of the controller is justified using a PID controller. The control logic is effortless, and for the tuning method of the controller, several and experimental evaluations were done. The result of 2-DOF RM is very robust and stable with the decided controller parameters. A nonlinear model control was broadly discussed by Li et al. in [4]. A fuzzy controller was used to investigate the plant configurations; they also elaborated the adaptive fuzzy filter observer for the estimation of unknown states. A new method was discussed in [5] as integral resonant control (IRC) scheme. This technology was applied to mitigate the unstable phases of joint angle as well as the vibration of the system. Various advantages of IRC were depicted in this model analysis where precision was given to the actuator–sensor synchronization. Using Kalman filter and tracking control technology, a two-link MIMO robotic manipulator was designed. Using brushless DC motor, two links were joined and examined. The dynamic model was designed by Choi et al., and to design the controller, various analyses such as trajectory tracking and external disturbance control were done. A disturbance observer was investigated in [10] using a linear plant of the two-link manipulator along with the establishment of robustness analysis. Liapunov function H_∞ was used for the controlling of robotic manipulator in [11]. Various applications of optimal controllers are provided in [12–22] which may depict precise result and accurate analysis of the model. To set the controller parameters, various algorithms, neural network or fuzzy controllers were used. Disturbance rejection may be asymptotically mitigated by those approaches. Observers also were introduced to estimate the un-measurable states of the plant. From all those analysis, researchers from worldwide have enhanced their knowledge about the complex nonlinearity of the model. It is very difficult to linearize the model with the uncertain parameters.

In this paper, one methodology using EFSO based on the linear quadratic regulator (LQR) is approached. In Sect. 6.2.1, the model description along with linearization is provided. Sections 6.2.2, 6.2.3 and 6.2.4 are proposing the controller design, state feedback gain and tuning algorithm.

6.2 Problem Formation

6.2.1 Model Description

It is a big challenge to establish an extended state observer for the quite popular robotic manipulator dynamics; in modern control research, many ideas have been

implemented to establish such approaches. Two-DOF/link robotic manipulator (2-LRM) is the commonly used model of mechatronics which consist of linear displacements x and y which may be expressed in terms of θ_1 and θ_2 [7]. L_1 and L_2 are two lengths of links 1 and 2, respectively, as per Denavit–Hartenberg model [7].

$$\begin{aligned}x_1 &= L_1 \sin \theta_1 \\y_1 &= L_1 \cos \theta_1 \\x_2 &= L_1 \sin \theta_1 + L_2 \sin(\theta_1 + \theta_2) \\y_2 &= L_1 \cos \theta_1 + L_2 \cos(\theta_1 + \theta_2)\end{aligned}\quad (6.1)$$

The very next kinetic energy generated in the system may be produced as Eq. 6.2.

$$K_E = \frac{1}{2}m_1v_1^2 + \frac{1}{2}m_2v_2^2 + \frac{1}{2}j_1\omega_1^2 + \frac{1}{2}j_2\omega_2^2 \quad (6.2)$$

Now, $v_1^2 = l_{g1}^2\dot{\theta}_1^2$

$$\begin{aligned}v_2^2 &= \left(l_{g1}^2\dot{\theta}_1 + 2l_1l_{g2}\dot{\theta}_1(\dot{\theta}_1 + \dot{\theta}_2) \cos \dot{\theta}_2 + l_{g2}^2(\dot{\theta}_1 + \dot{\theta}_2)^2 \right) \\ \omega_1^2 &= \dot{\theta}_1^2; \quad \omega_2^2 = (\dot{\theta}_1 + \dot{\theta}_2)^2\end{aligned}\quad (6.3)$$

Then after applying Eq. 6.3 in Eq. (6.2), we got

$$\begin{aligned}K_E &= \frac{1}{2}m_1l_{g1}^2\dot{\theta}_1^2 + \frac{1}{2}m_2\left(l_{g1}^2\dot{\theta}_1 + 2l_1l_{g2}\dot{\theta}_1(\dot{\theta}_1 + \dot{\theta}_2) \cos \dot{\theta}_2 + l_{g2}^2(\dot{\theta}_1 + \dot{\theta}_2)^2 \right) \\ &+ \frac{1}{2}j_1\dot{\theta}_1^2 + \frac{1}{2}j_2(\dot{\theta}_1 + \dot{\theta}_2)^2\end{aligned}\quad (6.4)$$

The next step is to find the potential energy

$$P_E = m_1gl_{g1} \sin \theta_1 + m_2g(l_1 \sin \theta_1 - (l_{g2} \sin(\theta_1 + \theta_2)))$$

Now to find the motion equation, Lagrangian method is applied to find the divergence between K_E and P_E , where j_1 and j_2 are moment of inertia for links 1 and 2, respectively. v_1 and v_2 are the linear velocity of links 1 and 2, m_1 and m_2 are respective masses, and ω_1 and ω_2 are the angular velocities for the same.

$$\mathcal{L} = K_E - P_E \quad (6.5)$$

Hence to calculate torque for both, links are shown in Eq. (6.6).

$$\begin{aligned}\tau_1 &= \frac{d}{dt} \left(\frac{\partial \mathcal{L}}{\partial \dot{\theta}_1} \right) - \frac{\partial \mathcal{L}}{\partial \theta_1} \\ \tau_2 &= \frac{d}{dt} \left(\frac{\partial \mathcal{L}}{\partial \dot{\theta}_2} \right) - \frac{\partial \mathcal{L}}{\partial \theta_2}\end{aligned}\quad (6.6)$$

Let the coefficient of friction be C , then the generalized Lagrangian–Euler equation can be modified as Eq. (6.7).

$$\begin{aligned}\tau_1 &= M_{11}\ddot{\theta}_1 + M_{12}\ddot{\theta}_2 + H_1 + G_1 + C_1\dot{\theta}_1 - C_2(\dot{\theta}_2 - \dot{\theta}_1) \\ \tau_2 &= M_{21}\ddot{\theta}_1 + M_{22}\ddot{\theta}_2 + H_2 + G_2 + C_2(\dot{\theta}_2 - \dot{\theta}_1).\end{aligned}\quad (6.7)$$

Here, M_{ij} is the effective inertia, M_{ji} is the effective coupling inertia, and H_j and G_j are centrifugal and Coriolis acceleration forces. After one revolution of both the joints, the torque equation may be rearranged, and the following equation is shown here below in no (6.8).

$$\begin{aligned}\begin{bmatrix} \tau_1 \\ \tau_2 \end{bmatrix} &= \begin{bmatrix} M_{11} & M_{12} \\ M_{21} & M_{22} \end{bmatrix} \begin{bmatrix} \ddot{\theta}_1 \\ \ddot{\theta}_2 \end{bmatrix} \\ &+ \begin{bmatrix} -2H\dot{\theta}_2 + C_1 + C_2 & -H\dot{\theta}_2 - C_2 \\ H\dot{\theta}_1 - C_2 & C_2 \end{bmatrix} \begin{bmatrix} \dot{\theta}_1 \\ \dot{\theta}_2 \end{bmatrix} + \begin{bmatrix} G_1 \\ G_2 \end{bmatrix}\end{aligned}\quad (6.8)$$

The state space nonlinear equation may be denoted by Eq. (6.8) where the values are provided in Eq. (6.9).

$$\begin{aligned}M_{12} &= M_{21} = m_2 \left[\frac{1}{3}L_2^2 + \frac{1}{2}L_1L_2C_2 \right] \\ M_{22} &= \frac{1}{3}m_2L_2^2 \\ H_2 &= \frac{1}{2}m_2L_1L_2s_2\dot{\theta}_1^2 \\ G_1 &= \left(\frac{1}{2}\dot{m}_1 + m_2 \right) gL_1C_1 + \frac{1}{2}m_2gL_2C_{12} \\ G_2 &= \frac{1}{2}m_2gL_2C_{12}\end{aligned}\quad (6.9)$$

Now let the states to be defined by Eq. (6.10)

$$\dot{x}_1 = x_3 \quad (6.10)$$

$$\dot{x}_2 = x_4 \quad (6.11)$$

$$\begin{aligned} \left[\alpha_1 - \frac{M_2}{\alpha_5} \cos^2(x_1 - x_2) \right] \dot{x}_3 &= M_1 - \frac{\alpha_2 M_2}{\alpha_5} \cos(x_1 - x_2) \\ &- \frac{\alpha_2 \alpha_3}{\alpha_5} \cos(x_1 - x_2) \sin(x_1 - x_2) x_4 \\ &+ \frac{\alpha_2 \alpha_6}{\alpha_5} \cos(x_1 - x_2) \cos x_3 - \alpha_4 \cos x_1 \end{aligned} \quad (6.12)$$

$$\dot{x}_4 = \frac{M_2}{\alpha_5} - \frac{\alpha_2 M_2}{\alpha_5} \cos(x_1 - x_2) + \frac{\alpha_3}{\alpha_5} \sin(x_1 - x_2) x_4 - \frac{\alpha_6}{\alpha_5} \cos x_2 \quad (6.13)$$

At equilibrium point, θ_1 and θ_2 become -90° and M_1 and M_2 at 0, and we can prove the linearized model. To establish the linearized model, Taylor series expansion was used, and the linearized model may be established in Eq. (6.14). [7]

Considering all variables of the state, x_1 will be

$$\frac{\partial \dot{x}_1}{\partial x_1} = 0, \quad \frac{\partial \dot{x}_1}{\partial x_2} = 0, \quad \frac{\partial \dot{x}_1}{\partial x_3} = 0, \quad \frac{\partial \dot{x}_1}{\partial x_4} = 0 \quad (6.14)$$

Considering all variables of the state, x_2 will be

$$\frac{\partial \dot{x}_2}{\partial x_1} = 0, \quad \frac{\partial \dot{x}_2}{\partial x_2} = 0, \quad \frac{\partial \dot{x}_2}{\partial x_3} = 0, \quad \frac{\partial \dot{x}_2}{\partial x_4} = 0 \quad (6.15)$$

Considering all variables of the state, x_3 will be

$$\begin{aligned} \frac{\partial \dot{x}_3}{\partial x_1} &= \frac{\alpha_4 \alpha_5}{\alpha_1 \alpha_5 - M_2}, \quad \frac{\partial \dot{x}_3}{\partial x_2} = \frac{\alpha_2 \alpha_6}{\alpha_1 \alpha_5 - M_2}, \\ \frac{\partial \dot{x}_3}{\partial x_3} &= 0, \quad \frac{\partial \dot{x}_3}{\partial x_4} = 0 \frac{1 - \alpha_2}{\alpha_5} \end{aligned} \quad (6.16)$$

Considering all variables of the state, x_4 will be

$$\begin{aligned} \frac{\partial \dot{x}_4}{\partial x_2} &= -\frac{\alpha_6}{\alpha_5}, \quad \frac{\partial \dot{x}_4}{\partial x_3} = 0, \quad \frac{\partial \dot{x}_4}{\partial x_4} = \frac{\alpha_3}{\alpha_5} \sin(x_1 - x_2), \\ \frac{\partial \dot{x}_4}{\partial x_4} &= 0 \end{aligned} \quad (6.17)$$

Considering all variables of the state, x_1 and x_2 will be

$$\frac{\partial \dot{x}_1}{\partial M_1} = 0, \quad \frac{\partial \dot{x}_1}{\partial M_2} = 0, \quad \frac{\partial \dot{x}_2}{\partial M_1} = 0, \quad \frac{\partial \dot{x}_2}{\partial M_2} = 0 \quad (6.18)$$

$$\frac{\partial \dot{x}_3}{\partial M_1} = \frac{\alpha_5}{\alpha_1 \alpha_5 - M_2}, \frac{\partial \dot{x}_4}{\partial M_2} = \frac{\alpha_5}{\alpha_1 \alpha_5 - M_2}, \frac{\partial \dot{x}_4}{\partial M_2} = 0, \frac{\partial \dot{x}_4}{\partial M_2} = \frac{1 - \alpha_2}{\alpha_5} \quad (6.19)$$

$$\begin{aligned} \begin{bmatrix} \partial \dot{x}_1 \\ \partial \dot{x}_2 \\ \partial \dot{x}_3 \\ \partial \dot{x}_4 \end{bmatrix} &= \begin{bmatrix} 0 & 0 & 1 & 0 \\ 0 & 0 & 0 & 1 \\ \frac{\alpha_4 \alpha_5}{\alpha_1 \alpha_5 - M_2} & \frac{\alpha_2 \alpha_6}{\alpha_1 \alpha_5 - M_2} & 0 & 0 \\ 0 & -\frac{\alpha_6}{\alpha_5} & 0 & 0 \end{bmatrix} \begin{bmatrix} \partial x_1 \\ \partial x_2 \\ \partial x_3 \\ \partial x_4 \end{bmatrix} \\ &+ \begin{bmatrix} 0 & 0 \\ 0 & 0 \\ \frac{\alpha_5}{\alpha_1 \alpha_5 - M_2} & \frac{\alpha_2}{\alpha_1 \alpha_5 - M_2} \\ 0 & \frac{1 - \alpha_2}{\alpha_5} \end{bmatrix} \begin{bmatrix} \partial M_1 \\ \partial M_2 \end{bmatrix} \\ y &= \begin{bmatrix} 0 & 0 & 1 & 0 \\ 0 & 0 & 0 & 1 \\ \frac{\alpha_4 \alpha_5}{\alpha_1 \alpha_5 - M_2} & \frac{\alpha_2 \alpha_6}{\alpha_1 \alpha_5 - M_2} & 0 & 0 \\ 0 & -\frac{\alpha_6}{\alpha_5} & 0 & 0 \end{bmatrix} \begin{bmatrix} \partial x_1 \\ \partial x_2 \\ \partial x_3 \\ \partial x_4 \end{bmatrix} + [0][D] \end{aligned} \quad (6.20)$$

$$\begin{aligned} \dot{X} &= Ax + Bu \\ Y &= Cx + Du \end{aligned} \quad (6.21)$$

6.2.2 Controller Design

The disturbance variable is defined by $d_i(t)$ for two states, namely yaw and pitch.

$$\begin{aligned} \dot{x} &= Ax + Bu + d_i(t) \\ Y &= Cx + Du \end{aligned} \quad (6.22)$$

The state space model is designed in (6.4) where $(A, B, C, 0)$ are state matrices, dimension of A is $n \times n$, dimension of B is $n \times 2$, and dimension of C is $r \times n$. In the case of input disturbance, it is proposed to define the model as $(A_d, B_d, C_d, 0)$. Here the plant state $x(t)$ and the disturbance state $d(t)$ will be estimated with the help of ESO. Now to define \dot{x}_d which is the disturbance state, the following equations are provided.

$$\begin{aligned} \dot{x} &= Ax + Bu \\ \dot{x}_d &= A_d x + B_d \end{aligned} \quad (6.23)$$

Here A_d and B_d are 0, and C_d is I_2 , where I_2 is the identical matrix of $\mathbb{R}^{2 \times 2}$.

In the following equation, augmented model of $(A_a, B_a, C_a, 0)$ state matrices is shown (6.8).

$$A_a = \begin{bmatrix} A & BC_d \\ 0 & A_d \end{bmatrix} = \begin{bmatrix} A & B \\ 0 & 0 \end{bmatrix}; B_b = \begin{bmatrix} B \\ B_d \end{bmatrix}; C_a = [C \ 0]; \quad (6.24)$$

For observer gain in [13], a simple method has been discussed that how to find it, and in this paper, the similar method is used. The procedure is to set the real variables of six states where two additional states ρ_1 and ρ_2 are also added in [8] by Goodwin. \hat{x}_d will be considered as estimated disturbances for the plant.

$$\begin{aligned} u(t) &= -[K_p C_d] \begin{bmatrix} \hat{x}_x(t) \\ \hat{x}_d(t) \end{bmatrix} \\ \Rightarrow k &= [K_p I_2] \end{aligned} \quad (6.25)$$

For selecting the pole locations, optimal control is required which depends on cost function. The cost function comprises the weighted summation of squares of the state errors and control. The method which is proposed comprises two parameters, namely K_p which is feedback control gain and L_a which is observer gain. In Fig. 6.1, the plant controller block diagram is shown. For this problem, LQR is a relevant design which is much robust for complex systems and has meticulous performance in minimizing the plant cost function J (6.26).

To choose the observer pole, one rule has been shown in [8], where in comparison with the controller poles, it may be 2 to 10 times faster. Now $-\lambda_1, -\lambda_2, -\lambda_3, -\lambda_4$ are chosen as CLP and $-\lambda_{d1}$ and $-\lambda_{d2}$ are disturbance poles for the MIMO system after satisfying the desired criteria.

$$J = \int_0^{\infty} [x^T Q_x + u^T R_u] dt \quad (6.26)$$

Arithmetic Riccati equation (ARE) is shown in (6.27), and P value can be found after solving ARE in terms of unique symmetric, positive semi-definite solution. This ARE is used to calculate the cost function of the plant controller.

$$PA + A^T P + Q - PBR^{-1}B^T P = 0 \quad (6.27)$$

Here after solving ARE, K_p which is state feedback gain also may be defined as follows.

$$K_p = (R^{-1}B^T P) \quad (6.28)$$

To solve the complex problem, one advanced optimized iteration method (AOIM) is proposed which will modify the parameters and measure the appropriate data from

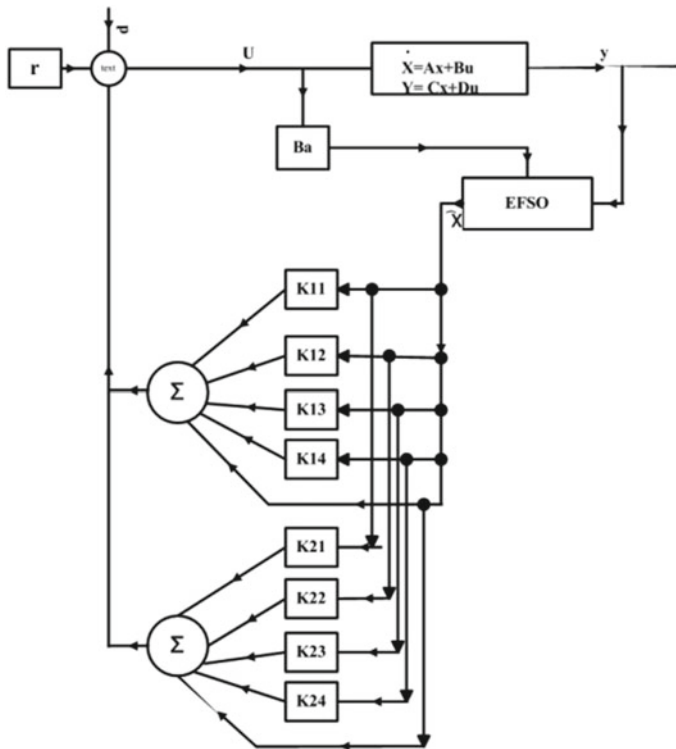


Fig. 6.1 Controller block diagram with EFSO

the system. After analysing the control variables, the algorithm was accepted. The major conditions to use this algorithm are provided in Remark 1.

$Q[aa] = Q[aa] + 0.01 a$ a = no of row and column of weighted matrix

$$\begin{aligned} \theta_{\min} &= 40^\circ < \theta_i \\ \theta_{\max} &= 55^\circ > \theta_i \quad i = \text{desired angle} \end{aligned} \tag{6.29}$$

Generally, the relation between plant damping ratio ξ and angle subtended from the pole to origin θ is $\zeta = \cos \theta$ [7]. The value of ξ for a stable plant controller should be within 0.7 [7], here using this principle, the algorithm iterations have been performed. The equation of cost function is represented in (6.26), and the elaborated form of the equation is shown below.

$$J = \int_0^\infty (q_1 x_1^2 + q_2 x_2^2 + q_3 x_3^2 + q_4 x_4^2 + R_1 u_1^2 + R_2 u_2^2) dt \tag{6.30}$$

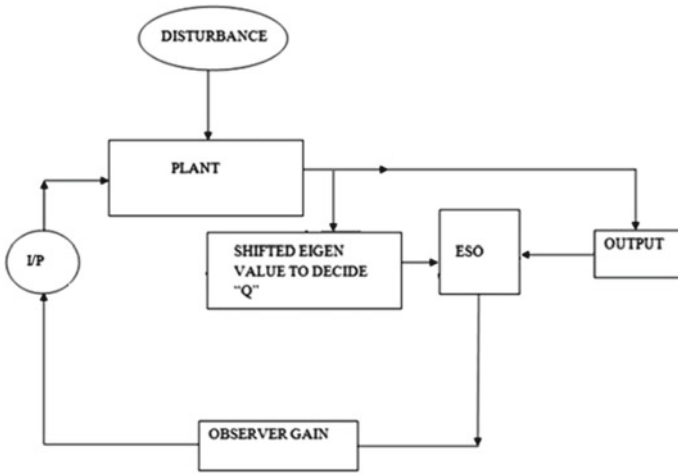


Fig. 6.2 Discrete block diagram using advanced optimization iteration method

Here q_1, q_2, q_3, q_4 are the weight gains, respectively, for link 1, link 2, velocity of link 1 and velocity of link 2. The first motor voltage is R_1 , and the second motor voltage is R_2 . Applying AOIM, the best result of cost function is determined and shown in full state matrix as $x = [x_1, x_2, x_3, x_4]^T$. In Fig. 6.2, the discrete block diagram is shown; from there, it can be observed how the external disturbances are also rejected. The controller gain matrix is shown below after analysing the feedback response.

$$K_P = \begin{bmatrix} K_{11} & K_{12} & K_{13} & K_{14} \\ K_{21} & K_{22} & K_{23} & K_{24} \end{bmatrix} \tag{6.31}$$

Shifting the eigen values of open loop poles is associated here by a value of ΔQ . Let M_i be a symmetric solution of the ARE for the weighted matrices Q and R and $\alpha = 0$ discussed in [24]. The degree of relative stability $\alpha = p$ is introduced, and the matrix Q is perturbed by $\Delta Q = -2pM_i$ given in [25] by Medanic.

Now the system matrix will be modified after shifting of eigen values and will be considered as A_i [25] which is given in Eq. (6.32). The algorithm is discussed in 2.4.

$$A_i = A_{i-1} + p_i I \quad A_0 = A$$

$$Q_i = Q_i - 2p_i M_i \tag{6.32}$$

An effective and simple method was described by Mdanic et al. in [7], which designs a controller after selecting the shifted values of individual eigen vectors of the open loop pole. Here R is considered to be nominal and $R = I$. If the solution of Eq. 6.27 is chosen as P , it can be denoted as

$$\begin{bmatrix} P_{11} & P_{12} & P_{13} & P_{14} \\ P_{21} & P_{22} & P_{23} & P_{24} \\ P_{31} & P_{32} & P_{33} & P_{34} \\ P_{41} & P_{42} & P_{43} & P_{44} \end{bmatrix}.$$

P is the stabilizing solution algebraic Riccati equation. Substituting the value of P in Eq. 6.28, the values of feedback gain matrix K can be found.

$$K = \begin{bmatrix} 0 & 0 \\ 0 & 0 \\ b_{31} & b_{32} \\ b_{41} & b_{42} \end{bmatrix} \times \begin{bmatrix} P_{11} & P_{12} & P_{13} & P_{14} \\ P_{21} & P_{22} & P_{23} & P_{24} \\ P_{31} & P_{32} & P_{33} & P_{34} \\ P_{41} & P_{42} & P_{43} & P_{44} \end{bmatrix}$$

where $R = \begin{bmatrix} 1 & 0 \\ 0 & 1 \end{bmatrix}$ (6.33)

For system (6.23), the extended state observer is designed as follows:

$$\begin{aligned} \dot{\hat{X}}_a &= A_a \hat{x}_a + B_a u + L_a (y - C_a \hat{x}) \\ \hat{y} &= C_a \hat{x}_a \end{aligned} \quad (6.34)$$

where $\hat{x} = [\hat{x}]^T$ are the estimates of the state variable x , ρ_1 and ρ_2 due to plant state and link 1 and link 2 angle disturbance, respectively.

After using Laplace transformation in Eq. (6.34), the reduced equation is shown in Fig. 6.3.

$$\begin{aligned} \hat{X}_a(s) &= [sI - A_a + L_a C_a^{-1}] B_a u(s) + [sI - A_a + L_a C_a^{-1}] L_a y(s) \\ &= [sI - A_a + L_a C_a^{-1}] B_a \begin{bmatrix} u_1(s) \\ u_2(s) \end{bmatrix} \\ &\quad + [sI - A_a + L_a C_a^{-1}] L_a \begin{bmatrix} x_1(s) \\ x_2(s) \end{bmatrix} \end{aligned} \quad (6.35)$$

where I is 6×6 identity matrix and

$$L_a = \begin{bmatrix} L_{a11} & L_{a12} & L_{a13} & L_{a14} & L_{a15} & L_{a16} \\ L_{a21} & L_{a22} & L_{a23} & L_{a24} & L_{a25} & L_{a26} \end{bmatrix}$$

is the observer gain.

The dimension of matrix L_a is $(N \times r)$ which is the observer gain shown in Fig. 6.2. The ESOBC law is $u = -K_p \hat{x}(t) - \hat{d}_i(t)$; (where $\hat{d} = \hat{x}_{n+1}$ and K_p is the feedback control gain) where $(A-BK)$ has its eigen values in the left-hand plane (LHP) and observer gain L_a is such that $(A_a - C_a L_a)$ eigenvalues also lie in LHP.

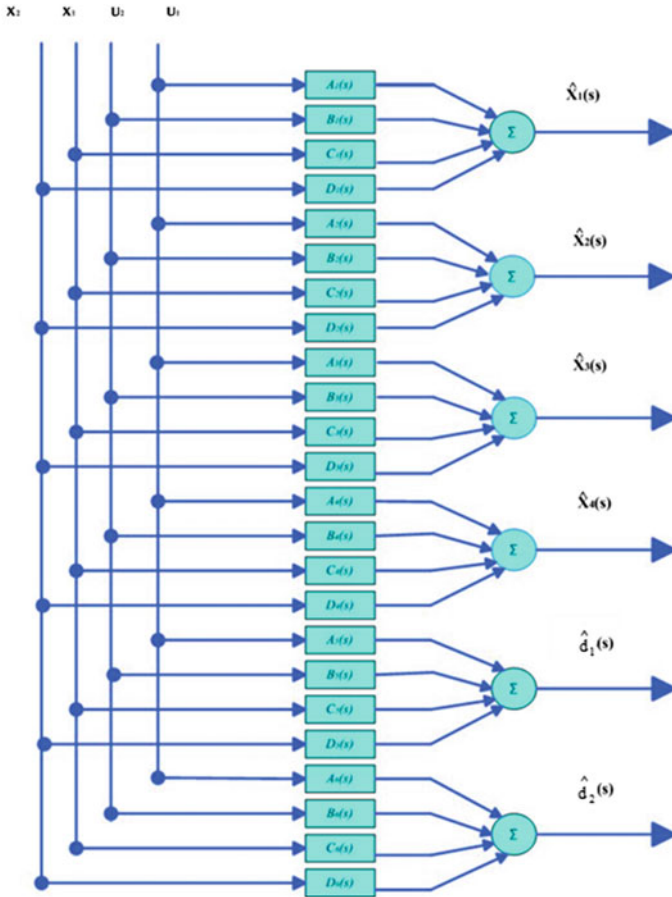


Fig. 6.3 Full state sixth-order controller using ESO

$$\hat{x}_1(s) = A_1(s)u_1(s) + B_1(s)u_2(s) + C_1(s)X_1(s) + D_1(s)X_2(s)$$

$$\hat{x}_2(s) = A_2(s)u_1(s) + B_2(s)u_2(s) + C_2(s)X_1(s) + D_2(s)X_2(s)$$

$$\hat{x}_3(s) = A_3(s)u_1(s) + B_3(s)u_2(s) + C_3(s)X_1(s) + D_3(s)X_2(s)$$

$$\hat{x}_4(s) = A_4(s)u_1(s) + B_4(s)u_2(s) + C_4(s)X_1(s) + D_4(s)X_2(s)$$

$$\hat{d}_1(s) = A_5(s)u_1(s) + B_5(s)u_2(s) + C_5(s)X_1(s) + D_5(s)X_2(s)$$

$$\hat{d}_2(s) = A_6(s)u_1(s) + B_6(s)u_2(s) + C_6(s)X_1(s) + D_6(s)X_2(s) \tag{6.36}$$

where

$$A_1 = \frac{a_5s^5 + a_4s^4 + a_3s^3 + a_2s^2 + a_1s + a_0}{\Delta(s)}$$

$$B_1 = \frac{b_5s^5 + b_4s^4 + b_3s^3 + b_2s^2 + b_1s + b_0}{\Delta(s)}$$

$$C_1 = \frac{c_5s^5 + c_4s^4 + c_3s^3 + c_2s^2 + c_1s + c_0}{\Delta(s)}$$

$$D_1 = \frac{d_5s^5 + d_4s^4 + d_3s^3 + d_2s^2 + d_1s + d_0}{\Delta(s)}$$

$$A_2 = \frac{e_5s^5 + e_4s^4 + e_3s^3 + e_2s^2 + e_1s + e_0}{\Delta(s)}$$

$$B_2 = \frac{f_5s^5 + f_4s^4 + f_3s^3 + f_2s^2 + f_1s + f_0}{\Delta(s)}$$

$$C_2 = \frac{g_5s^5 + g_4s^4 + g_3s^3 + g_2s^2 + g_1s + g_0}{\Delta(s)}$$

$$D_2 = \frac{h_5s^5 + h_4s^4 + h_3s^3 + h_2s^2 + h_1s + h_0}{\Delta(s)}$$

$$A_3 = \frac{i_5s^5 + i_4s^4 + i_3s^3 + i_2s^2 + i_1s + i_0}{\Delta(s)}$$

$$B_3 = \frac{j_5s^5 + j_4s^4 + j_3s^3 + j_2s^2 + j_1s + j_0}{\Delta(s)}$$

$$C_3 = \frac{k_5s^5 + k_4s^4 + k_3s^3 + k_2s^2 + k_1s + k_0}{\Delta(s)}$$

$$D_3 = \frac{l_5s^5 + l_4s^4 + l_3s^3 + l_2s^2 + l_1s + l_0}{\Delta(s)}$$

$$A_4 = \frac{m_5s^5 + m_4s^4 + m_3s^3 + m_2s^2 + m_1s + m_0}{\Delta(s)}$$

$$B_4 = \frac{n_5s^5 + n_4s^4 + n_3s^3 + n_2s^2 + n_1s + n_0}{\Delta(s)}$$

$$C_4 = \frac{o_5s^5 + o_4s^4 + o_3s^3 + o_2s^2 + o_1s + o_0}{\Delta(s)}$$

$$D_4 = \frac{p_5s^5 + p_4s^4 + p_3s^3 + p_2s^2 + p_1s + p_0}{\Delta(s)}$$

$$A_5 = \frac{q_5s^5 + q_4s^4 + q_3s^3 + q_2s^2 + q_1s + q_0}{\Delta(s)}$$

$$B_5 = \frac{r_5s^5 + r_4s^4 + r_3s^3 + r_2s^2 + r_1s + r_0}{\Delta(s)}$$

$$C_5 = \frac{s_5s^5 + s_4s^4 + s_3s^3 + s_2s^2 + s_1s + s_0}{\Delta(s)}$$

$$D_5 = \frac{t_5s^5 + t_4s^4 + t_3s^3 + t_2s^2 + t_1s + t_0}{\Delta(s)}$$

$$A_6 = \frac{v_5s^5 + v_4s^4 + v_3s^3 + v_2s^2 + v_1s + v_0}{\Delta(s)}$$

$$\Delta(s) = w_6s^6 + w_5s^5 + w_4s^4 + w_3s^3 + w_2s^2 + w_1s + w_0$$

All the equations can be determined using MATLAB.

Remark 1 A very important parameter in this algorithms is to evaluate the exact value of ω_n which is the undamped natural frequency. The other important parameter is damping ratio ξ . The iterations were based on selecting the nominal damping ratio using a shifted eigen value of CLP. If there are complex poles, that also may be defined using their real and imaginary part in Eq. 6.37.

$$S = -\sigma \pm j * \omega_d \quad (6.37)$$

The natural frequency is ω_d . The real part will be negative and in complex conjugate pair $\sigma = \xi\omega_n$ and $\omega_d = \omega_n\sqrt{1 - \xi^2}$. To find out overshoot, the equation is $M_p = e^{-\pi\xi/\sqrt{1-\xi^2}}$, where $0 \leq \xi \leq 1$ and for real and imaginary axis angle $\cos \theta = \xi$.

6.2.3 Algorithm Description

The discrete diagram of algorithm is shown in Fig. 6.2, from where it is very obvious that the parameters of LQR method are designed after several iterations.

6.2.4 Illustrative Example

An approach to generate the state estimates of 2-DOF RM with observer using an EFSO is proposed in this section. The extended observer solves the problem of disturbance attention by providing an effective approach in dealing with uncertainties encountered as a result of parameter variations or differences in working points. Now after applying all the values of Eqs. 6.17–6.20 in Eq. (6.21) provided in [7], the linearized equation will become:

$$A = \begin{bmatrix} 0 & 0 & 1 & 0 \\ 0 & 0 & 0 & 1 \\ -0.4568 & -0.6196 & 0 & 0 \\ 0.2485 & -6.6174 & 0 & 0 \end{bmatrix}, \quad B = \begin{bmatrix} 0 & 0 \\ 0 & 0 \\ 0.7870 & -0.0426 \\ 0.0426 & 0.1349 \end{bmatrix},$$

$$C = \begin{bmatrix} 1 & 0 & 0 & 0 \\ 0 & 1 & 0 & 0 \end{bmatrix}, \quad D = \begin{bmatrix} 0 & 0 \\ 0 & 0 \end{bmatrix} \quad (6.38)$$

Using AOIM, four weighted matrices have been decided to be the best optimized result. All the results and discussions are provided here in this section. Weighted matrix Q has been decided as case 1, case 2, case 3 and case 4 as given in Table 6.1.

In Table 6.1 for case 1, three of the states are considered for weighted components, whether in other three cases all the states were considered. Compared to all these four cases, case 4 acquired the best optimized result which is demonstrated in Fig. 6.4.

The augmented matrices (AM) are given in Table 6.2, two sets of close loop poles (CLP) and controller gains (CG) are given in Table 6.3, and observer poles (OP) and observer gain (OG) are given in Table 6.4, the latest output of using data of the said tables are drawn in (Fig. 6.5).

The open loop response of both the angles of links is shown in Fig. 6.6a and b, where it can be surveyed that the angle θ is in unstable condition. To control such

Table 6.1 Various weighted matrices

Q_1 (Case 1)	Q_2 (Case 2)
$\begin{bmatrix} 191.3 & 0 & 0 & 0 \\ 0 & 104.9 & 0 & 0 \\ 0 & 0 & 0 & 0 \\ 0 & 0 & 0 & 200.5 \end{bmatrix}$	$\begin{bmatrix} 41.7 & 0 & 0 & 0 \\ 0 & 14.8 & 0 & 0 \\ 0 & 0 & 71.4 & 0 \\ 0 & 0 & 0 & 100.7 \end{bmatrix}$
Q_3 (Case 3)	Q_4 (Case 4)
$\begin{bmatrix} 39.7 & 0 & 0 & 0 \\ 0 & 14.8 & 0 & 0 \\ 0 & 0 & 81.2 & 0 \\ 0 & 0 & 0 & 200.7 \end{bmatrix}$	$\begin{bmatrix} 201.2 & 0 & 0 & 0 \\ 0 & 39.6 & 0 & 0 \\ 0 & 0 & 84.8 & 0 \\ 0 & 0 & 0 & 101.1 \end{bmatrix}$

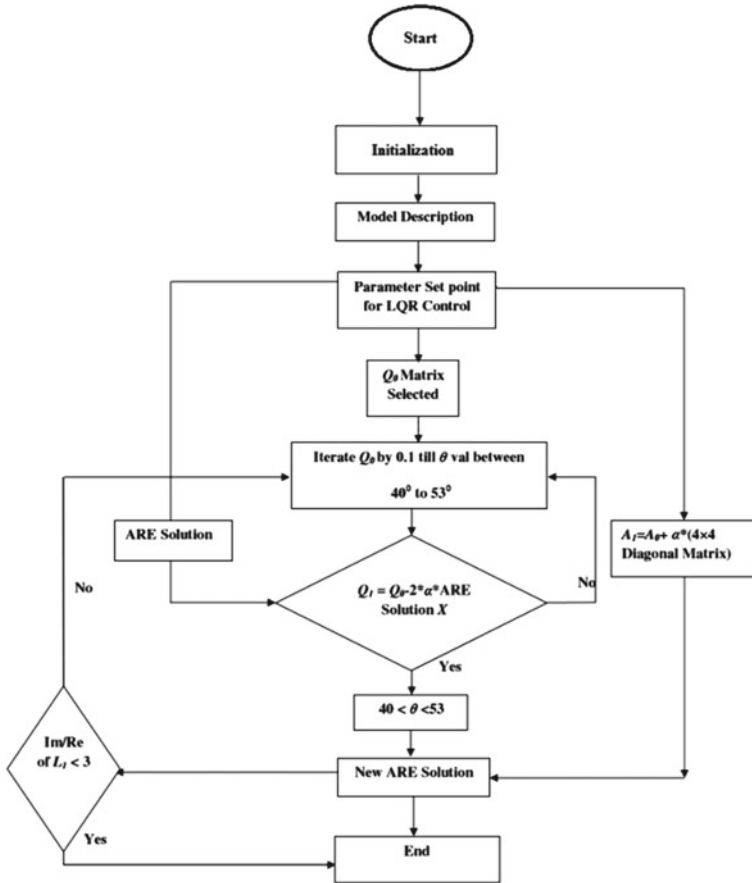


Fig. 6.4 Algorithm for advanced optimized iteration method (AOIM)

a complex plant using the results of Tables 6.1, 6.2, 6.3 and 6.4, linearized models were simulated which provides the best response acquired by the case 4, where a step input of 0.025 rad/sec was introduced and the rise time is 1.87 s and 1.72 s, respectively, for link 1 and link 2, which is the mitigated result among four cases. The settling time is 3.1 s and 6.4 s, respectively, for output 1 and 2, respectively. The overshoot is very less in link 2 and is 1.1, whereas in link 1, it is zero. Based on these performances, the result can be justified for the controller action and the system stability. The quadratic regulator action may be updated by using more fine-tuning methods used for the weighted matrices.

In all the case shown in Figs. 6.6, 6.7, 6.8, 6.9, 6.10, 6.11, 6.12 and 6.13, the disturbance was introduced at 12 sec and 10% amplitude of the step input, and it has been seen in all the cases that the robotic link output is converged to the equilibrium point vary rapidly. This mitigates lesser complexity of the system control. Due to the additional state operation, this disturbance \hat{d} gets resolute very easily. A very high

Table 6.2 Augmented matrices for four cases

A_a	B_a
$\begin{bmatrix} 0 & 0 & 1 & 0 & 0 & 0 \\ 0 & 0 & 0 & 1 & 0 & 0 \\ -0.4568 & -0.6196 & 0 & 0 & 0.7870 & -0.0426 \\ 0.2485 & -6.6174 & 0 & 0 & 0.0426 & 0.1349 \\ 0 & 0 & 0 & 0 & 0 & 0 \\ 0 & 0 & 0 & 0 & 0 & 0 \end{bmatrix}$	$\begin{bmatrix} 0 & 0 \\ 0 & 0 \\ 0.7870 & -0.0426 \\ 0.0426 & 0.1349 \\ 0 & 0 \\ 0 & 0 \end{bmatrix}$
C_a	D_a
$\begin{bmatrix} 1 & 0 & 0 & 0 & 0 & 0 \\ 0 & 1 & 0 & 0 & 0 & 0 \end{bmatrix}$	$\begin{bmatrix} 0 & 0 \\ 0 & 0 \end{bmatrix}$

Table 6.3 Controller parameters (poles, gain) for all cases

CLP		OG
$S_{1,2}$	$S_{3,4}$	K
Case 1	$-2.2955 \pm j2.3678 \quad -1.0012 \pm j2.3955$	$\begin{bmatrix} 13.1549 & 0.2023 & 5.7404 & 1.7422 \\ -0.9206 & 1.0675 & -0.8015 & 14.5837 \end{bmatrix}$
Case 2	$-6.4839, -0.7727 \quad -0.6926 \pm j2.4761$	$\begin{bmatrix} 5.7623 & -0.6385 & 9.1571 & 0.8823 \\ -0.3140 & 0.1967 & -0.8900 & 10.0789 \end{bmatrix}$
Case 3	$-6.9616, -0.7199 \quad -0.9728 \pm j2.3797$	$\begin{bmatrix} 5.7621 & -0.6348 & 9.6724 & 1.4351 \\ -0.3145 & 0.1965 & -1.0437 & 14.1529 \end{bmatrix}$
Case 4	$-7.0312, -1.5872 \quad -0.9728 \pm j2.3797$	$\begin{bmatrix} 13.5434 & -0.4756 & 10.8839 & 0.8357 \\ -0.7905 & 0.4459 & -1.0017 & 10.2677 \end{bmatrix}$

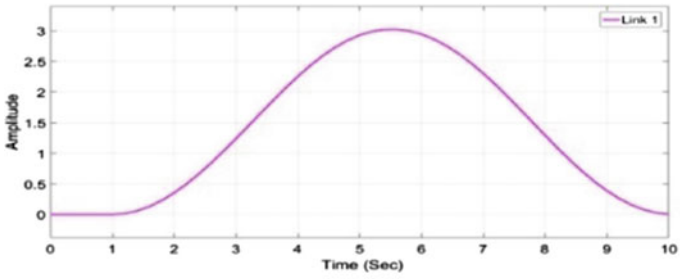
observer gain operation is required to curtail the external disturbances which is here smoothly operated by the EFSO. The vulnerable indication of the robotic manipulator is to control all the output responses at the same time, which seems to be a difficult job, but due to the EFSO this task became simple. Nurturing the stability of the system, it can be mentioned that after determining the close loop poles, it is observed that all the poles lie in the left-hand side of s-plane, which defines the systems are stable. For the case 3 in comparison with the other cases, rise time is lesser in both the outputs. The error signal \bar{e} is shown along with all the output responses. The reference here is considered to be step; in future, sine or square wave responses also may be examined for the 2-DOF RM model.

Table 6.4 Observer parameters (poles, gains) for all the cases

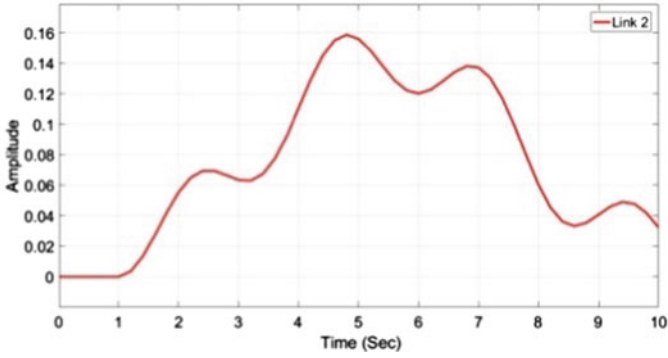
OP		OG
S _o		L
Case 1	$-6.8865 \pm j7.1034$ $-3.0036 \pm j7.1034$ -8 -9	$\begin{bmatrix} 18.6 & 0.1 & 159.8 & -26.6 & 669.5 & -1844.2 \\ 0.300 & 18.2 & 30.4 & 144.6 & 562 & 4366.0 \end{bmatrix}$
Case 2	-19.4518 -2.3182 $-2.0777 \pm j7.4282$ -8 -9	$\begin{bmatrix} 30.1 & -14.2 & 234 & -86 & 681.5 & 2586.5 \\ -0.10 & 12.8 & 4.9 & 82.4 & 234.5 & 3515.1 \end{bmatrix}$
Case 3	-20.8848 -2.1597 $-2.9183 \pm j7.1390$ -8 -9	$\begin{bmatrix} 18.3 & 17.4 & 83 & 201.9 & 213.9 & 3056.5 \\ 1.8 & 27.6 & -34.9 & 238.1 & -206.5 & 5413 \end{bmatrix}$
Case 4	-21.0935 -4.7615 -2.1160 ± 7.4391 -8 -9	$\begin{bmatrix} 25.5 & 13.8 & 210.1 & 187 & 921.7 & 3876.2 \\ 5.8 & 21.6 & 15.8 & 165.8 & -89.4 & 3970.3 \end{bmatrix}$

6.3 Conclusion

To linearize the nonlinear model here for 2-DOF RM is a big challenge for the researcher, although using Taylor series expansion, it has been linearized here. Extended state observer is used here to observe the unknown states and to mitigate the higher-order complex controller design. Since the estimator does not control the system on its own, a state feedback scheme is still required to attain the desired control performance. The combination of feedback control to the output of observer does not affect the overall controller design. The aspect of observer design in this work has been investigated for the linear regulator with quadratic cost function. Using a quadratic performance index method, the linear quadratic regulator observer estimation with feedback control is achieved. The output responses are quite stable and with a minor cost function. The purpose of the methodology was justified with the smooth disturbance rejection approach.

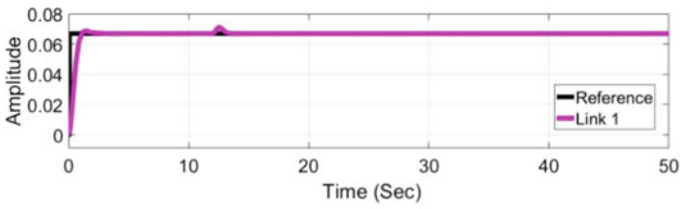


(a)

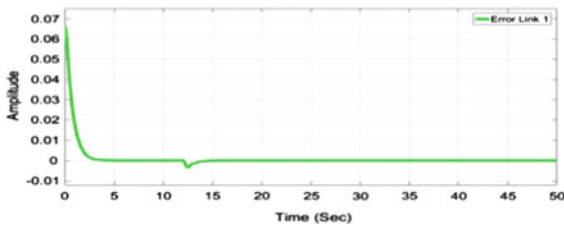


(b)

Fig. 6.5 a Open loop output of link 1, b open loop output of link 2



(a)



(b)

Fig. 6.6 ESO-LQR output a and error signal \bar{e} for robotic manipulator link 1, case 1

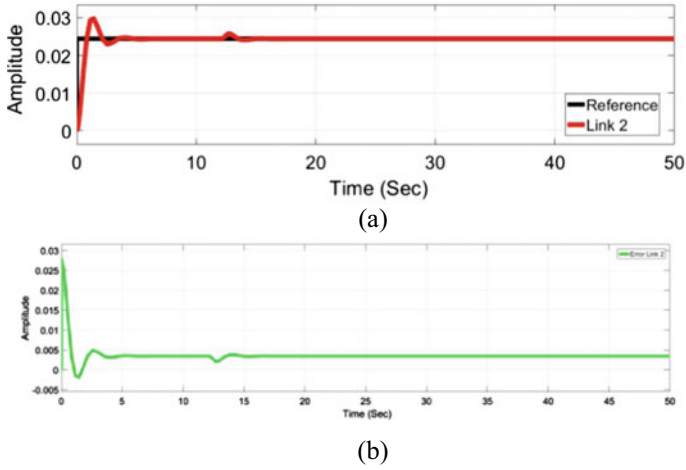


Fig. 6.7 ESO-LQR output \mathbf{a} and error signal $\bar{\mathbf{e}}$ for robotic manipulator link 2, case 1

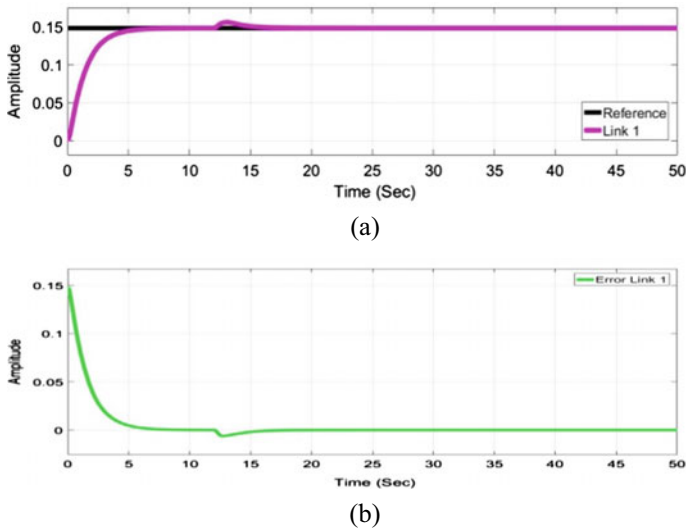
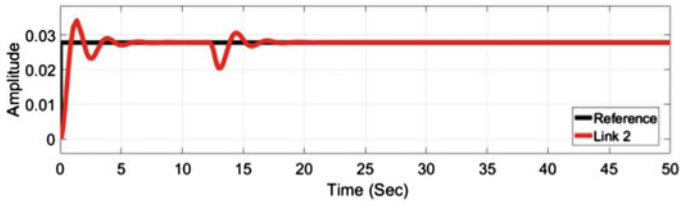
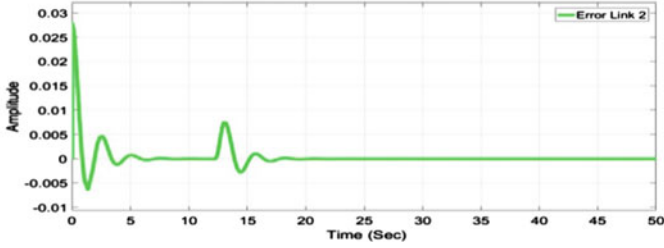


Fig. 6.8 ESO-LQR output \mathbf{a} and error signal $\bar{\mathbf{e}}$ for robotic manipulator link 1, case 2

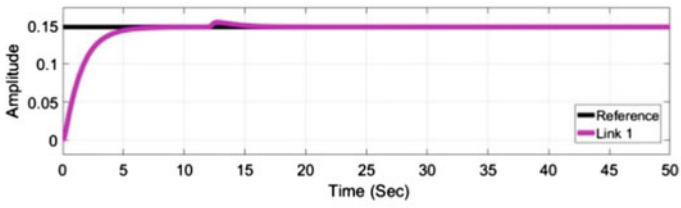


(a)

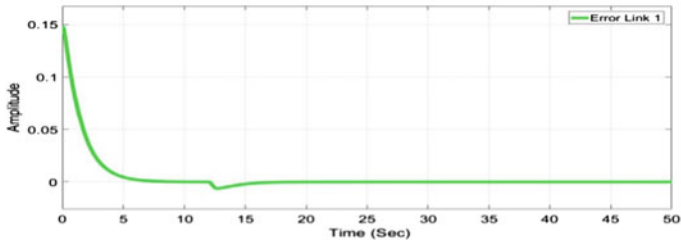


(b)

Fig. 6.9 ESO-LQR output \mathbf{a} and error signal $\bar{\mathbf{e}}$ for robotic manipulator link 2, case 2

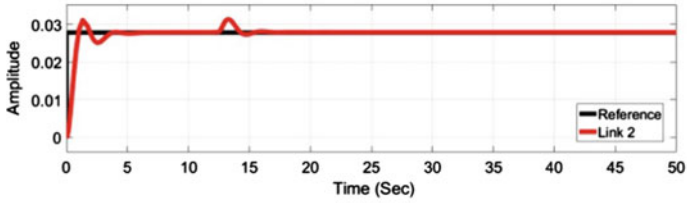


(a)

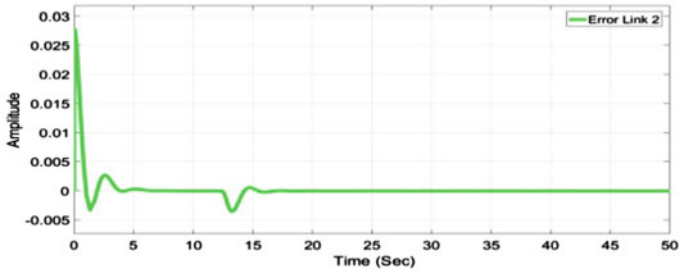


(b)

Fig. 6.10 ESO-LQR output \mathbf{a} and error signal $\bar{\mathbf{e}}$ for robotic manipulator link 1, case 3

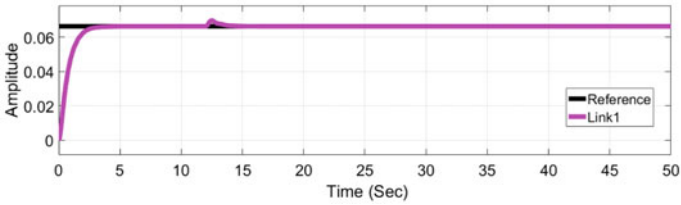


(a)

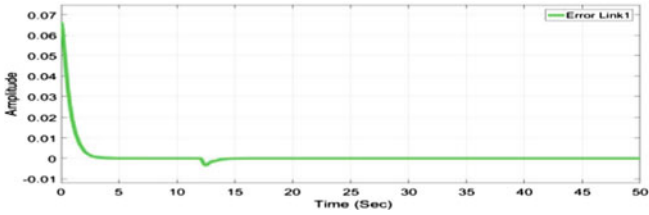


(b)

Fig. 6.11 ESO-LQR output \mathbf{a} and error signal $\bar{\mathbf{e}}$ for robotic manipulator link 2, case 3



(a)



(b)

Fig. 6.12 ESO-LQR output \mathbf{a} and error signal $\bar{\mathbf{e}}$ for robotic manipulator link 1, case 4

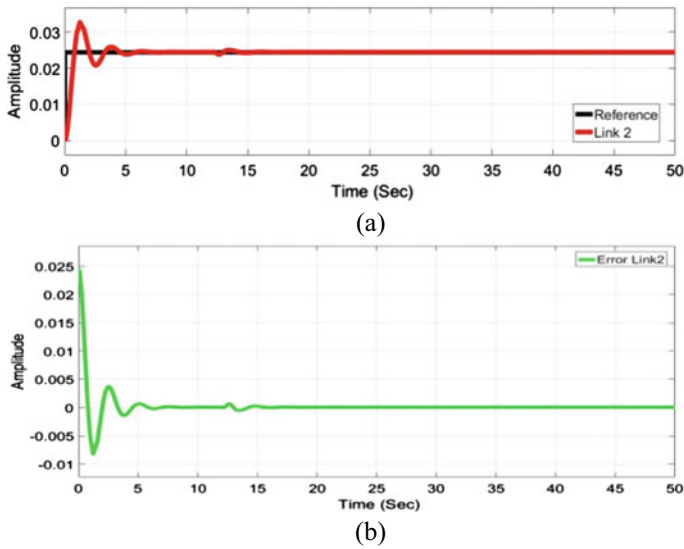


Fig. 6.13 ESO-LQR output \mathbf{a} and error signal $\bar{\mathbf{e}}$ for robotic manipulator link 2, case 4

References

1. Al-Saggaf, U.M., Mehedi, I.M., Mansouri, R., Bettyeb, M.: Rotary flexible joint control by fractional order controllers. *Int. J. Control and Autom. Syst.* **15**, 2561–2569 (2017). <https://doi.org/10.1007/s12555-016-0008-8>
2. Feliu, V., Rattan, K.S., Brown, H.B.: Modeling and control of single link flexible arms with lumped masses. *J. Dyn. Syst. Measur. Control Trans. ASME* **114**(59), 59–69 (1992)
3. Kim, D.H., Oh, W.H.: Robust control design for flexible joint manipulators: theory and experimental verification. *Int. J. Control Autom. Syst.* **4**, 495–505 (2006)
4. Li, Y., Tong, S., Li, T.: Adaptive fuzzy output feedback control for a single link flexible robot manipulator driven DC motor via back stepping. *Nonlinear Anal. Real World Appl.* **4**(1), 483–494 (2013)
5. Pereira, E., Aphale, S.S., Feliu, V., Moheimani, S.O.R.: Integral resonant control for vibration damping and precise tip positioning of a single link flexible manipulator. *IEEE/ASME Trans. Mechatron.* **16**(2), 232–240 (2011)
6. Ren, C., Ding, Y., Li, X., Zhu, X., Ma, S.: Extended state observer based robust friction compensation for tracking control of an omni directional mobile robot. *ASME. J. Dyn. Syst., Meas., Control.* **141**(10), 101001 (2019). <https://doi.org/10.1115/1.4043488>
7. Mustafa, A.M., A AL-SAIF: modeling, simulation and control of 2-R robot. *Glob. J. Res. Eng.* **14**(1) (2014)
8. Goodwin, G.C., Graebe, S.F., Salgado, M.E.: *Control system design*. Pearson (2000)
9. Choi, H., Oh, S., Kong, K.: Control of a robotic manipulator in the polar coordinate system using a biarticular actuation mechanism. *Int. J. Control Autom. Syst.* **14**, 1095 (2016). <https://doi.org/10.1007/s12555-014-0343-6>
10. Seok, J., Yoo, W., Won, S.: Inertia-related coupling torque compensator for disturbanceobserver based position control of robotic manipulators. *Int. J. Control Autom. Syst.* **10**, 753 (2012). <https://doi.org/10.1007/s12555-012-0411-8>

11. Ahmed, S., Wang, H., Aslam, M.S.: Robust Adaptive control of robotic manipulator with input time varying delay. *Int. J. Control Autom. Syst.* **17**, 2193 (2019). <https://doi.org/10.1007/s12555-018-0767-5>
12. Li, Z., Yang, K., Bogdan, S., Xu, B.: On motion optimization of robotic manipulators with strong nonlinear dynamic coupling using support area level set algorithm. *Int. J. Control Autom. Syst.* **11**, 1266 (2013). <https://doi.org/10.1007/s12555-011-9212-8>
13. Homayounzade, M., Khademhosseini: Disturbance observer-based trajectory following control of robot manipulators. *A. Int. J. Control Autom. Syst.* **17**, 203 (2019). <https://doi.org/10.1007/s12555-017-0544-x>
14. Brahmi, A., Saad, M., Gauthier: Adaptive control of multiple mobile manipulators transporting a rigid object. *G., Int. J. Control Autom. Syst.* **15**, 1779 (2017). <https://doi.org/10.1007/s12555-015-0116-x>
15. Chen, K.Y.: Robust optimal adaptive sliding mode control with the disturbance observer for a manipulator robot system. *Int. J. Control Autom. Syst.* **16**, 1701 (2018). <https://doi.org/10.1007/s12555-017-0710-1>
16. Chen, W., Ballance, D.J., Gawthrop, P.J., O'Reilly, J.: A nonlinear disturbance observer for robotic manipulators. *IEEE Trans. Ind. Electron.* **47**(4), 932–938 (2000)
17. Ge, S.S., Li, Z., Yang, H.: Data driven adaptive predictive control for holonomic constrained under actuated biped robots. *IEEE Trans. Control Syst. Technol.* **20**(3), 787–795 (2012)
18. Wang, Y., Chen, J., Yan, F., Zhu, K., Chen, B.: Adaptive super-twisting fractional-order nonsingular terminal sliding mode control of cable-driven manipulators. *ISA Trans.* **86**, 163–180 (2019)
19. Wang, Y., Yan, F., Chen, J., Ju, F., Chen, B.: A new adaptive time-delay control scheme for cable-driven manipulators. *IEEE Trans. Ind. Inf.* (2018). <https://doi.org/10.1109/TII.2018.2876605>
20. Ahmed, S., Wang, H.P., Tian, Y.: Adaptive high-order terminal sliding mode control based on time delay estimation for the robotic manipulators with backlash hysteresis. *IEEE Trans. Syst. Man, Cyber. Syst.* (2019). <https://doi.org/10.1109/TSMC.2019.2895588>
21. He, W., Huang, H., Ge, S.S.: Adaptive neural network control of a robotic manipulator with time-varying output constraints. *IEEE Trans. Cyber.* **47**(10), 3136–3147 (2017)
22. He, W., Dong, Y.: Adaptive fuzzy neural network control for a constrained robot using impedance learning. *IEEE Trans. Neural Netw. Lear. Syst.* **29**(4), 1174–1186 (2018)
23. Agrawal, O.P., Xu, Y.: On the global optimum path planning for redundant space manipulators. *IEEE Trans. Syst. Man, Cyber.* **24**(9), 1306–1316 (1994)
24. Medanic, J., Tharp, H.S., Perkins, W.R.: Pole placement by performance criterion modification. *IEEE Trans. Autom. Control* **33**(5), 469–472 (1988). <https://doi.org/10.1109/9.1229>
25. Author, F.: Article title. *Journal* **2**(5), 99–110 (2016)
26. Author, F., Author, S.: Title of a proceedings paper. In: Editor, F., Editor, S. (eds.) *Conference 2016, LNCS*, vol. 9999, pp. 1–13. Springer, Heidelberg (2016)
27. Author, F., Author, S., Author, T.: Book title, 2nd edn. Publisher, Location (1999)
28. Author, F.: Contribution title. In: 9th International Proceedings on Proceedings, pp. 1–2. Publisher, Location (2010)
29. LNCS Homepage, <http://www.springer.com/lncs>. Last accessed 2016/11/21

Chapter 7

Optimisation of Energy and Exergy Analysis of 100 W Solar Photovoltaic Module Using ANN Method



**I. R. Ganesh Kumar, S. Vijay Kumar, Jagannath Reddy, G. Rajendra,
Yoga Sainath Reddy, Sai Ranjith Reddy, and Biplab Das**

Abstract Renewable technologies are plentiful, long lasting, and eco-friendly. Solar energy, which generates both heat and light, is the most abundant source of energy. Solar photovoltaic modules use solar radiations to generate electricity and thermal energy, while the remaining solar radiation content is lost to the environment. The first law of thermodynamics was used to perform an energy analysis on a solar photovoltaic module, and the second law of thermodynamics was used to perform an exergy analysis to determine energy losses and exergy efficiency during the photovoltaic conversion process. The operating parameters of a solar photovoltaic module are as follows: ambient temperature, photovoltaic module surface temperature, overall heat transfer coefficient, short circuit current, open circuit voltage, fill factor and solar radiation. These were achieved on a sunny day in the month of February at R.L.J.I.T, Doddaballapur. The experimental data are utilised to calculate the solar photovoltaic module's energy and exergy efficiencies. The efficiency of the solar panel performance decreases as the temperature of the module rises. As a result, by reducing heat from the surface of the solar photovoltaic module, the module's efficiency can be increased. Surface heat can be eliminated by delivering water or air as a medium to the solar photovoltaic module. Finally, ANN model was developed to determine the performance prediction models using multilayer perceptron neural network, and it reveals that the developed model with six neurons gives better performance with a confidence interval of 95%.

I. R. Ganesh Kumar · S. Vijay Kumar · J. Reddy (✉) · G. Rajendra · Y. S. Reddy · S. R. Reddy
Department of Mechanical Engineering, R L Jalappa Institute of Technology, Doddaballapura,
Karnataka 561203, India
e-mail: jreddy.mech@gmail.com

S. Vijay Kumar
Department of Mechanical Engineering, Nitte Meenakshi Institute of Technology, Yelahanka,
Karnataka 56064, India

B. Das (✉)
Department of Mechanical Engineering, National Institute of Technology Silchar, Silchar, Assam
788010, India
e-mail: biplab.2kmech@gmail.com

Classification

η_{energy}	Efficiencies regarding energy (%)
η_{ex}	Exergy efficiency (%)
NOCT	Nominal operating cell temperature (°C)
V_{oc}	Voltage in the open circuit (V)
V	Voltage (V)
V_{mp}	Maximum power voltage (V_{max})
I_{mp}	Maximum power current (A_{max})
I_{sc}	Short circuit current (A)
I	Current (A)
I_l	Current was created by light
I_o	Current density at saturation
FF	Fill factor
Q	Electrons' charge (ev)
R_s	Series resistance (Ohm)
A	Modules surface area (m^2)
G_{sr}	Solar irradiation across the world (W/m^2)
K	Boltzmann constant (J/K)
P	Power (Watt)
P_{el}	Electrical power (W)
P_{max}	Maximum power (W_{max})
Ex_{Inlet}	Exergy inlet
$\text{Ex}_{\text{Outlet}}$	Exergy outlet
Ex_{Loss}	Exergy loss
$\text{Ex}_{\text{thermal}}$	Thermal exergy
Ex_{ele}	Electrical exergy
T	Temperature (K)
T_a	Ambient temperature
T_s	The sun's surface temperature
T_m	Module temperature
T_{sky}	Temperature in the sky
Q	Heat discharged into the atmosphere (W)
U	Overall heat loss coefficient ($\text{W}/\text{m}^2\text{K}$)
h_{conv}	Convective heat transfer coefficient ($\text{W}/\text{m}^2\text{K}$)
h_{rad}	Coefficient of radiant heat transfer ($\text{W}/\text{m}^2\text{K}$)
V_w	Wind velocity (m/s)
σ	Stefan–Boltzmann's constant ($\text{W}/\text{m}^2\text{K}$)
ε	Emissivity of the module

7.1 Introduction

Future technologies are primarily focused on the implementation of renewable energy resources. Because the combustion of fossil fuels on energy demands results in a massive amount of carbon emissions into the atmosphere, which disrupts the ecosystem. And fossil fuels are being depleted on a daily basis. Renewable energy resources must be used to replace the burning of fossil fuels. Energy demands are high all across the world, and meeting them without affecting the environment is a critical element to consider. As a result, renewable resources contribute to the reduction of carbon emissions in the energy supply.

India, as the world's most populous country, necessitates massive amounts of electricity generation. India, as we all know, is the world's third most polluted country. To reduce the impact on future generations while meeting energy demand, a greater emphasis on renewable resources is required. India is fortunate to receive a lot of sunlight throughout the year, it is located in between (8.7° , 37.6° N latitude and 68.7° , 97.25° E longitude). On an average, the solar concentration on earth differs from 5–7 kWh/m²day. A photovoltaic system captures more beam radiation, with small amount of diffused radiation [1]. The highest quantity of solar radiation is obtained to the surface that is perpendicular to the sun rays. As a result, the solar photovoltaic module must be tilted. It is essential to keep the panel slant at certain degree in order to capture maximum amount of solar energy and to increase the power generation. When the sun rays strike a solar cell, it generates electricity. The electrons in the panel are ejected from the atoms due to the intensity of solar radiations produced by sunlight. Electrons are pushed into the p-region, leaving holes in the n-region. Electric power is generated by the flow of electrons from one place to another. The ratio of power output from solar cells to energy produced by the panel is used to determine the energy efficiency of a solar panel. The energy efficiency of a solar panel can be measured with thermodynamics first law. However, the exergy analysis is measured on the basis of second law of thermodynamics. Energy analysis is concerned with the quantity of energy consumed and the efficiency of energy produced, whereas exergy is a quality of energy available for converting it into productive work. The maximum work potential that can be obtained through the given amount of energy is known as exergy [2]. Exergy analysis has been recognised as a good tool for evaluating the module's thermodynamic performance in general [3, 4]. Exergy analysis is based on the quantification and accounting of usable energy, which is referred as exergy, and the unusable energy is referred as irreversibility [5]. Exergy analysis offers a number of approaches for assessing and comparing the performance of solar photovoltaic systems.

Depending on insulation and module performance, a PV system's energy payback time ranges from 15 to 20 years. The photovoltaic array's performance can be increased by reducing the energy payback period. As a result, it is crucial to evaluate the PV array's performance as thoroughly as possible. The panel performance depends on different parameters such as ambient temperature, solar radiation intensity, module temperature, overall coefficient of heat loss, open circuit voltage, short

circuit current, maximum voltage, maximum current and the module size. PV array performance is also dependent on the climate and the design of the entire system [6]. Exergy analysis has gradually gained popularity over the last few decades by the advantages which outweigh energy analysis. The inlet and outlet energy and exergy of the module should be evaluated to obtain an equilibrium condition of the module. Geng et al. [7] have determined an exergy analysis on solar water heating system and measured efficiencies of energy and exergy. In terms of exergy analysis, (Joshi [8]) a model of a solar photovoltaic heating system was experimented. The primary purpose of this project is to demonstrate how to do research on a solar module's energy and exergy and to construct a realistic model of solar photovoltaic performance to classify the thermodynamic notion of heat transmission and determine exergy losses in solar photovoltaic modules.

The research of Pratish Rawat [9] proposed a 300 W solar photovoltaic module exergy performance analysis. The performance of solar photovoltaic module can be improved by removing the excess heat from the surface of the module. By this process, the lifespan of the panel can be increased, and the energy and exergy efficiency can also be improved. Sudhakar et al. [10] investigated the energy and exergy performance on 36 W solar PV module. In this experiment, they have determined that the temperature of a PV module can affect energy and exergy efficiencies significantly. The performance of a PV module can be increased by removing heat from the bottom surface. This research work concludes that if the temperature of the module rises, then the energy efficiency drops down. Rawat and Kumar [11] experimented with evaluating the performance of solar photovoltaic thermal (PVT) system. As a result of this experiment, they observed that the temperature of the photovoltaic module had a considerable impact on the system's varied efficiencies. Electrical efficiency can be improved by removing heat from the surface of a solar module. Yoga Sainath Reddy et al. [12] experimented for energy and exergy study on the 20 W solar photovoltaic module. The solar photovoltaic model's efficiency is depending upon the temperature on the module. To improve the panel performance and efficiency, heat must be taken out from the back surface of the PV module, with the help of water or air. (Pande et al. [13]) The energy and exergy performances of a typical solar photovoltaic module are accounted in this research in the month of February, May, June, September, October and December. The energy and exergy efficiencies are always greater than power conversion rate. Ankit Sing et al. [14] proposed an energy and exergy analysis of a crystalline silicon solar PV module. They investigated a polycrystalline solar photovoltaic module with a 10 W power output. The predicted energy, exergy, and power conversion efficiency of the module are all affected by solar radiation, wind speed, panel temperature, and ambient temperature. They discovered that PV module depends on sunlight. Manoj kumar Sharma et al. [15] investigated optimal tilt angle determination for photovoltaic panels. The results showed that the proposed method is quite effective in increasing the power generation of photovoltaic panels by 7–8% by using a 5 W panel with an angle of 10, 20, 25, 30, and 40. They tested the most efficient method for generating the most power from solar panels by orienting them at an angle to the sun's rays.

7.2 Method to be Consider

7.2.1 Solar Panel Energy Efficiency

The universal form of exergy balancing comparison for an open steady-state system can be denoted as follows using the first rule of thermodynamics:

$$E_{\text{inlet}} = E_{\text{outlet}} \quad (7.1)$$

Exergy balance is denoted as follows:

$$E_{\text{inlet}} + E_{\text{outlet}} = E_{\text{loss}} \quad (7.2)$$

Exergy must be the highest amount of productive work done during the process in order to keep the system balanced. It is a combined property of the system and its surroundings. The greatest amount of work done by the system in process is E_{outlet} in Eq. (7.2). Exergy losses are proportional to the amount of exergy utilised.

When sunlight strikes a solar cell, the energy conversion efficiency is the percentage of power converted to electricity. The ratio of energy inlet to energy outlet is the energy efficiency of a solar photovoltaic cell. The cell temperature and the amount of solar radiation received will determine the outlet energy of a solar photovoltaic cell. When solar radiation is absorbed by the panel, it converts it directly into electricity, while the remaining 70–75% of the absorbed rays are dissipated as heat to the surrounding environment while also raising the panel temperature. Thus, the efficiency of the solar panel will reduce. Also, the photoelectric conversion efficiency drops by 0.40.5% as the temperature of the solar panel rises by one degree Celsius.

The solar photovoltaic module's energy conversion efficiency equation is shown below [1]:

$$\eta_{\text{energy}} = \frac{V_{\text{oc}} \times I_{\text{sc}} \times \text{FF}}{A \times G} \quad (7.3)$$

The following equation can be used to calculate the I–V (current–voltage) characteristics of a solar cell:

$$I = I_1 - I_0 \times \exp\left[\frac{q \times (V - IR_s)}{A \times K \times T}\right] \quad (7.4)$$

The solar photovoltaic outlet electrical power is denoted as follows:

$$P_{\text{ele}} = I \times V \quad (7.5)$$

In addition, the formula given below shows the maximum electrical power output:

$$P_{\max} = V_{oc} \times I_{sc} \times FF = V_{mp} \times I_{mp} \quad (7.6)$$

As of the practical knowledge, the photovoltaic module converts solar energy into two ways: firstly electrical energy and the secondly thermal energy. Thermal energy is distributed through many methods of heat transmission. Conduction, convection and radiation are a few examples. As a result, the solar photovoltaic module design determines the heat transmission rate. The operating temperature T_{cell} (T_c) of a photovoltaic module, i.e., cell temperature, must be determined in order to achieve efficiency. For simplification, it might be assumed to be similar to the surface of the solar photovoltaic module, and it is dependent on atmospheric conditions. The temperature of the solar panels, or photovoltaics, is important because it determines how much electricity is generated by the solar cells. We know that the electric conversion efficiency of a solar cell increases as the radiation from the sun is absorbed and converted into electricity. As a result, solar cells must be naturally or artificially cooled by using water or air as a medium to remove heat from the solar cell's surface.

7.2.2 To Determine Solar Photovoltaic Modules Exergy Efficiency

Exergy analysis gives the most capable utilisation of energy potential, which may be identified by energy quality discussion. The following is the overall exergy balance of the solar photovoltaic module throughout the steady flow process [16]:

$$\text{Exergy}_{\text{inlet}} = \text{Exergy}_{\text{outlet}} + \text{Exergy}_{\text{loss}} + \text{Irreversibility} \quad (7.7)$$

The quality of the consumed energy throughout the conversion process is referred to as exergy losses. The exergy losses are referred to be irreversibility [17]. As mentioned, solar energy is converted into electrical energy and thermal energy by any solar panel. The electrical energy is used, whereas the thermal energy is lost to the atmosphere as heat, which is resulting in exergy losses.

The ratio of total output exergy to total intake exergy is often used to define the exergy efficiency of a solar module. [2, 16, 18]:

$$\eta_{\text{ex}} = \frac{\text{Ex}_{\text{outlet}}}{\text{Ex}_{\text{inlet}}} \quad (7.8)$$

In the intake exergy of a solar photovoltaic system, only solar radiation intensity is considered. [19]:

$$\text{Ex}_{\text{inlet}} = \text{AG} \left[1 - \frac{4}{3} \left(\frac{T_a}{T_s} \right) + \frac{1}{3} \left(\frac{T_a}{T_s} \right)^4 \right] \quad (7.9)$$

As shown below, the exergy outlet of a solar photovoltaic panel can be defined as the sum of electrical and thermal exergy.

$$\text{Ex}_{\text{outlet}} = \text{Ex}_{\text{thermal}} + \text{Ex}_{\text{electrical}} \quad (7.10)$$

The thermal exergy is mentioned as follows:

$$\text{Ex}_{\text{thermal}} = Q \left[1 - \frac{T_a}{T_s} \right] \quad (7.11)$$

where

$$Q = UA(T_m - T_a) \quad (7.12)$$

The overall heat loss coefficient of a photovoltaic module, including convection heat transfer and solar radiation heat transfer, is noted as follows:

$$U = h_{\text{conv}} + h_{\text{rad}} \quad (7.13)$$

The coefficient of convection heat transfer [20] is given below:

$$h_{\text{conv}} = 2.8 + 3 \times V_w \quad (7.14)$$

Coefficient of solar radiation heat transfer between a photovoltaic module and its surroundings [21]:

$$h_{\text{rad}} = \epsilon \sigma (T_{\text{sky}} + T_m) (T_{\text{sky}}^2 + T_m^2) \quad (7.15)$$

The NOCT value can be used to compute the temperature of a module:

$$T_m = T_a + (\text{NOCT} - 20) \cdot \frac{G}{800} \quad (7.16)$$

The following formula is used to calculate the efficiency of the sky's temperature [21]:

$$T_{\text{sky}} = T_a - 6 \quad (7.17)$$

Electrical exergy in the photovoltaic module's outlet electrical power [8] is calculated as follows:

$$\text{Ex}_{\text{Electrical}} = \text{Voc} \times \text{Isc} \times \text{FF} \quad (7.18)$$

7.3 Detailed Study of an Experiment

The research was conducted in Doddaballapur, a rural district of Bangalore, India. Bangalore enjoys a pleasant climate throughout the year, with low wind speeds and 280–290 days of sunshine on average. The experiment was conducted out in Doddaballapur's R.L.J.I.T mechanical engineering R&D centre. The temperature ranges from 18 to 35 °C. Open circuit voltage (V_{oc}), short circuit current (I_{sc}), wind velocity, solar radiations, ambient temperature, power and other well-known data were used to assess the performance of a 100 W solar photovoltaic panel. Data were collected at one-hour intervals from 8:00 to 16:00 h to calculate module performance. An anemometer and a temperature measurement device, as well as RTD-PT100 sensors, were used to detect wind velocity and ambient temperature. The intensity of solar radiation was measured with a pyranometer, and the temperature of the solar panel was measured with RTD-PT 100 thermocouples.

7.4 Result and Analysis

The research was conducted at RLJIT, Doddaballapur (latitude 13.2957 N and longitude 77.5364 E) in Bangalore rural on a clear sunny day in February. Using experimental data, that is, an influence of ambient temperature on the solar photovoltaic panel was examined and tested. Using the second law of thermodynamics and solar radiations, the exergy efficiency of a solar photovoltaic module was computed as the ratio of output to inlet exergy. A 100 W solar photovoltaic module's energy and exergy performances were assessed. Exergy analysis has been found to be a better method for determining the efficiency of solar panels. According to the findings, exergy analysis is a more capable and valuable method for analysing the performance of a solar photovoltaic panel.

Figure 7.2 shows that on the day of the experiment, the minimum and maximum temperatures were found to be 21.2–32.6 °C and between 349 and 1020 W/m². The maximum and minimum solar radiation levels were determined. As solar radiation increases, so does the output power of a solar module, raising the temperature of the solar cell and diminishing its efficiency.

Figure 7.3 depicts the change in ambient temperature and wind velocity. The temperature ranged from 21.2 to 32.6 °C, and the wind speed ranged from 0.8 to 2.2 m per second. Convective heat transmission between the surface of the solar photovoltaic module and its surroundings is affected by variations in wind speed.

Figure 7.4 displays changes in energy and exergy efficiencies as a function of ambient temperature. Maximum energy and exergy efficiencies are 47.755 and 53.860%, respectively, whereas the ambient temperature was 21.2 °C in the morning. When the temperature exceeded 32.6 °C, the minimum energy and exergy efficiencies were 16.333 and 26.599%, respectively. It is clear that when the temperature rises, the performance of a solar photovoltaic module falls gradually.

Figure 7.5 illustrates the outcomes of exergy inlet, outlet and loss of the solar PV module; the results indicate that the outlet exergy from the solar PV module is extremely low to irreversible exergy loss. The average daily exergy loss was 262.62 W/m^2 . The overall exergy inlet and outlet measurements were 459.23 and 150.53 W/m^2 , respectively.

After the conversion procedure, the percentage of exergy efficiency is shown in Fig. 7.6. In comparison with the inlet, the inlet exergy is higher, while the outflow exergy is lower. The remaining energy is either lost to the atmosphere or lost during the conversion process. There are more exergy losses. The maximum inlet exergy was 607.3961 W , the maximum outlet exergy was 189.816 W , and a large number of exergies were lost in the vicinity of 417.57969 W . The outlet exergy from the solar photovoltaic module falls as a result of the losses, as does the exergy efficiency. To improve efficiency, the surface temperature of the solar module can be reduced.

Figure 7.7 exhibits the energy and exergy efficiencies of the PV module on the day of testing. The highest exergy efficiency was the highest energy efficiency. A solar PV module's maximum exergy efficiency is 53.86% during 8:00am, corresponding to a module temperature of $21.2 \text{ }^\circ\text{C}$. The exergy efficiency drops as when the solar temperature goes up. To attain maximum exergy efficiency, the temperature of the solar photovoltaic module must always be carefully regulated via surface conditioning utilising air or water as a medium.

Above that the result (Fig. 7.8) demonstrates that as solar radiation increases, power generation starts to rise as well. The solar panel's output power improves when the sunrays are at their brightest. As the amount of power generated grows, the panel's efficiency begins to decline.

ANN models

The proposed research work used an MLPNN model which is a feed forward-backward propagation artificial neural network to predict the energy, exergy and power output by considering five input parameters such as time, solar radiation, ambient temperature, top and rare temperature. The structure of the model is developed in three different layers such as the input layer, hidden layer and output layer. The model developed is based on the multilayer perceptron neural network model with six neurons gives optimal values for all the combinations considered. In case of energy, exergy and power output, the output values are -3.099 , 1.3422 and 1.0522 , respectively.

During the training and testing process, the input parameters enter the feed forward neural networks as shown in Fig. 7.9; each product of input parameters (M_i) and a weight function (W_{ij}) is summed into the junction and is summed with bias (b_j) of the neurons as follows (Eq. 7.19). In the present investigation, the input parameters such as solar radiation, time taken, ambient temperature, top face temperature and bottom face temperature were considered. Similarly, the output is energy, exergy and power output that is considered.

The proposed research work used an MLPNN model is a feed forward-backward propagation artificial neural network to predict the energy, exergy and power output

Table 7.1 Given parameters were used as an input for the analysis

Input parameter	Value
Nominal operating cell temperature (NOCT)	45 °C
Constant of Stefan–Boltzmann (σ)	5.67×10^{-8} W/m ² -K
Emissivity of the panel (ϵ)	0.9
Temperature of sun	5780 k

by considering four input parameters such as time, solar radiation, ambient temperature, top and rare temperature. The structure of the model is developed in three different layers such as the input layer, hidden layer and output layer. The developed is based on the multilayer perceptron neural network model with six neurons which gives optimal values for all the combinations considered. In case of energy, exergy and power output, the output values are -3.099 , 1.3422 and 1.0522 , respectively (Table 7.2).

During the training and testing process, the input parameters enter the feed forward neural networks as shown in Fig. 7.1; each product of input parameters (M_i) and a weight function (W_{ij}) is summed into the junction and is summed with bias (b_j) of the neurons as follows (Eq. 7.1). In the present investigation, the input parameters such as solar radiation, time taken, ambient temperature, top face temperature and bottom face temperature were considered. Similarly, the output is energy, exergy and power output that is considered. Finally, performance prediction models were developed for all the three output parameters that were considered (Eqs. 7.20–7.22). Based on the trial and error method, for all the combinations considered, VAF, RMSE and MAPE are given in Table 7.3. Based on the above observations, the predicted and experimental values are plotted and shown in Figs. 7.10, 7.12, 7.14, respectively; similarly, the residual between the predicted and experimental values is shown in Figs. 7.11, 7.13, 7.15, respectively (Tables 7.4 and 7.5).

Table 7.2 Specifications of the experimental panel

Model	SUK-100 W
Maximum power of module	100 W
Open circuit voltage	21.4 V
Short circuit current	6.3A
Voltage at max. power (Vmp)	17.7 V
Current at max. power (Imp)	5.7A
Dimension of panel	(100 × 60 × 3.5)cm
Fill factor	0.74

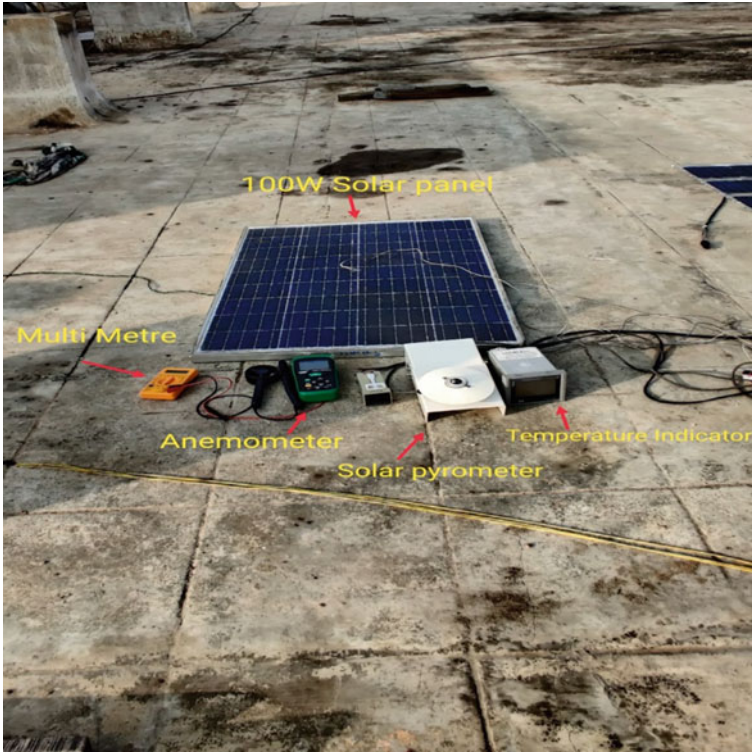


Fig. 7.1 100 W solar photovoltaic module at RLJIT, Doddaballapura

$$X = \left(\sum_{i=1}^n (W_{ij} M_i) \right) + b_j \quad (7.19)$$

$$\text{VAF} = 1 - \frac{\text{var}(y - y')}{\text{var}(y)} \times 100 \quad (7.20)$$

$$\text{RMSE} = \sqrt{\frac{1}{N} \sum_{i=1}^N (y - y')^2} \quad (7.21)$$

$$\text{MAPE} = \frac{1}{N} \sum_{i=1}^N \left| \frac{A_i - P_i}{A_i} \right| \times 100 \quad (7.22)$$

Table 7.3 Weights and bias of the optimum model (4-6-3) three outputs (energy, exergy and power output)

<i>Weights between the input and hidden layer (W_{6*4})</i>			
0.1726	2.1654	-0.47184	-0.75609
1.849	7.1998	-2.4565	1.6544
1.5794	2.5321	-2.9738	0.71647
-2.0003	-2.2489	-0.15613	-0.0218
-2.0062	1.2743	-1.575	-1.0477
0.97303	0.6656	1.2078	1.8114
<i>Bias in hidden layer (B_{3*6})</i>			
[1.3959, -7.3802, 0.6478, 1.3078, -0.8961, -3.7686]			
[-1.2876, -0.60079, 2.7323, 2.3094, 0.81326, -2.1987]			
[0.90067, 3.5294, 0.31521, 1.0036, -1.7543, 2.3658]			
<i>Weights to output layer (W_{1*6})</i>			
[-1.9314, -7.6927, -0.62732, -1.5551, -0.88452, 3.2481]			
<i>Bias in output layer (B_{3*1})</i>			
[-3.0996]			
[1.3422]			
[1.0552]			

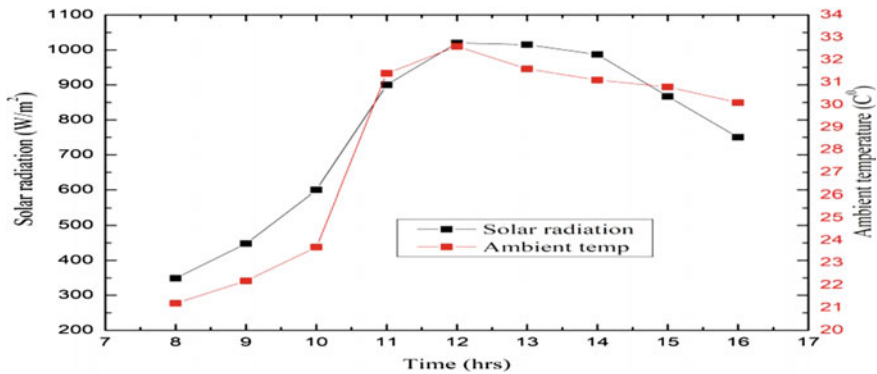


Fig. 7.2 Variations in the intensity of solar radiation and the ambient temperature

7.5 Conclusion

As part of this comprehensive analysis, an energy and exergy analysis of a 100 W solar photovoltaic module was undertaken at RLJIT, Doddaballapur, Bengaluru rural, India. On a warm day, the experimental findings were achieved by accurately observing multiple factors. Exergy losses throughout the conversion process, as well as the data collected to determine the optimum temperature that results in the best

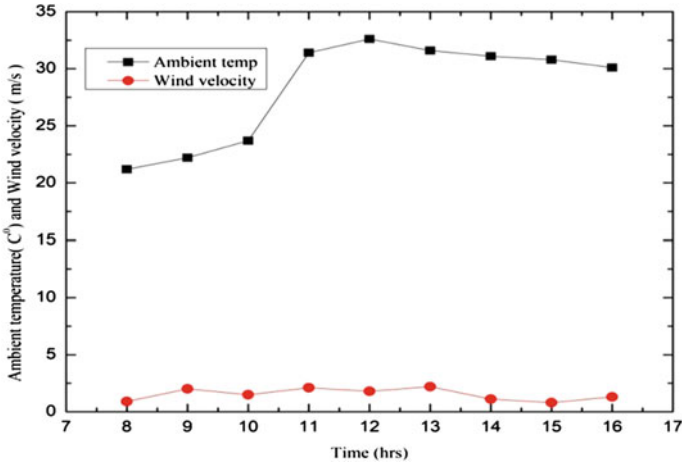


Fig. 7.3 Temperature and wind velocity variations

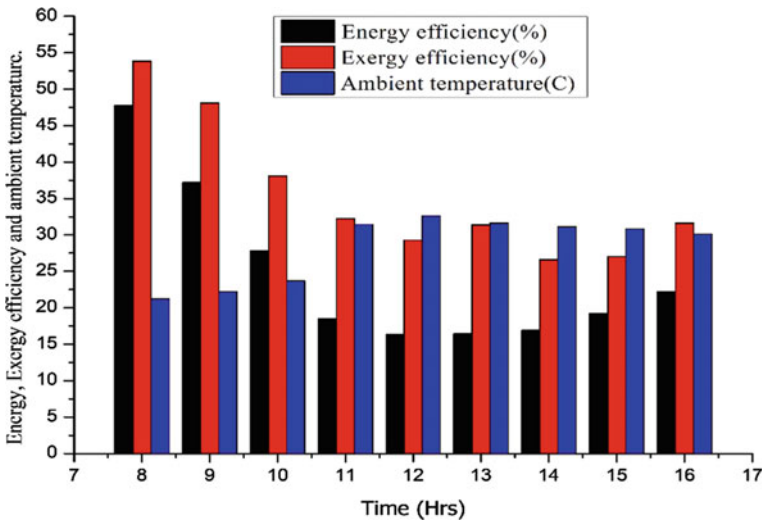


Fig. 7.4 Variation in energy and exergy efficiencies as a function of temperature

exergy efficiency, were also calculated. The following are the findings of this research project.

1. The final result shows the average exergy efficiency ($\eta_{ex} = 35.352 \%$). In terms of the solar photovoltaic module, the exergy analysis shows that today's silicon modules benefit very little from the high exergy content of solar radiation.

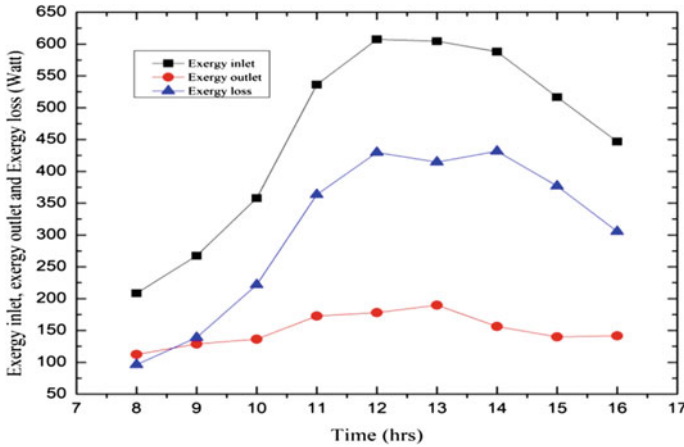


Fig. 7.5 Exergy inlet, exergy outlet and exergy loss variations

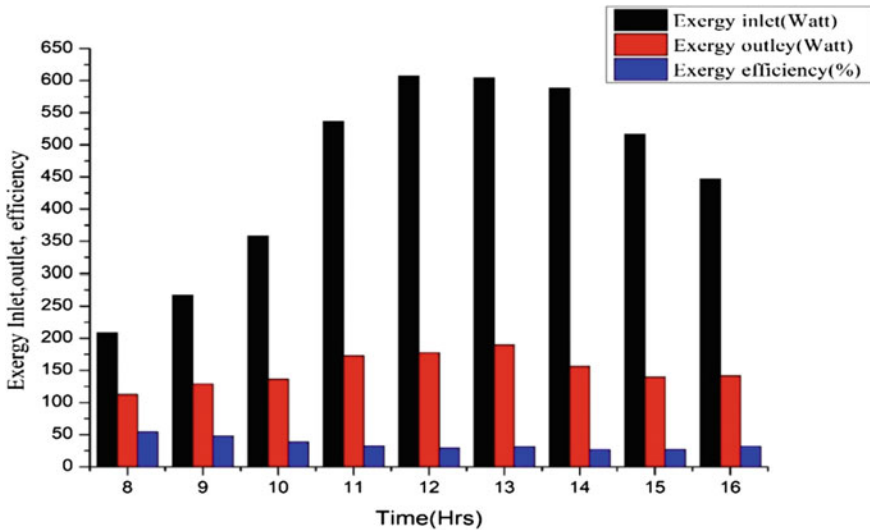


Fig. 7.6 Exergy efficiency's impact

2. The maximum value of energy and exergy efficiencies of the solar PV module in the morning hours was found to be 47.75 and 59.8606%, respectively. During peak hours, efficiency gradually declines.
3. The energy and exergy efficiencies decrease as the ambient temperature rises and due to an increase in cell temperature and irreversibility, while power generation rises due to more radiations during peak hours. The exergy efficiency of a PV module increases initially with increasing solar radiation intensity and then decreases after reaching its maximum point.

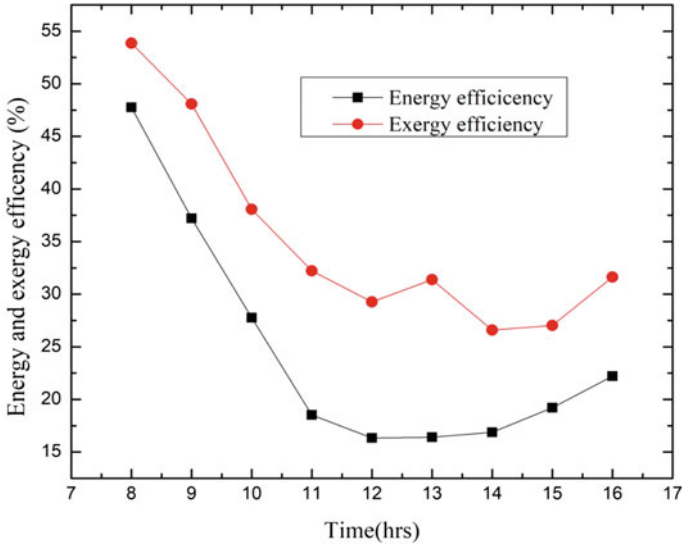


Fig. 7.7 Energy and exergy efficiencies of solar PV module

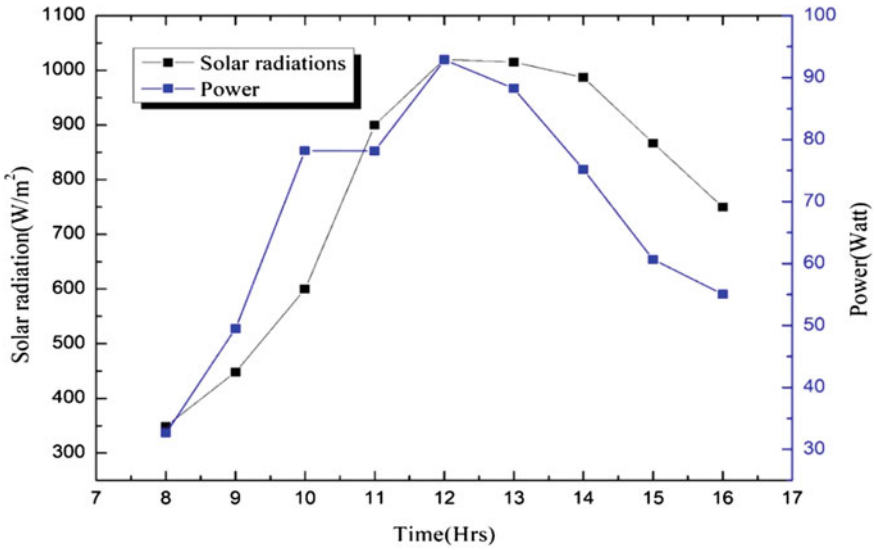


Fig. 7.8 Generation of electricity in relation to solar radiation

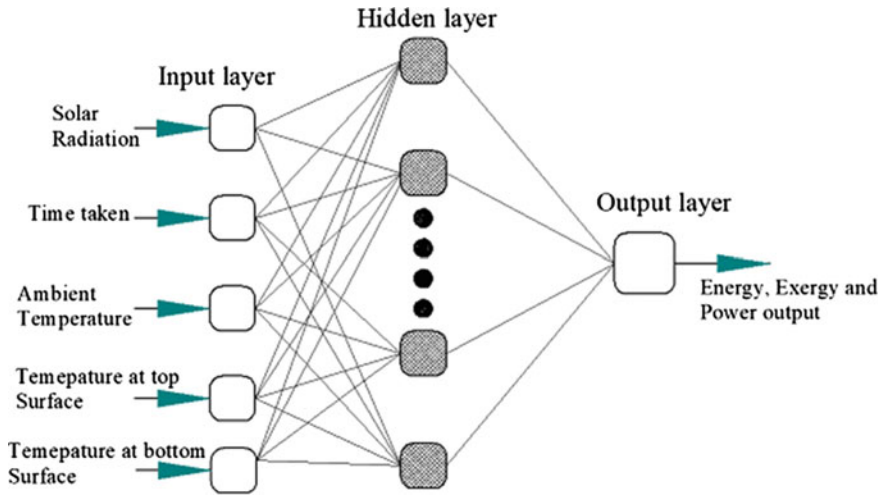


Fig. 7.9 Graphical representation of the MLPANN model for energy, exergy and power output

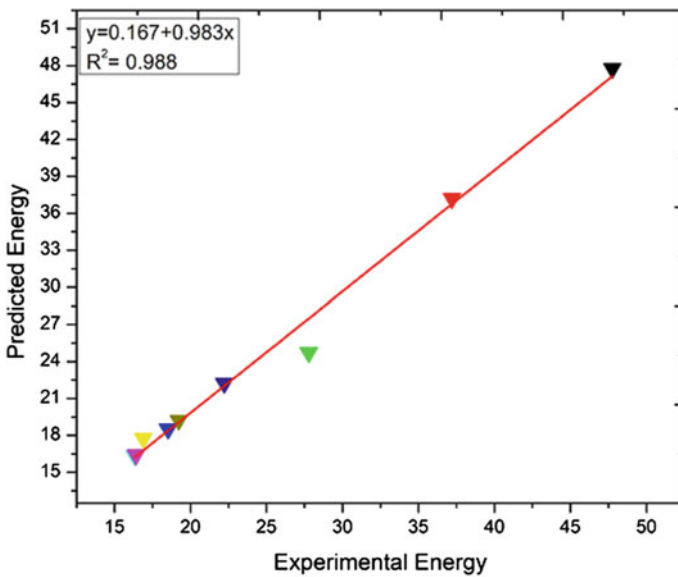


Fig. 7.10 Predicted and experimental values for energy

4. The efficiency of a solar panel decreases as the temperature of the panel rises. To improve panel performance, heat must be removed from the surface of the solar panel by cooling it. Cooling can be accomplished by providing a water and air medium.

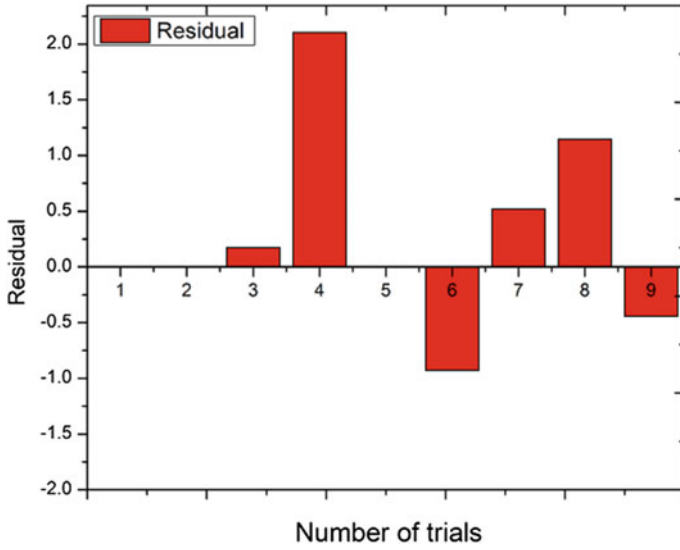


Fig. 7.11 Residual plots for energy between predicted and experimentation

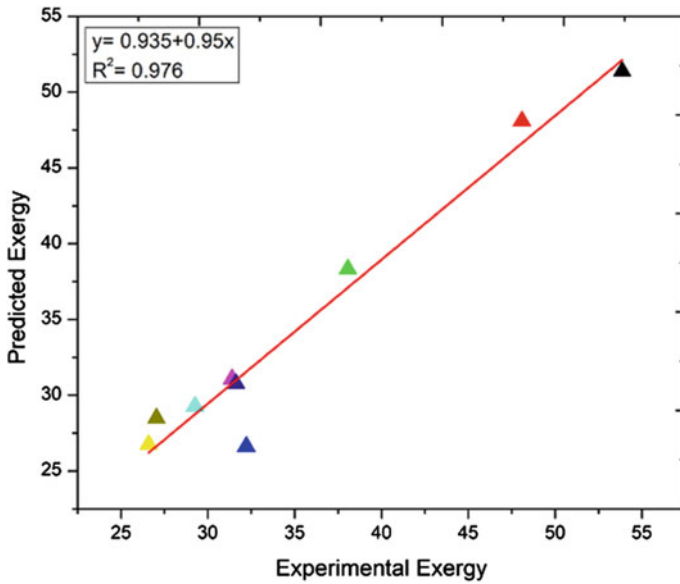


Fig. 7.12 Predicted and experimental values for exergy

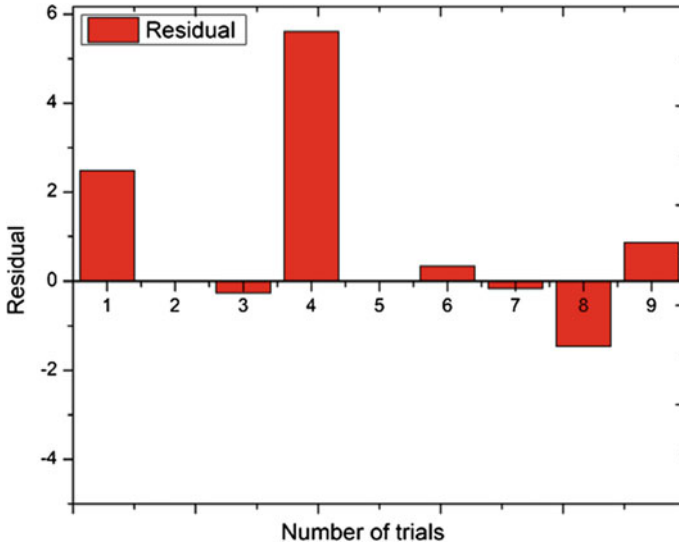


Fig. 7.13 Residual plots for exergy between predicted and experimentation

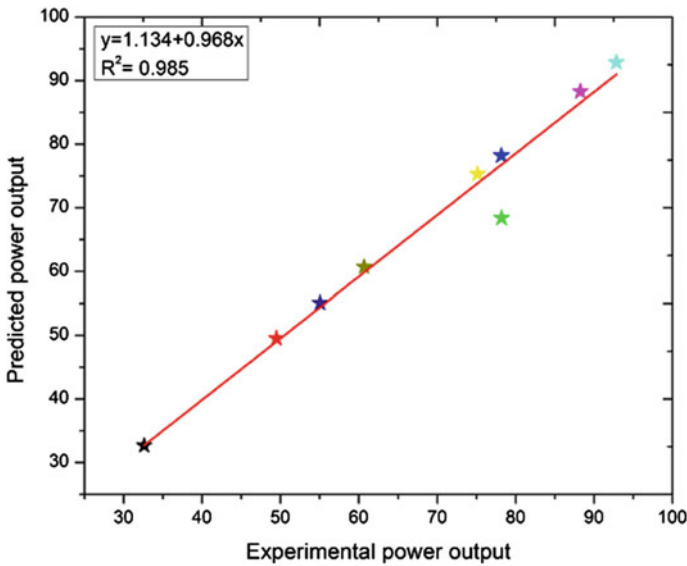


Fig. 7.14 Predicted and experimental values for power output

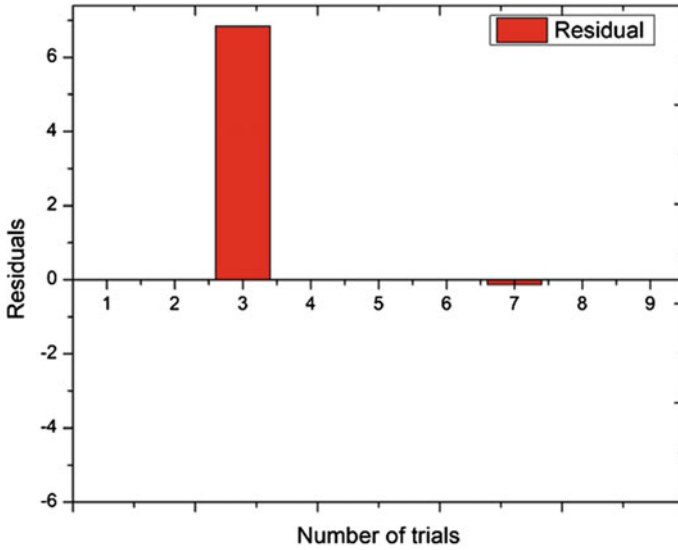


Fig. 7.15 Residual plots for power output between predicted and experimentation

Table 7.4 Performance prediction models for energy, exergy and power output

	VAF	RMSE	MAPE
Energy	99.01	1.0588	1.7918
Exergy	81.92	3.8913	5.1497
Power output	97.21	3.2800	1.4163

5. The developed ANN models for energy, exergy and power output are with an RMSE values of 1.058, 3.891 and 3.280, respectively. Therefore, the performance prediction models were optimum for six neurons with five input parameters. Hence, the R^2 (VAF) was 0.9901, 0.8182 and 0.9721, respectively.
6. Research and development aimed at increasing the efficiency of solar modules and developing low-cost semiconductor materials significantly reduce the cost of solar photovoltaic electricity. The upcoming modules should concentrate on the efficiency of the solar panel.

Table 7.5 Predicted data for all the combinations considered for four inputs with one hidden layer for six neurons

Energy			Exergy			Power output		
Experimental	Predicted	Error	Experimental	Predicted	Error	Experimental	Predicted	Error
47.75549	47.7553	0.000188	53.86068	51.37742	2.48326	32.636	32.63613	-0.00013
37.20238	37.20238	-3.78E-06	48.08918	48.08881	0.000368	49.5	49.50001	-9.59E-06
27.77778	24.72131	3.05647	38.07114	38.32536	-0.25421	78.21	68.37061	9.839388
18.51852	18.51852	-4.53E-06	32.2152	26.60932	5.605876	78.182	78.18202	-2.29E-05
16.33987	16.33987	-3.98E-09	29.26337	29.26313	0.000236	92.855	92.85418	0.000816
16.42036	16.42037	-8.64E-06	31.39749	31.06573	0.331759	88.263	88.263	-4.54E-06
16.88619	17.75126	-0.86508	26.59978	26.75379	-0.15401	75.1424	75.26625	-0.12385
19.22338	19.22338	-4.71E-06	27.04493	28.49679	-1.45186	60.669	60.66902	-2.39E-05
22.22222	22.22224	-1.36E-05	31.62654	30.76198	0.864564	55.0572	55.05724	-3.76E-05

Acknowledgements I am grateful to the management of R.L.J.I.T, Principal, and HODs of the mechanical department, for allowing me to conduct this experimental study. I would really like to take this opportunity to appreciate my mentor assistant Prof. Mr. Jaganath Reddy and also the mechanical department staff members, for their support in performing this experiment.

References

1. Wyman, C.J.C., Keith, F.: A review of collector and energy storage technology for intermediate temperature applications. *Solar Energy* **24**, 517–540 (1980)
2. Bejan, A.: *Advanced engineering thermodynamics*. Wiley interscience publisher, New York (1988)
3. Rosen, M.A., Hooper, F.C., Barbaris, L.N.: Energy analysis for the evaluation of the performance of closed thermal energy storage systems. *Trans. ASME J. Sol. Energy Eng.* **110**, 255–261 (1988)
4. Rosen, M.A., Dincer, L.: Thermal storage and exergy analysis: the impact of stratification. *Trans. CSME* **23**(1B), 173–186 (1999)
5. Cengel, Y.A.: *Thermodynamics: An Engineering Approach*, 5th edn. Tata McGraw hill, New York (2006)
6. Sarhaddi, F., Farahat, S., Ajam, H., Behzadmeh, A.: Exergetic optimization of a solar photovoltaic array. *Hindawi Publishing Corporation Journal of Thermodynamics* (2009)
7. Larson, D.L., Cortez, L.A.B.: Energy analysis: essential to effective energy management. *Trans. ASAE* **38**(4), 1173–1178 (1995)
8. Joshi, A.S., Dincer, I., Reddy, B.V.: Development of solar energy maps. *Int. J. Energy Res.* **33**, 709–718 (2009)
9. Rawat, P.: Energy performance analysis of 300W solar photovoltaic module. *Int. J. Eng. Sci. Res. Technol.* 381–390 (2017)
10. Sudhakar, K., Rajesh, M., Premalatha, M.: A Mathematical model to assess the potential of algal bio-fuels in India energy sources. Part A: Recovery, Utilisation *Environ. Effects* **34**(12), 1114–1120 (2012)
11. Rawat, P., Kumar, P.: Performance evaluation of solar photovoltaic/thermal (PV/T) system. *Int. J. Sci. Res.* **4**, 1466–1471 (2015)
12. Yoga Sainath Reddy, S., Reddy, J., Rajendra, G., Sai Ranjith Reddy, K., Ganesh Kumar, I.R.: Performance of 20w solar photovoltaic module for energy and exergy analysis. *Int. J. Modern Trends Sci. Technol.* **7**(05), 102–106 (2021)
13. Geng, L., Cengel, Y.A., Turner, R.H.: Energy analysis of a solar heating system. *J. Solar Energy Eng.* **1173**(3), 249–251 (1995)
14. Pandey, A.K., Pant, P.C., Sastry, O.S., Kumar, A., Kumar, S.: energy and exergy performance evaluation of a typical solar photovoltaic module. *Thermal Sci.* **19**, S625–S636 (2015)
15. Singh, A., Shukla, O.P., Nishant Saxsena, M.: Energy and exergy analysis of crystallin silicon of solar photovoltaic module. *Int. Res. J. Eng. Technol.* 1808–1826 (2016)
16. Wong, K.F.V.: *Thermodynamics for Engineers*. University of Miami, CRC Press LLC (2000)
17. Hepabsli, A.: A key review on exergetic analysis and assessment of renewable energy resources for sustainable future. *Renew. Sustain. Energy Rev.* **12**, 593–661 (2008)
18. Kotas, T.J.: *The exergy method of thermal plant analysis*. Krieger Publish Company, Malabar, FL (1995)
19. Petela, R.: Exergy of undiluted thermal radiation. *Sol. Energy* **74**, 469–488 (2003)
20. Boyle, G.: *Renewable Energy Power for a Sustainable Future*, 2nd edn. Oxford University Press, Oxford (2004)
21. Watmuff, J.H., Charters, W.W.S., Proctor, D.: Solar and wind induced external coefficients for solar collectors. *COM PLES 2nd Q.* **56**(2), 56 (1977)

Chapter 8

Obstructed Material Classification Using mmWave Radar with Deep Neural Network for Industrial Applications



Yi Sheng Leong, Sukanta Roy, and King Hann Lim

Abstract Radar sensing technology uses radio electromagnetic (EM) waves to provide 3D space localisation and 4D motion sensing. The mmWave radar shows advantages in low cost, low power, environment robustness and capability in material classification. In this paper, the capability of mmWave radar to perform industrial multi-material classification with obstruction is studied by measuring the reflected radar signal. The classified materials are common engineering materials which include metal, polymer, ceramic, composite and natural. The experiment is conducted using the IWR1443BOOST mmWave radar sensor. From a series of experiment results, the received radar signal is the unique material signature of a target object. The relative power measured by IWR1443BOOST is correlated to the target object's relative permeability and permittivity. This indicated the mmWave radar can easily pick up unique material properties as well as the physical structure of target object with minor assistance from deep neural network model. Three models which are linear classifier, fully connected neural network (FCNN) and convolution neural network (CNN) are trained and inference on the radar signal. CNN shows the most robust performance even under noise, while linear classifier converges fastest. All models achieved satisfactory accuracy with minimum amount of training epochs. This is because the radar signals are having clear discriminative distribution as proven in standard deviation against mean plot. The models also perform under 16 mm thick obstruction and can classify less than 5 mm thin material. From the experiment, the mmWave radar provides highly accurate multi-material classification with deep neural network. Due to its' capability in wall-penetration and environment robustness characteristics, mmWave radar is a new alternative solution for industrial automation and sensing application.

Y. S. Leong · S. Roy (✉) · K. H. Lim

Faculty of Engineering and Science, Curtin University Malaysia, 98009 Miri, Malaysia

e-mail: sukanta.roy@curtin.edu.my

8.1 Introduction

Radar sensing technology is an important technology applied to scan objects in various industrial applications such as automotive [1, 2], military [3], manufacturing [4] and various machine vision solutions [5]. Radar sensing uses radio electromagnetic waves to determine an object range, angle, elevation and 3D space localisation. To produce a good radar sensing resolution, several signal processing methods are applied to compute the velocity of the reflected signal to enable a 4D view in the 3D space [6, 7]. This enables the fundamental application in vital sensing or classification that is highly demanding in many industrial and consumer applications [6]. Innovation advances in machine learning and artificial intelligence (AI) technology [8, 9] are the drivers for mmWave radar technology implementation into unmanned aerial vehicles, service robots and autonomous vehicles. The market of mmWave radar technology shows a promising growth rate, rising from \$31 billion in 2016 to \$237 billion in 2020 [8].

One of the latest technologies in mmWave radar uses complementary–metal–oxide semiconductor (CMOS) sensors to obtain better resolution and performance for deployment into robotic systems [9]. Due to its prominent advantages, the applications of CMOS mmWave radar sensors in robots and automation are widespread. CMOS mmWave radar sensors allow the accurate measurements of the distance and the relative velocities of the objects in the sensing field. Compared to other vision and Lidar-base sensors, mmWave radar sensors perform better in extreme environmental conditions, such as heavy rain, dust, smoke, fog and frost [10]. In addition, mmWave sensors can perform even under poor lighting conditions such as complete darkness or direct sunlight glare, a crucial characteristic for robust environment sensing in autonomous vehicles (AV) applications and advanced driver assistance systems (ADAS). Physically, an industrial mmWave sensor is small and light, at approximately three times the size and half the weight of a miniature Lidar sensor [11]. Due to its unique properties in signal penetration, a mmWave radar sensor can be concealed without affecting performance, making it suitable for many consumer products and applications requiring aesthetically pleasing design [12]. Thus, mmWave radar technology is a promising solution in robotic industry applications. In addition, another prominent application of radar sensing technology is that it can act as a distinct signature for any material or object due to its special characteristic that enables the application of electromagnetic waves within a certain frequency range. Therefore, this paper evaluates the capability of mmWave radar for obstructed material classification using multiple deep learning approach, specifically for industrial application.

8.2 Literature Review

A radar emits radio waves that can potentially capture unique signatures of a target, such as its velocity, size, shape, smoothness and orientation. These properties can be extracted with appropriate feature algorithms developed for classification and sensing. One of the challenges when training an object classification model for industrial applications is scalability, resulting from the sensor-to-sensor uncertainty due to fabrication variability. Practically, due to cost and time constraints, it is impossible to train a sensor system to cater for all possible variations. In addition, discriminative deep learning models often face small intra-class variations and instinctive inter-class differences. This problem can be solved by using a Siamese neural network [13] with unique electromagnetic signatures from the radar sensor. Weis and Santra [14] introduced a novel architecture R-SiameseNet that learned the latent feature representation.

Besides that, RadarCat offers promising accuracy in utilising radar sensors for industrial sensing tasks, such as human-machine interactions and daily proximate interactions with digital devices [15]. RadarCat demonstrated excellent robustness and accuracy in multi-material classification of daily objects, transparent materials and different body parts. This can help to facilitate a quick inspection between similar textures and high-risk goods, such as corn starch and drug powder. Additionally, multi-class object classification can detect sensitive goods, especially in the logistic sector that requires a detailed inspection of every single cargo before it is shipped out. Mistakes in the material classification will lead to penalties and logistic delays. Based on material scattering and absorption properties at specific wavelengths, it is possible to conduct material classification without opening up the parcel [16]. Also, this enabled the application of dynamic interaction with materials wirelessly to reduce the chances of getting infected by Coronavirus due to physical contact [17, 18]. Radar material classification technology can help a logistic company recognise and differentiate the types of material inside the container and provides the high security standard that is crucial in the logistic industry. As many industrial material identification applications are performed with the packaging involved, the next challenge of the RadarCat project is to showcase the radar performance under various obstruction materials. The obstruction material can be materials with weak to strong radar electromagnetic reflection such as foam, plastic, wood, aluminium and brick. Moreover, mSense introduced the FMCW radar signal for material identification covering five common materials: aluminium, ceramic, plastic, wood and water. mSense reported an average accuracy of 93% and demonstrated the capability and advantage of using radar sensors for material classification even in mobile circumstances [19]. CMOS radar with an operating frequency range between 85 and 100 GHz also showed a high accuracy of 88% when performing material classification at varying distances [20]. The accuracy can be increased to 96% with a minor physical noise filtering setup such as the frequency comb receiver. In summary, previous studies have proven that mmWave radar is robust and can perform accurate material classification tasks even under mobile and varying distance conditions. However, the sensing only involves

static targets where the accuracy of moving targets such as objects on a moving conveyor belt is questionable.

8.3 Objectives

The research aims to validate the concept of obstructed material classification using mmWave radar across engineering materials. This is done using deep neural network classifier algorithm that inference based on pure radar signal. The scope of the project involves data collection, machine learning algorithm development and radar signal processing. Details derivation on neural network algorithm and machine learning model evaluation technique is not the cover in the project.

8.4 Method

The mmWave radar sensor used is IWR1443BOOST mmWave radar from Texas Instrument [21]. IWR1443BOOST mmWave Radar sensor has an operating frequency from 76 to 81 GHz with three transmitters and four receivers. The target material used in the experiment includes all common engineering materials subset such as metal, plastic, ceramic, composite and natural. These materials are TPE elastomer, borosilicate, aluminium, ABS, wood, cement and PVC foam. Empty air was used as controlled environment when comparing with the experiment setup. The experiment is split into two main setups which are radar classification with no obstruction and with obstruction. The purpose of splitting out the experiment setups is to use the result from radar classification without obstruction as a baseline performance to radar classification with obstruction. The obstructing object is a wood plank with a thickness of 16 mm and is placed approximate the mid-span between radar sensor and target object. The size of obstructed object is very large relative to the sensor size to ensure 100% of the radar field of view is blocked. This is representing the use case of radar classification of material inside a wooden box without opening it. An illustration of experiment setup is shown in Fig. 8.1a.

Sampling material for both obstruction and non-obstruction experiment setup is same to ensure reproducibility of the result. For each material type, a total of more than 2000 samples size are collected. Stratified K -Fold validation with the split of 3 is used on training process. Stratified K -Fold validation is a cross-validator algorithm where it processes training and validation data while preserving the percentage of samples for each class [22]. Therefore, the average accuracy of the model is calculated by taking the mean of 3 K -Fold test. This is to ensure the robustness of the model and continue to perform correctly on unseen samples [23]. The experiment is repeated with obstructed material with same sample size. The received radar signals on each material class by each receiver were averaged and stored as relative power using mmWave SDK designed by Texas Instrument [24]. Relative power is the average

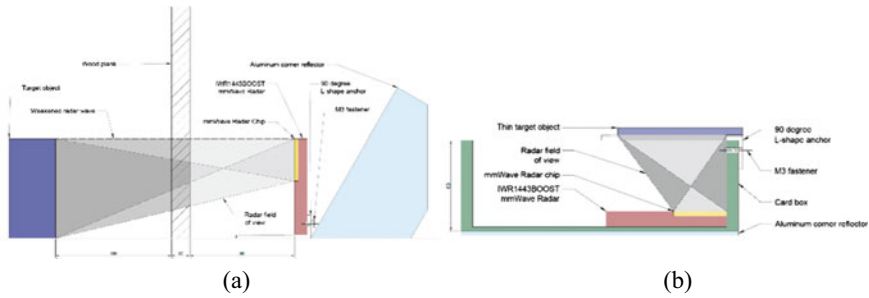


Fig. 8.1 Experiment setup with obstruction to perform **a** standard; **b** thin material classification

received radar signal power from each receiver, measure in dB. IWR1443 is having 63-range-index segmenting the radar field range linearly from 1 to 199 m or any closest wall. All the experiment data is stored into a log file format and uploaded to the GitHub [25] for further data analysis. Artificial neuron network classifier is constructed to perform materials classification with the collected radar signal. Since the complexity of the model is unknown, the neuron network model is started with three major models. This includes basic linear classifier model, fully connected neural network (FCNN) and convolutional neural network (CNN). The detail of each model is listed in Table 8.1.

The selected target objects have the nearest possible appearance to its natural colour. To enumerate, stainless steel is in shiny silver, borosilicate glass is in transparent and wood in clove brown. However, variety of surface roughness, colour or coating may result in different electromagnetic wave absorption which becomes an additional variable in the experiment. Hence, the mmWave radar may not fully capture the intrinsic material properties in relation to radar electromagnetic wave but it captured other factors. A secondary experiment setup shown in Fig. 8.1b is used to evaluate material classification capability on thin objects. These thin materials include a 2 mm thick acrylonitrile butadiene styrene (ABS) material, a 1 mm thick polyethylene low density (LDPE), paper card and polyester cloth. To enhance the consistency of the material classification test, four 3D printed objects with same colour and dimension ($15 \times 15 \times 0.5$ cm) are also used as target object. The printed materials are polylactic acid (PLA) and polyethylene terephthalate glycol (PETG) with the same mechanical density but different percentage of infill (25%, 50%, 75%). Black colour is chosen because black body radiation generally enhances the signal-to-noise ratio [26]. All thin materials face parallel to the mmWave radar chip and fully covered the entire chip. This is to ensure only radar electromagnetic ray is penetrating through the material itself and receive back the material properties. In addition, the target object is designed to have less than or equal to 5 mm of thickness to evaluate the robustness of radar sensor to classify material under very minimal radar wave absorption. Because the thickness of target object is very low, the material properties information received by radar is assumed to be minimal. If the radar sensor and the deep neural network model is inference based on other physical factor, such

Table 8.1 Summary of all models for material classification

Model Type	Linear Classifier	FCNN	CNN
Activation function	Softmax		
Loss function	Categorical cross entropy		
Optimiser	Adam		
Epoch	50		
Input layers	Single array of 63		
Layers			
1	Fully Connected 9—Softmax	Fully Connected 64	1D Convolution 32×64
2	–	Dropout 0.4	Dropout 0.4
3	–	Fully Connected 32	1D Convolution 32×32
4	–	Dropout 0.4	Dropout 0.4
5	–	Fully Connected 9—Softmax	Flatten
6	–	–	Fully Connected 9—Softmax

as dimension or surface shape, material classification task on the second setup will not be accurate.

8.5 Results

The data received by IWR1443BOOST mmWave radar is relative power stored in a single dimension array with size of 63. Figure 8.2 shows the relative power of all 18 classes of material and detecting condition. Dotted line is the relative power under wood plank obstruction, while the solid line is relative power under no obstruction. Generally, when a wood plank obstructing the transmission and reflected radar wave, the overall relative power is lowered (Fig. 8.2).

To study the pattern and relationship of the signal with respect to each material type, the mean and standard deviation of the signal is calculated. Figure 8.3 shows the mean versus standard deviation for 100 samples on each class for both experiment setups. The cluster of each non-obstructed class is relatively clear where materials like cement, stainless steel, aluminium and borosilicate having high distinct segment in the plot. Other material like ABS, wood, PVC foam and TPE elastomer

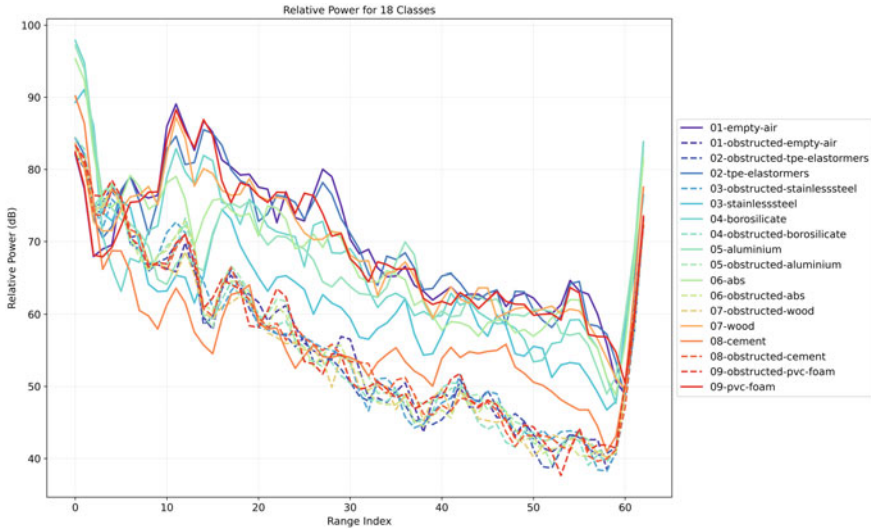


Fig. 8.2 Relative power for eight material classes and empty air under both no obstruction and obstruction sensing condition

have much closer RCS relationship with empty air. In the second experiment setup, the dataset is labelled with prefix of “obstructed”. Generally, when a wood plank obstructing the transmission and reflected radar wave, the overall relative power is lowered. This indicated more radar signal power have been absorbed by the wood plank and less energy received by the radar sensor. In addition, the standard deviation of each obstructed classes is higher than non-obstructed sensing condition. This is aligned with the hypothesis where the obstructing object has deviated from the radar signal, causing additional noise added to the final received signal. Radar waves must propagate through wood plank forward and backward to pass the target’s material properties of target material backward. The overall distribution of all classes under obstruction is relatively less scattering and clustered together. Although distinct mean and standard deviation of each obstructed classes is still visually differentiable, there are more overlapping points between classes compared to non-obstructed. This indicates greater data complexity in obstructed sensing condition.

Table 8.2 shows the validation accuracy of each model under various sensing conditions. When the models are trained and validated on individual non-obstructed and obstructed dataset, all models can achieve more than 98% of average accuracy. When combing both non-obstructed and obstructed dataset together, all models can maintain at high accuracy. However, when models are only trained on non-obstructed dataset and classify on both non-obstructed and obstructed dataset, the accuracy drops significantly. Although a deeper FCNN and CNN model is used, the average validation accuracy is low. In the second experiment, all models achieved 100% of accuracy. This is due to low data complexity and obvious distinct cluster between each class in relative power signal. Although each class does not have exact same amount

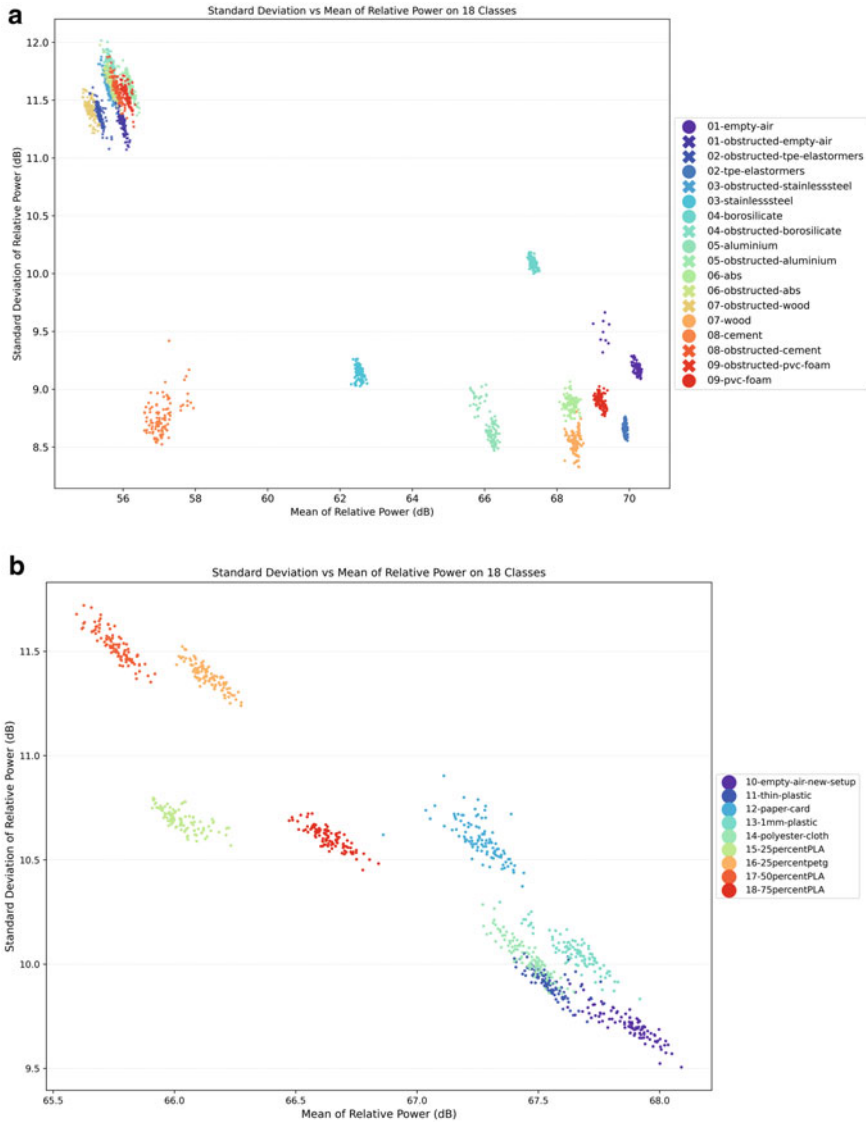


Fig. 8.3 Standard deviation versus mean of relative power for **a** both no obstruction and obstruction sensing condition; **b** thin material classification

of samples, the models remain robust. All 3D-printed parts with same dimension are easily classified by any model showing that mmWave radar is capturing unique object properties.

Table 8.2 Summary validation accuracy on each model for various sensing conditions

Dataset		Non-obstructed (%)	Obstructed (%)	Both combined (%)	Both separate (%)	Thin material (%)
Linear Classifier	K-Fold 1	99.97	100.00	99.87	14.09	100.00
	K-Fold 2	99.92	98.22	99.74	23.78	100.00
	K-Fold 3	99.99	98.26	99.93	20.43	100.00
	<i>Average Accuracy</i>	99.96	98.83	99.85	19.43	100.00
FCNN	K-Fold 1	99.97	100.00	99.90	18.08	100.00
	K-Fold 2	99.42	97.82	99.99	23.45	100.00
	K-Fold 3	99.84	98.17	99.97	18.95	100.00
	<i>Average Accuracy</i>	99.74	98.66	99.95	20.16	100.00
CNN	K-Fold 1	100.00	100.00	100.00	14.34	100.00
	K-Fold 2	100.00	98.40	99.84	24.38	100.00
	K-Fold 3	99.92	98.18	99.81	19.60	100.00
	<i>Average Accuracy</i>	99.97	98.86	99.88	19.44	100.00

8.6 Discussion and Evaluation

The high accuracy on all models when inference on non-obstructed and obstructed dataset is due to low data complexity in relative power. From the mean versus standard deviation plot, this distinction is clear for each class. A simple linear classifier model can handle it even with lower epoch of 10. However, the materials data is relatively simple and all models are able to achieve high accuracy even with lower amount of training time. When implementing onsite, various factors such as environment temperature, changes in targets shape, overlapping with other materials is the challenge of the model. Hence, a more complex model like CNN is still more favourable for industrial usage. This is because CNN captured and generalised the radar signal wave pattern instead of inference individual relative power at each range index. However, CNN has to train with larger and more sophisticated real-life training samples. GAN model can apply to generate simulated samples data, especially when training model to perform prediction on multiple radar system. This is because when inference on multiple radar signal as an input, high chances the relative power value is going to have overlapping or even higher data similarity between targets, hence GAN model help to generalise the inputs pattern. With GAN model, the conventional statistical method to generalise complex inputs is eliminated and this leads to more rapid research as well as radar technology implementation. Although closer cluster on obstructed dataset gives slightly higher data complexity, all models achieve more than 98% accuracy with only 50 epochs of training. As the training epochs doubled, the model accuracy started to drop showing a sign of curve fitting. Hence,

the training is stopped. From the result, linear classifier performs slightly better than FCNN model. This is unexpected and as deeper machine learning model theoretically should perform better than simple linear classifier model. FCNN model's performance is even worse when the epoch increases from 50 to 100. This is likely due to overfitting issues where FCNN model only learned the feature on training dataset and does not generalise to important feature of respective classes. However, this is not fully valid because from repetitive retraining of the model, average FCNN model training accuracy remains lower than linear classifier model. When all dropout nodes are removed from FCNN and CNN model, the accuracy increases, resulting less than 2% of error in validation dataset. CNN models perform slightly better than linear classifier even when training epoch increases. CNN model is even improved by 0.08% when epoch doubled. CNN model shows its robustness in capturing the reflected radar signal and less prone to curve fitting.

From the confusion of all three models, the classes that often have less classification accuracy is class index 6. Class index 6 is often misclassified into class index 7. Class index 6 is borosilicate, and class index 7 is obstruction with borosilicate. This accuracy reduction phenomenon is more significant in training dataset. This may be due to inconsistent data complexity between training and validation. Reviewing the standard deviation versus mean of relative power plot, this phenomenon is unlikely to happen as both classes is having distinct difference in the cluster. When performing data recording, log file of past data is clear first before reloading to new material set. Perhaps, the data is not fully clean and result in some noise in the box with borosilicate dataset. The experiment is recommended to repeat with a new clean dataset by re-record the dataset for both borosilicate and box with borosilicate. It is hypothesised that the performance on all 18 classes should perform with near 100% accuracy on a clean dataset. Regardless of the clean data, mmWave radar sensor is proven capable to perform material classification easily with minimal complexity of neuron network. The accuracy is maintained more than 98% even under both non-obstructed and obstructed sensing condition.

Supposed, when the radar signal is receiving back the material properties information and the model should generalised to identify the signal pattern of respective material. Therefore, all models should well generalise the signal pattern even through a change in the environment including the obstruction. The percentage of obstructed dataset in the validation data is 76.37%, while the non-obstructed dataset is 23.63%. The benchmark accuracy of the model should perform close to 23.63% which only predict correctly for non-obstructed dataset. When the model only train with non-obstructed dataset and classify on both non-obstructed and obstructed dataset, the accuracy drops to 19.43%, 20.16% and 19.44% for linear classifier, FCNN and CNN, respectively. The average validation accuracy remains close to the benchmark accuracy of 23.63% even though a deeper model is trained with higher training epochs. From the confusion matrix shown in Fig. 8.4, it is clear that the model only generalises non-obstructed class but not overall material properties signal. Based on the relative power signal on each class, although the overall signal pattern for non-obstructed and obstructed dataset are visually similar, the intrinsic difference on individual class

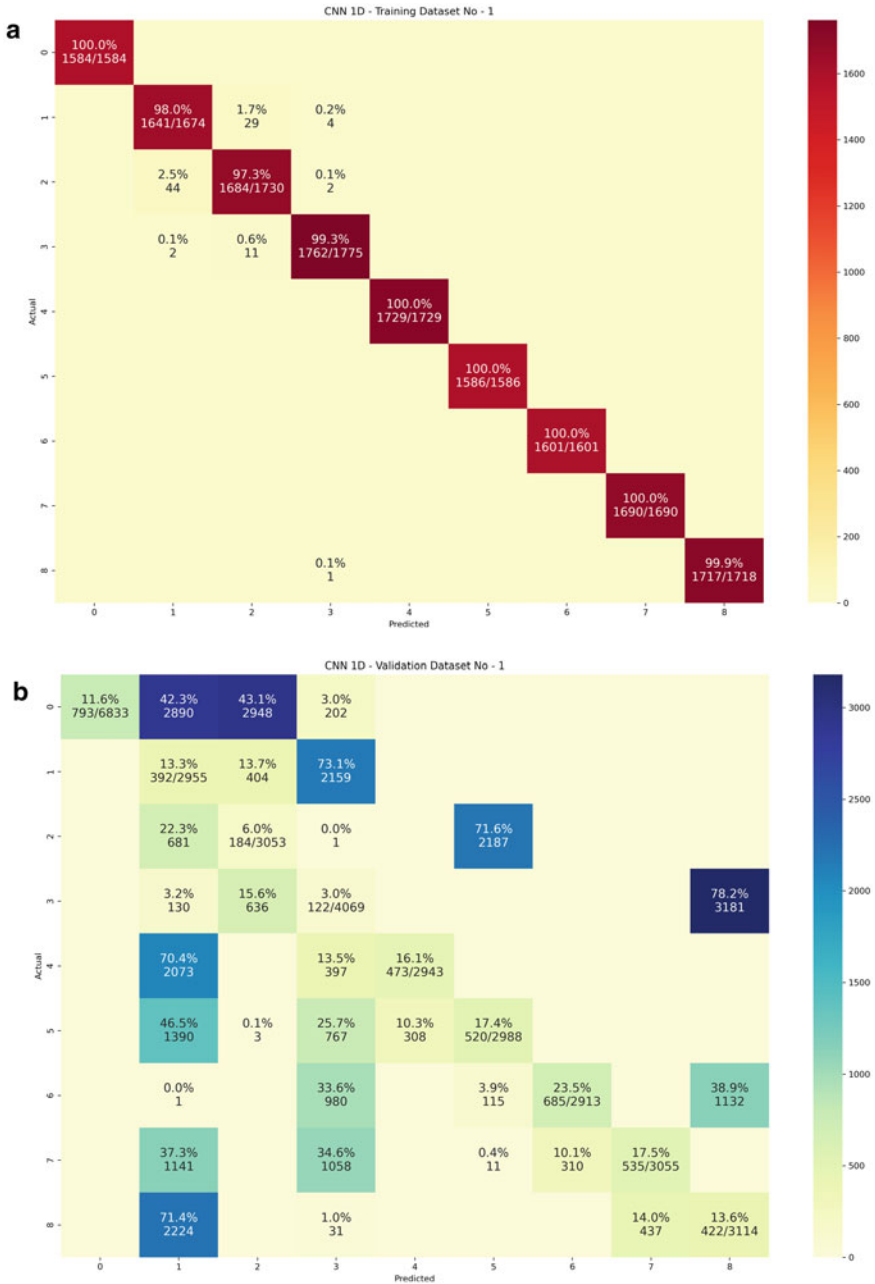


Fig. 8.4 Confusion matrix of 9 combined classes **a** training dataset; **b** validation dataset on CNN model using pure radar signal

is huge different. Due to wood plank obstruction, majority of the material properties signal is minimised and leaving a minimal difference on each class. This is observed from standard deviation versus mean of relative power on each class where all obstructed point has significantly lower mean and highly cluster to each other. Relatively to non-obstructed dataset, there is no clear cluster difference between each class on obstructed dataset. Moreover, the distribution of non-obstructed and obstructed dataset is inspected to have low correlation. Thus, the model cannot be generalised for non-obstructed and obstructed dataset based on only non-obstructed dataset. The engineer has to train the model for both non-obstructed and obstructed dataset in order to achieve high accuracy.

In thin material dataset, the thickness of target object is categorised into two groups. One is below 2 mm which are thin materials such as ABS, paper card, LDPE and polyester, while second is at fix 5 mm thickness which are 3D printed parts with PLA and PETG. The target object thickness is significantly smaller than initial experiment setup, but the mmWave radar is able to capture the unique material properties. Although 3D printed PETG and PLA has the same density and same weight, a unique cluster demonstrated two different group of materials. From Fig. 8.3b, the target objects that have greater thickness and weight are mostly having lower relative power. Targets with greater thickness and dense internal structure tend to have lower relative power as well. This is also emphasised on dataset with 16 mm wood plank obstruction, where all of the data is skewed to lower relative power value. Also, greater thickness and denser internal structure will have higher standard deviation of the relative power. This is because a denser bonding on physical matrix, leads to greater reflection and refraction of radar electromagnetic wave. This results in lesser energy propagate to radar sensor, and more noise-induced. Hence, a higher standard deviation signal commonly representing a thicker and denser physical material. Besides that, thinner material usually has very close cluster with empty air. It is important to note that, air is always having the greatest relative power value as compared to all the other materials. This justified that the received radar signal contains the information of energy absorption by target object within the field of view of radar sensor. Therefore, theoretically, we can conclude mean of relative power is dependent on materials thickness, while the standard deviation of relative power signal determines the density of physical structure.

However, dataset on 75%-infill PLA and polyester cloth does not align with the hypothetical conclusion. Suppose a denser internal structure of 75%-infill PLA should have lower relative power and greater standard deviation as compared to 50%-infill PLA. Also, polyester cloth has physically lower weight and less dense physically structure. The cluster should have higher relative power and closer standard deviation as compared to the thin plastic. Although it is justifiable that 75%-infill PLA has greater radar reflective index due to denser physical structure, this hypothesis does not apply to majority of the dataset. Because the IWR1443 mmWave radar sensor emits electromagnetic wave at frequency of 76–81 GHz, a study of relationship between material properties and electromagnetic wave is conducted. A propagating electromagnetic (EM) wave is carrying oscillation of electric field and magnetic field in transverse direction to each other. When EM wave propagate through an object,

three physical phenomena: reflection, absorption and transmission will occur [27]. The phenomenon of EM wave absorption is a process of energy conversion from EM energy into other form of undergoing due to target objects' material properties. This is the main factor of reduction in received radar signal. The magnitude of EM absorption by target object is measured in reflection loss, RL which is expressed as

$$RL = 20 \log \left| \frac{Z - Z_o}{Z + Z_o} \right| \quad (8.1)$$

$$Z = Z_o \sqrt{\frac{\mu_o \mu_r}{\epsilon_o \epsilon_r}} \tanh \left(i \frac{2\pi f d}{c} \sqrt{\mu_o \mu_r \epsilon_o \epsilon_r} \right) \quad (8.2)$$

where Z , μ_r and ϵ_r are the wave impedance, relative permeability and relative permittivity of the target object, $Z_o = \mu_o/\epsilon_o$, μ_o and ϵ_o are the wave impedance, permeability and permittivity of free space, respectively; f is the frequency; c is the propagation velocity of the wave in free space; and d is the thickness of target object [28]. From the reflection loss equation, evidently, the factors that determine the received radar signal are the wave impedance of the materials. The wave impedance is further influence by the ratio of electric permeability and magnetic permittivity which theoretically is material dependence. The exact value of specific object's permeability and permittivity is further affected by atomic and molecular structure. Conventionally, permeability and permittivity of target object have to be measured through specific laboratory setup. Although the same materials, different micro-physical structure, dimension and surface morphology is potentially deviate the permeability and permittivity value. External factors such as humidity, temperature, position of target object in the medium, and EM wave frequency applied are also needed to consider when measuring the permeability and permittivity value. According to relative loss formula, it is clear that the thickness, d and frequency, f of propagate EM wave is the variables to calculate the impedance. Therefore, the received relative power value on mmWave radar is influenced by permeability, permittivity, thickness of target object as well as the frequency of incident EM wave.

Measuring the wave impedance and studying of the molecular structure in relation to the electron and intermolecular force of each respective materials is beyond the scope of the research. However, from the equation of wave impedance, theoretically all frequency spectrum of EM wave can be used for material classification. As long as the incident EM wave has sufficient energy to transmit from sensor to target object and reflect back portion of unabsorbed EM wave, the material properties of the target can easily classify. When adopting the capability of material classification using mmWave radar, advance study on spectroscopy of desire target material especially in a function of mmWave radar wavelength and frequency is needed. In summary, the result and performance is aligned with RadarCat and other past research [14, 15, 20]. Although theoretically, it is potentially having different materials but close relative permeability and permittivity value, material classification task remain very acceptable for industrial application. This is due to the model only need to generalise

on desire items in the fixed environment like warehouse or specific manufactured product.

8.7 Conclusions

A large number of reproducible accurate and highly consistent results have proven mmWave radar sensor can capture material properties and work seamlessly with neural network in performing multi-material classification. A series of reliable and promising experiment result shows that mmWave radar remains robust in multi-material classification even with a 16 mm wood plank obstructing in between radar sensor and target object. Various thin (<5 mm) materials also are classified well with mmWave radar. This concluded that the reflected mmWave radar signal does not solely contain the physical appearance of target object but also the specific radar electromagnetic (EM) wave material properties. It is important to note that the relative power received by IWR1443BOOST mmWave radar sensor is a measure of the amount of radar energy reflected by target object. The radar EM wave that is radiated is absorpt and reflected back from the target object which is influenced by relative magnetic wave permeability and electric wave permittivity. Target object's relative permeability and permittivity are influenced by the thickness parallel to the EM wave propagation. From the study of spectroscopy, the relative permeability and permittivity are a measure of material properties in reaction to specific EM wave. Thus, it is concluded that theoretically it is feasible to use mmWave radar sensor to perform material classification for industrial application. The result as well as the performance is aligned with RadarCat and other past research [14, 15, 20]. Additionally, all deep neural network models can well generalise any type of experiment setup. Convolution neural network (CNN) is proven to have the most robust classification performance and immune towards noise in radar signal. However, linear classifier is easier to achieve satisfactory accuracy. While fully connected neural network (FCNN) shows balanced in performance and noise immunity while maintaining at high inference rate. From the mean and standard deviation plot of relative power signal, it shows the radar signal is dimensionally simple to classify. This results in high accuracy performance on all model even under low number of epochs.

8.8 Future Work

Future work should explore harsher environment sensing which include multiple obstructing material type and various obstructed material thickness. Besides that, different materials but similar relative permeability and permittivity as well as the physical geometry should use to validate the theoretical assumption on spectroscopy study. It is hypothesised that, this experiment may not successful because the received radar signal will highly close to each other. A deeper CNN should develop to capture

the hidden feature in the radar signal. Moreover, liquid material classification for drug industry is another potential work. This potentially reduced amount of time needed for chemical classification process. Scalability of the experiment is another issue that needed to be tackled. As the environment, experiment setup and other fixed variable changes, performance of radar sensor may not generalise and not reproducible by other researcher. Thus, a more standardised experiment setup has to develop to continue leverage the benefit of mmWave radar. As the radar capture unique material, it is potential alternative quality inspection sensor to identify good or defective product. It is assumed that objects with internal crack or huge porosity will have significantly large difference in radar signal compared to solid object even though the surface appearance is the same. Finally, object segmentation task with mmWave radar can explore to leverage the capability of material classification for a packed container. Perhaps, multiple radar sensor at various propagation angles can explore to improve the resolution of received signal.

Acknowledgements The authors wish to thank Phoong Stanley of Intel Corporation for supporting in the experiment.

References

1. Zhang, J., Feng, T., Yan, F., Qiao, S., Wang, X.: Analysis and design on intervehicle distance control of autonomous vehicle platoons. *ISA Trans.* **100**, 446–453 (2020). <https://doi.org/10.1016/J.ISATRA.2019.12.007>
2. Karimi Pour, F., Theilliol, D., Puig, V., Cembrano, G.: Health-aware control design based on remaining useful life estimation for autonomous racing vehicle. *ISA Trans.* **113**, 196–209. <https://doi.org/10.1016/J.ISATRA.2020.03.032>
3. Garnett, J.: The role of military power. In: *Contemporary Strategy*, pp. 50–64, Jan 2021. <https://doi.org/10.4324/9781003104339-4>
4. Zhong, R.Y., Xu, X., Klotz, E., Newman, S.T.: Intelligent manufacturing in the context of industry 4.0: a review. *Engineering* **3**(5), 616–630 (2017). <https://doi.org/10.1016/J.ENG.2017.05.015>
5. Züfle, M., Moog, F., Lesch, V., Krupitzer, C., Kounev, S.: A machine learning-based workflow for automatic detection of anomalies in machine tools. *ISA Trans.* (2021). <https://doi.org/10.1016/J.ISATRA.2021.07.010>
6. Peng, Z., et al.: A Portable FMCW interferometry radar with programmable low-IF architecture for localization, ISAR imaging, and vital sign tracking. *IEEE Trans. Microw. Theory Tech.* **65**(4), 1334–1344 (2017). <https://doi.org/10.1109/TMTT.2016.2633352>
7. Purvis, J.R., Al-Khalifa, A.: Artificial intelligence: can it be economically applied? *ISA Trans.* **28**(1), 59–71 (1989). [https://doi.org/10.1016/0019-0578\(89\)90058-X](https://doi.org/10.1016/0019-0578(89)90058-X)
8. Kumar, S.: Industrial robotics market forecast, trends to 2020, May 2015. https://www.researchgate.net/publication/275964852_Industrial_Robotics_Market_Forecast_Trends_To_2020. Accessed 26 Apr 2021
9. Barrett, D., Alvarez, A.: mmWave radar sensors in robotics applications, 2017. Accessed: 25 Apr 2021. [Online]. Available: <https://www.ti.com/lit/pdf/spry311>
10. Charvat, G.L.: *Small and short-range radar systems*. CRC Press (2014)
11. Barrett, D., Wang, D., Ahmad, A., Mahimkar, V.: Using mmWave sensors to enhance drone safety and productivity. Accessed: 26 Apr 2021. [Online]. Available: <http://www.electronicdesign.com>

12. Peng, Z., Li, C.: A 24-GHz portable FMCW radar with continuous beam steering phased array (Conference Presentation). In: Radar Sensor Technology XXI, vol. 10188, p. 41, Jun 2017. <https://doi.org/10.1117/12.2257324>
13. Koch, G.: Siamese neural networks for one-shot image recognition (2015)
14. Weis, J., Santra, A.: One-shot learning for robust material classification using millimeter-wave radar system. *IEEE Sens. Lett.* **2**(4), 1–4 (2018). <https://doi.org/10.1109/lSENS.2018.2878041>
15. Yeo, H.S., Flamich, G., Schrempf, P., Harris-Birtill, D., Quigley, A.: RadarCat: radar categorization for input & interaction. In: UIST 2016—Proceedings of the 29th Annual Symposium on User Interface Software and Technology, pp. 833–841, Oct 2016. <https://doi.org/10.1145/2984511.2984515>
16. Online, V.A., et al.: Recent advances on the electromagnetic wave absorption properties of Ni based materials. *Eng. Sci. Publ.* **3**(23), 5–40 (2018). <https://doi.org/10.30919/es8d735>
17. Yeo, H.-S., Minami, R., Rodriguez, K., Shaker, G., Quigley, A.: Exploring tangible interactions with radar sensing. *Proc. ACM Interact., Mobile, Wearable Ubiquit. Technol.* **2**(4), 1–25 (2018). <https://doi.org/10.1145/3287078>
18. Scientific brief: Modes of transmission of virus causing COVID-19: implications for IPC precaution recommendations. World Health Organization, 29 Mar 2020. <https://www.who.int/news-room/commentaries/detail/modes-of-transmission-of-virus-causing-covid-19-implications-for-ipc-precaution-recommendations>. Accessed 29 Apr 2021
19. Wu, C., Zhang, F., Wang, B., Liu, K.J.R.: MSense: towards mobile material sensing with a single millimeter-wave radio. *Proc. ACM Interact. Mobile Wearable Ubiquit. Technol.* **4**(3), 1–20 (2020). <https://doi.org/10.1145/3411822>
20. Jamali, B., Ramalingam, D., Babakhani, A.: Intelligent material classification and identification using a broadband millimeter-wave frequency comb receiver. *IEEE Sensors Lett.* **4**(7) (2020). <https://doi.org/10.1109/LSENS.2020.3002715>
21. IWR1443BOOST Evaluation board|TI.com: Texas Instruments (2021). <https://www.ti.com/tool/IWR1443BOOST#description>. Accessed 20 Oct 2021
22. Stratified K-Fold: Scikit Learn Documentation (2021). https://scikit-learn.org/stable/modules/generated/sklearn.model_selection.StratifiedKFold.html. Accessed 11 Nov 2021
23. Ebenezer, R.H.P.I.: Is there a rule of thumb that explains the splitting of a limited dataset into two-three subsets? 06 Nov 2015. <https://www.researchgate.net/post/Is-there-a-rule-of-thumb-that-explains-the-splitting-of-a-limited-dataset-into-two-three-subsets>. Accessed 20 May 2021
24. IWR1443: Texas Instruments (2021). <https://www.ti.com/product/IWR1443>. Accessed 06 Oct 2021
25. leopck: GitHub—leopck/iwr1443-material-dataset. Github, 05 Sep 2021. <https://github.com/leopck/iwr1443-material-dataset>. Accessed 06 Oct 2021
26. Gallagher, T.F., Cooke, W.E.: Interactions of blackbody radiation with atoms. *Phys. Rev. Lett.* **42**(13), 835 (1979). <https://doi.org/10.1103/PhysRevLett.42.835>
27. Huo, J., Wang, L., Yu, H.: Polymeric nanocomposites for electromagnetic wave absorption. *J. Mater. Sci.* 2009 4415, **44**(15), 3917–3927 (2009). <https://doi.org/10.1007/S10853-009-3561-1>
28. Xie, S., et al.: Recent progress in electromagnetic wave absorption building materials. *J. Build. Eng.* **27**, 100963 (2020). <https://doi.org/10.1016/J.JOBE.2019.100963>

Chapter 9

Modeling and Simulation of Plain and Corrugated Shell and Tube Heat Exchanger



A. Bora, A. P. Kalita, M. Bardalai, and Partha P. Dutta

Abstract In this paper, the shell and tube heat exchanger is analyzed with ANSYS Fluid Flow (Fluent), where the shell contains of tubes inside it. The hot water flows through the tubes and cold water flows through the shell side. The heat transfer, velocity, temperature, pressure, and streamline flow of the fluid are analyzed in this study. The analysis is undertaken for (a) single shell and tube heat exchanger (b) single shell and tube heat exchanger using a corrugated tube. The experimental study shows that the temperature drop (ΔT) and pressure drop (ΔP) of the heat exchanger in the tube side for counterflow is more than parallel flow configuration in both plain and corrugated pipes. Moreover, the corrugated pipe has approximately 6 K more temperature drop in the tube side than the plain pipe heat exchanger model. Consequently, the pressure drop in corrugated heat exchanger is 37.5 times more than that of the plain pipe heat exchanger. The results suggest that with increase of mass flow rates, the temperature difference between the inlet and the outlet of the pipe decreases. The variation of temperature in the shell and tube sides of the heat exchanger is found to be higher in case of few baffles are used as compared to no baffle conditions.

9.1 Introduction

A heat exchanger is a device that is used to transfer thermal energy (enthalpy) between two or more fluids, between a solid surface and a fluid, or between solid particulates and a fluid, at different temperatures and in thermal contact. The fluids are at different temperatures, and the one at higher temperature is known as hot fluid and another fluid is known as cold fluid. In most heat exchangers, heat transfer between fluids takes place through a separating wall or into and out of a wall in a transient manner. The most commonly used type of them is the shell and tube heat exchangers. To increase the performance of this equipment, baffles are used. With these components, the flow direction can be guided, the whole heat transfer area is involved in the heat transfer

A. Bora · A. P. Kalita · M. Bardalai (✉) · P. P. Dutta
Tezpur University, Assam, India
e-mail: monojb@tezu.ernet.in

and due to the decreased flow section, the velocities and the turbulence become higher, and this increased value causes a higher heat transfer coefficient and heat performance.

A wide range of research has been done over the years on the analysis of shell and tube heat exchangers and how to enhance the overall effectiveness and the heat transfer rate using different methods such as enhanced surfaces, tube deformation, using baffles, finning, tube inserts, augmentation, and enhancement of fouling or using nanofluids. Following are some noteworthy breakthrough researches by various researchers.

A model size shell and tube heat exchanger with horizontal baffles is investigated numerically and compared to the measured values using the commercial software SC-Tetra V11 by Petrik and Szepesi [1]. Determination of the heat transfer coefficients for the shell side depends on the type of the flow and the type of the baffles. Without baffles, the shell side medium leaves in the shortest way and dead zones are formed. With the usage of these baffles, the flow path is artificially formed and the flow velocity is increased because of the decreased flow area. These two effects cause a better heat transfer; however, on the other hand, this increases the weight of the heat exchanger. There are very simple experimental correlations for the segment and disk and donut types baffles.

In the paper authored by Aswin and Mohan [2], the shell tube heat exchanger is analyzed with ANSYS, where the shell contains of tubes inside it and hot water flows through it and cold water flows through the outer pathway of the tube on the shell. The heat transfer, velocity, and streamline flow of the fluid are analyzed in this paper. The analysis was undertaken for two various shell tube heat exchangers. The various shell tube heat exchangers are (a) shell tube heat exchanger without baffle (b) shell tube heat exchangers with baffles. Shell tube heat exchanger without baffle is the heat exchanger where a normal shell is proceeded to the analysis, and the result is extracted. Another review focuses on the various researches of CFD analysis in the field of heat exchanger carried out by Patel et al. [3].

Charate et al. [4] performed a broad discussion on the enhancement of heat transfer through heat exchangers. The use of process integration in heat transfer enhancement has many benefits. Firstly, enhanced heat exchangers require less heat transfer area for a given heat duty because of higher heat transfer coefficients. Also, the nanofluid possesses immense potential to improve heat transfer and energy efficiency in heat exchangers. Finally, the following enhancements in geometries are discussed: tube inserts, tube deformation, baffles, and finning. Mohanty et al. [5] studied a comprehensive approach in detail in order to analyze the effectiveness of the shell and tube heat exchanger with 50% baffle cuts (BC) with varying number of baffles. CFD simulations were conducted on a single pass and single tube heat exchanger using water as working fluid. A counterflow technique was implemented for this simulation study.

This study carried out by Prasad et al. [6] presented the application of differential evolution (DE) for the optimal design of shell and tube heat exchangers. The main objective in any heat exchanger design is the estimation of the minimum heat transfer area required for a given heat duty, as it governs the overall cost of the heat exchanger. Dhoria et al. [7] used ANSYS FLUENT 17.1 software and performed theoretical

calculations to analyze the temperature drops as a function of both inlet velocity and inlet temperature and investigated how these varied with the other. Each heat exchanger model was designed and simulated for both parallel flow and counterflow heat exchanger models. The results were compared between parallel and counterflow heat exchangers. CFD analysis was utilized to find the outlet temperatures of parallel and counterflow heat exchangers for the inlet velocity and inlet temperature of the fluid medium used. Similar type of simulation and modeling was also found in some other papers also [8, 9].

Judging and analyzing all the previous studies, it is found that most of the papers focused on improving the performance and effectiveness of the heat exchangers using different models and techniques. However, a graphical approach in the analysis of heat exchangers seems missing in most of the studies. Therefore, in this report we have attempted to analyze the shell and tube heat exchanger with a graphical approach for different trends (temperature, pressure, and mass flow rates of the fluids). This study mainly includes the modeling of plain and corrugated heat exchanger and comparative study on parallel and counterflow arrangement.

9.2 Methodology

The log mean temperature difference for both parallel and counterflow configurations in the shell and tube heat exchangers is denoted in Formulas (9.1) and (9.2), respectively [10, 11].

$$\Delta T_{lm,parallel} = \frac{(T_{h,i} - T_{c,i}) - (T_{h,o} - T_{c,o})}{\ln\left(\frac{T_{h,i} - T_{c,i}}{T_{h,o} - T_{c,o}}\right)} \tag{9.1}$$

$$\Delta T_{lm,counter} = \frac{(T_{h,i} - T_{c,o}) - (T_{h,o} - T_{c,i})}{\ln\left(\frac{T_{h,i} - T_{c,o}}{T_{h,o} - T_{c,i}}\right)} = \frac{\Delta T_L - \Delta T_S}{\ln\left(\frac{\Delta T_L}{\Delta T_S}\right)} \tag{9.2}$$

The rate of heat transfer in a heat exchanger is given by following Eqs. 9.3–9.4

$$Q = UA\Delta T_{lm} \tag{9.3}$$

$$\frac{1}{UA} = \frac{1}{h_h A_h} + \frac{1}{h_c A_c} \tag{9.4}$$

9.2.1 Governing Equations

In order to carry out the CFD simulation in ANSYS, the governing equations used for conservation of mass, momentum, and energy for incompressible fluid are presented in the following equations (Eqs. 9.5–9.7).

Mass conservation equation

$$\frac{\partial \rho}{\partial t} + \nabla \cdot (\rho \bar{V}) = 0 \quad (9.5)$$

Momentum conservation equation

$$\frac{\partial u}{\partial t} = -(u \cdot \nabla)u + \nabla \cdot (\vartheta \nabla u) - \frac{1}{\rho} \nabla p + f \quad (9.6)$$

where ϑ is kinematic viscosity, ρ is density, and f is the external force.

Energy conservation equation

$$\nabla \cdot (\rho e v) = -p \nabla \cdot V + \nabla \cdot (k \nabla T) + q + \varphi \quad (9.7)$$

where φ is the dissipated heat.

9.2.2 Modeling

Modeling of single tube heat exchanger (STHE). The model of the single tube heat exchanger designed in ANSYS Design Modeler is illustrated in Fig. 9.1. The dimensions of the components used in this model are as follows:

The components used in the model have the following specifications:

- Shell diameter (D): 45 mm
- Shell opening diameter (d): 30 mm
- Tube inside diameter (d_i): 20 mm
- Tube outside diameter (d_o): 22 mm
- Length of the shell (l_s): 150 mm
- Length of the tube (l_t): 200 mm
- Number of tubes (N_t): 1
- Number of shells (N_s): 1
- Initial temperature at tube inlet (T_{ti}): 300 K
- Initial temperature at shell inlet (T_{si}): 373 K
- Initial mass flow rate of hot water (m_h): 5.6 kg/s
- Initial mass flow rate of cold water (m_c): 1.2 kg/s
- Initial gauge pressure at both inlets: 500 Pa

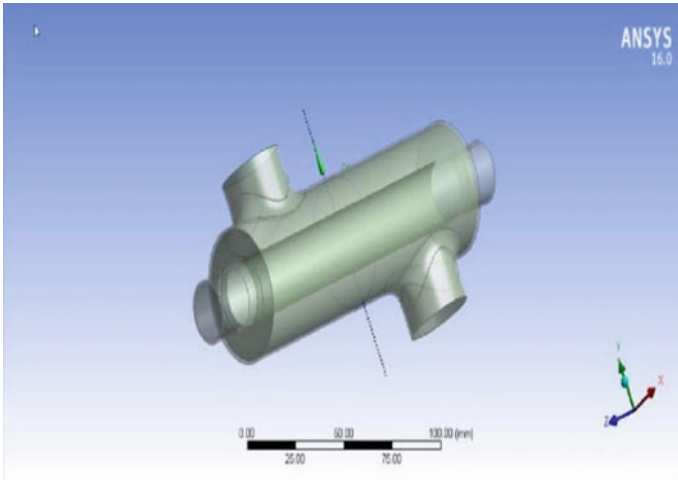


Fig. 9.1 Single tube heat exchanger

Modeling of corrugated tube heat exchanger (CTHE). The model of the corrugated tube heat exchanger designed in ANSYS Design Modeler is illustrated in Fig. 9.2. The components used in this model are considered to have the following specifications:

- Shell diameter (D): 45 mm
- Shell opening diameter (d): 30 mm
- Tube inside diameter (d_i): 20 mm

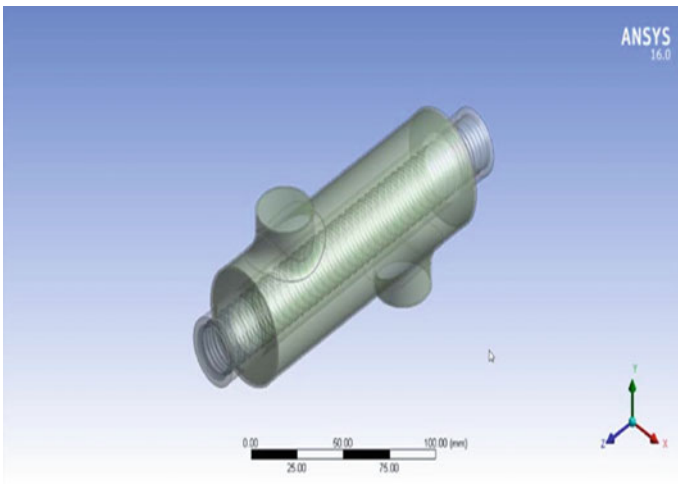


Fig. 9.2 Corrugated tube heat exchanger (CTHE)

- Tube outside diameter (d_o): 22 mm
- Length of the shell (l_s): 150 mm
- Length of the tube (l_t): 200 mm
- Number of tubes (N_t): 1
- Number of shells (N_s): 1
- Initial temperature at tube inlet (T_{ti}): 300 K
- Initial temperature at shell inlet (T_{si}): 373 K
- Initial mass flow rate of hot water (m_h): 1.2 kg/s
- Initial mass flow rate of cold water (m_c): 5.6 kg/s
- Initial gauge pressure at both inlets: 500 Pa

Modeling of straight tube heat exchanger with baffles. The model of the straight tube heat exchanger (with baffles) designed in ANSYS Design Modeler is illustrated in Fig. 9.3. Fluid used in running the simulation of all the models mentioned above is liquid water. The dimensions used in this model are as follows:

- Shell diameter (D): 200 mm
- Tube inside diameter (d_i): 49.5 mm
- Baffle cut: 50%
- Distance between the inlet and first baffle: 125 mm
- Distance between the outlet and last baffle: 125 mm

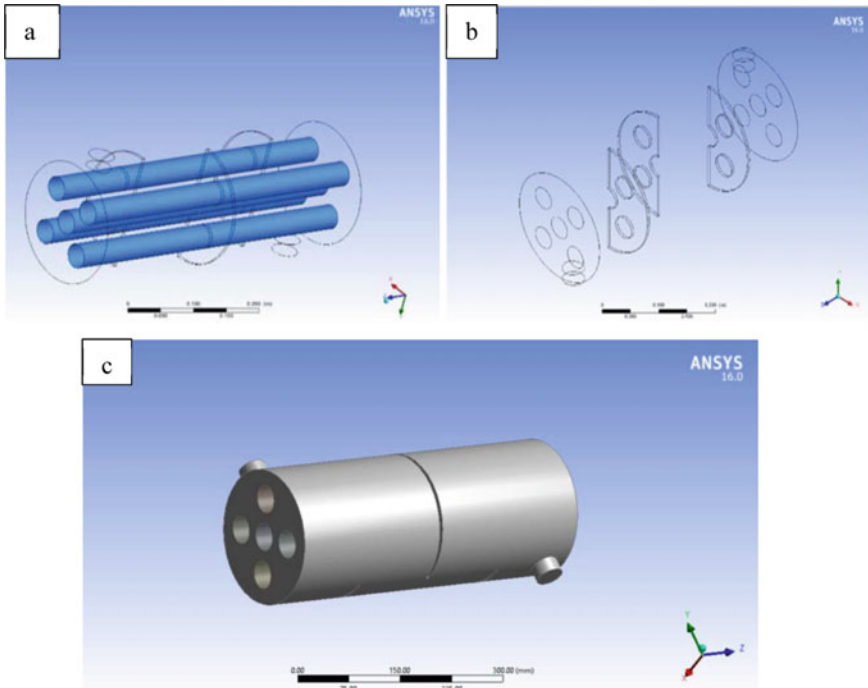


Fig. 9.3 Models of **a** tubes; **b** baffles; **c** straight tube heat exchanger (with baffles)

- Number of tubes (N_t): 5
- Number of shells (N_s): 1
- Baffle spacing: 125 mm
- Tube diameter (d): 40 mm

9.3 Results and Discussion

9.3.1 Straight Tube Heat Exchanger

The temperature variation along the pipe length in tube side of the heat exchanger is shown in Fig. 9.4, and the temperature variation in shell side is shown in Fig. 9.5 for both parallel and counterflow configurations. In Fig. 9.4, we find that the temperature drop of the tube side fluid is more in counterflow configuration than in parallel flow configuration. Since the simulation is done in miniature models, the temperature

Fig. 9.4 Variation of temperature in the tube side

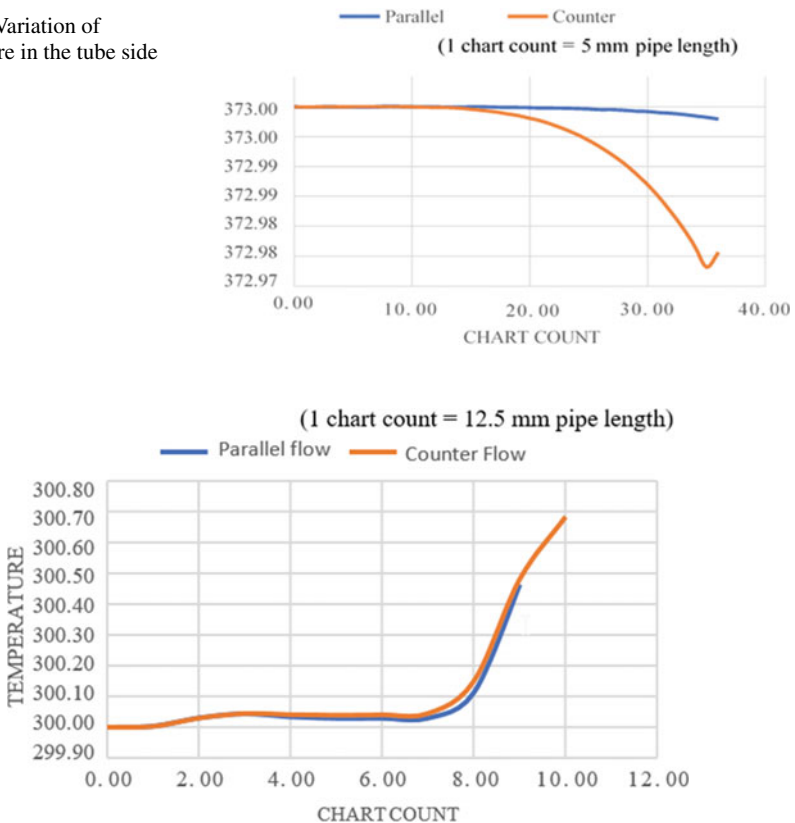


Fig. 9.5 Variation of temperature in the shell side

drop is infinitesimally small. In Fig. 9.5, we find that the temperature rise in the shell side fluid is again more in counterflow than in parallel flow configuration. These charts are obtained considering a single streamline in the flow domain for simplicity. Hence, the very small amount of temperature difference. If we go on increasing the streamlines the temperature difference between the inlet and the outlet ends of the pipe will go on increasing simultaneously.

The variation of pressure and pressure drop in the tube side along the length of the exchanger linearly decreases both for parallel flow and counterflow (Refer Fig. 9.6a, b). However, the rate of decreasing is lower in case of counterflow as compared to parallel flow. Similarly, the pressure and pressure drop variation along the pipe length in shell side of the heat exchanger is shown in Fig. 9.7a, b which reveals the similar trend for both parallel and counterflow.

The temperature variation in tube and shell side is shown in Fig. 9.8a, b for both parallel and counterflow configurations at different mass flow rates. In the tube side, temperature drop is found to be more at higher mass flow rate. On the other hand, in the shell side fluid, mass flow rate does not have any effect upto the length more than

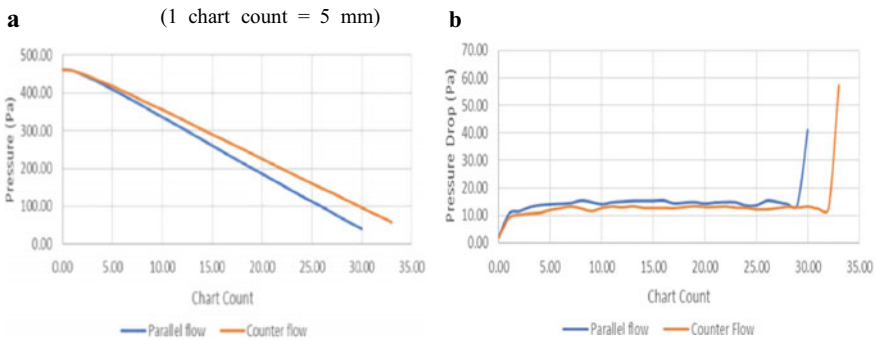


Fig. 9.6 Variation of a pressure and b pressure drop in the tube side

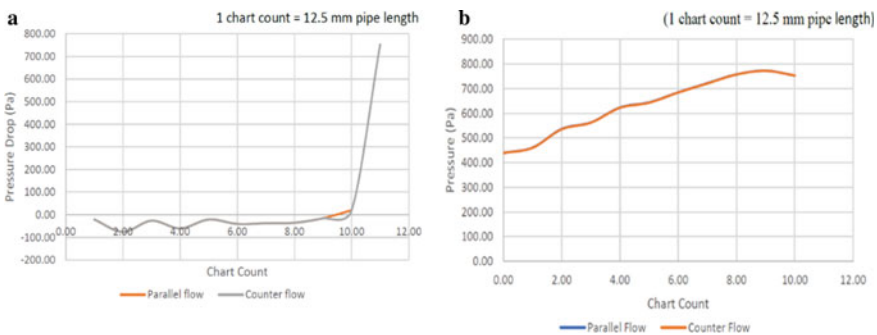


Fig. 9.7 Variation of a pressure and, b pressure drop in the shell side

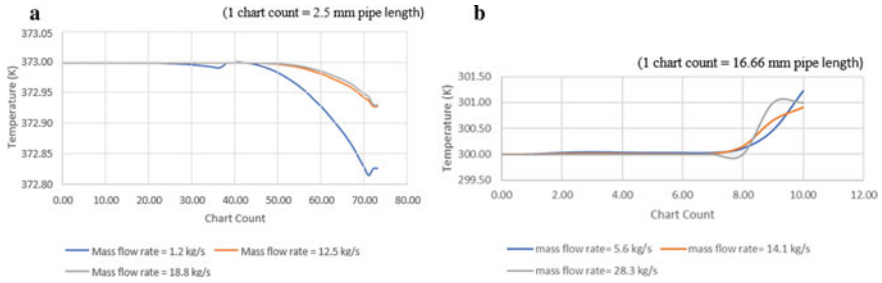


Fig. 9.8 Temperature variation in **a** tube side and, **b** shell side

half of the exchanger. However, mass flow rate influences the rise on temperature beyond certain length of the exchanger as shown in Fig. 9.8b.

9.3.2 Corrugated Heat Exchanger

The temperature variation along the pipe length in tube side and shell side of the heat exchanger is shown in Fig. 9.9a and in Fig. 9.10b, respectively, for parallel flow configuration. The temperature drop in the corrugated pipe is higher (about 7 °C) than the plain pipe which is due to more heat transfer as the result of corrugation. The shell side temperature variation is shown in Fig. 9b which is significant at the end of the exchanger.

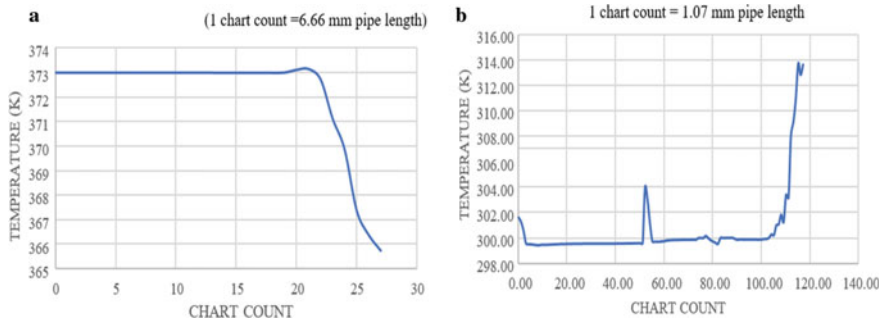


Fig. 9.9 Temperature variation in **a** tube side and, **b** shell side in corrugated pipe for corrugated heat exchanger

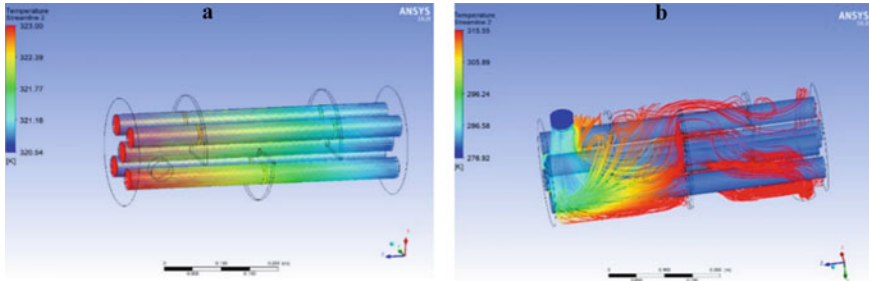


Fig. 9.10 Temperature profiles in **a** tube side and **b** shell side fluids with baffles

9.3.3 Straight Tube Heat Exchanger with Baffles

Few single-segmented baffles were applied across the length of the exchanger as seen in Fig. 9.10a. It is seen that the streamlines of the fluids in all five tubes changing its color from inlet to the outlet. At the inlet portion, the color of the streamlines is found to be reddish which gradually changes to greenish at the middle and finally becomes bluish at the outlet. This reveals that the temperature of the tube side fluid has reduced from 322.39 to 320.54 K which is about 0.57% and relatively higher than the exchanger without baffles. The streamlines in the shell side fluids as seen in Fig. 9.10b change the color from bluish shade in the inlet end to reddish shades at the outlet. This indicates that the temperature of the shell side fluid increases when it comes in contact with the tubes which is estimated at about 10.5% and much higher when there is no baffles.

9.4 Conclusion

In this work, two types of heat exchangers are modeled and studied the performance for parallel and counterflow arrangements. We have obtained results in the form of charts, streamlines and by theoretical calculations. Based on the study, the following conclusions can be drawn:

- In the shell side fluid, the temperature profile is just alike except that the temperature difference in case of counterflow is more.
- The results that we have obtained suggest that with increase of mass flow rates, the temperature difference between the inlet and the outlet of the pipe decreases and thus the rate of heat energy increases.
- The temperature drop for the parallel flow in the corrugated type heat exchanger is almost 6 K more than that of the plain pipe heat exchanger. This result supports the fact that heat exchange is more in a corrugated than in plain heat exchanger.
- The temperature rise in the shell side fluid of corrugated heat exchanger is 20 K which is much greater than plain pipe shell side fluid.

- The variation of temperature in both tube and shell sides is relatively higher when baffles are used than without baffles.

References

1. Petrik, M., Szepesi, G L.: Shell side CFD analysis of a model shell-and-tube heat exchanger. *Chem. Eng. Trans.* **70**, 313–318 (2018)
2. Aswin, P.S., Mohan, A.: CFD analysis of shell tube heat exchanger with and without baffles. *Int Res J Eng Technol* **08**(01), 1302–1307 (2021)
3. Patel, D.S., Parmar, R.R., Prajapati, V.M.: CFD analysis of shell and tube heat exchangers—a review. *Int. Res. J. Eng. Technol.* **02**(09) (2015)
4. Charate, T., Awate, N., Badgujar, J., Jadhav, S.: Review of literature on heat transfer enhancement in heat exchangers. *Int. J. Sci. Eng. Res.* **06**(12) (2015)
5. Mohanty, S., Arora, R.: CFD analysis of a shell and tube heat exchanger with single segmental baffles. *India Int. J. Automot. Mech. Eng.* **17**(02) (2020)
6. Prasad, A.K., Anand, K.: Design & analysis of shell & tube type heat exchanger. *Int. J. Eng. Res. Technol.* **09**(01) (2020)
7. Dhoria, S.H., Kumar, E.M., Yeswanth, I.V.S., Jayanti, L.: CFD analysis on concentric tube heat exchanger in parallel and counter flow direction. *J. Eng. Res. Appl.* **08**(06) (2018)
8. Ghandouri, I. EL., Maakoul, A. EL., Mezaine, M., Choab, N., Naim, Y., Saadeddine, S.: Numerical study of shell and tube heat exchangers with different baffle cuts. In: 6th International Renewable and Sustainable Energy Conference (IRSEC). IEEE (2018)
9. Ali Abd, A., Kareem, M.Q., Naji, S. Z.: Performance analysis of shell and tube heat exchanger: parametric study. *Case Stud. Thermal Eng.* **12** (2018)
10. Shah, R.K., Sekulic, D.P.: *Fundamentals of Heat Exchanger Design*. Wiley, USA (2003)
11. Bergman, T.L., Lavine, A.S., Incropera, F.P., DeWitt, D.P.: *Fundamentals of Heat and Mass Transfer*, 6th edn. Wiley, USA (2007)

Chapter 10

Computational Fluid Dynamics Analysis of Wind Turbine Blades at Various Angles of Attack



Nabanikha Das, Amir Sohail, Rajesh Doley, and Shikha Bhuyan

Abstract The airfoil blades have significant impact on the aerodynamic efficiency of the wind turbine. In this regard, the current work focuses on the investigation of wind turbine-based airfoil blade profiles at different wind velocities and angle of attacks. In this paper, CFD analysis is carried out using Ansys Fluent to select the most suitable blade geometry for use in the wind rotors. For the current simulation, three NACA airfoils, namely NACA 2412, NACA 4412, and NACA 0012, are selected, and with this, the computed results are validated with the existing experimental results. With the validated CFD method, the different values of drag coefficients and lift coefficients have been calculated for the above-mentioned airfoils at various wind velocities and angles of attack. From the CFD analysis that is carried out, it can be concluded that NACA 4412 provides the maximum lift and drag making it suitable for the use in rotors as compared to the other blade profiles selected in our study.

10.1 Introduction

In a very recent time, there is a huge demand in the research area of renewable energies and investigation on wind energy has taken a new birth during this course of time. However, in general the wind turbine still suffers from lower efficiencies when it comes to the design prospects and demands in-depth research in this section. In order to extract much of the benefits from this horizon of renewable energy, researchers concentrated on effective blade geometry design.

In this regard, many researches are being done. Elsakka et al. [1] computationally analyzed the angle of attack for vertical axis wind turbine blade. The work proposed an accurate method of calculating constantly changing angle of attack (AOA). It was discovered that utilizing the flow information from the two reference focuses at the areas 0.5 airfoil chord length upstream and 1 chord away from each side of the airfoil can give the most precise assessment across a scope of tried AOAs. In view of the proposed AOA assessment strategy, the presentation of a decent pitch and the

N. Das · A. Sohail · R. Doley · S. Bhuyan (✉)
Department of Mechanical Engineering, Tezpur University, Tezpur, Assam, India
e-mail: shikha5@tezu.ernet.in

sinusoidal variable pitch vertical axis wind turbine (VAWT) designs are broken down and contrasted and one another. Small-scale wind turbine's blade airfoil size effects were investigated by Yossri et al. [2]. Study on combination of four airfoils, namely NACA0012, NACA 4412, NACA 0015, and NACA 4415, at three different rotor diameter sizes are made. The 2D analysis shows that out of all blade profiles NACA 4412 outperforms well and yields the highest lift to drag ratio at a freestream velocity of 4 m/s. Different methods of determining the angle of attack on wind turbine blades were evaluated by Rahimi et al. [3]. The results obtained by the authors show that the assessed strategies are in acceptable concurrence with one another at the mid-range except few deviations at the root and tip regions of the blade which are minor ones. A rotation improvement study was made by Sun et al. [4] for VAWT by offsetting pitching angles and changing blade numbers. The examination of the flow field of the turbine showed that the counterbalancing blade number and pitching point could postpone the vortex partition, and accordingly work on the general exhibition of the turbine.

After the extensive literature review and utilizing the Computational Fluid Dynamics (CFD) programming "ANSYS," the three airfoils in particular NACA 2412, NACA 4412, and NACA 0012 were made and reenacted and simulated for different angles of attack at constant wind velocities and mesh elements. Coefficient of drag, coefficient of lift, pressure, and velocity contours of the fluid were gotten from the recreation. For 2D flows, setting various boundary conditions were the crucial step for solving the continuity and Navier–Stokes equation. Furthermore, the approvals of the current work are gotten by contrasting it and the test results.

10.2 Blade Geometry and Computational Domain

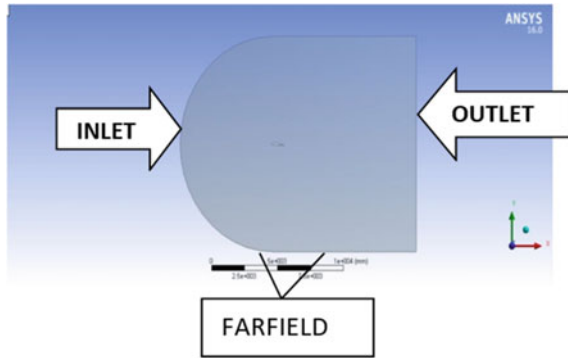
The first step of computational investigation is creating a geometry on which analysis has to be done. Accordingly, NACA airfoils geometries were obtained by having the standard coordinates of these blade profiles and then is imported into the ANSYS programming. The points have been joined using proper tools in order to generate complete airfoil profiles. Figure 10.1 shows the geometries of the airfoil profiles namely NACA 2412, NACA 4412, and NACA 0012 created in ANSYS workspace.

Picking a reasonable computational area is a critical stage in accurately duplicating fluid dynamic phenomena. The airfoil chord has been kept of unit length for



Fig. 10.1 Schematic of blade profiles for the current study

Fig. 10.2 Computational domain around the airfoil



simplicity. The computational space of the airfoil is comprising of inlet for wind stream over airfoil which has been taken a good way off of multiple times of the airfoil chord length.

As shown in Fig. 10.2, the different sides of the computational area have been taken as far-fields which are again a good way off of multiple times the chord length of the airfoil.

10.2.1 Meshing

Having a suitable computational domain is a key thing to having an optimized and correct meshing which leads to correct result analysis when it comes to computational study. For this, too small or too big a computational domain would lead to unnecessary chaos in the simulation. The airfoil chord is kept of unit length, and the computational domain as depicted in Fig. 10.3 is consisting of inlet which is seven times the airfoil

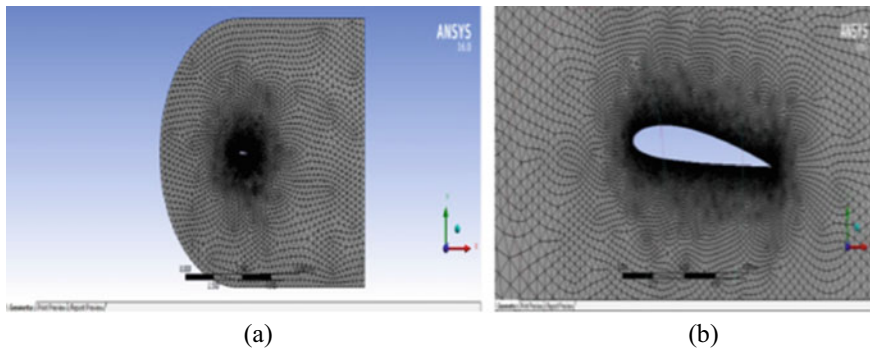


Fig. 10.3 NACA 2412 **a** C type structured mesh, **b** C type structured mesh around the modified airfoil

Table 10.1 Fluent setup

Data type	Specifications
General setting	Pressure-based, Absolute, Steady, planar
Model used	Inviscid, Realizable $k-\varepsilon$ (2 eqn.)
Materials used	Air
Boundary conditions	<p><i>Inlet</i></p> <p>Velocity specification method (Components)</p> <p>Velocity inlet</p> <p>Wind velocity = 2.5 m/s</p> <p>Angle of Attack (AOA) = 5 °</p> <p>$V_x = 2.5$ m/s</p> <p>$V_y = 0$</p> <p>Initial gauge pressure = 0 Pa</p> <p>Turbulent intensity (%) = 5%</p> <p>Hydraulic diameter = 1 m</p> <p><i>Outlet</i></p> <p>Pressure outlet</p> <p>Gauge pressure = 0 Pa</p> <p>Turbulent intensity (%) = 5%</p> <p>Hydraulic diameter = 1 m</p>

chord length. Outlet is considered at a distance of ten times of the airfoil chord length, and the two sides of the domain are considered as the far fields keeping at a space of 7 times of the chord length of the airfoil.

10.2.2 Setting the Boundary Conditions

The boundary conditions (BC) were defined after the mesh is generated. Table 10.1 shows the fluent setup done for the current simulation work which also mentions the boundary conditions applied to the computational domain. It is worth noting that, a “symmetry” type boundary condition is applied for the lateral surface of the fluid domain as because of it the solver considers the wall as part of a larger domain and can avoid real effects of wall [5].

A numerical analysis has been performed on the airfoil using ANSYS Fluent software at angles of attacks ranging from 0 to 45° and at 3 different velocities with a turbulence intensity of 5%.

The solver settings used are mentioned below:

- First-order upwind discretization method is used;
- Least squares cell-based method is used for gradient;
- SIMPLE algorithm is employed.

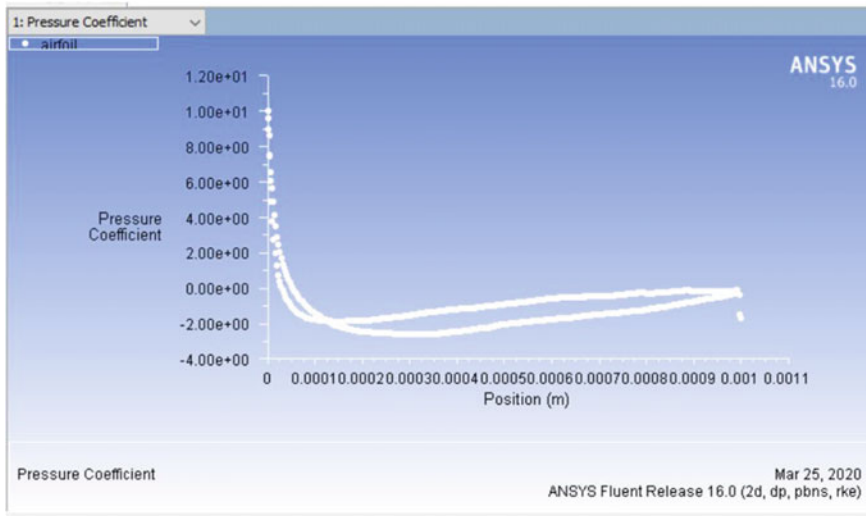


Fig. 10.4 Validation of result

10.3 Validation

Figure 10.4 shows the pressure coefficient distribution for NACA 2412 airfoil at zero angle of attack which is obtained from the present computational study of the NACA 2412 airfoil at the same operating conditions of the existing experimental result [6] which has been purely generated for the validation purpose. The same process is carried out for the remaining airfoils for validation purpose.

The pressure coefficient distribution of the NACA 2412, NACA 0012, and NACA 4412 profile obtained in the present study is in a good agreement with the experimental results.

10.4 Result and Discussions

The airfoils are tested under inviscid flow condition against various angle of attacks. The velocity vector is plotted for the airfoils individually and shown in figures (Fig. 10.5). The velocity vector gives the clear picture of the velocity distribution over an airfoil.

It is clearly evident from the contours that, high pressure exists at the leading edge and an area of low pressure exists on the upper surface of the airfoil. From Bernoulli's condition, we realize that at whatever point there is high speed, we have low pressing factor as well as the other way around. The tension on the lower surface of the airfoil seems at the leading edge which accordingly pushed the airfoil in the vertical direction.

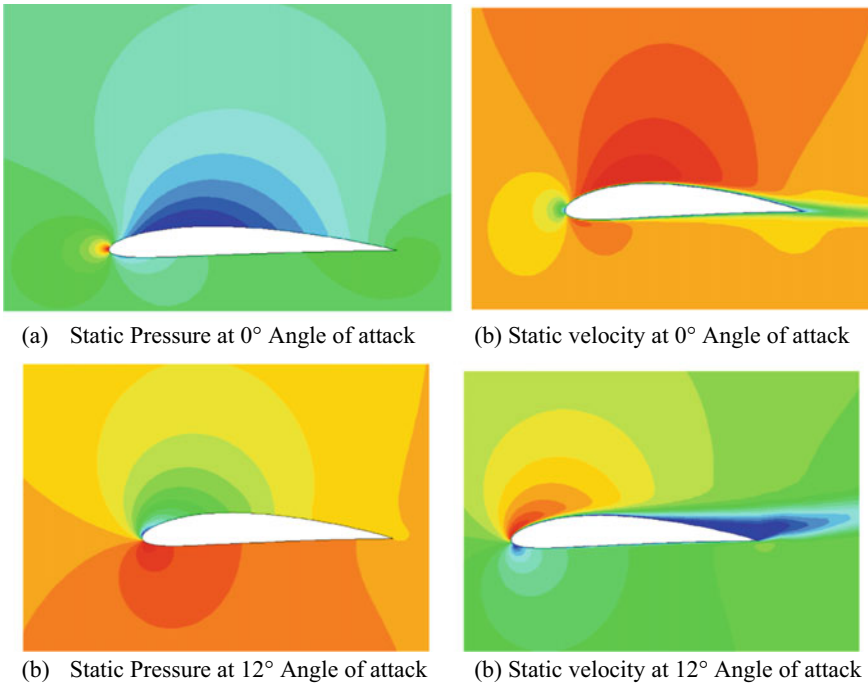


Fig. 10.5 Static pressure and static velocity contours at 0 and 12° angle of attack for NACA 4412

The lift coefficient and drag coefficients of the selected three NREL airfoils are computed at three different wind velocities, namely 2.5, 5, and 7.5 m/s, and plotted in graphs as shown in Figs. 10.6, 10.7, and 10.8.

It can be seen from the graphs that, at initial wind speed of 2.5 m/s NACA 4412 has the highest lift coefficient among all and NACA 2412 is the lowest in the stack at 2.5 m/s wind speed. Also, with further increase in wind speed, the blade profile NACA 4412 provides higher values of lift force. And NACA 0012 has been found to show a stable curve for lift coefficient at all values of wind speed.

Similarly, in case of drag coefficient versus angle of attack plots, it is evident that at all values of wind speed NACA 0012 provides the lowest drag coefficient value which is highly desirable. NACA 4412 gives higher values of drag coefficient at all values of wind speed which is undesirable.

It is likewise clear that with expansion in speeds, the upsides of coefficient of lift for all edge profile increments. It increments directly with approach causing stream being smooth and joined over the vast majority of the upper surface of the airfoil. Past 35° approach, there is a sensational abatement in coefficient of lift showing that 35° is the slow down point (stall angle) which is likewise valid for different profiles. Also, the drag coefficient increments with expansion in angle of attack. From 30° onwards, there is a fast expansion in drag coefficient esteems, demonstrating the stream has isolated from the upper surface well before the following edge. A lower

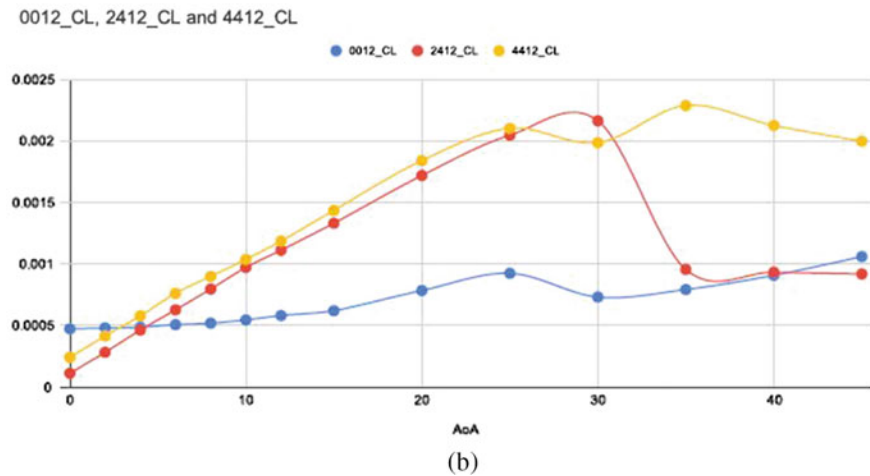
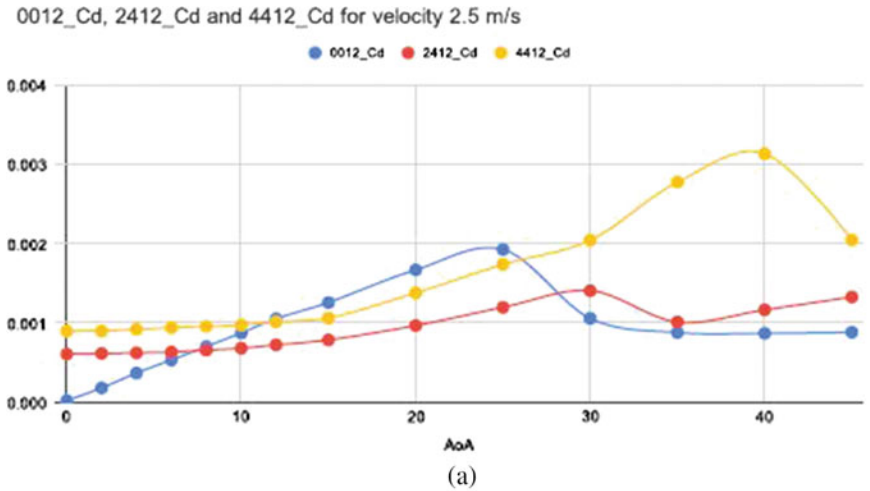


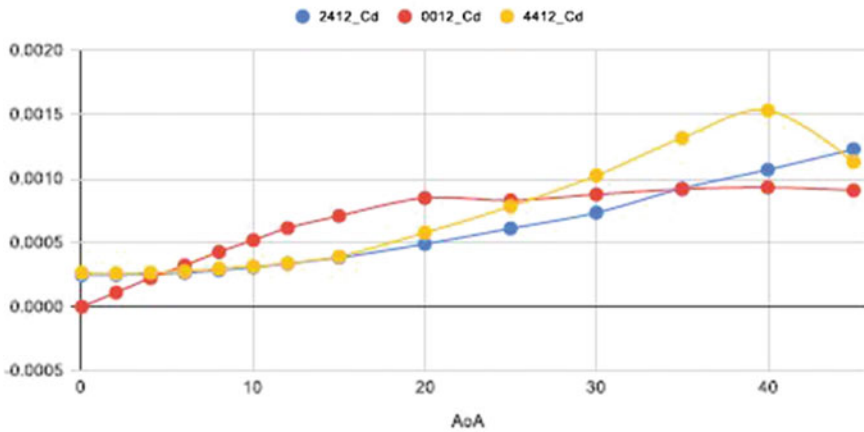
Fig. 10.6 **a** Drag coefficient versus angle of attack for 2.5 m/s wind velocity; **b** Lift coefficient vs. angle of attack for 2.5 m/s wind velocity

angle of attack is subsequently suit capable for the airfoil to work at to protect it from slowing down.

10.5 Conclusion

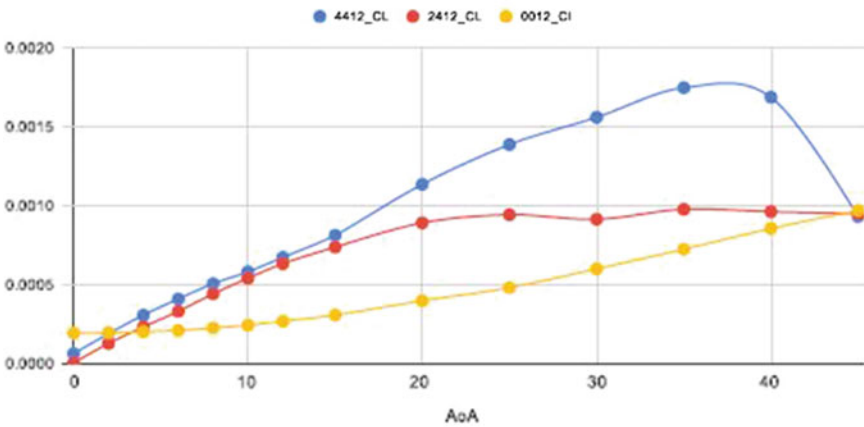
An extensive parametric study is conducted, and it can be observed that high pressure exists at the leading edge and an area of low pressure exists on the upper surface of the airfoil. From Bernoulli’s condition, we realize that at whatever point there is high

2412_Cd, 0012_Cd and 4412_Cd for vel. 5 m/s



(a)

4412_CL, 2412_CL and 0012_CL for velocity 5 m/s



(b)

Fig. 10.7 **a** Drag coefficient versus angle of attack for 5 m/s wind velocity; **b** Lift coefficient vs. angle of attack for 5 m/s wind velocity

speed, we have low pressing factor as well as the other way around. The tension on the lower surface of the airfoil seems at the leading edge which accordingly pushed the airfoil in the vertical direction. Also, from the CFD analysis that is carried out, it can be concluded that NACA 4412 provides the maximum lift and drag making it suitable for the use in rotors as compared to the other blade profiles selected in our study.

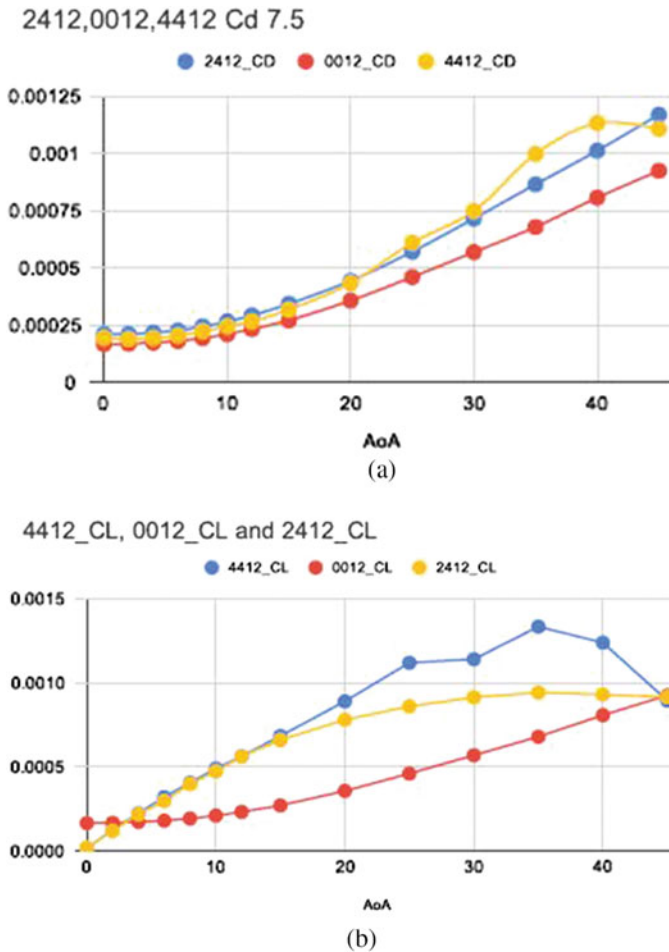


Fig. 10.8 **a** Drag coefficient versus angle of attack for 7.5 m/s wind velocity; **b** Lift coefficient vs. angle of attack for 7.5 m/s wind velocity

References

1. Elsakka, M.M., Ingham, D.B., Ma, L., Pourkashanian, M.: CFD analysis of the angle of attack for a vertical axis wind turbine blade. *Energy Convers. Manag.* **182**, 154–165 (2019)
2. Yossri, W., Ayed, S.B., Abdelkefi, A.: Airfoil type and blade size effects on the aerodynamic performance of small-scale wind turbines: computational fluid dynamics investigation. *Energy* **229** (2021)
3. Rahimi, H., Schepers, J.G., Shen, W.Z., Ramos García, N., Schneider, M.S., Micallef, D., Simao Ferreira, C.J., Jost, E., Klein, L., Herráez, I.: Evaluation of different methods for determining the angle of attack on wind turbine blades with CFD results under axial inflow conditions. *Renew. Energy* **125**, 866–876 (2018)

4. Sun, X., Zhu, J., Li, Z., Sun, G.: Rotation improvement of vertical axis wind turbine by offsetting pitching angles and changing blade numbers. **215** (2021)
5. Lanzafame, R., Mauro, S., Messina, M.: Wind turbine CFD modeling using a correlation-based transitional model. *Renew. Energy* **52**, 31–39 (2013)
6. Wolfe, W.P., Ochs, S.S.: CFD calculations of NACA 2412 aerodynamic characteristics, AIAA-97-0973 (1997)

Chapter 11

Computational Analysis of Air Energy Extractors for Guided Flow Exhaust Applications



Enderaaj Singh, Sukanta Roy, Yam Ke San, Ming Chiat Law, and Perumal Kumar

Abstract Increased usages of non-renewable carbon-based energy sources are rapidly depleting its reserve and releases environmentally harmful greenhouse gases. Hence, it is essential to find alternative renewable, sustainable, and green energy solutions to support global and local energy generation. Extensive research on vertical axis wind turbines (VAWT) has shown the potential of harnessing wind energy at locations, where conventional horizontal axis wind turbines (HAWT) are not suitable, such as in urban areas of Malaysia. However, inconsistent wind speed throughout the year poses a problem in harnessing wind energy efficiently. An alternative way of extracting wind energy is possible from unnatural sources such as exhaust systems. The present research aims to conduct three-dimensional numerical investigations of a cooling tower exhaust air energy extractor using VAWT. The performance of the exhaust VAWT system has been measured through unsteady simulations, and its aerodynamics properties have been evaluated. Then, using flow guiding techniques, the overall performance of the air energy extractors has been analyzed using computational simulations. This investigation has shown a significant performance gain for the VAWT and provided a good understanding of VAWT aerodynamics and flow behavior under accelerated wind conditions to contribute to a green technology system for renewable energy generation.

11.1 Introduction

Population and industrial growth have caused increased energy demand with fossil fuels supplying 84% of the world total energy [1]. Fossil fuels are heavily relied on as primary energy source as it is efficient, cheap, and easily available. Carbon emission from fossil fuel combustions has reached a record high of 32.3 billion metric tons in 2012 and is predicted to be 43.2 billion metric tons by 2040 [2]. This causes rise in environmental issues such as global warming. Moreover, the conventional energy source is depleting, as only 50 years of oil reserves are left, and this further

E. Singh · S. Roy (✉) · Y. Ke San · M. C. Law · P. Kumar
Faculty of Engineering and Science, Curtin University Malaysia, 98009 Miri, Malaysia
e-mail: sukantamech07@gmail.com; sukanta.roy@curtin.edu.my

© The Author(s), under exclusive license to Springer Nature Singapore Pte Ltd. 2023
B. Das et al. (eds.), *Advances in Smart Energy Systems*, Smart Innovation, Systems and Technologies 301, https://doi.org/10.1007/978-981-19-2412-5_11

185

increases the need to find alternative energy source to cover future energy demands [1]. Problems with energy demand and fossil fuel use have raised awareness and global attention to the need to find alternative ways to provide greener energy and control greenhouse gas emissions from fossil fuel use. Cleaner and more sustainable energy sources are becoming increasingly important, and continuous work to develop this energy source is required. Wind energy production has proven to be a reliable source of renewable energy due to its stability and growth rate, with a steady global capacity increment of 50–60 GW annually from 2014 to 2019 and a record increase of 93GW in 2020 [3]. However, the rate of growth associated with this method of energy production is insufficient to meet the ever-increasing demand for energy. Horizontal axis wind turbines (HAWT) are the conventional method used for wind energy extractions from strong natural winds, mainly available at higher places or remote locations in open areas. Urbanization and energy-intensive human lifestyle have caused a rise in energy demand. The vertical axis wind turbines (VAWT) offer flexibility for urban uses with their smaller and simpler design, lower starting speed, omnidirectional properties, low noise level, and adaptability to turbulent wind conditions [4]. Savonius (drag type) and Darrieus (lift type) are the two main types of VAWT [4]. H-Darrieus wind turbines (HDWT) have been widely studied as it provides better advantages compare to other VAWT types such as wider range of operation and produces higher average power coefficient compared to Savonius turbines [4–6].

However, most countries with unpredictable and low wind conditions throughout the year face difficulties to efficiently harness natural wind power. For example, in Malaysia, the average annual wind speed is 2 m/s [7]. Harnessing wind energy from man-made, unnatural sources, such as the strong and consistent exhaust air from a cooling tower outlet with wind speeds of up to 16 m/s [8] can be a solution for generating efficient power. There have been very few studies done on harnessing cooling tower exhaust air for power generation. A group of researchers conducted series of studies on wind turbine application in cooling towers using a five-bladed lift type VAWT with FX63-137 airfoils [9–12]. Initially, Chong et al. performed an experimental study on a laboratory scaled cooling tower with one orientation of diffusers and straight guide vanes revealed that the VAWT rotational speed increased by 30.4% [9]. Following that, four straight guide vanes were used in the follow up study to optimize the angles of each guide vanes. Each guide vanes configuration yielded different results, with four guide vanes configured at (40°, 70°, 70°, and 40°) yielded an 8.38% increase in turbine rotational speed and a 1.98% decrease in cooling tower power consumption [10]. Fazlizan et al. then performed a computational fluid dynamics (CFD) study to achieve optimum VAWT positioning for best power extraction, both horizontally (distance of turbine center shaft to center of cooling tower outlet) and vertically (distance of the turbine nearest circumference to cooling tower discharge outlet) [11]. It was discovered that the best VAWT location is horizontally further from the cooling tower center, where discharge wind speed is higher, and vertically higher positioned. At this location, the VAWT produced maximum C_p of 0.106, generating 1 kW power from 7.5 kW fan motor which is equivalent to 13% energy being recovered. Tabatabaieikia et al. then continued optimizing the design

in a CFD study using modified plate diffusers with adjoining semi-circular shapes on the inner side of the diffuser to improve wind concentration [12]. The effect of adding straight and modified separator plates was also compared to the results of not using a separator plate [12]. The best augmented arrangement was achieved by using the plate diffuser with a 30° angled semi-circular pattern on the inner side with modified separator. These flow augmentation designs increased wind turbine output power by 48.6% compared to the baseline design, showing maximum C_p of 0.2210 and 0.2104 from experiments and simulations, respectively [12]. There were also studies conducted on other exhaust systems, such as using a drag-based, small-scale wind turbine (SSWT) for electrical power generation in a cement manufacturing plant with high exhaust air speed of 16 m/s from a bag filter duct [13]. Before numerically testing the three-bladed and six-bladed drag-based turbines, Nimje and Gandhi optimized the distance, diameter, and depth of a single hemispherical blade in a CFD study [13]. The six-bladed turbine produced more torque with a blade depth of 100 mm and a diameter constrained at 320 mm depending on duct size [13]. The results were compared to the experiment study, indicating good agreement, with the six-bladed set-up producing power output of 35 W while the three-bladed set-up only produced 12.22 W. Berhanu et al. used a Savonius VAWT, a drag force blocker, and an enclosure to experimentally recover energy from a composite textile mill exhaust fan outlet [14]. The drag force blocker increased the exhaust wind speed by four times, potentially increasing overall system efficiency by 86.8%. The system's maximum power output was 140 kW. Berhanu et al. also numerically analyzed the VAWT blades for pressure distribution and maximum stress; however, the power coefficient of the VAWT was not computed [14].

According to the available research, VAWT performance for exhaust air energy extractions is poor, with energy recovery as low as 13% [11]. Better selection of VAWT types and parameters is lacking from previous exhaust air recovery studies. Using H-Darrieus VAWT (HDWT) can improve the power coefficient of the exhaust air recovery system as it has higher efficiency and performs better compared to Savonius VAWT [4–6]. Moreover, the airfoil utilized has a significant impact on HDWT efficiency. Hashem and Mohamed concluded that for HDWT, the S-1046 is the best performing airfoil among the 24 airfoils tested from various family groups [5]. Sun et al. conducted CFD study on three types of symmetrical and three asymmetrical airfoils and found that at wind speed higher than 6 m/s, the HDWT with S-1046 airfoils produced highest power coefficient and gave best fatigue performance as it has smallest deviation of aerodynamic force [15]. Other than that, many previous studies done under free stream conditions have demonstrated that choosing the right solidity and number of blades of HDWT can influence the power coefficient at various TSR values [6, 16–18]. Qamar and Janajreh performed a two-dimensional CFD analysis on a three-bladed HDWT with NACA 4312 airfoils of three different chord lengths ($c = 0.2, 0.5, \text{ and } 1.0$) from low to high TSRs [16]. At lower TSRs values from 1.0 to 3.5, the higher solidity HDWT obtained greater C_p than the lower solidity HDWT. However at higher TSRs, the low solidity HDWT produced higher C_p . Qamar and Janajreh also evaluated the use of two-bladed and three-bladed HDWT, where the three-bladed HDWT gave a higher C_p . Subramanian et al. performed

a three-dimensional transition SST simulation on HDWT solidities by using two, three, and four blades with NACA 0012 and NACA 0030 airfoils [17]. This study found that VAWT with two and three blades performed well, whereas the four-bladed HDWT performed poorly. Also, the two-bladed HDWT performs better at higher TSR but has poor self-starting performance at lower TSR due to having lower solidity. Li et al. conducted experimental investigation on small HDWT which showed that higher number of blades degrades VAWT performance as it reduces the pressure difference between the suction and pressure side of the blades [18].

Furthermore, other designs and methods of flow augmenters, particularly diffusers with shroud and flange which has showed good power augmentation in many previous studies under free stream flow condition, have not been investigated under accelerated condition of cooling tower exhaust air [6, 19]. Dilimulati et al. used computational fluid dynamics (CFD) simulation to optimize wind flow over a building to guide and accelerate the airflow using a shrouded diffuser with a cycloidal curved inlet and flanged outlet to verify the benefits of using these augmentation method and to study the diffuser's flow interaction [20]. It was shown by Dilimulati et al. that the flange creates low pressure region behind the diffusers, creating suction that draws in more air and accelerates wind velocity by 1.6 times, potentially increasing wind power by up to four times [20]. Effort to further improve diffuser designs and parameters was done in few studies [21–23]. The shrouded flat-panel diffuser with flange is widely used to enhance VAWT performance. In a wind tunnel experiment investigation, Wang et al. compared the HDWT performance with and without the flat-panel diffuser and showed that the diffuser increased HDWT output power by 26.3% [21]. Watanabe et al. carried out experimental study in a wind tunnel to improve the flat-panel diffuser design and showed the VAWT performance improved the most when the diffuser's semi-open angle (exit angle) is 20° with diffuser length of $0.5 D$ ($D =$ VAWT diameter) [22]. Inclusion of shroud for the diffuser inlet also increased the VAWT performance. Watanabe et al. also found that maximum performance was achieved when the throat of the diffusers is aligned with the center of VAWT. Altogether, these flat-panel diffuser parameters and arrangement showed power augmentation factor of 2.0. Dessoky et al. conducted a CFD analysis to also optimize the design parameters of a flat-panel diffuser by altering diffuser length, diffuser semi-open angle, shroud length, shroud angle, and flange height to increase the performance of a 2-bladed H-Darrieus VAWT [23]. Diffuser length of $1D$, diffuser angle of 29° , shroud length of $0.25D$, shroud angle of 4° , and flange height of $0.5D$ were the best design parameter which gave maximum increase of VAWT power coefficient of 84% at TSR 2.5. Both Hashem and Mohamed [5] and Dessoky et al. [23] conducted CFD study to improve VAWT power coefficient by using three different diffusers shapes and showed that the cycloidal diffuser gives highest power augmentation compared to the flat-panel diffuser and curved-surface diffuser.

From the literature discussed on exhaust air recovery systems with flow augmentation, there are not many types of flow augmentation technique used in previous studies. The cycloidal diffuser has shown great power augmentation capability in many studies done under free stream flow condition. Moreover, there have been very few numerical studies on the exhaust air recovery system, particularly on the

aerodynamic flow study of the VAWT. Analyzing how the flow interacts with the turbine blades at various rotational positions, as well as the flow vorticity, flow separations, blade vortex interaction, and near wake region in accelerated flow situations is critical to understand the reasons behind its performance. Therefore in this paper, the average power coefficient of a three-bladed HDWT with S-1046 airfoil is measured under accelerated wind condition from cooling tower and flow augmentation technique using cycloidal diffuser and guide vanes are used to improve the performance by evaluating the instantaneous moment coefficient and flow properties around the HDWT.

11.2 Methodology

11.2.1 Key Performance Parameters

In this study, tip speed ratio (TSR) and solidity (σ) are the key design parameters, shown in Eqs. (11.1) and (11.2), respectively, where ω is the HDWT angular velocity [rad/s], R is the HDWT radius [m], V_∞ is the wind velocity [m/s], N is the number of blades, c is the chord length [m], and D is the HDWT diameter [m]. The performance of HDWT is measured in terms of average moment coefficient, C_m and average power coefficient, C_p as shown in Eqs. (11.3) and (11.4), respectively, as function of average mechanical torque, T [Nm], density, ρ [kg/m³], HDWT swept area, A [m²], and wind velocity V_∞ [m/s].

$$\text{TSR} = \frac{\omega R}{V_\infty} \quad (11.1)$$

$$\sigma = \frac{Nc}{D} \quad (11.2)$$

$$C_m = \frac{T}{0.5\rho ARV_\infty^2} \quad (11.3)$$

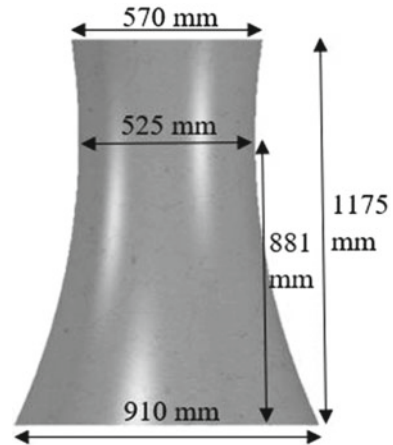
$$C_p = \frac{T\omega}{0.5\rho AV_\infty^3} = \frac{T}{0.5\rho ARV_\infty^2} \times \frac{R\omega}{V_\infty} = C_m \times \text{TSR} \quad (11.4)$$

11.2.2 H-Darrieus Wind Turbine and Cooling Tower Parameters

The HDWT used is shown in Table 11.1 as the three-bladed with S-1046 blades gave good results from previous study by the author [24]. This study involves modeling a

Table 11.1 HDWT parameters

Parameters	Values
Airfoil profile	S-1046
Number of blades (N)	3
Diameter (D)	456 mm
Span (H)	200 mm
Chord length (c)	68.4 mm
Solidity ratio (σ)	0.450

Fig. 11.1 Cooling tower measurements

cooling tower as part of the computational domain to simulate accelerated air flow of the cooling tower which has different velocities at different locations throughout the cooling tower outlet diameter. Figure 11.1 shows the cooling tower measurements, scaled down by factor of 200 of an actual cooling tower size, adapted from a study by Liu et al. [25].

11.2.3 Flow Augmentation Study Methods for Cooling Tower Exhaust Air Energy Extractions

In this study, the performance of bare HDWT under cooling tower accelerated flow will first be measured at TSRs of 1.5 and 2.0 at two different distance, 0.5 D and 1.0 D ($D =$ HDWT diameter) measuring from the cooling tower outlet to the center of the HDWT. The HDWT was chosen to be placed at distance 1.0 D to make space for positioning the guide vanes and cycloidal diffusers later on. The average power coefficient values of the bare HDWT at the 2 distances mentioned were calculated and compared as shown in subsect. 3.1. Next, the cycloidal diffusers and guide vanes

were added separately to the exhaust air energy system to improve the performance of HDWT at distance 1.0 D. The performance of HDWT at distance 1.0 D, with and without using the flow augmentation, was evaluated at TSRs of 1.5 and 2.0 by comparing the instantaneous moment coefficient values for a complete rotation, and flow analysis around the HDWT is discussed subject. 3.2.

11.2.3.1 Cycloidal Diffusers Design

The cycloidal diffuser dimensions used for this study are shown in Table 11.2. The cycloidal diffusers were placed so that the throat aligned to the center of the HDWT rotor as shown in Fig. 11.2a, b. The cycloidal diffuser was used to increase the HDWT performance at distance 1.0D away from the cooling tower outlet. The parameter chosen was mostly based on the study to optimized flat-panel diffuser as discussed in literature review [22, 23, 26]. The exit angle was chosen as 30° as the bigger angle has showed better performance in previous studies by Watanabe et al. [22], Dessoky et al. [23], and Kuang et al. [26]. The best shroud angle (inlet angle) for diffusers

Table 11.2 Cycloidal wind lens dimensions

Parameters	Dimensions
Shroud length (L_f)	0.5D (228 mm)
Diffuser length (L_b)	0.75D (342 mm)
Total length (L_t)	1.25D (570 mm)
Inlet angle (γ)	4°
Exit angle (ϕ)	30°
Throat width (D_{dt})	486 mm
Clearance (c)	15 mm
Height (H_{df})	300 mm
Flange width (W)	0.5D (228 mm)

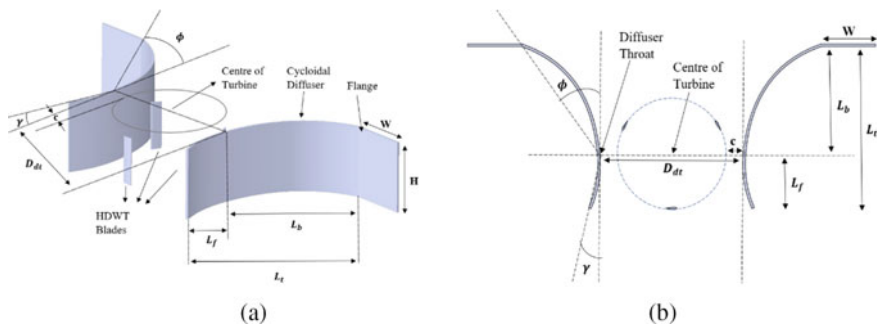


Fig. 11.2 Cycloidal diffuser design parameters and arrangement with HDWT; **a** Three-dimensional view, **b** two-dimensional view

was suggested to be between 0 and 4° in previous studies found in literature [23, 26]; so for this study, the 4° inlet angle was chosen. The flange width was chosen to be of width $0.5 D$ as this can greatly cause pressure drop at the wake region of the HDWT, shown in previous studies [22, 23, 26], hence drawing more air flow through the diffuser and accelerates the air toward the HDWT.

11.2.3.2 Guide Vanes Placement

Two guide vanes were placed at the cooling tower outlet as shown in Fig. 11.3 to enhance the blade instantaneous C_m at windward and leeward locations of the HDWT, where the values are found to be lower here from the results of the bare HDWT simulation. The first guide vane (left side) was placed -200 mm away from the center of the cooling tower outlet and at angle of 75° to the horizontal axis, while second guide vane (right side) was placed 220 mm away to the right and was angled at 55° to minimize blockage. The thickness of the guide vanes used is 5 mm with length of 300 mm, to guide the wind toward full length of the HDWT blades.

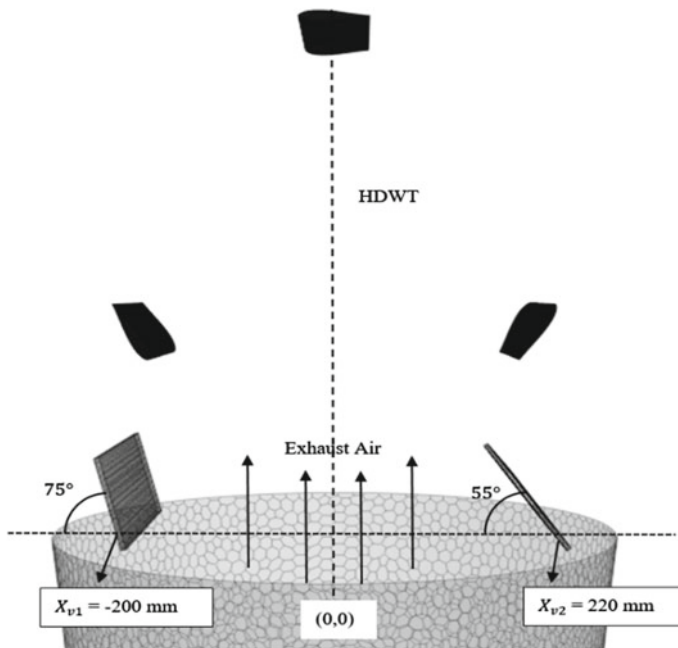


Fig. 11.3 Guide vanes placement tested to enhance HDWT performance under cooling tower exhaust air condition

11.2.4 Computational Domain, Mesh, and Flow Physics Conditions

The meshed computational domain consists of stationary and rotating zone is shown in Fig. 11.4. The domain and HDWT were designed in Solidworks and imported into Star CCM+ for three-dimensional numerical study. The stationary domain is a combination of a cooling tower and rectangular control volume. The dimension of cooling tower control volume was mentioned in Sect. 2.2, while cuboidal control volume was set using diameter of the cooling tower outlet ($D_o = 570$ mm). The HDWT is placed in the rotating region, created by forming a circular domain of $1.5D$ around the HDWT which is large enough to ensure pressure and velocity continuity and minimize numerical errors. The HDWT will be placed and measured at two different heights, $0.5D$ and $1.0D$ ($D =$ HDWT diameter) away from the cooling tower outlet. Two velocity inlet is set, one to include ambient air effect of 2 m/s and another inlet was set as 3.7 m/s at the cooling tower base to achieve 9 m/s at cooling tower outlet accelerated by the converging shape. The downwind side of the cuboid domain (top side) is set as pressure outlet with $p = 0 P_a$. The left and right side of the cuboidal domain was set as symmetry boundary condition. The cooling tower shape and HDWT blades were designated as no-slip wall boundaries. An interface was created to unite the fixed and rotating regions, and a sliding mesh was employed to rotate the circular rotating zone. Once the bare HDWT simulation is done, the cycloidal diffuser was added and positioned with the throat aligned to the center of HDWT as shown in Fig. 11.5. Guide vanes are also included to enhance the HDWT

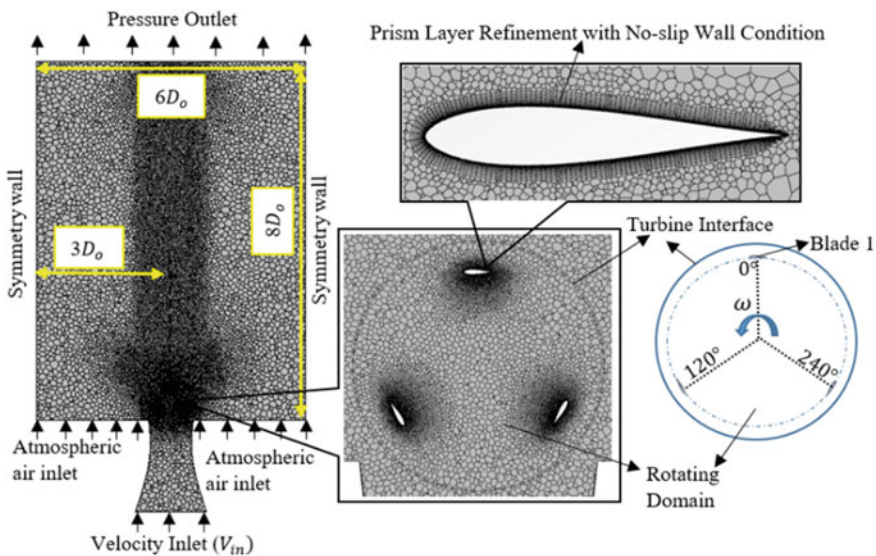


Fig. 11.4 Two-dimensional view of the meshed computational domain

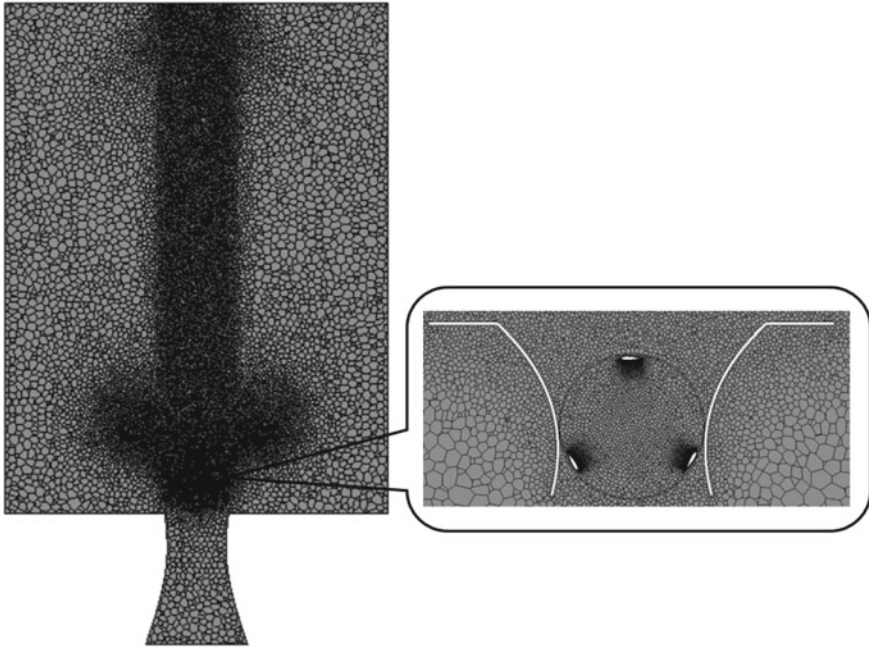


Fig. 11.5 Two-dimensional view of the meshed computational domain with cycloidal diffusers

performance, as shown previously in Fig. 11.3. Both the diffusers and guide vanes geometry will be set as no-slip wall boundaries. Unstructured 3D polyhedral mesh is generated for this study. Refinement was done around the rotating region of HDWT and around the blades to accurately capture the flow around the HDWT and inside the rotating region. On the blade surface, finely structured grid is created by setting 15 number prism layers with total thickness of 1% of the HDWT diameter, growth rate of 1.2 and first-layer thickness of about 3×10^{-5} m to maintain the dimensionless wall distance, y^+ value lower or close to 1. The downstream behind the HDWT is also refined to capture the wake flow. The concentration of cells at the interface boundaries is made sure to be uniform. For the flow physics, three-dimensional implicit unsteady Reynolds-Averaged Navier–Stokes (URANS) equations of conservation of mass and conservation of momentum were solved using shear stress transport (SST) (Menter) $k-\omega$ turbulence model solver. The segregated flow solver and second-order temporal discretization is applied. The SIMPLE algorithm was used to realize the pressure–velocity coupling. The effect of cooling tower exhaust air temperature is ignored in this study because the main goal of this study is to investigate the aerodynamic performance of HDWT under accelerated wind conditions. Therefore, constant air density of 1.18415 kg/m^3 and dynamic viscosity of $1.85508 \times 10^{-5} \text{ Pa}\cdot\text{s}$ was applied. Turbulence intensity was assumed and set as 5%. The rotational speed of turbine was set at 59.211 and 78.947 rad/s to obtain TSR 1.5 and 2.0. Inner iteration was set at

20 to obtain converged solution. residuals convergence criterion kept at 1×10^{-5} for all variables to keep the residuals small enough [26].

11.2.5 Grid Independence and Time Step Sensitivity Test

The mesh independence test for this study was done at TSR 1.5 by refining mesh around the HDWT blades and rotating region. Once the solution converged after five rotations, the C_m value was calculated by averaging the value of the sixth and seventh rotations. The HDWT C_m was plotted for every refinement as shown in Fig. 11.6, which shows the best cell size for this study is 5.1 million cells as further mesh refinement gives C_m difference of less than 1%. Next, the time step size test was conducted. Four values of time steps were set which are 2.94767×10^{-4} , 7.36917×10^{-4} , 1.47383×10^{-3} , and 2.94767×10^{-3} to rotate the HDWT by 1° , 2.5° , 5° and 10° degrees, respectively. The instantaneous C_m value of a single blade was plotted against azimuthal angle as shown in Fig. 11.7. The larger time step overpredicts the C_m produced by the blade in the HDWT leeward direction, shifting the peak blade C_m toward greater azimuthal angle. This clearly demonstrates that a smaller time step yields a more accurate result. As this is a 3D simulation study, the final time step chosen was $d\theta = 2.5^\circ$ to balance computational time because it reaches quasi-static convergence after 72 h (three days), while the 1° time step converges

Fig. 11.6 Grid independence study for bare HDWT at TSR 1.5

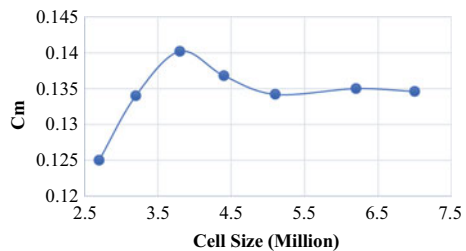
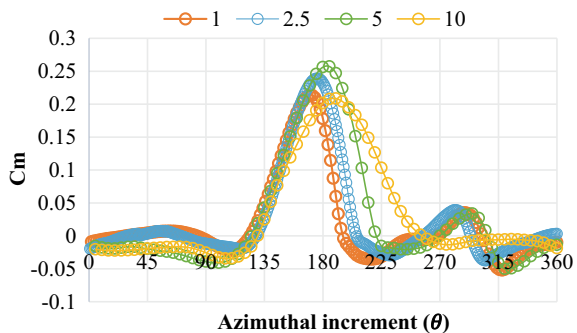


Fig. 11.7 Time step size test



after 180 h, which is a costly computing time. Furthermore, 3D CFD studies found in open literature have indicated that 2° and 2.5° are appropriate for providing accurate results for wind turbine studies [17, 26].

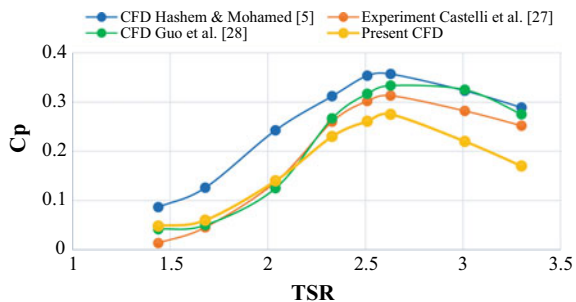
11.2.6 Model Validation

To ensure the accuracy of the computational domain, physics conditions, and mesh generated for this study, validation is performed using three-bladed HDWT with NACA 0021 airfoils, diameter of 0.515 m, blade length of 0.2 m, and solidity of 0.25 at TSRs of 1.44–3.30. The computational domain shape is adjusted to be entirely cuboidal by removing the cooling tower shape and extending the cuboidal domain at the inlet side such that it is 5D away from the center of the HDWT. The inlet velocity was set as 9 m/s. The results are compared to previous experimental studies of Castelli et al. [27], and 2D CFD study of Hashem and Mohamed [5], and Guo et al. [28] as shown in Fig. 11.8. The numerical results show good agreement to the available literature and confirm the suitability of the current mesh and physics conditions.

11.3 Results and Discussions

The performance of bare HDWT under cooling tower exhaust air conditions at distances of 0.5D and 1.0D was measured at TSRs of 1.5 and 2.0 in this study. Then, the guide vanes and cycloidal diffusers were used to enhance the HDWT performance at distance 1.0D at TSRs of 1.5 and 2.0. The coefficient of moment and coefficient of power of the HDWT with and without flow augmentors are provided in subsect. 3.1. In subsect. 3.2, flow analysis around HDWT was done, and discussion on how the guide vanes and cycloidal diffusers affects the performance at certain HDWT rotation angles is provided.

Fig. 11.8 Validation of the current model against other studies



11.3.1 Average Moment and Power Coefficients

Table 11.3 shows the moment coefficient and power coefficient of the bare HDWT and HDWT with flow augmenters used. It is observed that moving the HDWT further away from the cooling tower outlet results in performance drop at both the TSRs. At TSR 2.0, the power coefficient of HDWT dropped by 40.06% from 0.3196 at distance 0.5D to 0.1916 at distance 1.0D. At distance of 1.0D, the use of flow augmenters can enhance HDWT performance as both the guide vanes and cycloidal diffusers increased the HDWT’s performance at TSR 1.5. However, only the cycloidal diffuser managed to increase the HDWT performance at TSR 2.0 to C_p of 0.259, which is an increase of 23.92% compared to the bare HDWT. To compare the performance between the bare HDWT and the HDWT with flow augmenters for one complete rotation, the instantaneous moment coefficient against azimuthal angle plots at TSR of 1.5 and 2.0 is provided in Figs. 11.9 and 11.10, respectively. It can be observed that the guide vanes worked well to boost the coefficient of moment at azimuthal location of 190–220°. It also increases the instantaneous moment at lower azimuth angles (0–110°) at TSR 1.5. However, the instantaneous moment from 210 to 240° was greatly reduced at TSR 2.0. For the case of using cycloidal diffusers, the angle of continuous positive moment of the HDWT was increased (110–270°) which can greatly enhance the HDWT performance especially at TSR 2.0. High instantaneous moment was observed from 230 to 270° compared to the bare HDWT case.

Table 11.3 Moment and power coefficient under accelerated cooling tower exhaust air for bare HDWT placed at distance 0.5D, 1.0D, HDWT with guide vanes at 1.0D and HDWT with cycloidal diffusers at 1.0D

HDWT configurations	TSR 1.5		TSR 2.0	
	C_m	C_p	C_m	C_p
Bare HDWT at 0.5D	0.1342	0.2013	0.1598	0.3196
Bare HDWT at 1.0D	0.1246	0.1869	0.1045	0.2090
HDWT with guide vanes at 1.0D	0.1333	0.2000	0.0958	0.1916
HDWT with cycloidal diffusers at 1.0D	0.1337	0.2006	0.1296	0.2592

Fig. 11.9 Single blade instantaneous C_m against azimuthal angles for bare HDWT, HDWT with guide vanes and HDWT with diffusers at TSR 1.5

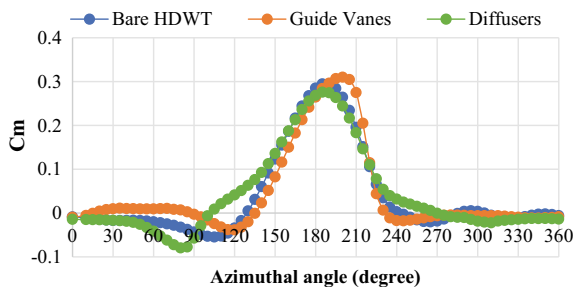
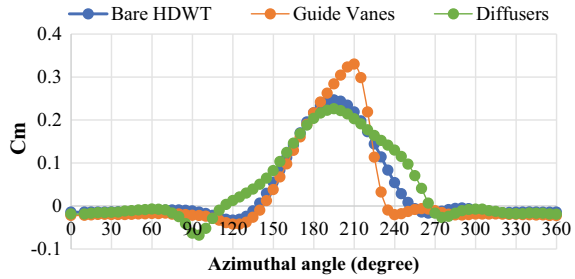


Fig. 11.10 Single blade instantaneous C_m against azimuthal angles for bare HDWT, HDWT with guide vanes and HDWT with diffusers at TSR 2.0



11.3.2 Flow Analysis Around Bare HDWT and HDWT with Guide Vanes at TSR 1.5

Figures 11.11 and 11.12 show the velocity contour and pressure contour, respectively, around the bare HDWT and HDWT with guide vanes at TSR 1.5. For this section, the HDWT at rotational angle (θ) of 0 and 90° with respect to blade 1 and y-axis, are provided as these are the angles where the most obvious change in instantaneous C_m was observed as shown in Figs. 11.9 and 11.10. At $\theta = 0^\circ$, the guide vane on the right blocks the wind from approaching blade 3 (B3, circled) as shown by the velocity contour in Fig. 11.11a, which is at azimuthal position 240°. This results in the blade having lower pressure difference between the suction and pressure side of the blades compared to the case of bare HDWT as shown in Fig. 11.12a. At $\theta = 90^\circ$, the guide vanes diverted the exhaust air from the cooling tower to the leading edge of blade 2 (B2, circled) which is at azimuthal position 210° as shown in Fig. 11.11b. This causes the blade to interact with higher wind speed which causes increase in pressure at the pressure side of the blade at this rotational position. This causes higher pressure difference between the pressure and suction side of the blade compared to the bare HDWT blade. Therefore, the guide vanes managed to improve the instantaneous C_m of the HDWT at this azimuthal angle as seen in Fig. 11.9 earlier. Moreover, blade 1 also showed slight improvement of instantaneous C_m as there is a slight drop in pressure at the suction side near the leading edge of the blade.

11.3.3 Flow Analysis Around Bare HDWT and HDWT with Cycloidal Diffusers at TSR 2.0

Figures 11.13 and 11.14 show the velocity contour and pressure contour, respectively, around the bare HDWT and HDWT with cycloidal diffusers at TSR 2.0, at rotational angle (θ) of 0 and 90° with respect to blade 1 and y-axis. The pressure contour clearly shows high pressure region at the upwind area of the HDWT as observed in Fig. 11.14a, b. The diffusers guide and accelerate the exhaust air (as seen in Fig. 11.13) which creates high pressure difference between blades surface at the

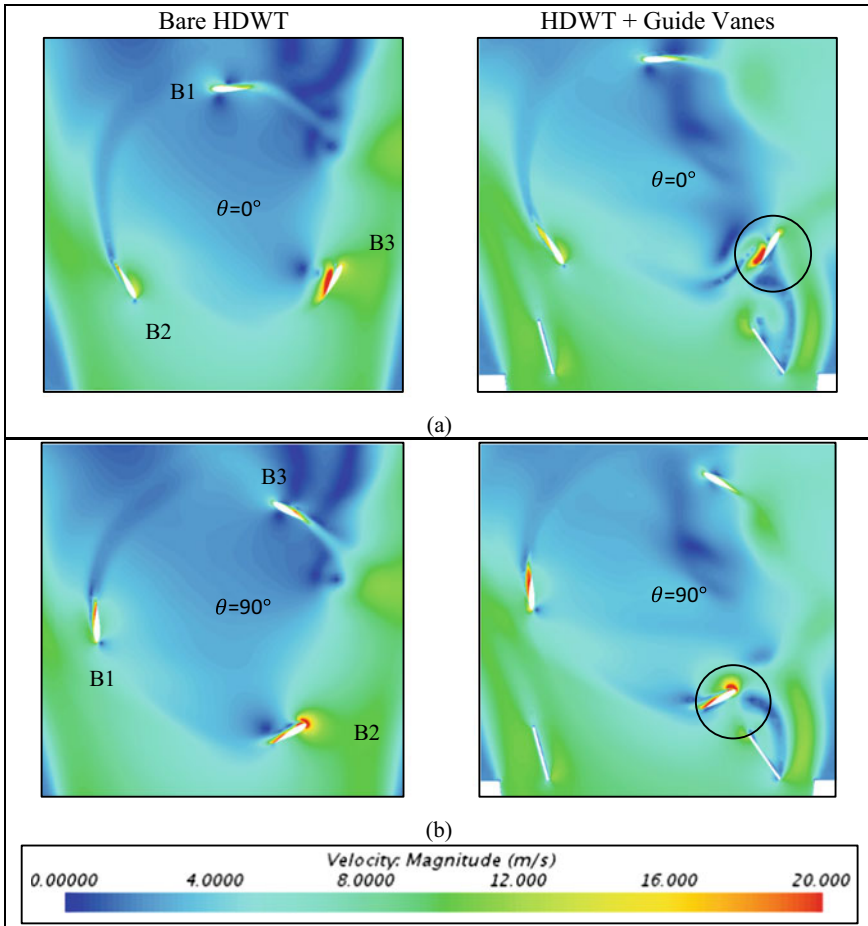


Fig. 11.11 Velocity contour around bare HDWT (left) and HDWT with guide vanes (right) at TSR 1.5 at rotational position of; **a** $\theta = 0^\circ$, **b** $\theta = 90^\circ$

upwind locations. Therefore, from azimuthal of $120\text{--}265^\circ$, the HDWT blades have high positive instantaneous moment coefficient which greatly improved the power coefficient of the turbine. However, when the blade rotates close to the diffuser wall, its moment coefficient drops, especially at the winward side when the blade is at azimuthal 90° . This is because the blade experience low pressure on both sides as shown by blade 1 (circled) in Fig. 11.14b which hinders the lift generation. The bare HDWT blade performs better at this azimuth angle.

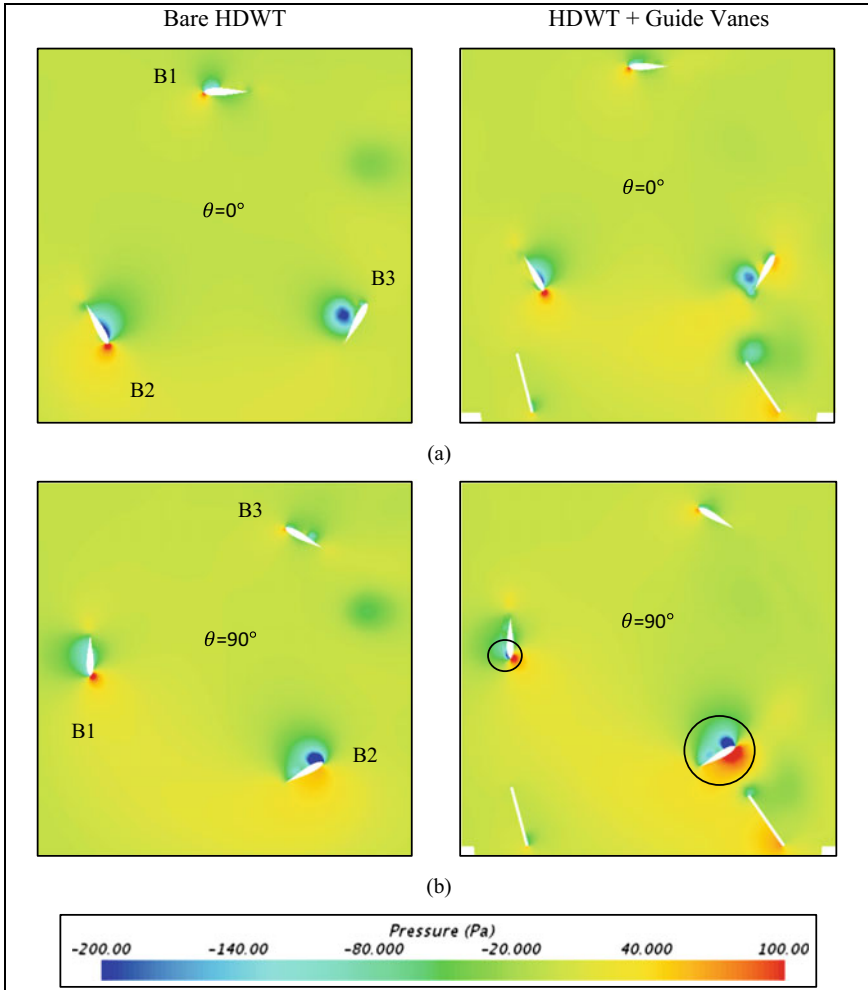


Fig. 11.12 Pressure contour around bare HDWT (left) and HDWT with guide vanes (right) at TSR 1.5 at rotational position of; **a** $\theta = 0^\circ$, **b** $\theta = 90^\circ$

11.4 Conclusion

The present study was done to numerically study the cooling tower exhaust air energy extractor system using the H-Darrieus wind turbine (HDWT). Three-dimensional unsteady URANS simulation using SST $k-\omega$ turbulence model solver was conducted to measure and improve the performance of a three-bladed HDWT with S-1046 airfoils by using flow guiding techniques. The performance of the bare HDWT was first measured at distance of 0.5D and 1.0D away from the cooling tower outlet. Then, two different flow augmentation techniques, namely guide vanes and cycloidal

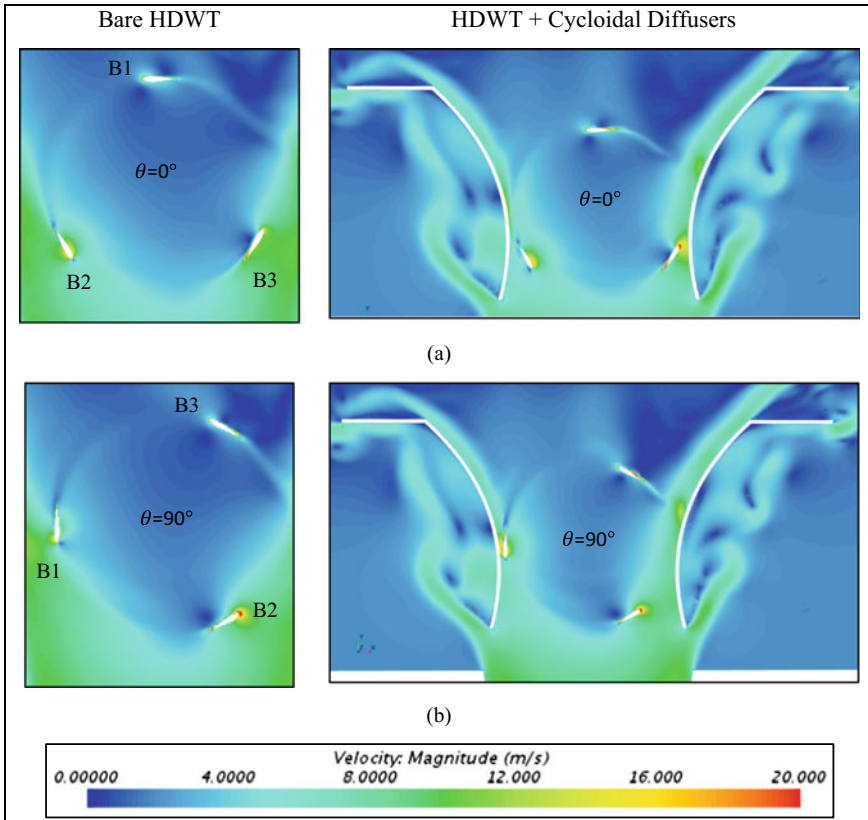


Fig. 11.13 Velocity contour around bare HDWT (left) and HDWT with cycloidal diffusers (right) at TSR 2.0 at rotational position of; **a** $\theta = 0^\circ$, **b** $\theta = 90^\circ$

diffuser, were added to the exhaust air energy extractor design to improve the moment and power coefficient of the HDWT at distance 1.0D. The HDWT with flow augmentation was tested at TSRs of 1.5 and 2.0. The results of this study have shown that guided flow augments are able to significantly improve the HDWT performance under the accelerated flow condition of cooling tower exhaust air. Using guide vanes has improved the power coefficient of the system by 8.33% at TSR 1.5 while the cycloidal diffuser gave highest improvement of 23.92% at TSR 2.0, producing power coefficient of 0.259. The aerodynamics of the bare HDWT and augmented HDWT at critical rotational location was also evaluated which provided good understanding of the flow behavior under cooling tower accelerated flow. However, the power coefficient of the HDWT with cycloidal diffuser at distance 1.0D and TSR 2.0 is still lower than that of the bare HDWT at distance 0.5D which was calculated as 0.3196. Therefore, using cycloidal diffuser at distance 0.5D will be investigated in future study. The diffuser parameters will also be optimized to further increase the wind acceleration and concentration toward the HDWT.

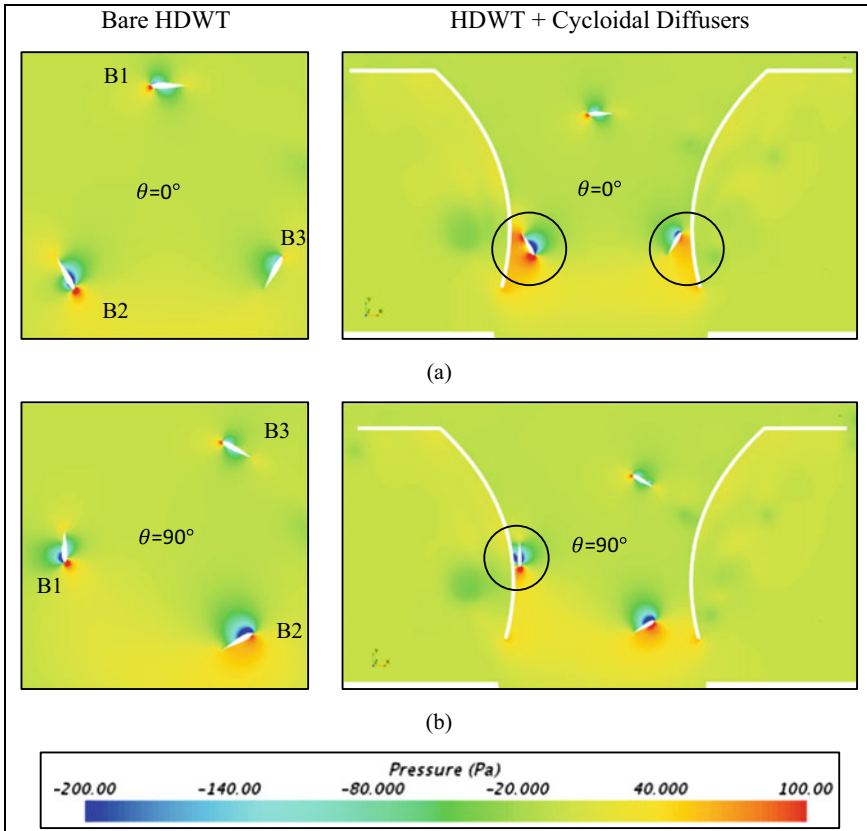


Fig. 11.14 Pressure contour around bare HDWT (left) and HDWT with cycloidal diffusers (right) at TSR 2.0 at rotational position of; **a** $\theta = 0^\circ$, **b** $\theta = 90^\circ$

Acknowledgements The authors would like to thank the Ministry of Higher Education (MOHE) Malaysia for the financial support by awarding the Fundamental Research Grant Scheme (FRGS Grant: FRGS/1/2018/TK10/CURTIN/03/1) to carry out this project.

References

1. Looney, B.: Statistical review of world energy globally consistent data on world energy markets. and authoritative publications in the field of energy. *Rev. World Energy Data* **70**, 8–20 (2021)
2. Kibria, A., Akhundjanov, S.B., Oladi, R.: Fossil fuel share in the energy mix and economic growth. *Int. Rev. Econ. Financ.* **2019**(59), 253–264 (2018)
3. International Energy Agency.: Global energy review 2021. *Glob. Energy Rev.* 2020, pp. 1–36 (2021), [Online]. Available: <https://iea.blob.core.windows.net/assets/d0031107-401d-4a2f-a48b-9eed19457335/GlobalEnergyReview2021.pdf>. 21. Renewables 2021 global status report (2021). [Online]. Available: https://www.ren21.net/wp-content/uploads/2019/05/GSR2021_Full_Report.pdf

4. Kumar, R., Raaheemifar, K., Fung, A.S.: A critical review of vertical axis wind turbines for urban applications. *Renew. Sustain. Energy Rev.* [Internet]. **89**(Apr), 281–91 (2018). Available from: <https://doi.org/10.1016/j.rser.2018.03.033>
5. Hashem, I., Mohamed, M.H.: Aerodynamic performance enhancements of H-rotor Darrieus wind turbine. *Energy* [Internet]. **142**, 531–45 (2018). Available from: <https://doi.org/10.1016/j.energy.2017.10.036>
6. Hand, B., Kelly, G., Cashman, A.: Aerodynamic design and performance parameters of a lift-type vertical axis wind turbine: a comprehensive review. *Renew. Sustain. Energy Rev.* [Internet]. **139**(Dec 2019), 110699 (2021). Available from: <https://doi.org/10.1016/j.rser.2020.110699>
7. Salih, S.A., Mat, S., Sopian, K., Saleh, E., Alkhair, M.: Simulation analysis of Venturi-Vertical Axis Wind Turbine (V-VAWT), no. Nov, pp. 191–196 (2014). <https://doi.org/10.13140/2.1.2290.9122>
8. Hensley, J.C.: *Cooling Tower Fundamentals*. Compiled from the knowledge and experience of the entire SPX Cooling Technologies staff. SPX Cooling Technologies. Inc Overl Park Kansas USA (2009)
9. Chong, W.T., et al.: Design of an exhaust air energy recovery wind turbine generator for energy conservation in commercial buildings. *Renew. Energy* **67**, 252–256 (2014). <https://doi.org/10.1016/j.renene.2013.11.028>
10. Chong, W.T., et al.: The experimental study on the wind turbine's guide-vanes and diffuser of an exhaust air energy recovery system integrated with the cooling tower. *Energy Convers. Manag.* **87**, 145–155 (2014). <https://doi.org/10.1016/j.enconman.2014.07.009>
11. Fazlizan, A., Chong, W.T., Yip, S.Y., Hew, W.P., Poh, S.C.: Design and experimental analysis of an exhaust air energy recovery wind turbine generator. *Energies* **8**(7), 6566–6584 (2015). <https://doi.org/10.3390/en8076566>
12. Tabatabaeikia, S., et al.: Computational and experimental optimization of the exhaust air energy recovery wind turbine generator. *Energy Convers. Manag.* **126**, 862–874 (2016). <https://doi.org/10.1016/j.enconman.2016.08.039>
13. Nimje, A.A., Gandhi, N.M.: Design and development of small wind turbine for power generation through high velocity exhaust air. *Renew. Energy* **145**, 1487–1493 (2020). <https://doi.org/10.1016/j.renene.2019.06.065>
14. Berhanu, H., Gudeta, D., Haiter Lenin, A., Karthikeyan, B.: Numerical and experimental investigation of an exhaust air energy recovery Savonius wind turbine for power production. *Mater. Today Proc.* **46** (2021). <https://doi.org/10.1016/j.matpr.2021.02.675>
15. Sun, X., Zhu, J., Hanif, A., Li, Z., Sun, G.: Effects of blade shape and its corresponding moment of inertia on self- starting and power extraction performance of the novel bowl-shaped floating straight-bladed vertical axis wind turbine. *Sustain. Energy Technol. Assessments* **38**(Dec 2019), 100648 (2020). <https://doi.org/10.1016/j.seta.2020.100648>
16. Qamar, S.B., Janajreh, I.: A comprehensive analysis of solidity for cambered darrieus VAWTs. *Int. J. Hydrogen Energy* **42**(30), 19420–19431 (2017)
17. Subramanian, A., et al.: Effect of airfoil and solidity on performance of small scale vertical axis wind turbine using three dimensional CFD model. *Energy* **133**, 179–190 (2017). <https://doi.org/10.1016/j.energy.2017.05.118>
18. Li, Q., Maeda, T., Kamada, Y., Murata, J., Furukawa, K., Yamamoto, M.: Effect of number of blades on aerodynamic forces on a straight-bladed vertical axis wind turbine. *Energy* **90**, 784–795 (2015). <https://doi.org/10.1016/j.energy.2015.07.115>
19. Wong, K.H., Chong, W.T., Sukiman, N.L., Poh, S.C., Shiah, Y.C., Wang, C.T.: Performance enhancements on vertical axis wind turbines using flow augmentation systems: a review. *Renew. Sustain. Energy Rev.* **73**(January), 904–921 (2017). <https://doi.org/10.1016/j.rser.2017.01.160>
20. Dilimulati, A., Stathopoulos, T., Paraschivoiu, M.: Wind turbine designs for urban applications: a case study of shrouded diffuser casing for turbines. *J. Wind Eng. Ind. Aerodyn.* **175**(Nov 2017), 179–192 (2018). <https://doi.org/10.1016/j.jweia.2018.01.003>
21. Wang, X.H., Wong, K.H., Chong, W.T., Ng, J.H., Xiang, X.B., Wang, C.T.: Experimental investigation of a diffuser-integrated vertical axis wind turbine Experimental investigation of a diffuser-integrated vertical axis wind turbine. In: *IOP Conference Series: Earth and Environmental Science*, vol. 463 (2020). <https://doi.org/10.1088/1755-1315/463/1/012153>

22. Watanabe, K., Takahashi, S., Ohya Y.: Application of a diffuser structure to vertical-axis wind turbines. *Energies* **9**(6) (2016). <https://doi.org/10.3390/en9060406>
23. Dessoky, A., Bangga, G., Lutz, T., Krämer, E.: Aerodynamic and aeroacoustic performance assessment of H-rotor darrieus VAWT equipped with wind-lens technology. *Energy* **175**, 76–97 (2019). <https://doi.org/10.1016/j.energy.2019.03.066>
24. Singh, E., Roy, S., San, Y.K.: Numerical analysis of exhaust air energy extractor for cooling tower applications. In: IOP Conference Series: Materials Science and Engineering, vol. 943, no. (1) (2020)
25. Liu, Z., Zhang, C., Ishihara, T.: Numerical study of the wind loads on a cooling tower by a stationary tornado-like vortex through LES. *J. Fluids Struct. [Internet]* **81**, 656–72 (2018). Available from: <https://doi.org/10.1016/j.jfluidstructs.2018.06.001>
26. Kuang, L., Su, J., Chen, Y., Han, Z., Zhou, D.: Wind-capture-accelerate device for performance improvement of vertical-axis wind turbines: external diffuser system. *Energy* **239**, 122196 (2022). <https://doi.org/10.1016/j.energy.2021.122196>
27. Raciti Castelli, M., Englaro, A., Benini, E.: The Darrieus wind turbine: proposal for a new performance prediction model based on CFD. *Energy* **36**(8), 4919–4934 (2011). <https://doi.org/10.1016/j.energy.2011.05.036>
28. Guo, Y., Li, X., Sun, L., Gao, Y., Gao, Z., Chen, L.: Aerodynamic analysis of a step adjustment method for blade pitch of a VAWT. *J. Wind Eng. Ind. Aerodyn.* 188(Oct 2018), 90–101 (2019). <https://doi.org/10.1016/j.jweia.2019.02.023>

Chapter 12

Computational Simulations on the Performance of Savonius Turbines in a Solar Chimney Power Plant



Pavitri Apparavoo, Sukanta Roy, and Yam Ke San

Abstract The increase in global population has caused a higher demand for energy be it for the upsurge in industrialization or daily consumption. Nevertheless, the high levels of carbon emissions from major energy resources such as coal, petroleum and gas are alarming as repercussions through rising sea levels are posing a threat to modern civilization. Thus, renewable energy sources such as wind energy and solar energy are being ventured into as these natural resources cause minimal to no harm to the environment. Previous literature suggests that minimal studies are performed on the enhancement of the turbine component of the solar chimney power plant (SCPP) for power augmentation. This work proposes the study of the performance of the Savonius-style wind turbine (SSWT) in the SCPP. The sliding mesh approach is adopted for the SSWT model, whereas the radiation model is used for the SCPP model in ANSYS Fluent. The SSWT was validated against previous numerical and experimental results, while the SCPP model is validated using the outcomes obtained from the Manzanares plant. The numerical study is carried out at a tip speed ratio (TSR) of 1.0, where the velocity and pressure fluid flow profiles are examined at four different azimuth angles for its performance capabilities. The outcome of the study suggests that SSWT performs well in the SCPP, but is hindered by negative torque at certain azimuthal angles which reduces its overall power producing capacity. It is suggested that TSRs lower than TSR 1.0 may exhibit better drag formation which may lead to an improved turbine performance. Also, flow optimization solution is encouraged for an improved overall torque output, performance and power production by the SSWT in the SCPP.

P. Apparavoo · S. Roy (✉) · Y. K. San
Faculty of Engineering and Science, Curtin University Malaysia, 98009 Miri, Malaysia
e-mail: sukantamech07@gmail.com; sukanta.roy@curtin.edu.my

12.1 Introduction

12.1.1 Solar Chimney Power Plant

The global carbon emissions significantly increase annually, causing global warming that harms living beings. The Paris Agreement in 2015 states that the total global warming should be maintained well below 2 °C. In line with that, popular energy players expect a significant decrease in non-renewable energy extraction such as gas, petroleum and coal by the year 2050 [1]. As such, renewable energy resources such as wind energy and solar energy are increasingly being ventured since these energy types result in minimal to no harm towards the surrounding population and environment.

The solar chimney power plant (SCPP) is a green system that utilizes solar energy for power production. The system operates based on solar radiation and natural convection. The main structure of the SCPP is made up of three main components: the solar air collector, chimney and the energy extractor (i.e. turbine) as shown in Fig. 12.1. During the day, the solar air collector receives solar radiation from the sun, which heats the air within the collector and the ground or absorber. The temperature change between the ambient fluid and the system's fluid results in a density difference, which causes the heated air in the solar air collector to move towards the collector exit, also known as the chimney's inlet. The pressure differential due to the chimney height causes the heated air to move towards the outlet of the chimney. The kinetic energy from the flowing fluid drives the pressure-staged turbine at the bottom of the chimney to generate power. During low solar radiation, the heat absorbed by the ground or absorber is released into the air of the solar collector, thus allowing continuous power production through the buoyancy effect at night.

The first prototype was constructed in Manzanares, Spain, where the plant operated for seven years. The operation of the prototype proved that the SCPP is a feasible

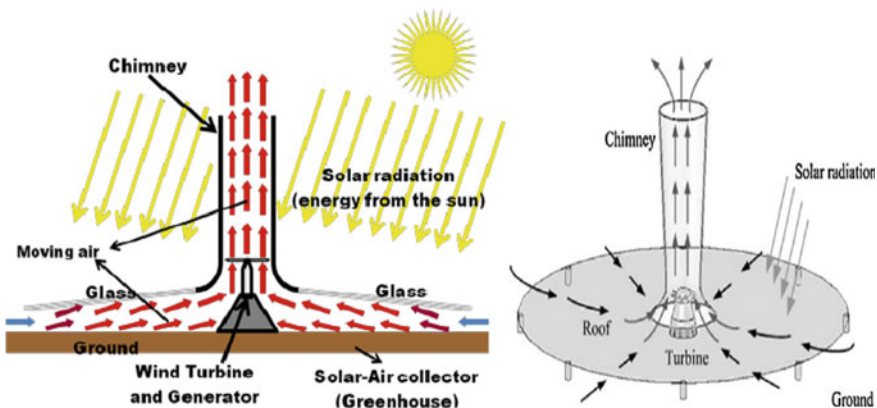


Fig. 12.1 Schematic of the solar chimney power plant operation [2]

concept that can be further enhanced for power production in different regions worldwide. The Manzanares plant was able to generate up to 50 kW of power during high solar intensities. Through the study of the Manzanares plant, the authors suggested that large lands are required for higher power augmentation with the conventional design. Thus, the plant was recommended to be constructed in unused lands with high solar radiation, like deserts. However, extensive research is being performed to enable power production for regions with minimal land and low solar radiation.

12.1.2 Wind Turbines

Wind turbines are devices that convert energy for electricity generation. These energy extractors convert kinetic energy to mechanical energy and finally electrically energy which accounts for 90% conversion efficiency as typically 10% is lost through transmission and heat loss. These devices are manufactured in wide ranges of sizes based on its application. Modern wind turbines can be classified accordingly to their axis of rotation, namely the horizontal axis wind turbines (HAWTs) and the vertical axis wind turbines (VAWTs).

HAWTs are the most popular kinds of wind turbines used in industries as it is able to generate high power. These types of wind turbines commonly installed in large numbers, from hundreds to thousands, are called wind farms. Wind farms are located in regions identified with strong wind velocities and are able to generate compensate power demands of nearby populations. Smaller wind turbines rating up to 100 kW or less are able to power homes or small industries. HAWTs have large tip speed ratios (TSRs) (i.e. ratio of the turbine's rotation to the free stream velocity) that allow it to generate higher power with increasing wind velocities. However, the biggest disadvantage of the HAWT is the noise level that is the resultant of the high tip speed ratios. Figure 12.2 illustrates the structure of a HAWT consisting of a large rotor, gearbox and generator.

VAWTs are wind turbines that are increasingly gaining attention as it has smaller sizes and are more applicable in areas with minimal bare land. Two main types of the VAWT are the Savonius-style wind turbine (SSWT) and the Darrieus wind turbine as presented in Fig. 12.3. VAWT typically operates at lower TSRs, thus not being able to generate high power unlike the HAWT. However, the simple designs of the VAWTs make it easier for these turbines to be installed in any regions, even with low wind velocities. Moreover, the gearbox and generator that are installed on the ground enables easier access for VAWT maintenance. Both drag and lift principles are used by the VAWTs, where the Savonius and Darrieus mainly operate based on drag and lift, respectively.

The SSWT is one of the simplest designed turbines first developed by Sigurd Johannes Savonius in 1920. The Savonius consists of two to three blade profiles that are convex and concave in shapes which converts wind force into torque on a rotating shaft. Though the SSWT has low power production, the simple design, easy construction and maintenance make it a popularly used turbine especially in

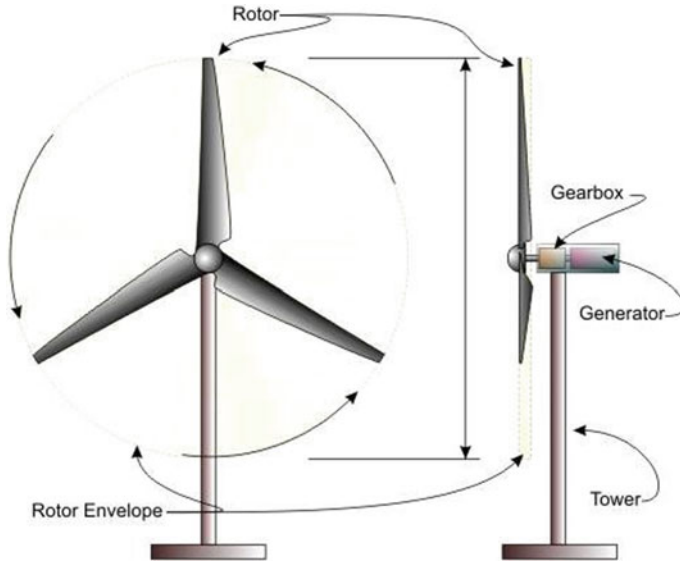


Fig. 12.2 Horizontal axis wind turbine [3]

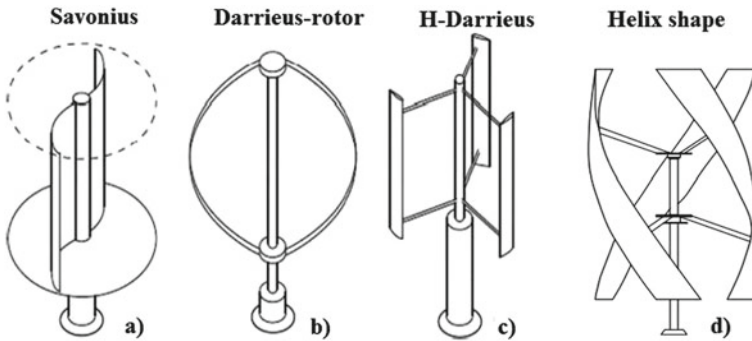


Fig. 12.3 Vertical axis wind turbines [4]

urban areas. Furthermore, the low cut-in speed of less than 2 m/s allows easier power generation by the energy extractor.

12.2 Application of SSWT

The conventional solar chimney power plant uses a four-bladed vertical axis wind turbine installed at the chimney inlet for power production [5]. However, subsequent enhancement studies have shown improved power generation through parametrical effects, environmental influences and hybrid means. Esmail, A-Elmagid [6] studied axial-flow turbines using three different designs: matrix through flow method (MTFM), classic blade element theory (BET) and modified BET (taking into consideration the enclosure of the turbine duct). The study suggested that the modified BET presented the highest generated power [6]. Zuo, Dai [7] proposed the implementation of an axial-flow hydraulic turbine impeller for power enhancement in the SCPP. The research indicates that the suggested model generates 30.46% more electricity than the Manzanares plant and has a wider range of high-performance turbine rotational speed under increased solar radiation [7].

Balijepalli, Chandramohan [8] proposed a small-scaled SCPP design to power household devices. The plant design obtained a power output of 0.82 W, although 40.15% lower than the theoretically calculated output power [8]. Rabehi, Chaker [9] incorporated a fan model as the turbine component in the SCPP. The study suggests that using the fan model results in an error of 30.02% due to unaccounted structural parameters of a real turbine [9]. Negrou, Rahmouni [10] proposed a turbine model using the inverse design methodology incorporated with guide vanes for operational characteristics anticipation in a geothermal coupled SCPP. The coupled design is suggested to obtain a maximum power output of 5 MW with a turbine efficiency of 77% [10].

Zuo, Dai [11] analysed the performance of a wind supercharging SCPP combined with gas waste heat recovery and desalination of seawater. The results indicate that increasing the rotor speed reduces the amount of freshwater generated while increasing the turbine shaft power to a peak at 200 rpm before declining [11]. Guo, Li [12] investigates the performance of a four-bladed pressure-staged turbine in a SCPP using three-dimensional analysis. The work suggests that using a real turbine in numerical studies provides more accurate results than the adoption of a fan model [12].

The energy extractor is installed 9 m from the ground, where the turbine's operation starts with a cut-in speed of 2.5 m/s [5]. The material selection of the turbine is suggested to be less stringent since it is situated within an enclosed area that prevents rapid changes in fluid flow velocity and flow separation [5]. Therefore, the SSWT is proposed to be installed in the collector region of the SCPP for power generation. The work focuses on energy extraction from the system at mid-day under a tip speed ratio (TSR) of 1.0. The performance of the Savonius is studied for one complete rotation at four different azimuthal angles based on the velocity and pressure profiles of the fluid flow.

12.3 Methodology

12.3.1 Computational Modelling

The present work adopts a two-dimensional numerical analysis approach using SOLIDWORKS and ANSYS R3 for the SSWT validation, SCPP validation and combined investigations. The SSWT and SCPP validations were verified using previous numerical work and experimental data [13–15]. The fluid flow characteristics, such as pressure and velocity data, were extracted from the verified SCPP model and applied on the SSWT domain to analyse the performance of the SSWT in the SCPP at various turbine rotational speeds. The following section presents the equations used to compute the turbulent characteristics of the SSWT and the SCPP.

12.3.2 Mathematical Modelling

The continuity and momentum equations were used in the model validations and current simulations to compute the turbulent flow behaviour of the SSWT in the SCPP, as shown in Eqs. (12.1), (12.2), (12.3) and (12.4).

Continuity equation (conservation of mass):

$$\frac{\partial \rho}{\partial t} + \nabla \cdot (\rho v) = 0 \quad (12.1)$$

Conservation of momentum:

$$\rho u \frac{\partial u}{\partial x} + v \frac{\partial u}{\partial y} + w \frac{\partial u}{\partial z} = -\frac{\partial p}{\partial x} + \frac{\partial}{\partial x} \mu \frac{\partial u}{\partial x} + \frac{\partial}{\partial y} \mu \frac{\partial u}{\partial y} + \frac{\partial}{\partial z} \mu \frac{\partial u}{\partial z} \quad (12.2)$$

$$\rho u \frac{\partial v}{\partial x} + v \frac{\partial v}{\partial y} + w \frac{\partial v}{\partial z} = -\frac{\partial p}{\partial y} + \frac{\partial}{\partial x} \mu \frac{\partial v}{\partial x} + \frac{\partial}{\partial y} \mu \frac{\partial v}{\partial y} + \frac{\partial}{\partial z} \mu \frac{\partial v}{\partial z} \quad (12.3)$$

$$\rho u \frac{\partial w}{\partial x} + v \frac{\partial w}{\partial y} + w \frac{\partial w}{\partial z} = -\frac{\partial p}{\partial z} + \frac{\partial}{\partial x} \mu \frac{\partial w}{\partial x} + \frac{\partial}{\partial y} \mu \frac{\partial w}{\partial y} + \frac{\partial}{\partial z} \mu \frac{\partial w}{\partial z} \quad (12.4)$$

The buoyancy of the fluid as a function of density fluctuation (thermally induced) is computed in Eq. (12.5) using the Boussinesq approximation.

$$\rho = \rho_0 [1 - \beta(T - T_0)] \quad (12.5)$$

Equation (12.6) expresses energy in a control volume in a buoyantly induced flow. Conservation of energy:

$$C_p \rho \left(\frac{\partial(uT)}{\partial x} + \frac{\partial(vT)}{\partial y} + \frac{\partial(wT)}{\partial z} \right) = k \left(\frac{\partial^2 T}{\partial x^2} + \frac{\partial^2 T}{\partial y^2} + \frac{\partial^2 T}{\partial z^2} \right) + S_E \quad (12.6)$$

The RNG k-epsilon model, as represented in Eqs. (12.7) and (12.8), was used to calculate the turbulence in the SCPP's fluid flow.

RNG k-epsilon:

$$\frac{\partial}{\partial t}(\rho k) + \frac{\partial}{\partial x_i}(\rho k u_i) = \frac{\partial}{\partial x_j} \left[\alpha_k \mu_{eff} \frac{\partial k}{\partial x_j} \right] + G_k + G_b + \rho \varepsilon - Y_M + S_k \quad (12.7)$$

$$\frac{\partial}{\partial t}(\rho \varepsilon) + \frac{\partial}{\partial x_i}(\rho \varepsilon u_i) = \frac{\partial}{\partial x_j} \left[\alpha_\varepsilon \mu_{eff} \frac{\partial \varepsilon}{\partial x_j} \right] + C_{16} \frac{\varepsilon}{k} (G_k + C_{3\varepsilon} G_b) - C_{2z} \rho \frac{\varepsilon^2}{k} - R_\varepsilon + S_\varepsilon \quad (12.8)$$

The fluid turbulence parameters affecting the SSWT were computed using the SST k-omega model, as shown in Eqs. (12.9) and (12.10).

SST k-omega model:

$$\frac{\partial}{\partial t}(\rho k) + \frac{\partial}{\partial x_i}(\rho k u_i) = \frac{\partial}{\partial x_j} \left[(\Gamma_k) \left(\frac{\partial k}{\partial x_j} \right) \right] + \tilde{G}_k - Y_k + S_k \quad (12.9)$$

$$\frac{\partial}{\partial t}(\rho \omega) + \left(\frac{\partial}{\partial x_i} \right) (\rho \omega u_i) = \frac{\partial}{\partial x_j} \left[(T_\omega) \left(\frac{\partial \omega}{\partial x_j} \right) \right] + G_\omega - Y_\omega + D_\omega + S_\omega \quad (12.10)$$

The moment coefficient of the SSWT was determined using Eq. 12.11, where the moment of both blade moments was taken into account as expressed in Eq. 12.12.

Coefficient of moment:

$$C_M = \frac{M}{\frac{1}{2} \rho A R V^2} \quad (12.11)$$

$$M = M_1 + M_2 \quad (12.12)$$

The performance coefficient is expressed in Eq. (12.13) as the ratio of the SSWT's output power to the available wind power. The coefficient of performance is also shown as a function of the SSWT blades' angular speed, rotor radius, magnitude of the incoming velocity and moment coefficient.

Performance coefficient:

$$C_P = \frac{P_{turbine}}{P_{available}} = \frac{P}{\frac{1}{2} \rho A V^3} = \frac{M}{\frac{1}{2} \rho A R V^2} \frac{\omega_s R}{V} = C_M \lambda \quad (12.13)$$

The wind energy is stated in Eq. (12.14), where the incoming wind speed is the cube of the available power.

Available power in the wind:

$$P = \frac{1}{2} \rho A V^3 \tag{12.14}$$

Equation (12.15) depicts the conversion of wind energy to mechanical energy, where the SSWT’s performance coefficient is a function of the produced power.

Power generated by the wind turbine:

$$P = \frac{1}{2} \rho A V^3 C_P \tag{12.15}$$

12.3.3 Turbine Validation

The novel turbine geometry is adopted from the work of Roy and Saha [13], where the coordinates of the blade profile are reconstructed to a diameter of 0.25 m using SOLIDWORKS. A two-dimensional approach is taken to study the performance of the SSWT using ANSYS Fluent, where the SST k-omega turbulence model is adopted for a more accurate prediction of the flow separation and adverse pressure gradient. With the presence of the k-omega function, the turbulence model is able to solve near-wall regions with higher precision. The sliding mesh approach is implemented to enable turbine rotation with respect to the inlet free stream velocity. Figure 12.4 shows the turbine validation consisting of the turbine with diameter, D , circular domain (2D) and rectangular domain ($14D \times 8D$). A series of parametric studies are conducted to

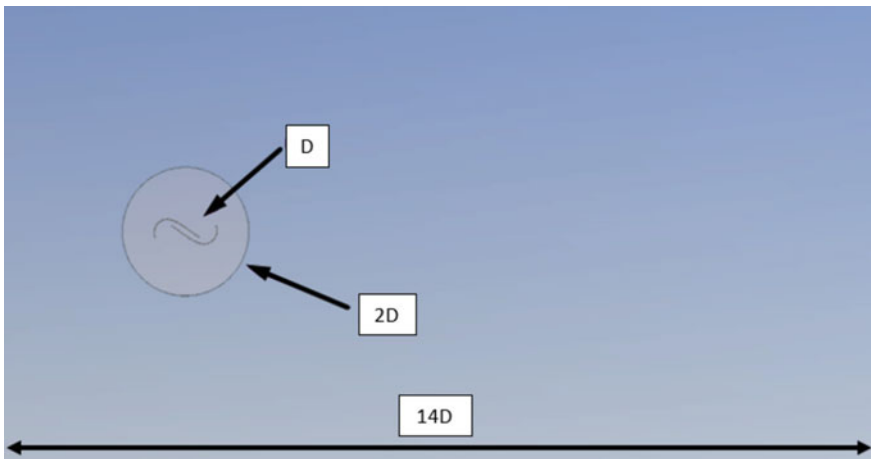


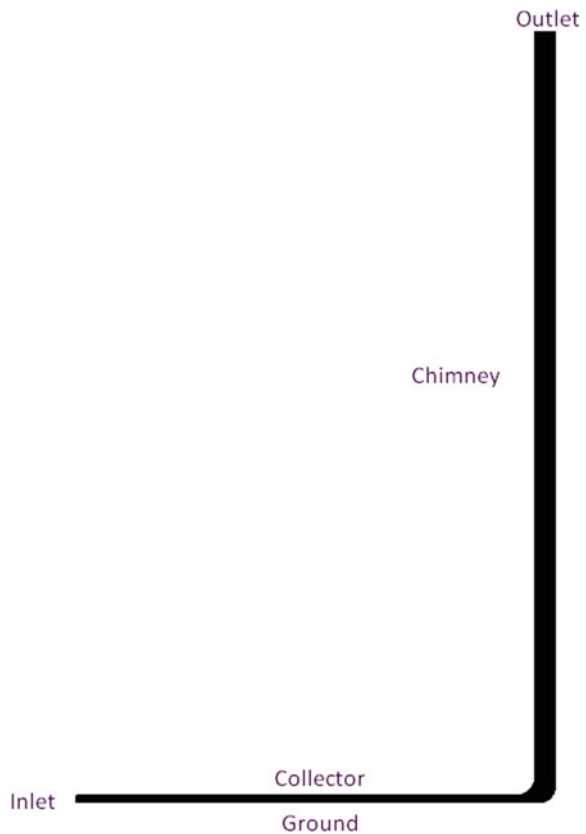
Fig. 12.4 Domain dimensions for the turbine validation

obtain the mesh leading to the closest solution accuracy. Grid independence test (GIT) is performed to obtain an accurate solution at minimal cost and computational time. Free stream velocity of 7.8 m/s is chosen with turbulent intensity and viscosity ratio of 5% and 10, respectively, based on medium-ranged wind speeds. The pressure–velocity interaction is deduced using the SIMPLE scheme. The geometry, domain dimensions and mesh settings used in the turbine validation are maintained to study the performance of the SSWT in the SCPP, where the height of the domain was altered to resemble the height of the collector region.

12.3.4 SCPP Validation

A two-dimensional axisymmetric SCPP structure is modelled using the dimensions obtained from the Manzanares plant [14, 15] as shown in Fig. 12.5. The triangular mesh is used to maintain an orthogonal quality closer to 1 and skewness lower than 1. The pressure-based solver was chosen with a steady-state 2D space, where the RNG

Fig. 12.5 Axisymmetric SCPP geometry



k-epsilon turbulence model with standard wall functions and full buoyancy effect was utilized in ANSYS Fluent. The discrete ordinates (DOs) and energy function are adopted for the radiation model and activation of thermal settings, respectively. The Boussinesq approximation was used to ensure the change in air density under the influence of fluid temperature. An atmospheric temperature of 293.15 K and pressure of 101,325 Pa are maintained. The inlet and outlet of the SSCP are set with a turbulent intensity of 5% for medium-ranged fluid flow and a turbulent length scale of 0.01 m that resembles a natural convective fluid flow.

12.4 Results and Discussion

12.4.1 Turbine Validation

Figure 12.6 shows the convergence of the GIT at 437,322 number at elements with a moment coefficient of 0.39, upon which the C_m value remained constant for a larger element number. Since the studied flow has a low Reynolds number, the average y^+ value is maintained below 1 for a better near-wall friction prediction and blade surface boundary layer detachment [16]. Figure 12.7 shows the validation of the present model to previous work where 4.85% and 16.82% error is obtained against the numerical model and experimental model, respectively. The discrepancies in values may have been due to mesh settings used and environmental fluid property fluctuation.

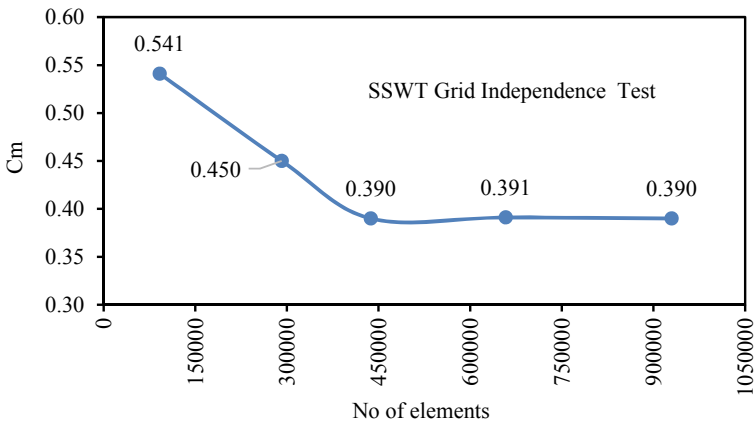


Fig. 12.6 Grid independence test for turbine validation

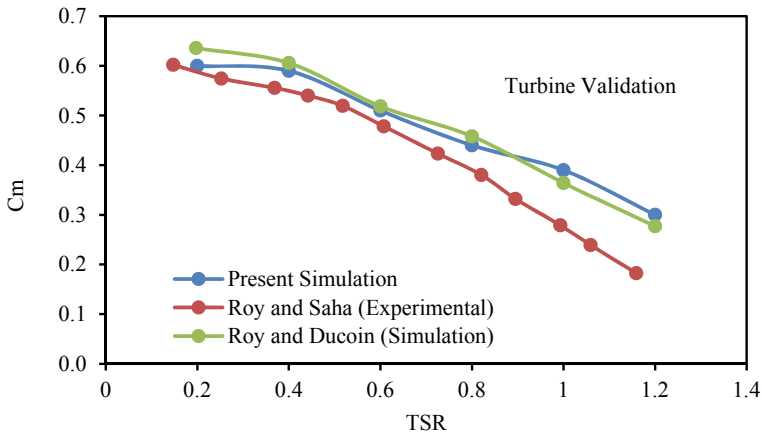


Fig. 12.7 Turbine validation against previous studies

12.4.2 SCPP Validation

A GIT is performed for the SCPP model where the smallest grid structure with the closest possible results accuracy is obtained at 249,696 number of elements. The results are validated against the experimental results from the Manzanares plant, where the chimney inlet velocity of 13.2 m/s and temperature rise of 22 °C is obtained. Figures 12.8 and 12.9 present the velocity and temperature profiles obtained with the averaged fluid flow velocity 9 m away from the chimney's centre.

12.4.3 Performance of SSWT in the SCPP

The operation of the SSWT in the collector region of the SCPP resulted in a moment coefficient of 0.35. At TSR 1.0, the performance coefficient produced is 0.35. The power output by the SSWT is 25.79 W for one turbine. Figure 12.10 shows the instantaneous moment coefficient plotted for one complete turbine rotation. The results suggest that performance of the SSWT is adversely affected by the negative torque starting with a drop at azimuthal angles 100°–130°. A similar occurrence is seen at azimuth angles 280°–310°. At azimuth angles 20°–30°, the peak moment coefficient is achieved by the SSWT. Similarly, azimuth angles 200°–210° exhibit similar maximum torque characteristics.

Four different azimuth angles were selected to study the fluid flow characteristics of the SSWT in the SCPP at TSR 1.0. These are azimuth angles 0°, 45°, 90° and 135°, where the velocity and pressure profiles are presented in Figs. 12.11 and 12.12, respectively. The curvature of the SSWT blade design allows better lift contribution compared to the conventional SSWT which can be seen in Fig. 12.11b. The Coanda

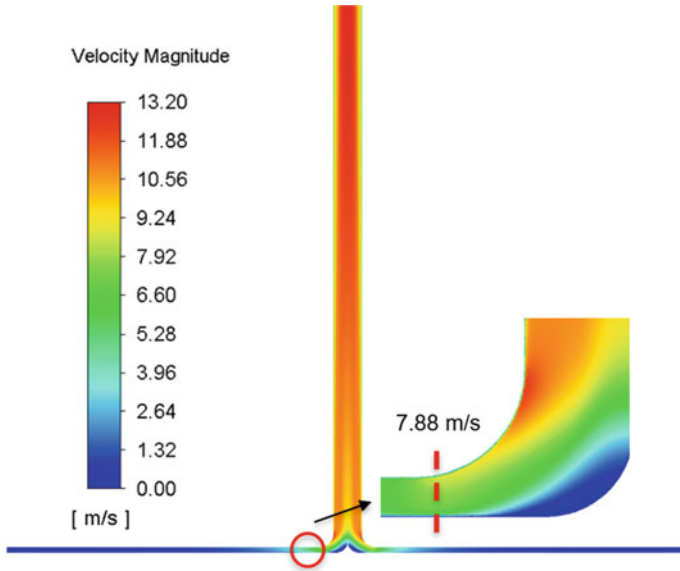


Fig. 12.8 SCPP velocity profile

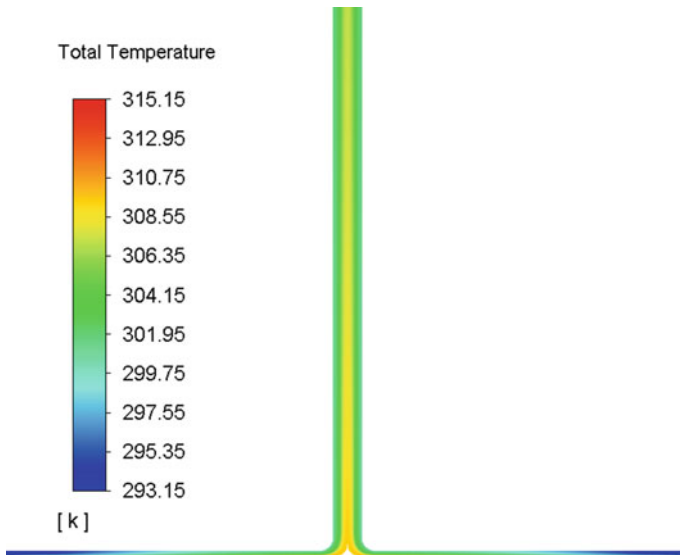


Fig. 12.9 SCPP temperature profile

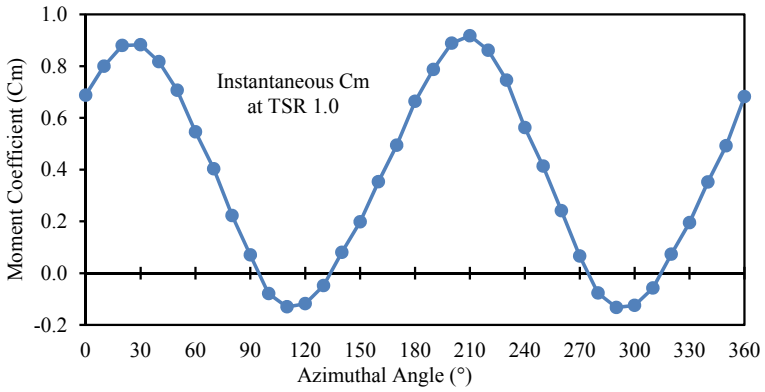


Fig. 12.10 Instantaneous moment coefficient at TSR 1.0

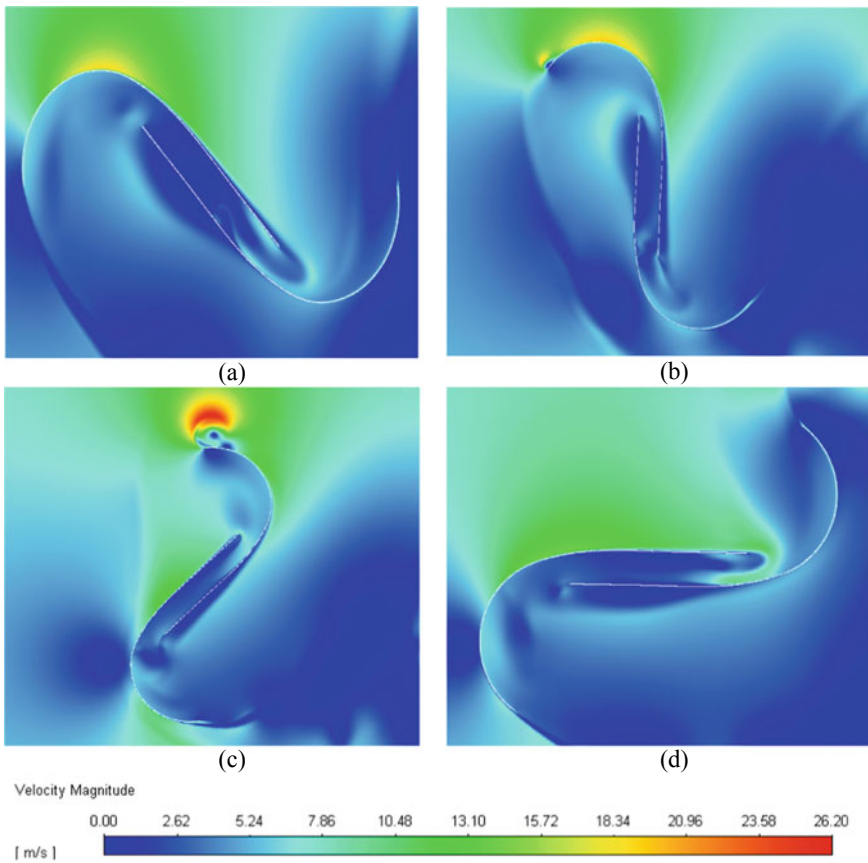


Fig. 12.11 Velocity magnitude contours at four azimuth angles a 0°, b 45°, c 90°, d 135°

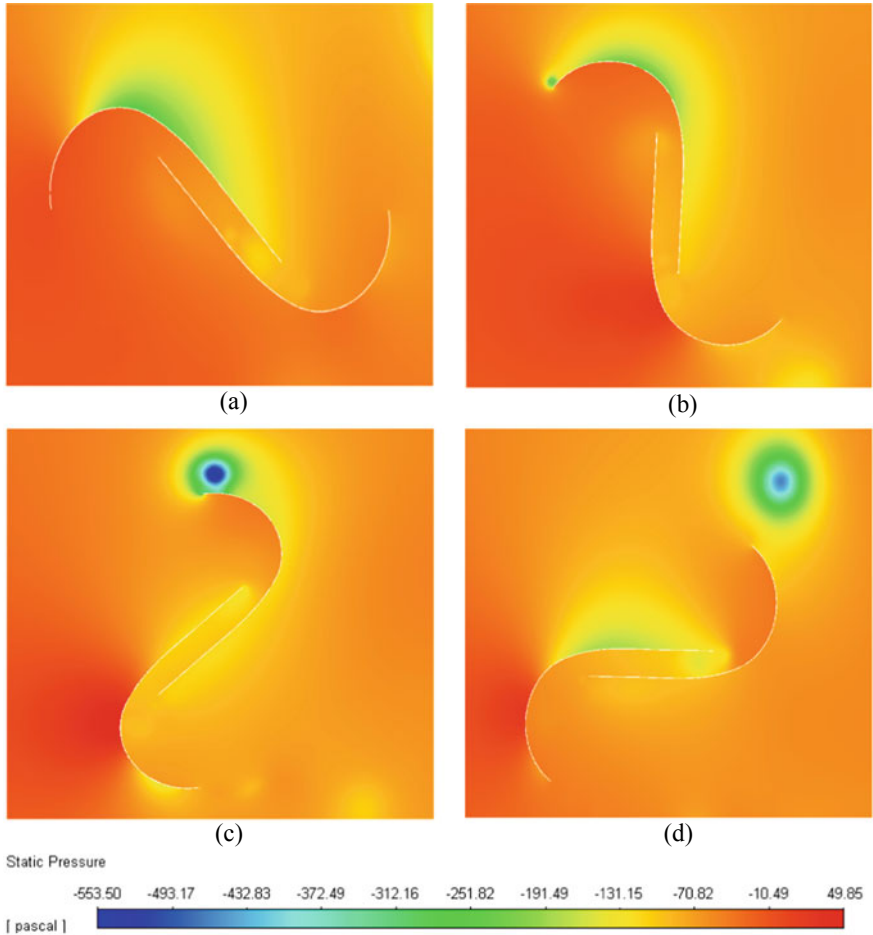


Fig. 12.12 Pressure profile at four azimuth angles **a** 0°, **b** 45°, **c** 90°, **d** 135°

effects are seen in Fig. 12.11a, b. This is due to the curvature of the SSWT which forms a lower pressure region on the surface of the blade during fluid flow as shown in Fig. 12.12a, b.

At 90° azimuthal angle, drag aids the operation of the rotor as a pressure difference between the concave and convex sides of the advancing blade is observed. However, a higher pressure on the convex of the returning blade suggests that the negative torque influence of the total torque produced is prominent. This is reflected by a lower moment coefficient at azimuth angle 90° as seen in Fig. 12.10. The poor lift and drag formation on the advancing blade at azimuth angle 135° as shown in Fig. 12.11d may have caused a lower positive torque formation. Moreover, the higher pressure on the convex of the negative blade suggests that the negative torque is highly influential

at this blade angle. As such, a total negative torque may have been formed at this azimuth angle which is seen in Fig. 12.10.

12.5 Conclusion

From the presented work, the SSWT is able to perform in the SCPP at a TSR of 1.0. The moment coefficient and performance coefficient obtained are 0.35, respectively, with a power output of 25.97 W. The power output can be attributed to the diameter of the SSWT, at 0.25 m, which is comparatively small in size as compared to the available volume of fluid flow. Hence, it is suggested that a larger SSWT diameter should be analysed for its performance and power generating characteristics. The performance of the SSWT is reduced due to the negative torque that adversely affects the overall torque generation at azimuth angles 100° – 130° and 280° – 310° . With optimization solutions such as deflectors, the effect of the negative torque can be minimized for higher power generation.

References

1. Moriarty, P., Honnery, D.: Global renewable energy resources and use in 2050. In: *Managing Global Warming*, pp. 221–235. Elsevier (2019)
2. Arzpeyma, M., et al.: Solar chimney power plant and its correlation with ambient wind effect. **141**(2), 649–668 (2020)
3. Kazi, J.: Design, fabrication and testing of VAWT w/Wind deflectors (2021)
4. Castellani, F., et al.: Experimental vibration analysis of a small scale vertical wind energy system for residential use. **7**(2), 35 (2019)
5. Schlaich, J.: *The Solar Chimney: Electricity from the Sun*. Edition Axel Menges (1995)
6. Esmail, M.F., et al.: A numerical comparative study of axial flow turbines for solar chimney power plant. **26**, 101046 (2021)
7. Zuo, L., et al.: Design and optimization of turbine for solar chimney power plant based on lifting design method of axial-flow hydraulic turbine impeller. **171**, 799–811 (2021)
8. Balijepalli, R., Chandramohan, V., Kirankumar, K.J.R.E.: Development of a small scale plant for a solar chimney power plant (SCPP): a detailed fabrication procedure, experiments and performance parameters evaluation. **148**, 247–260 (2020)
9. Rabehi, R., et al.: Numerical simulation of solar chimney power plant adopting the fan model. **126**, 1093–1101 (2018)
10. Negrou, B., et al.: Inverse design method of wind turbine in solar chimney power plants coupled with geothermal energy. In: *Exergy for A Better Environment and Improved Sustainability 1*, pp. 159–170. Springer (2018)
11. Zuo, L., et al.: Numerical analysis of wind supercharging solar chimney power plant combined with seawater desalination and gas waste heat. **223**, 113250 (2020)
12. Guo, P., et al.: Numerical study on the performance of a solar chimney power plant. **105**, 197–205 (2015)
13. Roy, S., Saha, U.K.: Wind tunnel experiments of a newly developed two-bladed Savonius-style wind turbine. *Appl. Energ.* **137**, 117–125 (2015)
14. Haaf, W., et al.: Solar chimneys part I: principle and construction of the pilot plant in Manzanares. *Int. J. Solar Energ.* **2**(1), 3–20 (1983)

15. Haaf, W.: Solar chimneys: part II: preliminary test results from the Manzanares pilot plant. *Int. J. Sustain. Energ.* **2**(2), 141–161 (1984)
16. Roy, S., Ducoin, A.: Unsteady analysis on the instantaneous forces and moment arms acting on a novel Savonius-style wind turbine. *Energ. Convers. Manage.* **121**, 281–296 (2016)

Chapter 13

Presentation of Real-Time Lab Analysis for Multiple-Area Renewable Sources-Thermal-Hydro System by Implementation of Cat Swarm Optimization



Arindita Saha, Lalit Chandra Saikia, Naladi Ram Babu, Sanjeev Kumar Bhagat, Manoj Kumar Behera, Satish Kumar Ramoji, and Biswanath Dekaraja

Abstract This work explores automatic generation control learning under traditional situation for a three-area system: Sources in area-1 are thermal–solar thermal (ST); thermal–geothermal power plant (GPP) in area-2; and thermal–hydro in area-3. The work involves various assessments in the presence of constraints such as governor rate constraint, governor dead band, and time delay. An original endeavor has been set out to execute cascade controller with amalgamation of proportional-derivative and fractional order integral-derivative (FOID), hence named as PD-FOID. The performance of PD-FOID has been compared with varied controllers like integral (I), proportional-integral (PI), and proportional-integral-derivative (PID). Various investigation express excellency of PD-FOID controller over other controller from outlook regarding lessened level of peak_overshoot (P_O), peak_undershoot (P_U), settling_time (S_T). A swarm-based meta-heuristic cat swarm optimization (CSO) algorithm is applied to acquire the controller’s gains and parameters. Action in existence of redox flow battery is also examined which provides with noteworthy outcome. PD-FOID parameter values at nominal condition are appropriate for higher value of disturbance without the need for optimization.

A. Saha

Department of Electrical Engineering, Regent Education and Research Foundation Group of Institutions, Kolkata, India

L. C. Saikia (✉) · S. K. Bhagat · M. K. Behera · S. K. Ramoji · B. Dekaraja

Department of Electrical Engineering, NIT Silchar, Silchar, India

e-mail: lcsaikia@yahoo.com

N. R. Babu

Department of Electrical and Electronics Engineering, Aditya Engineering College, East-Godavari, Andhra Pradesh 533437, India

13.1 Introduction

Automatic generation control (AGC) is primarily used to reduce the mismatch between load and generation units [1]. When this mismatch is broken, it causes frequency and tie-power aberrations. Early AGC research began with single-area systems [2] and progressed to multi-area systems [3]. The authors in [4, 5] presented thermal AGC systems with hydro and gas integration using GRC, reheat turbines, and GDB. Excess carbon emissions and the decline of fossil fuels are causing renewable energy to gain traction. Wind and solar power outnumber all other renewables. The integration of wind, geothermal, and solar thermal with thermal of two-area only was presented by the authors in [6–9]. As a result, research into the integration of geothermal and solar thermal in three-area systems is required.

The current AGC research focuses on secondary controller design. These controllers aid in the elimination of errors. AGC makes use of controllers such as integer order (PI, PID, PIDN) [15], fractional order (FOPI, FOPID) [16], tilt (TID) [17], and cascade of integer-fractional order controllers [8]. A new proportional-derivative and fractional order integral-derivative (FOID) cascade (PD-FOID) is proposed, which allows for comprehensive research.

When the controller's gains are optimized, the controller's performance will be at its peak. Classical and evolutionary algorithms can be used to accomplish optimization (EA). Tuning by hand is time-consuming and inefficient, whereas EAs produce the best results. Whale optimization [6], sine-cosine optimization [8], firefly optimization [18], biogeography optimization [19], particle swarm optimization [20], coyote optimization [21], and other EAs are accessible. There is a more recent EA named cat swarm optimization (CSO) algorithm [22–24]. It is based on the cat food-seeking behavior. Surprisingly, the use of CSO will be assessed in LFC research.

System dynamics during abnormal conditions can also be improved with the integration of energy storage devices (ESD). Integration of ESD such as UC [5], fuel cells [13], and RFB [14] can also improve system dynamic performance. The above LFC studies, however, do not include ACHVDC with RFB. Furthermore, there are no studies related to RFB in earlier literatures, necessitating future research.

Authors in [4, 26, 27] proposed sensitivity analysis (SA) based on deviations from nominal values in system characteristics such as inertia (H) and loading condition (LC). The SA of CSO optimized PI-FOID controller settings for the AGC system, on the other hand, is not reported. MATLAB software is used to mimic the AGC studies mentioned above. However, according to the literature, there is no validation of AGC investigations in a real-time simulation laboratory (RT-Lab). This opens up the possibility of more research.

From the above-mentioned literature, the objectives are as follows:

- (a) To develop an unequal three-area thermal integrated with solar thermal, geothermal, and hydro units.
- (b) Application of CSO algorithm for optimization of controller gains among controllers like I, PI, PID, and the proposed PD-FOID controller.

- (c) To perform SA and to check the robustness of the proposed controller.
- (d) Application of RFB in AGC studies.
- (e) Validation of the obtained results in RT-Lab software.

The following is a summary of the research paper: The first portion explains the introduction. In Sect. 13.2, a brief overview of the examined system under investigations is given. Section 13.3 explains the suggested PD-FOID controller and CSO algorithm. In Sect. 13.4, the results and analysis are explained, and in Sect. 13.5, the conclusion is given.

13.2 System Investigated

The considered system comprises of three-area thermal system integrated with solar thermal in area-1, geothermal in area-2, and hydro unit in area-3. The area capacity ratio of 1:2:3 is considered. GRC of 3%/min and droop of 4% are considered in thermal systems for realistic approach. The investigated system in Fig. 1a is provided with PD-FOID controller whose gains are optimized by CSO algorithm subjecting to ISE as performance index in (13.1) with area numbers as i, j , and k .

$$\eta_{ISE} = \int_0^t \{(\Delta F_j)^2 + (\Delta P_{j-k})^2\}.dt \quad (13.1)$$

13.3 Proposed Cascade PD-FOID Controller

A new cascade controller, namely PD-FOID, is proposed which is a combination of integer and fractional order controllers. The transfer function (TF) of PD-FOID is given by (13.2, 13.3).

$$TF_{PD} = K_{Pj} + K_{Dj1}s \quad (13.2)$$

$$TF_{FOID} = \frac{K_{Ij}}{s^{\lambda_j}} + K_{Dj2}s^{\mu_j} \quad (13.3)$$

The TF diagram of cascade PD-FOID controller is in Fig. 1b. The proposed PD-FOID controller gains are optimized by CSO with constraints in (13.4).

$$\left. \begin{aligned} 0 \leq K_{Pj}(\text{Proportional}) \leq 1, \quad 0 \leq K_{Dj1}, K_{Dj2}(\text{Derivative}) \leq 1 \\ 0 \leq K_{Ij}(\text{Integral}) \leq 1, \quad 0 \leq \lambda_j(\text{Integral parameter}) \leq 1 \text{ and} \\ 0 \leq \mu_j(\text{Derivative parameter}) \leq 1 \end{aligned} \right\} \quad (13.4)$$

13.4 Cat Swarm Optimization (CSO)

Chu et al. have developed a novel intelligence algorithm called cat swarm algorithm (CSA). It is inspired by natural behaviors of cats. Cats often look like lazy and most of their time spent in sleeping. During their sleep, they are highly alert and continuously observe their surroundings. So that when they see a target, they can run quickly toward the target. Basically, CSA works in two modes such as (a) seeking and (b) tracing behavior of cats. In seeking mode, the cats are sleeping but in stay in alert mode toward target in order to next move. However in tracing mode, cats continuously tracing the target. In CSA, each cat has its own position: velocity in N dimension search space. The fitness values of each cats are calculated in each iteration, and best fitness value are considered as a solution.

The mathematical expression for velocity and fitness value of each cats is given by (13.5)–(13.7)

$$V_{k,d} = V_{k,d} + r_1 c_1 (X_{\text{best}} - X_{k,d}) \quad (13.5)$$

Update the position of each cat by using (13.6)

$$X_{k,d} = X_{k,d} + V_{k,d} \quad (13.6)$$

where position (X), velocity (V) with fitness value is calculated by (13.7).

$$F_i = \frac{|FS_i - FS_b|}{FS_{\text{max}} - FS_{\text{min}}} \quad (13.7)$$

where $FS_b = FS_{\text{max}}$ (for minimization problem) and $0 < i < 1$. The flowchart of CSO is shown in Fig. 1c.

13.5 Results and Analysis

The performance of multi-area AGC system is integrated with solar thermal, geothermal, and hydro units and is provided with controllers like I, PI, PID, and PD-FOID. AGC system is evaluated in MATLAB and validated with RT-Lab software using ode4. Simulations are carried by controller with CSO optimized technique. Controller with optimum values are linked with RT-Lab, and the results are to be compared with MATLAB. The execution of LFC model in RT-Lab is compiled and is shown in Fig. 13.1.

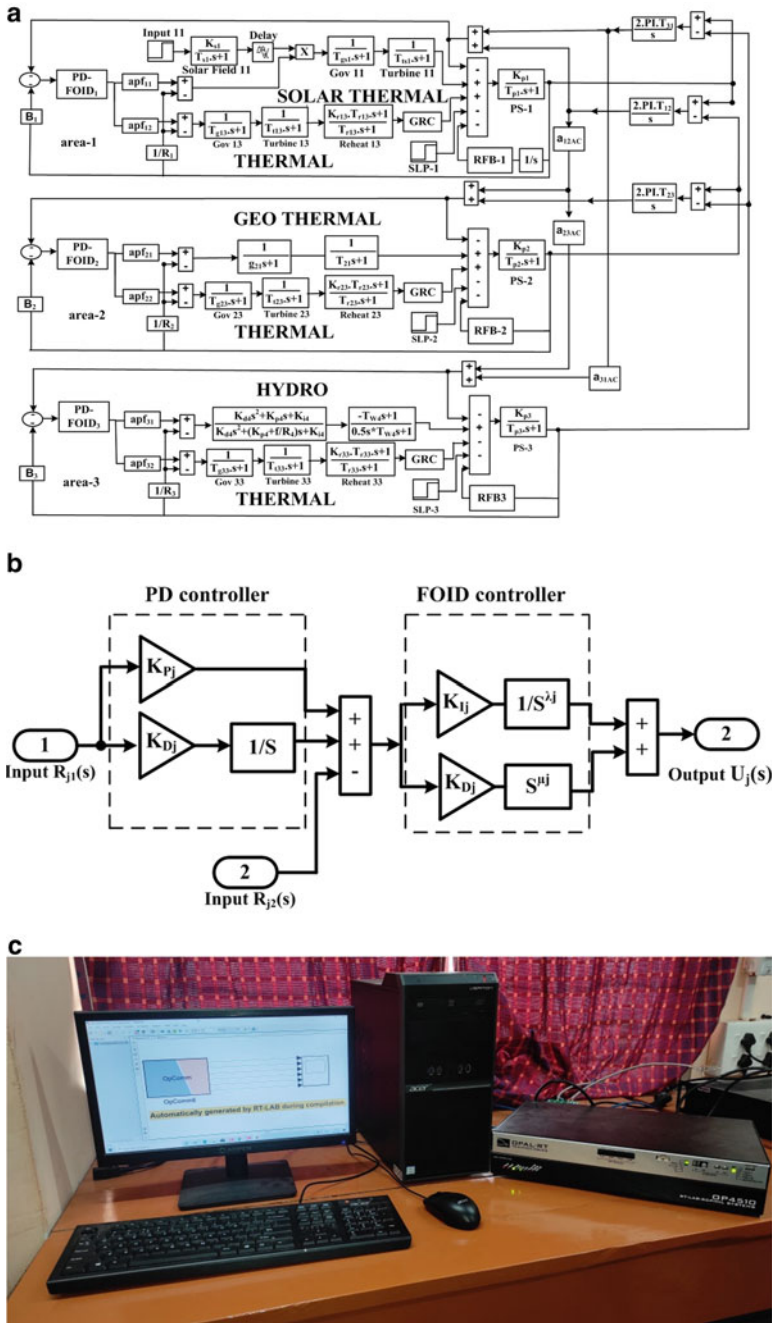


Fig. 13.1 (a) The investigated three-area thermal system model, (b) The proposed cascade PD-FOID controller, (c) Hardware setup of RT-Lab

Table 13.1 CSO optimized controller gains of thermal system considering ISE

PI controller						
	K_{Pj}			K_{Ij}		
Area-1	0.6212			4.2090		
Area-2	0.0591			3.6985		
Area-3	0.4612			4.8450		
PID controller						
	K_{Pj}			K_{Ij}	K_{Dj}	
Area-1	0.4066			0.3920	0.1843	
Area-2	0.7380			0.1120	0.8466	
Area-3	0.9580			0.1694	0.3752	
PD-FOID controller						
	K_{Pj}	K_{D1j}	K_{Ij}	λ_j	K_{D2j}	μ_j
Area-1	0.4841	0.8209	0.3167	5.0136	0.0571	0.3288
Area-2	0.5802	0.1797	0.8103	7.1903	0.4100	0.8729
Area-3	0.5981	0.6388	0.7724	6.2639	0.8801	0.7384

13.5.1 System Dynamics with Thermal System

13.5.1.1 Controller Comparison Among PI, PID, and PD-FOID in Thermal Systems

The three-area thermal system in Fig. 1 with capacity ratio of 1:2:4 is considered and provided with controllers like PI, PID, and the proposed PD-FOID controllers. The controller gains are optimized by CSO considering ISE. The obtained optimum gains are listed in Table 13.1, and their respective responses are shown in Fig. 13.2a, b. Careful observations of Fig. 13.2 explore that the responses with PD-FOID show better responses.

13.5.1.2 System Dynamics with the Application of RT-Lab Software

The system in Sect. 13.1 is investigated with PD-FOID controller and ISE whose gains are optimized by CSO. The optimized parameters of controller are noted in Table 13.1a considering CSO from MATLAB software are swapped by a virtual plant in software in loop and are interlinked with hardware in the loop in OP4510 simulator. The obtained dynamics considering RT-Lab are compared with MATLAB software and are shown in Fig. 13.3a, b. It is noticed that the dynamic responses with RT-Lab outperform over MATLAB software. Hence in rest of the paper, investigations are carried out with the RT-Lab software.

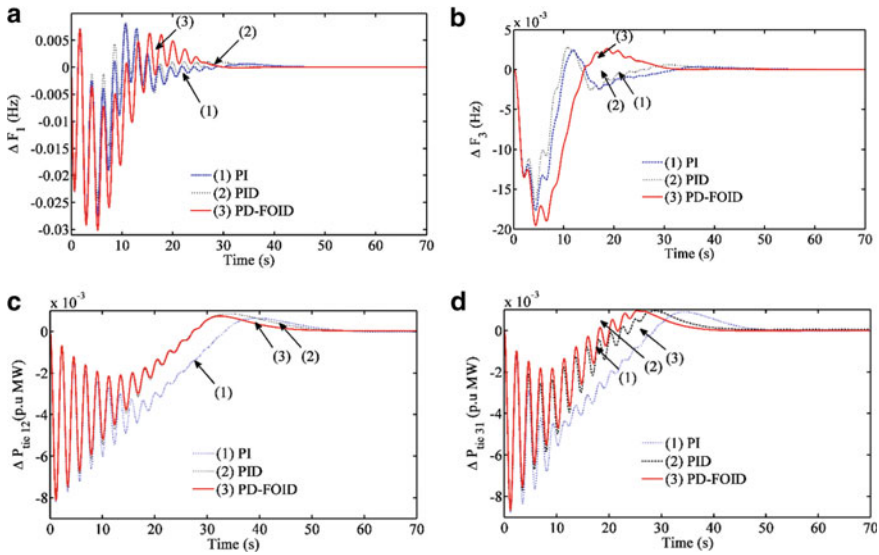


Fig. 13.2 System dynamics with three-area thermal system **a** ΔF_1 , **b** ΔF_3 , **c** ΔP_{12} , and **d** ΔP_{31} with MATLAB

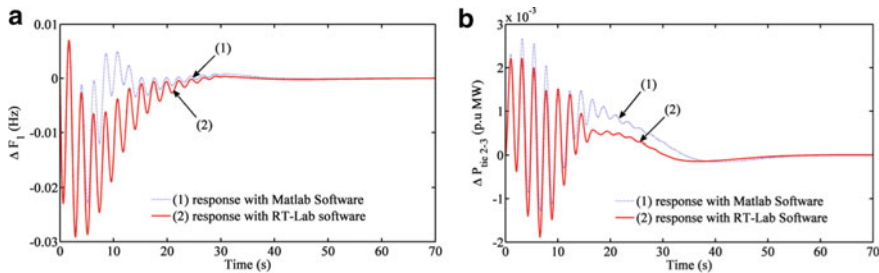


Fig. 13.3 System dynamics with three-area thermal system **a** ΔF_1 and **b** ΔP_{23} with MATLAB and RT-Lab

13.5.1.3 System Dynamics with Integration of Solar Thermal, Geothermal, and Hydro Units

Thermal system in Sects. 5.1.1 and 5.1.2 is integrated with solar thermal in area-1, geothermal in area-2, and hydro unit in area-3. PD-FOID controller is provided and is optimized with CSO technique. Its optimum gains are listed in Table 13.2, and its corresponding dynamics are plotted in Fig. 13.4. Critical observations explore that the responses with solar thermal, geothermal, and hydro unit's integration show better responses.

Table 13.2 CSO optimized PD-FOID controller gains with integration of solar thermal, geothermal, and hydro units

	K_{Pj}	K_{D1j}	K_{Ij}	λ_j	K_{D2j}	μ_j
Area-1	0.0230	0.1222	0.1164	2.0970	0.0417	0.2482
Area-2	0.1466	0.3136	0.3307	7.0064	0.8992	0.4131
Area-3	0.7176	0.5498	0.0575	2.0224	0.3975	0.5370

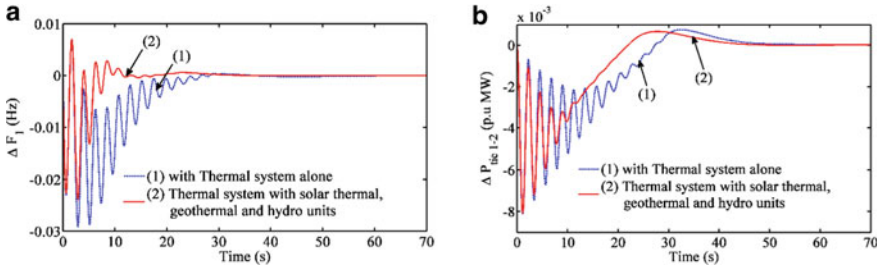


Fig. 13.4 Comparison of system dynamics with the integration of solar thermal, geothermal, and hydro units **a** ΔF_1 and **b** ΔF_1 in RT-Lab software

Table 13.3 CSO optimized PD-FOID controller gains with the integration of RFB units

	K_{Pj}	K_{D1j}	K_{Ij}	λ_j	K_{D2j}	μ_j
Area-1	0.7423	0.1084	0.5779	0.9268	0.2111	0.2497
Area-2	0.1525	0.0019	0.8729	0.5243	0.4298	0.8548
Area-3	0.7507	0.0389	0.9579	0.8559	0.4603	0.7561

13.5.1.4 System Dynamics with the Integration of RFB

System in Sect. 5.1.3 is integrated with RFB and is provided with PD-FOID controller whose gains are optimized by CSO. The optimum values are listed in Table 13.3. Responses with and without RFB systems in RT-Lab software are compared with RT-Lab and illustrated in Fig. 13.5a, b. From Fig. 13.5, it is observed that responses with RFB system show better responses.

13.5.1.5 Sensitivity Analysis of Thermal System Integrated with Solar Thermal, Geothermal, Hydro, and RFB Units with PD-FOID Controller

System in Fig. 1 is considering and is subjected to variations in inertia constant (H), i.e., $\pm 15\%$ from nominal values. In this case, PD-FOID controller is provided and investigation is carried out in RT-Lab software. The obtained responses are illustrated in Fig. 13.6. From Fig. 13.6, it is observed that variations in inertia conditions, the

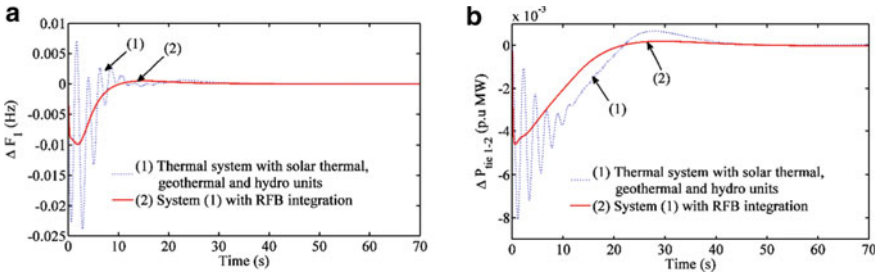


Fig. 13.5 Comparison of system dynamics with RFB integration **a** ΔF_1 and **b** ΔP_{tie1-2} with the application of RT-Lab software

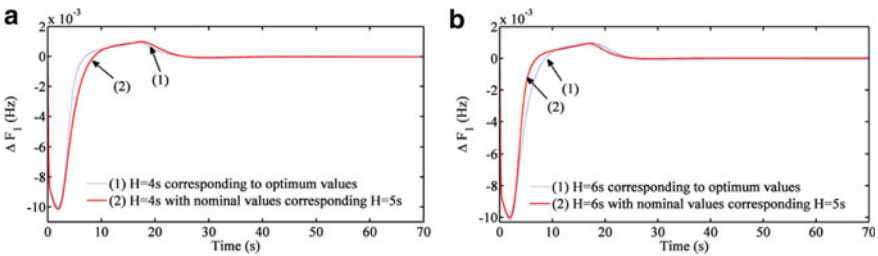


Fig. 13.6 SA condition with variation in H at 15% from nominal values **a** ΔF_1 and **b** ΔP_{12} with RT-Lab

responses are more or less same. From this, we can conclude that, the proposed controller is robust.

13.6 Conclusions

A maiden attempt has been made to utilize the RT-Lab software in AGC studies. Investigations are performed with a new controller, namely PD-FOID controller, and its values are optimized by novel technique named by cat swarm optimization. Studies with PD-FOID controller outperform over others like PI and PID controllers. It is also evident that the system dynamics with the application of RT-Lab outperforms over MATLAB results. Moreover, integration of solar thermal in area-1, geothermal in area-2, and hydro units in area-3 with thermal systems shows better responses over thermal. Further incorporation of RFB improves system dynamics. Sensitivity analysis with inertia variations suggests that proposed PD-FOID controller is robust. Furthermore, the system dynamics obtained with MATLAB are validated with RT-Lab software and its responses outperform over MATLAB software.

Appendix

Nominal system Parameters: $F = 60$ Hz, $T_{jk,AC} = 0.086$ pu MW/rad, $H_j = 5$ s, $K_{pj} = 120$ Hz/MW pu, $D_j = 8.33 \times 10^{-3}$ pu MW/Hz, $B_j = 0.425$ pu MW/Hz, $R_j = 2.4$ pu MW/Hz, $T_{gj} = 0.08$ s, $T_{ij} = 0.3$ s, $T_{rj} = 10$ s, $K_{rj} = 0.5$ s, $T_{pj} = 20$ s, $K_{sj} = 1.8$, $T_{sj} = 1.8$ s, SLP = 1%, loading = 50%, $P_{r1} = 1000$ MW, $P_{r2} = 2000$ MW, $K_{DC} = 0.5$, $T_{DC} = 0.03$ s A.

References

1. Elgerd, O.I.: *Electric Energy Systems Theory: An Introduction*. Tata McGraw-Hill, New Delhi (2007)
2. Kundur, P.: *Power System Stability and Control*, 5th edn. Tata McGraw Hill, New Delhi (1993)
3. Golpira, H., Bevrani, H., Golpira, H.: Application of GA optimization for automatic generation control design in an interconnected power system. *Energ. Convers. Manage.* **52**, 2247–2255 (2011)
4. Nanda, J., Mangla, A., Suri, S.: Some new findings on automatic generation control of an interconnected hydrothermal system with conventional controllers. *IEEE Trans. Energ. Convers.* **21**(1), 187–194 (2006)
5. Javad, M., Kazem, Z., Mehrdad, T.H.: Applying fractional order PID to design TCSC-based damping controller in coordination with automatic generation control of interconnected multi-source power system. *Eng. Sci. Technol. Int. J.* **20**(1), 1–17 (2017)
6. Saha, A., Saikia, L.C.: Utilization of ultra-capacitor in load frequency control under restructured STPP-thermal power systems using WOA optimized PIDN-FOPD controller. *IET Gener. Transm. Distrib.* **11**(13), 3318–3331 (2017)
7. Sharma, Y., Saikia, L.C.: Automatic generation control of a multi-area ST-thermal power system using Grey Wolf Optimizer algorithm based classical controllers. *Int. J. Electr. Power Energ. Syst.* **73**, 853–862 (2015)
8. Tasnin, W., Saikia, L.C.: Maiden application of an sine-cosine algorithm optimised FO cascade controller in automatic generation control of multi-area thermal system incorporating dish-Stirling solar and geothermal power plants. *IET Renew. Power Gener.* **12**(5), 585–597 (2018)
9. Saikia, L.C., Chowdhury, A., Shakya, N., Shukla S., Soni, P.K.: AGC of a multi area gas-thermal system using firefly optimized IDF controller. In: *Annual IEEE India Conference (INDICON)*, Mumbai, pp. 1–6 (2013)
10. Adeuyi, O.D., et al.: Frequency support from modular multilevel converter based multi-terminal HVDC schemes. In: *IEEE Power and Energy Society General Meeting*, Denver, CO, pp. 1–5 (2015)
11. Rakhshani, E., Rodriguez, P.: Inertia emulation in AC/DC interconnected power systems using derivative technique considering frequency measurement effects. *IEEE Trans. Power Syst.* **32**(5), 3338–3351 (2017)
12. Singh, O., Nasiruddin, I.: Optimal AGC regulator for multi-area interconnected power systems with parallel AC/DC links. *Cogent Eng. J.* **3**(1) (2018)
13. Sharma, G., Ibraheem, Niazi, K.R., Bansal R.C.: Adaptive fuzzy critic based control design for AGC of power system connected via AC/DC tie-lines. *IET Gener. Transm. Distrib.* **11**(2), 560–569 (2016)
14. Sharma, G., Nasiruddin, I., Niazi, K.R.: Robust automatic generation control regulators for a two-area power system interconnected via AC/DC tie-lines considering new structures of matrix Q. *IET Gener. Transm. Distrib.* **10**(14), 3570–3579 (2016)

15. Jagatheesan, K., Anand, B., Samanta, S., Dey, N., Ashour, A.S., Balas, V.E.: Design of a proportional-integral-derivative controller for an automatic generation control of multi-area power thermal systems using firefly algorithm. *IEEE/CAA J. Automatica Sinica*. <https://doi.org/10.1109/JAS.2017.7510436>
16. Pan, I., Das, S.: Fractional order AGC for distributed energy resources using robust optimization. *IEEE Trans. Smart Grid* **7**(5), 2175–2186 (2016)
17. Topno, P.N., Chanana, S.: Tilt integral derivative control for two-area load frequency control problem. In: 2nd International Conference on Recent Advances in Engineering and Computational Sciences, pp. 1–6 (2015)
18. Raju, M., Saikia, L.C., Sinha, N., Saha, D.: Application of antlion optimizer technique in restructured automatic generation control of two-area hydro-thermal system considering governor dead band. In: *Innovations in Power and Advanced Computing Technologies*, Vellore, pp. 1–6 (2017)
19. Rahman, A., Saikia, L.C., Sinha, N.: Load frequency control of a hydro-thermal system under deregulated environment using biogeography-based optimised three-degree-of freedom integralderivative controller. *IET Gener. Transm. Distrib.* **9**(15), 2284–2293 (2015)
20. Huang, K.-W., Wu, Z.-X.: CPO a crow particle optimization algorithm. *Int. J. Comput. Intell. Syst.* **12**(1), 426–435 (2018)
21. Pierezan, J., Dos Santos Coelho, L.: Coyote optimization algorithm: a new metaheuristic for global optimization problems. In: *IEEE Congress on Evolutionary Computation*, Rio de Janeiro, pp. 1–8 (2018)
22. Babu, N.R., Saikia, L.C.: Automatic generation control of a solar thermal and dish-Stirling solar thermal system integrated multi-area system incorporating accurate HVDC link model using crow search algorithm optimised FOPI Minus
23. Babu, N.R., Saikia, L.C.: AGC of a multiarea system incorporating accurate HVDC and precise wind turbine systems. *Int. Trans. Electr. Energ. Syst.* 1–18 (2019)
24. Askarzadeh, A.: A novel metaheuristic method for solving constrained engineering optimization problems: crow search algorithm. *J. Comput. Struct.* **169**, 1–12 (2016)
25. Pathak, N., Hu, Z.: Hybrid-peak-area-based performance index criteria for AGC of multi-area power systems. *IEEE Trans. Industr. Inf.* **15**(11), 5792–5802 (2019)
26. Rahman, A., Saikia, L.C., Sinha, N.: AGC of dish-Stirling solar thermal integrated thermal system with biogeography based optimised three degree of freedom PID controller. *IET Renew. Power Gener.* **10**(8), 1161–1170 (2016)
27. Dash, P., Saikia, L.C., Sinha, N.: Comparison of performances of several FACTS devices using Cuckoo search algorithm optimized 2DOF controllers in multi-area AGC. *Electr. Power Energ. Syst.* **65**, 316–324 (2015)

Chapter 14

Impact of Electric Vehicles and Wind Turbine in Combined ALFC and AVR Studies Using AFA-Optimized CFPD-PIDN Controller



Biswanath Dekaraja, Lalit Chandra Saikia, Satish Kumar Ramoji, Manoj Kumar Behera, Sanjeev Kumar Bhagat, Arinditi Saha, and Naladi Ram Babu

Abstract Sophisticated technology developments and numerous ancillary services in the modern smart grid are taking part in electric vehicles (EVs). In the competitive electric market, EVs provide superior power management services. EV is a new distributed energy storage and can be used to compensate for power mismatch. This article discusses the significant impact of EVs on the unified control of voltage and frequency in a three-area thermal system including a wind turbine into all areas. A new cascade fuzzy PD and PID with filter coefficient (N) (CFPD-PIDN) controller, EVs and wind system are provided in all areas for combined voltage and frequency control under various investigations. Artificial flora algorithm is employed to obtain the CFPD-PIDN controller gains and other parameters under numerous scenarios. Various simulations are performed to validate the superiority of the proposed control strategy.

14.1 Introduction

The integration of renewable energy sources (RESs) in the power grid increases all over the world and causes frequency and voltage stability problems. The system inertia is gradually reduced when more and more RESs are connected to the power grid. Although, the interconnected power system enhances system inertia to some extent; the frequency and voltage deviate from their schedule value when power mismatch occurs. Automatic load frequency control (ALFC) is used to maintain system frequency within the desirable limit, whereas the system voltage is controlled by an automatic voltage regulator (AVR). However, the published articles [1–9] have been investigated the secondary frequency control in presences of RESs such as wind, solar thermal power plant, dish-Stirling thermal systems under ALFC scenarios. The

B. Dekaraja (✉) · L. C. Saikia · S. K. Ramoji · M. K. Behera · S. K. Bhagat · A. Saha · N. R. Babu
Department of Electrical Engineering, National Institute of Technology, Silchar, Assam, India
e-mail: biswaju10@gmail.com

AVR loop is not considered in the above studies. In the realistic power system, there is a weak coupling between the ALFC loop and AVR loop for a small-signal analysis [10, 11]. Hence, it needs further studies.

A lot of research articles were published on the combined voltage and frequency control under conventional power systems [12–29]. The authors in [12, 13] presented an isolated thermal system in an amalgamated ALFC loop and AVR loop without considering the physical constraints of the plant. Governor dead band (GDB), communication delay (CTD), generation rate (GRC), boiler dynamics (BD) constraints are the physical constraints equipped with the plants to make the system more realistic. Two-area hydrothermal systems were investigated in [14, 15] considering BD and GDB for thermal plants. The authors in [16] presented two-area hydrothermal systems considering GRC and GDB for both plants. The participation of RESs can be compensated for the power mismatch and improve the system dynamics under ALFC [4, 5]. The authors in [17] had studied two test systems; test system-1 was a two-area thermal system without nonlinearities and test system-2 was a two-area system having reheat thermal plant, hydro, gas turbine, diesel, wind and solar photovoltaic plant with appropriate GRC for both thermal and hydroplants. Two-area thermal systems incorporating wind turbine in area-1 and PV arrays in area-2 are investigated in [18] considering the suitable value of GRC, GDB, and CTD. The authors in [19] presented an interconnected power system having thermal, solar thermal plant (STP) and small hydroplant (SHP) with proper system nonlinearities constraint for thermal plant. The authors in [20] have studied three-area multisource systems based on thermal, hydro, wind, STPP, and geothermal power plants (GTPP) considering GDB and GRC for both hydrothermal plants. The authors in [21] investigated three-area thermal-diesel-STPP systems considering suitable values of GDB and GRC for the thermal unit. From the comprehensive literature, it is seen that limited studies have been conducted on multiarea thermal systems incorporating RESs. Hence, there is a potential scope to explore for the same.

A large number of RESs integrated into the power grid cause some problems in an interconnected power system, e.g. frequency fluctuations and distribution voltage rise. Energy storage system (ESS) is one of the solutions to these problems. The authors in [22, 23] studied the performance comparison of various ESS such as capacitive energy storage (CES), superconducting magnetic energy storage (SMES), flywheel, redox flow battery (RFB), and ultra-capacitor on the system dynamic response under ALFC scenario. The authors in [24–26] investigated the effect of SMES on the system dynamic response in the combined ALFC-AVR system. Impact of SMES and CES on the combined ALFC-AVR system was studied in [27]. Moreover, the performance analysis of RFB in the combined ALFC-AVR system was investigated in [20]. Due to the high cost of an energy storage system (ESS), an application of controllable loads like electric vehicles (EVs) to the power system is used to reduce the required capacity of ESS [2].

Due to environmental concerns and the continuing fossil fuels depletion, the usage of EVs has been encouraged in the present years. Researchers have discovered that EVs are the alternative energy source for automobiles, given the rapid rise in petroleum prices and the ever-increasing global climate change, both of which

are producing severe environmental difficulties. Large-scale integration of aggregate EVs into the power grid for charging/discharging and referred to as a large power plant. The authors in [2, 5–7, 28] proposed the new control strategy of the EVs model for the load frequency control. From the literature, it is seen that the implementation of EVs is confined merely to ALFC studies. However, to date, no studies have been conducted considering EVs in the combined ALFC-AVR system.

When EV aggregators engage in combined ALFC-AVR systems, it is critical to design a suitable controller to handle the influence of time-changing delayed reactions of electric vehicles on the stability in the combined systems. Hence, the researchers are mainly highlighted to design a supplementary controller for the ALFC loop as well as the AVR loop's controller. In the literature, conventional controllers such as integral controller [11–13], proportional–integral–derivative (PID) [14, 17, 18], fractional-order PID [15], fractional-order PI [16], TDOF-PID and PID with filter multistage controller [19], cascade FOPDN-FOPIDN [20], and integral-double-derivative with filter [21] have been implemented successfully in combined ALFC-AVR studies. The cascade controller provided better system performance compare to a single-loop controller [4, 6, 20]. A new fuzzy-based cascade controller called fuzzy PD-PID with filter coefficient (N), CFPD-PIDN, is proposed for ALFC loop and integer-order PID with filter (PIDF) controller for AVR loop. The controller performs effectively when its various control parameters are optimal. The conventional optimization techniques may fail to obtain the optimal values due to the system complexity or in a large search space. Hence, the researchers have been employed different meta-heuristic optimization algorithms such as simulated annealing [14], moth flame optimization [15], artificial flora algorithm (AFA) [20], lightning search algorithm [21], etc. to optimize the controller gains in the amalgamated ALFC-AVR pattern. In this study, an AFA is applied to optimize the various control parameters of the suggested CFPD-PIDN controller under numerous studies. Moreover, from the literature survey, it is found that the fuzzy logic controller (FLC)-based PID [7, 8] controller has selected input/output scaling factors (SFs) after going through several trials and hit runs. The FLC performance depends on the appropriate selection of SFs and the optimum value of the SFs may not possible to obtain from the hit and trial method. The inputs/output SFs of the FLC are optimized employing a recently developed optimization algorithm called AFA [29].

In various literature in the unified ALFC-AVR model, every controller gains and other control parameters are optimized at 50% system loading using several optimization techniques by minimizing performance index having a 1% step load disturbance (SLD). But, in a realistic environment, the system may face several disturbances which can affect the system's dynamic responses. Hence, in the literature, the analysis of sensitivity has been conducted to substantiate the sturdiness of the ALFC loop's controller by the researchers. The authors in [20] studied the durability of the ALFC loop's controller by unevenly the system loading condition and system parameters. In this study, the proposed controller robustness will be tested by varying system loading conditions, change in magnitude of SLD, and partially removing EVs from the system.

From the above comprehensive literature review, the following are the main objectives.

- (a) Develop three-area thermal-wind systems incorporating EVs in combined ALFC-AVR model with appropriated physical constraints like CD and GRC for the thermal unit.
- (b) To optimize various control parameters of the CFPD-PIDN and PIDN controller for ALFC loop's using AFA to find superior one.
- (c) Analyse the effect of EVs and wind turbine on the proposed system with the best controller obtained in (b).
- (d) Analysis of sensitivity will be conducted to authenticate the robustness of the best controller in (b).

14.2 Methodology

The methodology of the study is as follows. It comprises a system investigation, relationship between ALFC and AVR, modelling of EV, and proposed controller followed by an optimization algorithm.

14.2.1 System Investigation

The study system comprises three unequal areas having thermal and wind in all areas incorporating EVs. For the system investigation, the rated capacity of area-1 = 2000 MW, area-2 = 4000 MW, and area-3 = 8000 MW is considered. GRC and GDB of the thermal unit are taken as 3% p.u. MW/m, and 0.036 Hz, respectively. Figure 14.1 shows the transfer function model of the study system. The area participation factor (apf) is taken as $\text{apf}_{11} = \text{apf}_{21} = \text{apf}_{31} = 0.7$ and $\text{apf}_{12} = \text{apf}_{22} = \text{apf}_{32} = 0.3$, where first and second subscripts indicate the control area and its plant. An aggregate EVs model consists of participation factors, time delay, and dynamic model of battery ESS shown in Fig. 14.2a. For each control area, the load frequency control (LFC) signal is used as an input to EVs for charging/discharging. To investigate the system dynamics, 1% step load disturbance (SLD) is applied in Area-1 at time 1 s at 50% system loading. The proposed controller, along with PIDN controller parameters, is optimized using AFA. The optimum values of the proposed controller parameters are obtained using AFA by minimizing integral square error (ISE), integral absolute error (IAE), integral time absolute error (ITAE), and integral time square error (ITSE) performance indices. The other PIs are given in (14.12)–(14.14). To optimize the various controller parameters, J_1, J_2, J_3 , and J_4 are considered as a cost function given in (14.1).

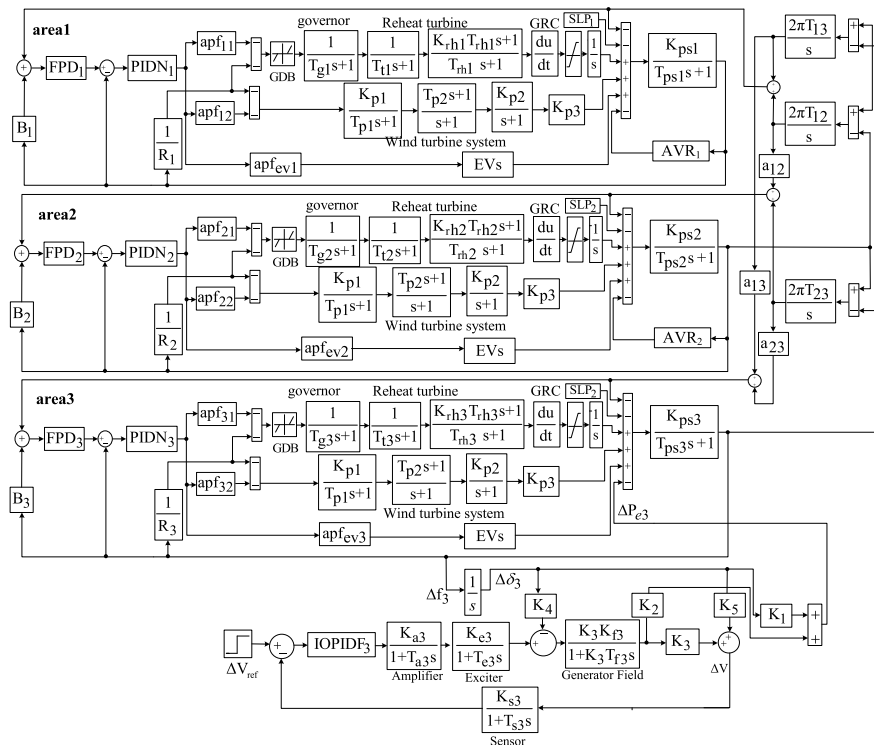


Fig. 14.1 Proposed three-area thermal-wind unified ALFC-AVR system

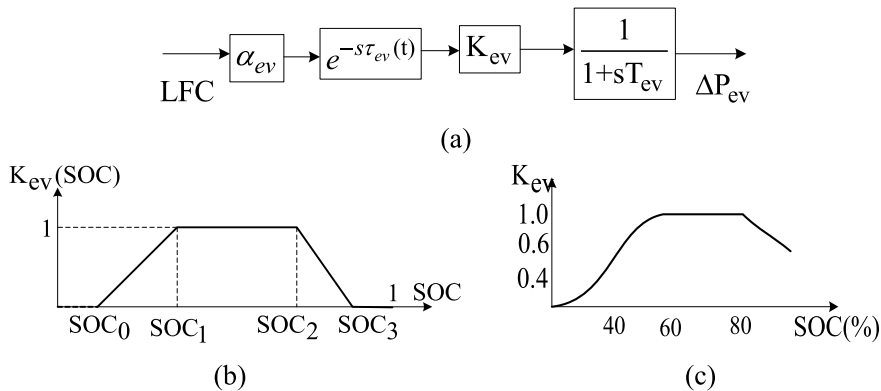


Fig. 14.2 a Schematic diagram of EV model, b mode of operation of EV, c K_{ev} varies with SOC

$$\text{Min } J_1 = \int_0^T (\Delta f_i^2 + \Delta P_{\text{tie},i,j}^2 + \Delta V_i^2) dt \quad (14.1)$$

where $i, j = 1, 2$ and $i \neq j$, T is the simulation time (120 s), Δf_i , ΔV_i , and $\Delta P_{\text{Tie } ij}$ are the frequency, voltage deviation of area i , and tie-line power deviation between area i and area j , respectively.

14.2.2 ALFC and AVR Loops Interaction

The objective of combined ALFC-AVR loops in an interconnected power system is to maintain the synchronous generator's system frequency and terminal voltage within prescribed limits. The AVR loop composes four elementary components such as exciter, generator, amplifier, and sensor. The AVR dynamics settle before they make themselves in a slower ALFC system. However, there is a small interaction between AVR and ALFC loops. Owing to this, the small change in real power with respect to a small change in terminal voltage of synchronous generator [10]. After combining the AVR loop with the ALFC loop, the generator load system has one more input added which are given in (14.2), where j denotes the control area.

$$\Delta f_j(s) = \left(\sum_{i=1}^{\text{ng}} \Delta P_{m,i} - \Delta P_{d,j} - \Delta P_{e,j} \right) \frac{K_{ps,j}}{T_{ps,j}s + 1} \quad (14.2)$$

where K_{ps} and T_{ps} are the gain and time constant of the power system, ng is the number of generating plants in an area, ΔP_m is the change in mechanical power, ΔP_d is the SLD, and ΔP_e is the electric power support via AVR loop [10].

$$\Delta P_e = K_1 \Delta \delta + K_2 \Delta V_F \quad (14.3)$$

The small change in rotor angle will be effect on the terminal voltage of the synchronous generator, given in (14.4) [11]

$$\Delta V_t = K_5 \Delta \delta + K_6 \Delta V_F \quad (14.4)$$

The generator field winding voltage changes when the rotor angle and stator emf changes, and it represents as (14.5) [20]

$$\Delta V_F = \frac{K_3 K_f}{1 + s K_3 T_f} (\Delta V_e - K_4 \Delta \delta) \quad (14.5)$$

where K_3 and K_4 are constants. The coupling coefficients are K_1 , K_2 , K_5 , and K_6 .

14.2.3 Modelling of Thermal and Wind Plants

The thermal unit consists of a single-stage large reheat turbine and a governor with physical constraints such as GDB and GRC. The turbine output is given in (14.5)

$$\Delta P_{mi}(s) = \left(\frac{1}{1 + T_{gi}s} \times \frac{1}{1 + sT_{ti}} \times \frac{1 + K_{ri}T_{ri}s}{1 + sT_{ri}} \right) \times \left(\Delta P_{ci} - \frac{\Delta f_i(s)}{R_i} \right) \quad (14.6)$$

where T_{gi} , T_{ti} , T_{ri} , and K_{ri} the governor time constant, turbine time constant, reheat turbine time constant, and coefficient of the reheat turbine in area- i . ΔP_{ci} is the governor set point and R_i is the speed regulation in area- i . The GRC and GDB are not shown in Eq. (14.6).

The wind plant comprises

$$\Delta P_w(s) = \left(\frac{1 + T_{p2i}s}{1 + s} \times \frac{K_{p1i}}{1 + T_{p1i}s} \times \frac{K_{p2i}}{s + 1} \right) \times K_{p3i} \left(\Delta P_{ci} - \frac{\Delta f_i(s)}{R_i} \right) \quad (14.7)$$

where K_{p2} and T_{p2} are the coefficient and time constant of pitch response, K_{p1} and T_{p1} are the gain and time constant of hydraulic pitch actuator, T_{p2} is the pitch control time constant, and K_{p3} is the data characteristics.

14.2.4 Modelling of Electric Vehicles

The penetration of variable renewable energy sources in the power system increases throughout the globe. Various articles were published to explore how integrating EVs into the power grid improves primary frequency regulation and secondary load frequency regulation [2, 5–7]. The dynamic model of EVs aggregator is denoted as a first-order time-delay transfer function given in (14.8) [28]

$$G_{EV}(s) = \left(\frac{K_{ev}}{1 + sT_{ev}} \right) \quad (14.8)$$

where K_{ev} and T_{ev} are the gain and time constant of the battery system.

An exponential transfer function $e^{-s\tau}$ is used to describe the CTD that occurs when transmitting the control signal from the aggregator EV to the individual EV and the aggregator EV's scheduling delay.

The EVs are operated in three modes of operation. The modes of operations are charging, discharging, and idle mode. In charging mode of operation, EVs compensate for the increasing power grid frequency. In discharging mode, EVs supplied the power to the power grid. EVs participate both in primary frequency control (PFC) and secondary frequency control (SFC). When the state of charge (SOC) is more

than 60% and less than 80%, then $K_{ev} = 1$. Below 60% and above 80% of SOC K_{EV} vary between 0 and 1.

14.2.5 Proposed Cascade Fuzzy PD and PIDN (CFPD-PIDN) Controller

A cascade controller composes two or more than two controllers. It has a good capability to diminish the system disturbance rejection compare with a single controller [4, 20]. In this study, fuzzy PD controller and PID with filter coefficient (N), PIDN controller are cascaded. The basic structure of the fuzzy controller is shown in Fig. 14.3. Fuzzy controller is in between pre-processing and post-processing blocks. Crisp inputs are converted into fuzzy sets by fuzzification. Here, if-then format is used as rule base, considering derivative of ACE and ACE are input variables. These two inputs give the output in fuzzy form. Defuzzification is used to convert output fuzzy form into crisp value which is applied in the system.

Figure 14.4 depicts the proposed controller transfer function model. Performance of the fuzzy logic controller (FLC) controller in area-1 depends on the input scaling factors (SFs) k_{p1} and k_{d1} and output SF k_{o1} . Similar kind FLC in area-2 and area-3 are equipped with input SFs k_{p2} , k_{d2} , k_{p3} , and k_{d3} , and output SFs k_{o2} , and k_{o3} . As a result, the input and output SFs of the FLC must be carefully chosen in order to achieve a superior closed-loop system dynamic response. When subjected to a minor step load perturbation, the expected dynamic response should settle quickly with no overshoot and undershoot. Different conventional methods such as Ziegler–Nichols, trial and error are used to determine the controller gains. But these methods may not yield

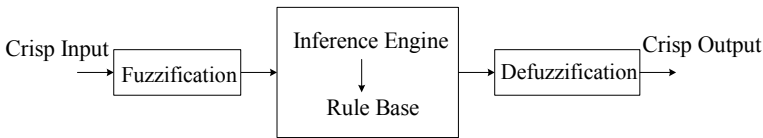


Fig. 14.3 Fuzzy controller building block

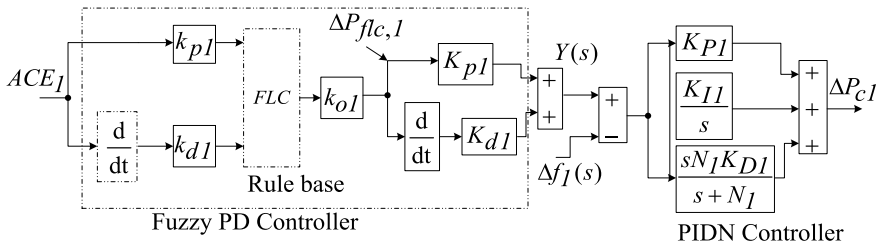


Fig. 14.4 Proposed controller

the optimal value of the controller gains. Last few decades, researchers have been employed a meta-heuristic optimization algorithm to obtain optimum value in these combined ALFC-AVR studies. In this study, AFA is used to determine the optimal controller gains in order to extract better system performance from the proposed controller in this combined system.

For fuzzy logic controller (FLC), ACE_1 and derivative of ΔACE_1 are the inputs of FLC in area-1, and P_{flc1} is the input of the PD controller. The FLC output is transformed into five linguistic variables, viz. big positive (BP), big negative (BN), small positive (SP), small negative (SN), and zero (ZE). In this study, triangular membership functions (MFs) are used to design FLC and the MFs input/output is shown in Fig. 14.5. Also, similar kinds of linguistic variables are used in inputs. FLC (both inputs and output) has five membership functions, and 25 rules (Table 14.1) are required to obtain the desired output of the FLC in each control area. Fuzzy rules play a significant role in the performance of the FLCs, and as a result, the rules are thoroughly explored in this study by investigating the system’s dynamic behaviour. Using the Mamdani interface engine, the firing strength of fuzzy control rules is evaluated.

The output of fuzzy PD controller is obtained using Eq. (14.9) and use as a reference signal for the PIDN controller.

Fig. 14.5 Inputs/output membership functions

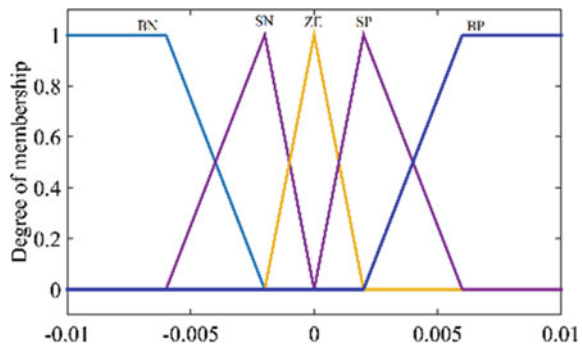


Table 14.1 Fuzzy rules

ACE	ΔACE				
	BN	SN	ZE	SP	BP
BN	BN	BN	BN	SN	ZE
SN	BN	BN	BN	ZE	SP
ZE	BN	SN	ZE	SP	BP
SP	SN	ZE	SP	BP	BP
BP	ZE	SP	BP	BP	BP

$$P_{\text{flc},1} = f\left(k_{p1} \times \text{ACE}_1, k_{d1} \times \frac{d}{dt}\text{ACE}_1\right) \times k_{o1} \quad (14.9)$$

where k_{p1} , k_{d1} , and k_{o1} are the inputs and output SFs of the FLC.

The cascade controller provided better system dynamics due to more tuning knobs. The output of the proposed controller is fed into the governor set point. The controller output is given in (14.10)

$$P_{c,1} = \left(K_{P1} + \frac{K_{I1}}{s} + \frac{sN_1K_{D1}}{s + N_1}\right)(Y(s) - \Delta f_1(s)) \quad (14.10)$$

$$Y_1(s) = (K_{p1} + sK_{d1}) \times P_{\text{flc},1} \quad (14.11)$$

where $\text{ACE}_1 = \Delta P_{\text{tie},1-2} + \Delta P_{\text{tie},1-3} + B_1 \Delta f_1$ and K_{p1} , K_{d1} , K_{I1} , K_{D1} , and K_{P1} are the gains of the CFPD-PIDN controller in area-1, N_1 is the filter coefficients of the controller in area-1.

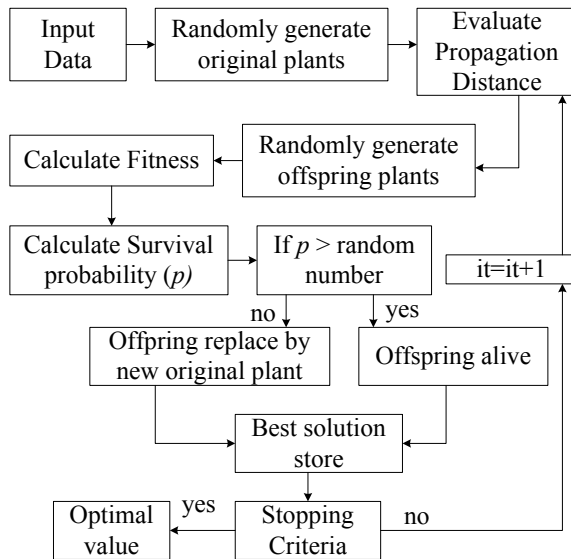
The objective function (14.1) is minimized by optimizing the proposed controller gains using AFA. The controller gains are optimized within their maximum and minimum limits (minimum zero, maximum 1). For each model under consideration, the AFA optimization process is reiterated 20 times, with the best final result among the 20 runs chosen as the CFPD-PIDN controller's gains settings. Voltage, tie-line power, and frequency deviation with regard to settling time, maximum overshoot/undershoot of the dynamic responses during the unexpected system disturbance are evaluated and the relative assessment between proposed ISE and other performance indices (PIs) such as IAE (J_2), ITAE (J_3), and ITSE (J_3) are carried out. The speed of the analysed models' dynamic response profiles is indicated by the values of these parameters. For comparative analysis, the proposed ISE is defined in (14.1) and the rest of J_2 , J_3 , and J_4 are given in (14.12)–(14.14).

$$J_2 = \int_0^T |\Delta f_i + \Delta P_{\text{tie},ij} + \Delta V_i| dt \quad (14.12)$$

$$J_3 = \int_0^T t \cdot |\Delta f_i + \Delta P_{\text{tie},ij} + \Delta V_i| dt \quad (14.13)$$

$$J_4 = \int_0^T t \cdot (\Delta f_i^2 + \Delta P_{\text{tie},ij}^2 + \Delta V_i^2) dt \quad (14.14)$$

Fig. 14.6 AFA flowchart



14.3 Artificial Flora Algorithm

The authors in [29] developed AFA and it's validated tested by the benchmark functions along with its accuracy and stability compared with artificial bee colony and particle swarm optimization techniques. AFA is the simplest optimization algorithms based on the natural phenomenon. Plant cannot move, but it can spread seeds within a certain region. This algorithm consists of three steps, namely evolution, spreading, and selection behaviour. First, the algorithm generates random plants having their location and propagation distance. Secondly, the offspring plants are generated randomly by considering the original plants' location and propagation distance. Lastly, the best offspring plant is considered as a new original plant via selection properties. Detailed mathematical derivations are available in [20]. Here, only a flowchart is shown (Fig. 14.6).

14.4 Result Analysis

The study system is shown in Fig. 14.1. It is simulated on the MATLAB/Simulink platform having 1% SLD in area-1 at nominal system loading. Ode45 is used as a solver to analyse the system. The system data are taken from [5, 6].

14.4.1 Comparison of Performance Index with AFA-PIDN

The amalgamated ALFC-AVR model of three-area thermal systems provides wind turbine system and PIDN as a secondary controller in all areas and simultaneously, optimize the controller gains using AFA by minimizing the $J_1, J_2, J_3,$ and J_4 PIs in order to obtain the best performance index. Corresponding dynamic responses are obtained. Figure 14.7a–c shows the comparison of time-domain dynamic responses. The transient features such as maximum overshoot (MO), maximum undershoot (MU), and settling time (ST) of the PIs (J_1, J_2, J_3, J_4) are shown in Table 14.2. From Table 14.2, it is inferred that the J_1 PI provides a better dynamic response compared to other PIs. Moreover, the J_1 performance index demonstrated better convergence compared to others. Hence, further studies are carried out having an ISE performance index.

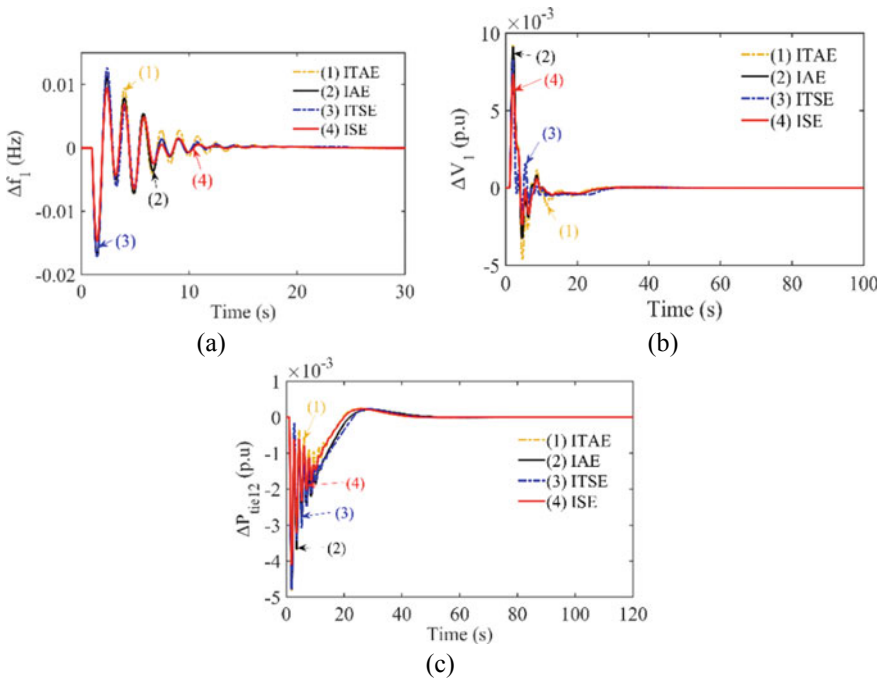


Fig. 14.7 Time-domain dynamic response, a $\Delta f_1(t)$, b $\Delta V_1(t)$, c $\Delta P_{tie,12}$

Table 14.2 Settling time (ST), maximum undershoot (MU), maximum overshoot (MO), and cost function value at different PIs condition

PIs	ST	MU	MO	Cost function value
ISE (Fig. 14.5a)	13	0.0142	0.0085	0.000527
ITSE (Fig. 14.5a)	15	0.0171	0.0142	0.001909
IAE (Fig. 14.5a)	18	0.0165	0.0135	0.162039
ITAE (Fig. 14.5a)	20	0.0162	0.0143	1.223490

14.4.2 Comparison of GWO-PIDN, TLBO-PIDN, and AFA-PIDN

In this case study, the amalgamated ALFC-AVR scenario of three-area thermal systems having a wind turbine system and PIDN as a secondary controller in all areas has been already investigated in Sect. 14.4.1.

Now, the controller gains are optimized using teaching learning-based optimization (TLBO) and grey wolf optimization (GWO) techniques separately and correspondingly, their convergence curves and dynamic responses are obtained. The optimum value of the controller parameters is not displayed. Figure 14.8a shows the comparison of convergence curves among AFA, GWO, and TLBO. The AFA seems to have superior convergence characteristics and good optimal settings for PIDN controller gains and other parameters. Figure 14.8b depicts the comparison of time-domain dynamic responses are obtained from AFA-PIDN, GWO-PIDN, and TLBO-PIDN optimized controllers. AFA-PIDN optimized provides superior to GWO-PIDN, and TLBO-PIDN optimized. Only one response is shown to validate this statement.

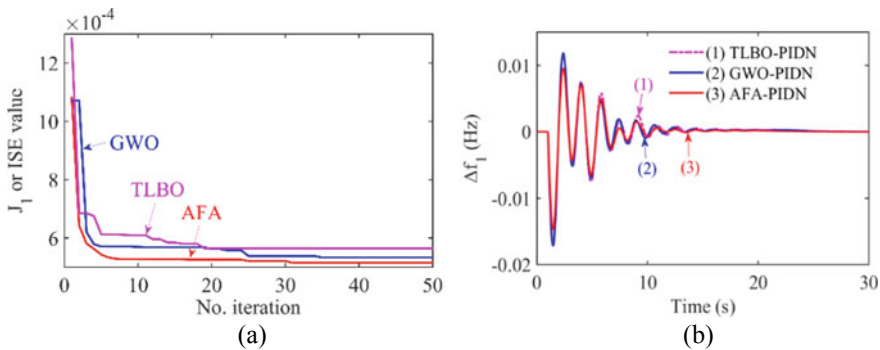


Fig. 14.8 **a** Convergence characteristics curves, **b** time-domain dynamic response of $\Delta f_1(t)$

14.4.3 Comparison of System Performance with PIDN and CFPD-PIDN Controllers

Combined ALFC and AVR model of three-area thermal systems integrating wind turbine is investigated the dynamics responses with PIDN and CFPD-PIDN as a secondary ALFC loop controller and PIDN controller in AVR loop subjected 1% SLP in Area-1 at $t = 1$ s. AFA is employed to achieve the optimum values of the controller parameters one at a time. Table 14.3 shows the optimal values of various controller parameters and obtained time-domain responses, accordingly. Figure 14.9 depicts the controller’s comparisons with various dynamics responses. Figure 14.9a–c, it is examined that the proposed CFPD-PIDN controller outperformed the PIDN controller with regard to maximum deviations and settling time. Figure 14.9d indicates that the generating unit-1 in area-1 (thermal) is supplied approximately 0.0065 p.u MW to satisfy the SLP in Area-1 with CFPD-PIDN controller whereas with PIDN controller deliver approximately 0.005 to satisfy the SLP. Moreover, Fig. 14.9e, f indicates that the generating unit-2 in area-2 (wind turbine), and unit-2 in area-3 (wind turbine) have provided very slow dynamic responses with PIDN controller whereas with CFPD-PIDN controller provided very fast responses. From the above simulation results analysis, it is confirmed that the proposed CFPD-PIDN controller is better than the PIDN controller. Hence, further studies are carried out using CFPD-PIDN as the secondary controller of the ALFC loop.

Table 14.3 At nominal system condition, PIDN and CFPD-PIDN controllers’ optimum values

Controller	Controller optimum values			
PIDN	$K_{p1}^* = 0.4644$	$K_{I1}^* = 1.3789$	$K_{D1}^* = 0.1227$	$N_1^* = 2.1985$
	$K_{p2}^* = 0.2641$	$K_{I2}^* = 1.631$	$K_{D2}^* = 0.6038$	$N_2^* = 39.059$
	$K_{p3}^* = 0.2032$	$K_{I3}^* = 0.224$	$K_{D3}^* = 0.1025$	$N_{23} = 50.045$
	$K_{pav1}^* = 0.0014$	$K_{iav1}^* = 0.6345$	$K_{dav1}^* = 0.5384$	$N_{av1}^* = 0.4560$
	$K_{pav2}^* = 0.4406$	$K_{iav2}^* = 1.1442$	$K_{dav2}^* = 0.0024$	$N_{av2}^* = 11.854$
	$K_{pav3}^* = 0.3105$	$K_{iav3}^* = 0.6771$	$K_{dav3}^* = 0.1051$	$N_{av3}^* = 20.218$
CFPD-PIDN	$K_{p1}^* = 0.0134$	$K_{d1}^* = 1.1487$	$K_{p2}^* = 0.001$	$K_{d2}^* = 0.0094$
	$K_{p3}^* = 0.0451$	$K_{d3}^* = 0.1214$	$k_{p1}^* = 0.054$	$k_{d1}^* = 0.8153$
	$k_{o1}^* = 0.8541$	$k_{p2}^* = 0.6341$	$k_{d2}^* = 0.0847$	$k_{o2}^* = 0.2389$
	$k_{p3}^* = 0.3649$	$k_{d3}^* = 0.1152$	$k_{o3}^* = 0.4921$	$K_{p1}^* = 0.1584$
	$K_{I1}^* = 0.3198$	$K_{D1}^* = 0.6685$	$N_1 = 50.984$	$K_{P2}^* = 0.3611$
	$K_{I2}^* = 0.0131$	$K_{D2}^* = 0.0187$	$N_2 = 10.345$	$K_{P3}^* = 0.8441$
	$K_{I3}^* = 0.4162$	$K_{D3}^* = 0.5128$	$N_3 = 29.154$	$K_{pav1}^* = 0.0236$
	$K_{iav1}^* = 1.0276$	$K_{dav1}^* = 0.0010$	$N_{av1}^* = 11.0448$	$K_{pav2}^* = 0.001$
	$K_{iav2}^* = 0.4103$	$K_{dav2}^* = 0.9510$	$N_{av2}^* = 10.9692$	$K_{pav3}^* = 0.801$
	$K_{iav3}^* = 0.3107$	$K_{dav3}^* = 0.4380$	$N_{av3}^* = 19.1456$	–

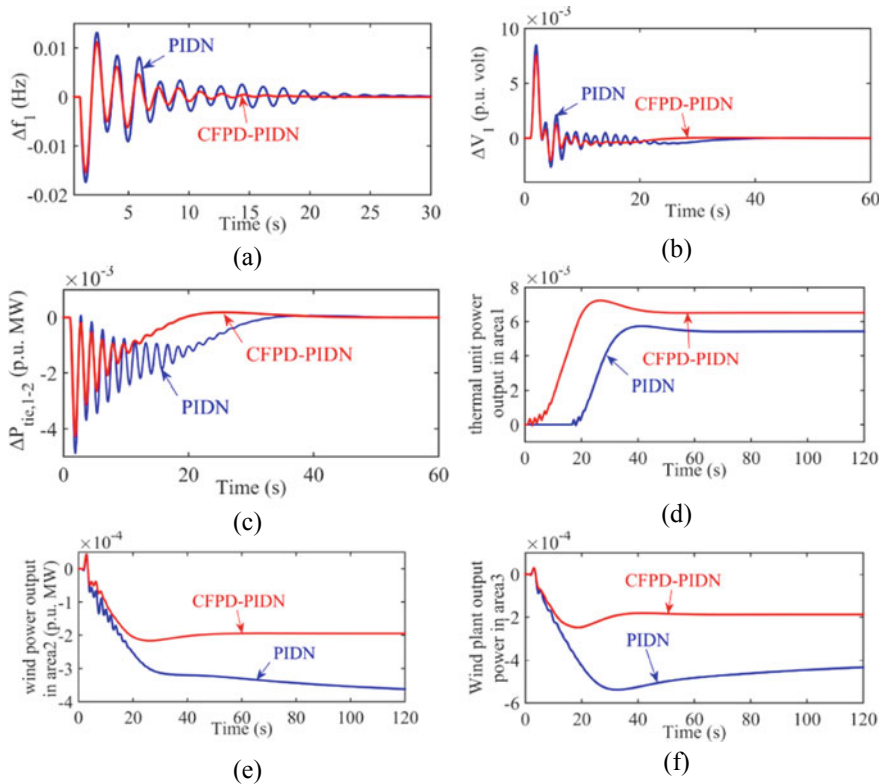


Fig. 14.9 Dynamics responses versus time, deviation of **a** area-1 frequency, **b** voltage in area-1, **c** power flow between area-1 and area-2, **d** output power of thermal unit in area-1, **e** wind turbine power generation in area-2, **f** wind turbine power generation in area-3

14.4.4 Effect of EVs on System Dynamics

In Sect. 14.4.3, the proposed investigated system has been already studied with various controllers without EVs and their dynamics responses are shown in Fig. 14.9. In order to analyse the impact of EVs on the system dynamics, the EVs are integrated into all areas. The various controller parameters are optimized using AFA subjected to 1% SLP in area-1 at $t = 1$ s, and according to their dynamics responses are obtained. The optimal values are not displayed. Figure 14.10a–c shows that the time-domain responses of frequency, tie-line power (between areas 1 and 2), and voltage deviation with and without EVs with both controllers, CFPD-PIDN and PIDN. From Fig. 14.10a–c, the proposed controller provides better responses than the PIDN controller. Figure 14.10d shows the power generation of the generating units in the area-1 are decreased in the presence of EVs in all areas. The EVs in area-1 supply power to the grid is approximately 0.001 p.u. MW.

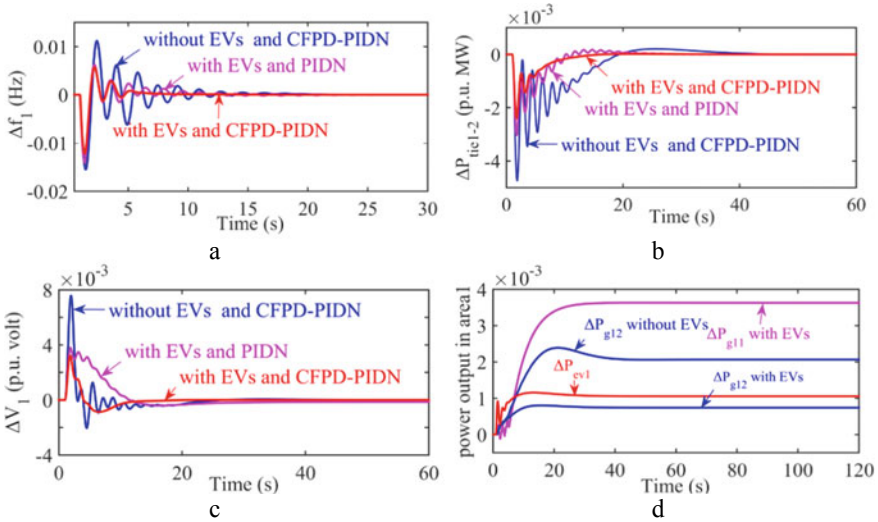


Fig. 14.10 Time-domain dynamic responses: a $\Delta P_{tie,12}(t)$, b $\Delta f_1(t)$, c $\Delta f_2(t)$, d $\Delta V_1(t)$

14.4.5 Effect of K_{ev} Variations on the System Dynamics

The combination of ALFC and AVR model of three-area thermal-wind systems incorporating EVs in all areas has been already studied in Sect. 14.4.4. The battery of EV efficiency, reliability, and life span mainly depends on the SOC. The gain, K_{ev} of EVs is a function of SOC. The nominal value of $K_{ev} = 0.5$ is considered, and using this value in Sect. 14.4.4 has been studied. Now, the K_{ev} is taken as 0.1 and 1.0 to study the effect of parameter variation of EVs on the system dynamics. In both values (0.1 and 1.0) of K_{ev} , the proposed CFPD-PIDN controller’s various parameters are optimized separately using AFA subjected to 1% SLP in area-1 at $t = 1$ s and 50% system loading. The optimal values are not displayed. The time-domain responses are obtained in both values. Figure 14.11 shows the comparisons of dynamics responses with three different values of K_{ev} . From Fig. 14.11a, b, it is clearly showed that the peak deviation and settling time drastically increases with decreasing K_{ev} value. Figure 14.11c confirms that the power generation from the wind plant in the area-1 decreases when K_{ev} value increase. Moreover, Fig. 14.11d indicates that the power contribution from the EVs to the grid is increased with increases K_{ev} value.

14.4.6 Wind System Impact on System Dynamics

In Sect. 14.4.3, three-area thermal-wind systems without EVs have been already studied in combination of ALFC and AVR loop. The dynamics responses of the

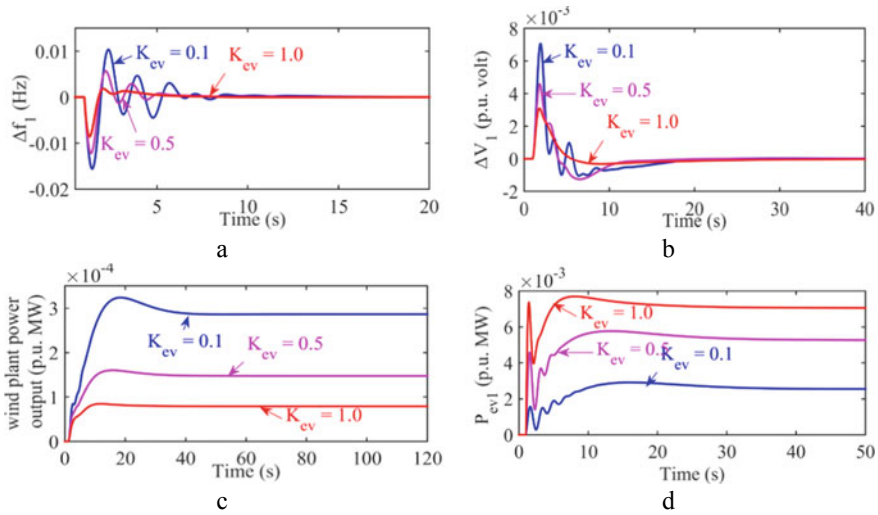


Fig. 14.11 Comparisons of dynamic responses at different value of K_{ev} versus time: **a** Δf_1 , **b** ΔV_1 , **c** wind plant power output in area-1, **d** P_{ev1} in area-1

various controllers have been shown in Fig. 14.9. Now, the wind turbine is excluded from the considered system and obtained the various controller’s parameters using AFA by minimizing ISE performance index given in (14.1). Accordingly, dynamics responses are obtained and optimal values are not displayed. Figure 14.12 shows the dynamics responses comparisons with various controllers. From Fig. 14.12, it is clearly seen that the proposed controller performed outstanding compare to the PIDN controller. Moreover, the system damping improves in the presence of wind turbines for the small-signal stability analysis.

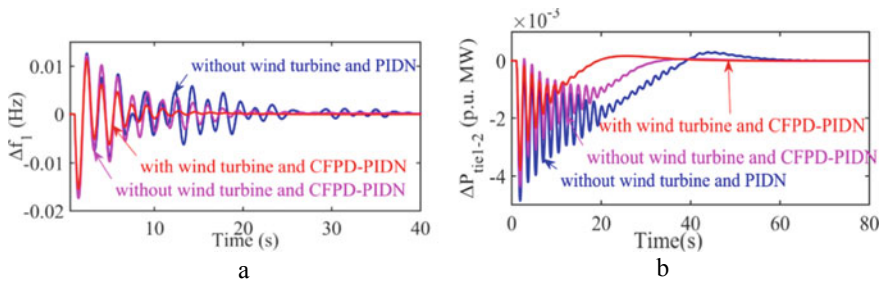


Fig. 14.12 Dynamic responses comparisons with and without wind plant: **a** Δf_1 versus time and **b** $\Delta P_{tie,12}$ versus time

14.4.7 Sensitivity Analysis

In Sect. 14.4.4, amalgamated ALFC and AVR pattern of three-area thermal systems incorporating aggregate EVs model and wind turbine in all areas has been already studied. The proposed CFPD-PIDN controller provided in each area, and the system dynamics responses have been obtained using AFA subjected to 1% SLP in area-1 at $t = 1$ s. In order to analyse the robustness of the proposed CFPD-PIDN controller, two cases are considered: (a) the magnitude of SLP in area-1 is changed from 1 to 3%, and (b) remove EVs from area-1. In both cases, the proposed CFPD-PIDN controller's various parameters are optimized using AFA separately and obtained dynamics responses, accordingly. Figure 14.13a–d shows the dynamics responses comparison between the previously obtained dynamics responses at the nominal condition in Sect. 14.4.4 and changed in system conditions (Sect. 14.4.6). From Fig. 14.13, it is seen that in both conditions the proposed CFPD-PIDN controller provided almost the same responses with high accuracy.

In Sect. 14.4.4, the proposed CFPD-PIDN controller parameters have been obtained at nominal system loading (50% loading). Now, the system loading is changed uniformly $\pm 25%$ in all areas from its 50% loading, and accordingly, the proposed controller parameters are optimized in the modified system conditions using AFA by minimizing the ISE performance index. The optimal values are not displayed. Figure 14.14a–d compares the dynamic responses of CFPD-PIDN controller for modified system condition with corresponding optimal values with the dynamic

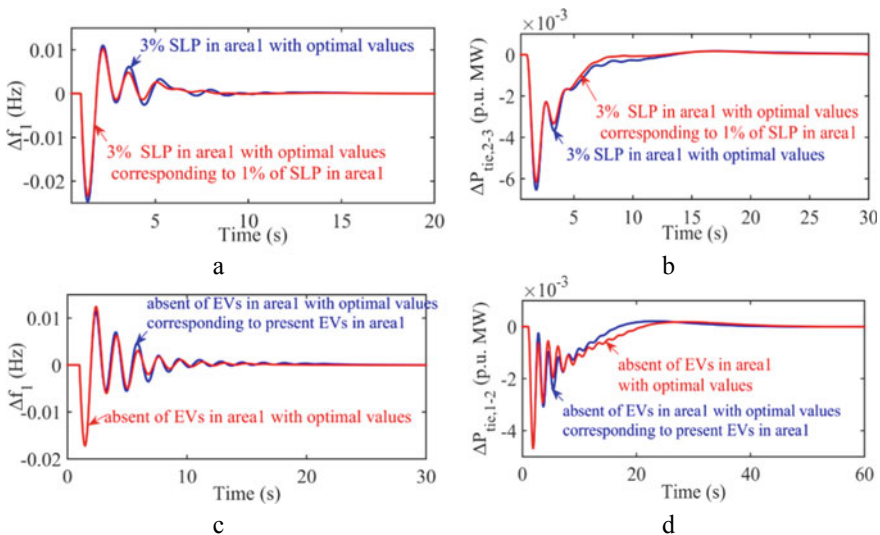


Fig. 14.13 Dynamic responses comparison between the nominal and modified system conditions. deviation of **a** $\Delta f_1(t)$ at 3% of SLD in area-1, **b** $\Delta P_{tie,12}(t)$ at 3% SLD in area-1, **c** $\Delta f_1(t)$ at EVs remove from area-1, **d** $\Delta P_{tie,12}(t)$ at EVs remove from area-1

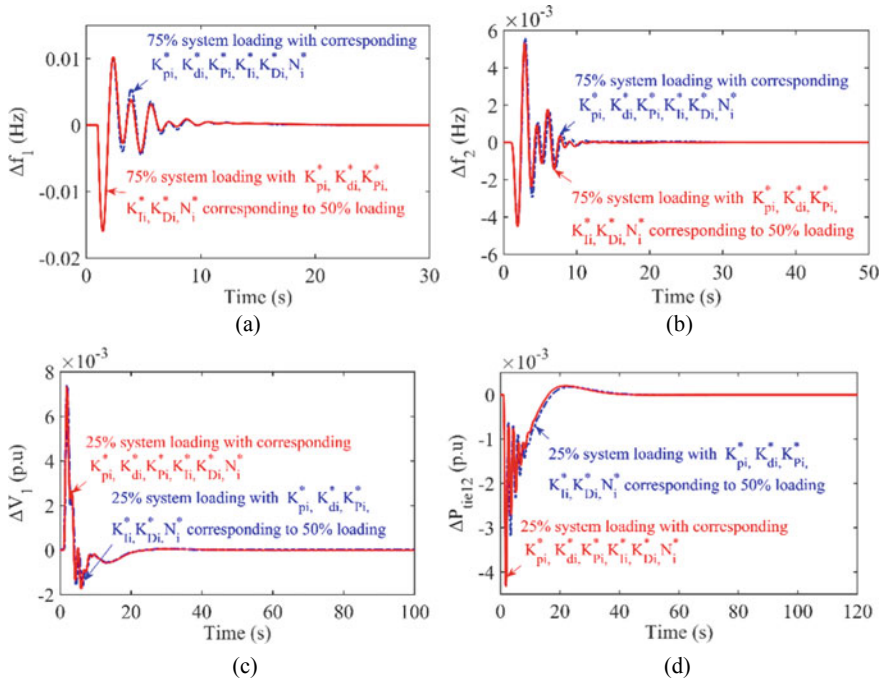


Fig. 14.14 Time-domain dynamic response of $\pm 25\%$ wide variation of system loading from its nominal loading, **a** $\Delta f_1(t)$, **b** $\Delta f_2(t)$, **c** $\Delta V_1(t)$, and **d** $\Delta P_{tie,12}(t)$

response for modified system condition corresponding with optimal values obtained at nominal conditions. From Fig. 14.14a–d, it is observed that there is no noticeable difference between these two responses. Hence, the CFPD-PIDN controller parameters are obtained quite robust at nominal condition and need not be reset repeatedly against the system uncertainties.

14.5 Conclusion

This paper investigated the fuzzy logic-based cascade controller approach for combined ALFC-AVR of three-area thermal-wind systems integrated with EVs under conventional power systems. To make the system more realistic results, GRC and GBD are equipped with thermal units. Investigation showed that the proposed CFPD-PIDN controller provided better results than the PIDN controller. Simulation results clearly showed that the integration of EVs in all areas provided significant improvement of the tie-line power, frequency, and voltage deviations. Further, the parameter variation of K_{ev} shows that the system is more stable when $K_{ev} = 1$ rather than the lower value of K_{ev} . Integration of wind systems into all areas enhanced system

stability. The robustness of the proposed CFPD-PIDN controller has tested against physical nonlinearities such as a sudden increase in the magnitude of SLD from 1 to 3% in area-1, suddenly disconnection of EVs from the area-1, and system loading varied $\pm 25\%$ from its nominal loading. Since AFA conducts a comprehensive domain search by utilizing its exploration and exploitation potential, an AFA is provided to optimize the various control parameters of the considered controllers.

Appendix

The nominal parameters of the system are:

$R = 4\%$ p.u, $B = 0.425$ p.u. MW/Hz, $T_{ps} = 20$ s, $K_{ps} = 120$ Hz/p.u MW.

Thermal plant: $T_g = 0.08$ s, $T_t = 0.30$ s, $T_r = 10.0$ s, $K_r = 5$.

References

1. Saikia, L.C., Nanda, J., Mishra, S.: Performance comparison of several classical controllers in AGC for multi-area interconnected thermal system. *Int. J. Electr. Power Energ. Syst.* **33**(3), 394–401 (2011)
2. Debbarma, S., Dutta, A.: Utilizing electric vehicles for LFC in restructured power systems using fractional order controller. *IEEE Trans. Smart Grid* **8**(6), 2554–2564 (2017)
3. Saha, D., Saikia, L.C.: Performance of FACTS and energy storage devices in a multi area wind-hydro-thermal system employed with SFS optimized I-PDF controller. *J. Renew. Sustain. Energ.* **9**(2), 024103 (2017)
4. Tasnin, W., Saikia, L.C.: Maiden application of a sine–cosine algorithm optimised FO cascade controller in automatic generation control of multi-area thermal system incorporating dish-Stirling solar and geothermal power plants. *IET Renew. Power Gener.* **12**(5), 585–597 (2018)
5. Arya, Y.: Effect of electric vehicles on load frequency control in interconnected thermal and hydrothermal power systems utilising CF-FOIDF controller. *IET Gener. Transm. Distrib.* **14**(14), 2666–2675 (2020)
6. Saha, A., Saikia, L.C.: Renewable energy source-based multiarea AGC system with integration of EV utilizing cascade controller considering time delay. *Int. Trans. Electr. Energ. Syst.* **29**(1), e2646 (2019)
7. Arya, Y.: Impact of hydrogen aqua electrolyzer-fuel cell units on automatic generation control of power systems with a new optimal fuzzy TIDF-II controller. *Renew. Energ.* **139**, 468–482 (2019)
8. Arya, Y., Kumar, N.: BFOA-scaled fractional order fuzzy PID controller applied to AGC of multi-area multi-source electric power generating systems. *Swarm Evol. Comput.* **32**, 202–218 (2017)
9. Elgerd, O.L.: *Electric Energy Systems Theory—An Introduction*, 2nd ed. Tata McGraw Hill, New Delhi (2000)
10. Saadat, H.: *Power System Analysis*, 3rd ed. Tata McGraw Hill, New Delhi (1994)
11. Rakhshani, E., Rouzbehi, K., Sadeh, S.: A new combined model for simulation of mutual effects between LFC and AVR loops. In: *Asia-Pacific Power and Energy Engineering Conference*, pp. 1–5 (2009)

12. Rakhshani, E., Sadeh, J.: Application of power system stabilizer in a combined model of LFC and AVR loops to enhance system stability. In: International Conference on Power System Technology, pp. 1–5 (2010)
13. Gupta, M., Srivastava, S., Gupta, J.R.P.: A novel controller for model with combined LFC and AVR loops of single area power system. *J. Inst. Eng. India Ser. B* **97**, 21–29 (2016)
14. Chandrakala, K.V., Balamurugan, S.: Simulated annealing based optimal frequency and terminal voltage control of multi source multi area system. *Int. J. Electr. Power Energy. Syst.* **78**, 823–829 (2016)
15. Lal, D.K., Barisal, A.K.: Combined load frequency and terminal voltage control of power systems using moth flame optimization algorithm. *J. Electr. Syst. Inform. Technol.* **6**(1), 1–24 (2019)
16. Dekaraja, B., Saikia, L.C., Ramoji, S.K., Babu, N.R., Bhagat, S.K., Behera, M.K.: Modeling and simulation of a multi-area hydro-thermal interconnected system using FOPI^μ controller for integrated voltage and frequency control. In: Modeling, Simulation and Optimization: Proceedings of CoMSO, pp. 275–285. Springer Singapore (2020)
17. Naga Sai Kalyan, C., Sambasiva Rao, G.: Coordinated control strategy for simultaneous frequency and voltage stabilisation of the multi-area interconnected system considering communication time delays. *Int. J. Ambient Energ.* 1–13 (2021)
18. Hasanien, H.M., El-Fergany, A.A.: Salp swarm algorithm-based optimal load frequency control of hybrid renewable power systems with communication delay and excitation cross-coupling effect. *Electr. Power Syst. Res.* **176**, 105938 (2019)
19. Pati, S.S., Mishra, S.K., Panda, A.: Combined frequency and voltage control of a multi-area renewable-based interrelated power structure. In: Advances in Energy Technology, pp. 267–276. Springer, Singapore (2021)
20. Dekaraja, B., Saikia, L.C.: Performance of redox flow battery in combined frequency and voltage control of multi-area multi-source system using CFOPDN-FOPIDN controller. *Int. Trans. Electr. Energy. Syst.* **31**(3), e12782 (2021)
21. Rajbongshi, R., Saikia, L.C.: Combined control of voltage and frequency of multi-area multisource system incorporating solar thermal power plant using LSA optimised classical controllers. *IET Gener. Transm. Distrib.* **11**(10), 2489–2498 (2017)
22. Elsisi, M., Aboeela, M., Soliman, M., Mansour, W.: Design of optimal model predictive controller for LFC of nonlinear multi-area power system with energy storage devices. *Electr. Power Compon. Syst.* **46**(11–12), 1300–1311 (2018)
23. Tasnin, W., Saikia, L.C.: Comparative performance of different energy storage devices in AGC of multi-source system including geothermal power plant. *J. Renew. Sustain. Energ.* **10**(2), 024101 (2018)
24. Kalyan, N.S., Rao, G.S.: Stabilizing frequency and voltage in combined LFC and AVR system with coordinated performance of SMES and TCSC. In: Control Applications in Modern Power System, pp. 65–76. Springer, Singapore (2021)
25. Sai Kalyan, Ch.N.: UPFC and SMES based coordinated control strategy for simultaneous frequency and voltage stability of an interconnected power system. In: 2021 1st International Conference on Power Electronics and Energy (ICPEE), pp. 1–6 (2021)
26. Dekaraja, B., Saikia, L.C., Ramoji, S.K., Babu, N.R., Bhagat, S.K., Behera, M.K.: Coordinated control of voltage and frequency in a three-area multisource system integrated with SMES using FOI-FOPDF controller. In: 2020 IEEE 17th India Council International Conference (INDICON), pp. 1–7 (2020)
27. Rajbongshi, R., Saikia, L.C.: Performance of coordinated FACTS and energy storage devices in combined multiarea ALFC and AVR system. *J. Renew. Sustain. Energ.* **9**(6), 064101 (2017)
28. Patel, N.C., Sahu, B.K., Debnath, M.K.: Automatic generation control analysis of power system with nonlinearities and electric vehicle aggregators with time-varying delay implementing a novel control strategy. *Turk. J. Electr. Eng. Comput. Sci.* **27**(4), 3040–3054 (2019)
29. Cheng, L., Wu, X., Wang, Y.: Artificial flora (AF) optimization algorithm. *Appl. Sci.* **8**(3), 329 (2018)

Chapter 15

A QSSA Optimized Fractional-Order Controller for Improving Transient Response in AC Autonomous Microgrid VSC System



Manoja Kumar Behera, Lalit Chandra Saikia, Satish Kumar Ramoji, Biswanath Dekaraja, Arindita Saha, Sanjeev Kumar Bhagat, and Naladi Ram Babu

Abstract As part of the primary control of the autonomous microgrid (MG) voltage source converter (VSC) system, the inner loop voltage and current controller help to provide a fast transient response for frequency and voltage restoration. This paper proposed a fractional-order proportional plus integral (FOPI) controller for effective voltage and frequency management in autonomous MG VSC systems. Because of their fractional features, FO controllers make the VSC system more resilient than traditional PI controllers. Along with the conventional PI controller K_p and K_i gains, the FOPI controller has an extra edge of flexibility “ λ ”. The FO controllers parameters are tuned using the quasi-oppositional salp swarm algorithm (QSSA), a novel metaheuristic process. A droop controller that utilizes the dynamic change in the droop coefficients is also used to condense power transient and enhance the systems dynamic response while operating in the islanded mode. Furthermore, simulating the MG system in MATLAB Simulink, the dynamic performance of the proposed controllers is validated for the various abrupt change in system condition such as different initial load switching conditions for unequal ratings of distributed generation inverter and the effect of momentary fault (i.e., double line to ground fault). This paper compares the performance of conventional droop with PI controllers in inner voltage and current controllers and the suggested QSSA optimized FOPI controller with modified droop controller for autonomous MG systems. The simulation findings showed that the MG performance has improved using the proposed controller.

M. K. Behera (✉) · L. C. Saikia · S. K. Ramoji · B. Dekaraja · S. K. Bhagat · N. R. Babu
Department of Electrical Engineering, National Institute of Technology Silchar, Silchar, Assam
788010, India
e-mail: manoj04manoj04@gmail.com

A. Saha
Department of Electrical Engineering, Regent Education and Research Foundation Group of
Institutions, Kolkata, India

15.1 Introduction

The microgrid (MG) idea was developed as a result of recent advancements in small-scale distributed generating systems and the usage of sophisticated power electronic systems [1]. There has been a growing interest in converters control since micro-power sources are linked to the MG via power converters [2]. An MG is a network connected with distributed generations (DG), energy sources, distributed loads, and proper control arrangement that can operate in two modes of operation: (a) grid-connected or (b) autonomously. For the grid-connected mode of operation, the available power was fed into the grid after supplying powers to the local loads [3]. In island mode, power output should meet load demand in order to keep the MG voltage and frequency within allowable limits.

DGs balance the MG voltage profile and provide appropriate power-sharing during island operation [4]. The traditional droop control technique is primarily used at this primary control level [5–7] and is implemented without any communication set up. However, owing to impedance mismatches in the feeders, the accuracy of reactive power-sharing suffers. The use of large reactive power droop gains reduces reactive power-sharing error [8]. With a rise in droop gains, the systems relative stability diminishes, potentially resulting in risky MG operation. The dynamic system response becomes oscillatory when the stability margin is reduced [9]. During transient conditions, poor transient response results in a voltage/frequency difference between the sources. Therefore, while operating in islanded mode, a trade-off must be made between the precision of power-sharing accuracy and the dynamic response of the MG.

The active power injected defines the MG frequency, while the reactive power injected determines the node voltage [10]. In the case of a fully resistive MG, this control should be reversed [11, 12]. In reality, the impedance is complex in the vast majority of instances [11]. Therefore, using the traditional droop control method, it is difficult to achieve an acceptable power-sharing distribution. As a result, virtual impedance control is utilized to adjust the droop controls voltage input and guarantee precise power-sharing among the DGs [11]. Power-sharing is described as each DG linked to the MG system providing active and reactive power according to its droop ratio. In the case of a specific MG topology, the virtual impedance value is calculated, and it may be automatically updated in the event of a topology change through communication signals [13, 14]. When communication is unavailable, however, appropriate power-sharing cannot be ensured.

According to the findings, improved droop controllers can be used to improve the dynamic response of the MG while simultaneously increasing the stability margin of the MG when the droop gains are large. It is shown in [15] that adding power derivative-integral components to a standard droop scheme significantly improves transient response. At the same time, abrupt changes in load demand may cause dominating poles to move in the direction of the imaginary axis of $j - \omega$ plane. The transient response of MGs is enhanced by computing the integral and derivative gains in an adaptive way. In [16], the authors suggested a droop controller in which droop

gains are calculated depending on the amount of power delivered to the load by each DG source. Load power demand changes step-by-step; thus, adaptive modification in coefficients of derivative terms helps to reduce oscillations in power output. In this study, the dynamic change in droop gains of $(P - \omega)$ and $(Q - V)$ characteristics is employed to minimize transient power peaks supplied by DG sources and hence enhances the dynamic response of MG in the islanded mode without sacrificing power-sharing accuracy at steady state. The change in active power supplied by the DG sources determines the rate of change in droop gain. As a result, during a step change in load power demand, the oscillations in power provided by DG sources are kept to a minimum. The modified droop controller behaves as a normal droop in a steady state; hence, the systems steady-state response is unaffected.

While the DG droop control sets the amplitude and frequency of the DG systems operating voltage, the resilience and speed of the system are controlled by the controller type used in the inner voltage and current control unit. Many controllers, both linear and nonlinear, are suggested in the literature, including proportional-integral (PI) [17], hysteresis [18], dead beat controller [19], and model predictive controller [20]. Depending on the system and operating condition, each one has its own set of benefits and disadvantages to contend with. PI controllers, which are simple and efficient, are the most frequent control methods utilized in MG current and voltage controllers. One of the major drawbacks of PI controllers is that their integrator causes saturation and reduces the stability margin due to phase lag. These controllers are also susceptible to parameter changes and disruptions [21]. A fractional-order PI controller, often known as FOPI, was developed by [22] to improve the performance and resilience of the systems. It is claimed in [22] to have much more excellent performance than traditional PI controllers. The performance of autonomous MG systems has been enhanced via the use of FO controllers [23, 24]. This research regulates voltage source inverters in an autonomous MG system using the FOPI controller in order to achieve more resilient performance.

In recent years, there has been a great deal of research into frequency control of isolated and multi-area MG systems that use renewable energy sources with various metaheuristic optimization methods such as genetic algorithm (GA) [25], particle swarm optimization (PSO) [26], water cycle algorithm (WCA) [27], butterfly optimization (BFO) [28], and quasi-oppositional selfish herd optimization (QSHO) [29]. This encourages further work on the MG systems voltage and frequency control using a new quasi-oppositional salp swarm algorithm (QSSA) [30]. It is often used because of its rapid convergence and high accuracy. A little chance of it catching up with local optima compared to other techniques [30]. Considering these observations, this research investigates the efficacy of the QSSA base FOPI controller in regulating voltage and frequency in the supposed MG system.

The following is a summary of the current work contribution:

1. A modified droop control is adopted for multi VSC-based DG in an autonomous MG system.
2. A fractional-order proportional-integral (FOPI) controller is adopted for the VSC-based DG autonomous MG inner loop voltage and current controller.

3. A new quasi-oppositional salp swarm algorithm (QSSA) is adopted to tune the FOPI controller parameter for optimal control operation.
4. A comparison of proposed control with convention droop with PI controller in distinct load disturbance and momentary fault in MG system is executed.

The first section will introduce some literature surveys, and the remaining of the paper organized as follows. The suggested control scheme and MG system are explained in Sect. 15.2. Simulation results are present in Sect. 15.3. The conclusion of the study is provided in Sect. 15.4.

15.2 MG System and Proposed Control Scheme

A two-DG based MG is examined in this study. VSI powers each DG on a common reference frame, which is controlled via a droop-based power-sharing technique. Figure 15.1 depicts a detailed model of the VSI, which consists primarily of inverter, output LC filter, droop controller unit, voltage, and current control loops. The DG inverters are connected to the DG terminal through a connecting line of (L_{ci} and R_{ci}). A local baseload (Load1) is connected to the DG₁ terminal. The DG₁ terminal is connected to the point of common coupling (PCC) through a distribution feeder line

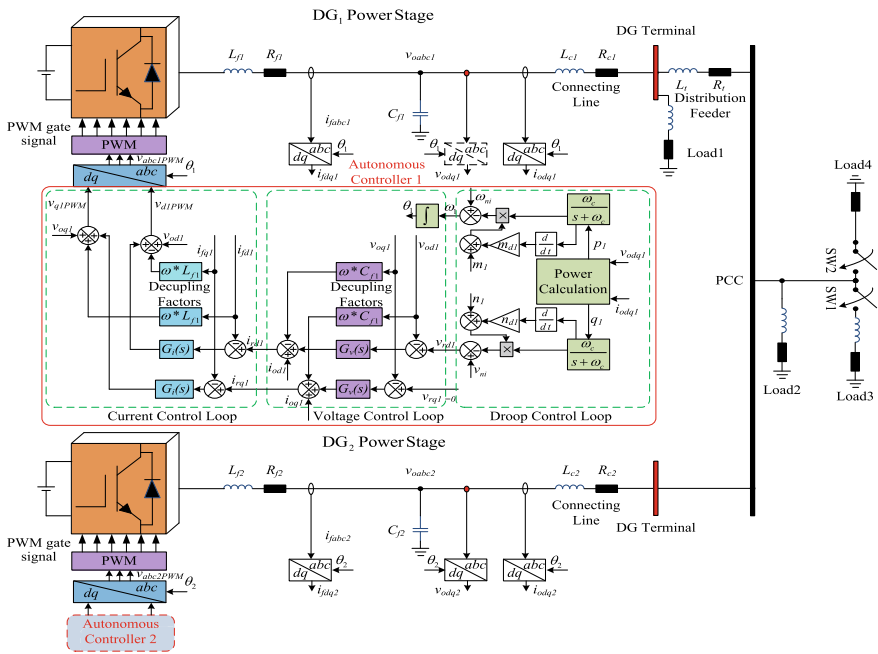


Fig. 15.1 Schematic representation for the studied MG system

Table 15.1 System parameters

Parameters	Values
DC-rated voltage V_{dc}	700 V
Microgrid PCC voltage	381 V (L-L) RMS
Microgrid PCC frequency f	50 Hz
Switching frequency f_{sw}	10 kHz
LC filter parameters	$R_{f1} = R_{f2} = 50 \text{ m}\Omega$ $L_{f1} = L_{f2} = 4.5 \text{ mH}$ $C_{f1} = C_{f2} = 50 \text{ }\mu\text{F}$
Low pass filter (LPF)	$\omega_{cl} = 31.4 \text{ rad/s}$
Connecting line impedance	$R_{c1} = 15 \text{ m}\Omega$; $L_{c1} = 2.9 \text{ mH}$
Droop coefficients	$m_{p1} = 9.4\text{e-}5 \text{ rad/s/W}$ $m_{p2} = 14.1\text{e-}5 \text{ rad/s/W}$ $n_{q1} = 1.3\text{e-}3 \text{ rad/s/VAr}$ $n_{q2} = 1.95\text{e-}3 \text{ rad/s/VAr}$ $m_{d1} = m_{d2} =$ $0.14\text{e-}5 \text{ rad/s/W}$ $n_{d1} = n_{d2} =$ $0.202\text{e-}3 \text{ rad/s/VAr}$
Virtual impedance	$L_{v1} = L_{v2} = 1 \text{ mH}$
Distribution feeder impedance	$R_t = 0.32 \text{ }\Omega$; $L_t = 132.08 \text{ }\mu\text{H}$
Loads	Load1 = ($P_1 = 5 \text{ kW}$; $Q_1 = 1 \text{ kVAr}$) Load2 = ($P_2 = 8 \text{ kW}$; $Q_2 = 3 \text{ kVAr}$) Load3 = ($P_3 = 4 \text{ kW}$; $Q_3 = 2 \text{ kVAr}$) Load4 = ($P_4 = 10 \text{ kW}$)

(L_t and R_t), where DG_2 is directly connected to PCC. Baseload (Load2), Load3 RL load types, and a high resistive type load (Load4) are connected to the PCC of the MG. The MG system parameters and load are provided in Table 15.1. The DC source of the DG inverter is supplied by photovoltaic (PV) and battery, neglecting the source side dynamics. The switching frequency $f_{sw} = 10 \text{ kHz}$ and the switching dynamics are ignored [22]. The power-sharing controllers use voltage and frequency droop control to regulate both active and reactive power. The voltage regulator unit included feed-forward terms is illustrated in Fig. 15.1. Similarly, Fig. 15.1 depicts the block diagram for the current controller unit. This study uses more robust FOPI controllers for DG inverters current and voltage control loops. Section 15.2.1 discusses the proposed controller comprehensive design.

15.2.1 Droop Controller for Improved Transient Response

The oscillations in power output (i.e., active power (p_i) and reactive power (q_i)) supplied by i_{th} DG source can be reduced by adopting modified droop control expressed as (15.1) and (15.2).

$$\omega_i = \omega_{ni} - m_i^* p_{fi} \quad (15.1)$$

$$v_{r di} = v_{ni} - n_i^* q_{fi} \quad (15.2)$$

where v_i and ω_i denote instantaneous voltage magnitude and angular frequency of i_{th} DG source, respectively. v_{ni} and ω_{ni} denote nominal voltages magnitude and angular frequency of i_{th} DG source. q_{fi} and p_{fi} denote the filtered average values of the reactive and active and power output of i_{th} DG source, respectively. n_i^* and m_i^* denote the slopes of $Q - V$ and $P - \omega$ droop, respectively. The dynamic droop gains (m_i^* and n_i^*) are given by (15.3) and (15.4).

$$m_i^* = m_i + m_{di} \frac{dp_{fi}}{dt} \quad (15.3)$$

$$n_i^* = n_i + n_{di} \frac{dq_{fi}}{dt} \quad (15.4)$$

The droop coefficients m_{di} and n_{di} are constants whose values are chosen to provide stability and better dynamic response. DG sources with low inertia, such as power electronic-based sources, are affected by variations in load power demand, which imposes frequency and voltage differential between DG sources. Maximum voltage and frequency variation are experienced by DG sources connected near the load when load demand changes abruptly. Thus, to mitigate these voltage and frequency deviations, the DG source located closer to the load supplies more power than the distant DG source. However, under transient circumstances, the nearby DG sources active and reactive power will exhibit greater oscillations than that from distance DG sources from load. Non-zero dp_{fi}/dt and dq_{fi}/dt values change the modify instantaneous values of dynamic droop gains. Droop gains m_i^* , n_i^* have a higher effective value for nearby DG sources than distant ones. As a result, the associated source will provide less power. Other DG sources will share the leftover power while the system is in transition. These new values of m_i^* and n_i^* enhance the transient response of the MG by reducing peak overshoot in DG sources power output. Modified droop controllers behave as conventional droop control when the DG sources power output obtains a new steady-state value. Substituting m_i^* from (15.3) to (15.1) and n_i^* from (15.4) to (15.2) results in a modified droop control that is stated as (15.5) and (15.6).

$$\omega_i = \omega_{ni} - (m_i + m_{di} \frac{dp_{fi}}{dt}) p_{fi} \quad (15.5)$$

$$v_{rdi} = v_{ni} - (n_i + n_{di} \frac{dq_{fi}}{dt})q_{fi} \quad (15.6)$$

The droop equations provided in (15.5) and (15.6) increase the systems dynamic response by modifying the instantaneous values of m_i and n_i . The values of m_i^* and n_i^* depends on the coefficient's values of m_{di} and n_{di} , and time derivative of p_{fi} and q_{fi} .

The instantaneous power output p_i and q_i of i_{th} DG source is given by $p_i = v_{odi}i_{odi} + v_{oqi}i_{oqi}$ and $q_i = v_{odi}i_{oqi} - v_{oqi}i_{odi}$. Where v_{odi} and v_{oqi} , denote the d - q components of three phase output voltage of i_{th} DG source, respectively, i_{odi} and i_{oqi} denote the d - q components of three phase current output of i_{th} DG source, respectively. With the LPF, the filtered values of active power (p_{fi}) and reactive power (q_{fi}) can be presented as (15.7) and (15.8).

$$\dot{p}_{fi} = -\omega_{cl}p_{fi} + \omega_{cl}p_i \quad (15.7)$$

$$\dot{q}_{fi} = -\omega_{cl}q_{fi} + \omega_{cl}q_i \quad (15.8)$$

15.2.2 Inner Loop Voltage and Current Controller

The inner loop voltage controller regulates the VSC output voltage. New FOPI voltage controllers, feed-forward components, and decoupling terms produce reference currents for the inner loop current controller in the d - q axis. The inner loop voltage control dynamics can be expressed as (15.9).

$$\left. \begin{aligned} i_{rdi} &= G_v(s)(v_{rdi} - v_{odi}) - \omega C_{fi}v_{oqi} + i_{odi} \\ i_{rqi} &= G_v(s)(v_{rqi} - v_{oqi}) + \omega C_{fi}v_{odi} + i_{oqi} \end{aligned} \right\} \quad (15.9)$$

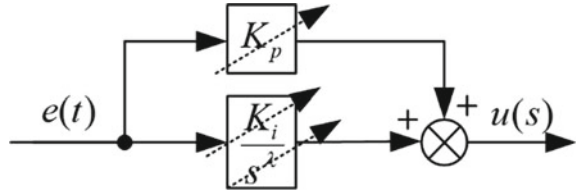
where

$$G_v(s) = K_{vp} + \frac{K_{vi}}{s^{\lambda_v}} \quad (15.10)$$

here K_{vp} , K_{vi} , and λ_v are the parameters of the primary voltage loop FOPI controller.

In the meantime, the inner loop current controller is essential control the real filter inductor current to match with the reference current generated by the voltage control loop. A new FOPI current controllers, feed-forward components, and decoupling terms regulated the real currents in the d - q axis. The inner current control loops dynamics are expressed as (15.11).

Fig. 15.2 FOPI controller structure



$$\left. \begin{aligned} v_{di\text{PWM}} &= G_i(s)(i_{r\text{di}} - i_{f\text{di}}) - \omega L_{fi}i_{f\text{qi}} + v_{odi} \\ v_{qi\text{PWM}} &= G_i(s)(i_{r\text{qi}} - i_{f\text{qi}}) + \omega L_{fi}i_{f\text{di}} + v_{oqi} \end{aligned} \right\} \quad (15.11)$$

where

$$G_i(s) = K_{cp} + \frac{K_{ci}}{s^{\lambda_c}} \quad (15.12)$$

here K_{cp} , K_{ci} , and λ_c are the parameters of the primary current loop FOPI controller. Figure 15.2 depicts the proposed new FOPI controller block diagram. The FOPI controller has an control input of $e(t)$ and controller output of $u(s)$. For the optimal performance of the FOPI controller, its three parameters, such as proportional gain (K_p), integral gain (K_i), and fractional integral order (λ) are needed to be tuned. To serve this purpose, a new QSSA is used explained in Sect. 2.3.

15.2.3 Overview of the Optimization Algorithm

Slap Swarm Algorithm (SSA). Salps are the member of salpidae family. Their tissues are like jellyfish, and they move in a similar fashion. Figure 15.3a, b was presented an individual salp and a salp chain-forming by a group of salps, respectively. The swarming behavior of salps is one of their distinctive behaviors that Mirjalili et al. [31] mathematically incorporated to create SSA. The whole salp population is split into leaders and followers in the salp chains. Leader leading from the front of the slap chain, the leader salp acts as a guide; the other salps are followers, following the salp in front of them. The following are the stages elaborate SSA algorithm:

- (a) *Initialization.* The random initialization of salp population in the predefined upper and lower bound is given as (15.13).

$$x_i = x_{\min} + (x_{\max} - x_{\min}) \times \text{rand} \quad (15.13)$$

where x_{\min} and x_{\max} are denoted the minimum and maximum limits of problem variables, and “rand” function generate an arbitrary number in the range of [0,

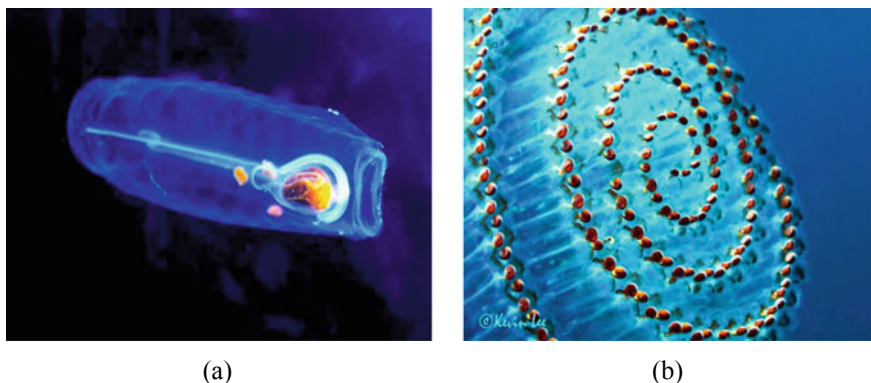


Fig. 15.3 Single salp and group of salps behavior; **a** single salp and **b** salp chain

1]. After fitness function evaluation, the solution vector of size [number of population (NP) \times dimension (D)] is sorted. The best solution obtained is kept at the top and named as leader, followed by the second best in the second place, and so on.

- (b) *Update Leader Position.* Leader position is updated using the relationship provided in (15.14).

$$x_i^1 = \begin{cases} F_i + c_1(c_2(x_{i,\max} - x_{i,\min}) + x_{i,\min}); & c_3 < 0.5 \\ F_i - c_1(c_2(x_{i,\max} - x_{i,\min}) + x_{i,\min}); & c_3 \geq 0.5 \end{cases} \quad (15.14)$$

where $x_{i,\max}$ and $x_{i,\min}$ are denoted the maximum and minimum limits of variables, respectively, and c_2 , and c_3 are denoted the random numbers in the range $[0, 1]$, respectively. “ c_1 ” is the critical parameters of SSA, which equally balance between exploration and exploitation which is expressed as (15.15).

$$c_1 = 2e^{-\left(\frac{4k}{k_{\max}}\right)^2} \quad (15.15)$$

where k and k_{\max} are denoted the current iteration and maximum number of iterations, respectively.

- (c) *Update Followers Position.* The positions of the followers are updated based on the relationship provided in (15.16).

$$x_i^m = \frac{1}{2}(x_i^m - x_i^{m-1}) \quad (15.16)$$

where m denoted the position of follower where (i.e., $m \geq 2$).

- (d) *Newly Generated Population Evaluation After Updation.* The upper and lower bounds are used to set upper and lower boundaries for the newly produced population. The new populations fitness is then assessed, and the best-performing solution is saved.
- (e) Repeat steps “b–d” until stopping conditions are reached.

Quasi-Oppositional Algorithm. Tizhoosh [32] established the idea of opposition-based learning in 2005, and it has since been used in a variety of areas of study. The metaheuristic optimization process starts with a random set of solutions, repeatedly updates solutions at various stages to improve the performance, and eventually reaches an optimal solution. When certain halting conditions are fulfilled, the procedure comes to an end. These methods are computationally expensive since they begin with the initial guess that may or may not be close to the optimum answer. Simultaneously, generating opposite guesses and evaluating their performances increase the likelihood of arriving at a solution closer to the optimum. This allows us to choose a more appropriate result at the start of the process, increasing the likelihood of faster convergence. The said method can be employed in the initialization stage of the optimization algorithm as well as in the current iteration. The opposite number for a real number with “ n ”-dimensional space can be expressed as (15.17).

$$x_{i,op} = a_i + b_i - x_i \tag{15.17}$$

A large number of studies have shown that quasi-opposite points are more closely related to the optimum solution than opposing points [32]. Search spaces have a center and opposing numbers. The quasi-opposite number is between the two. As a result, for a number (x) whose searching space spread over a to b in n dimension, quasi-opposite points may be expressed as (15.18).

$$x_{i,qop} = \begin{cases} S_i + (x_i - S_i) \times \text{rand}(0, 1) & \text{if } x_i < 0.5 \\ S_i + (S_i - x_i) \times \text{rand}(0, 1) & \text{Or else} \end{cases} \tag{15.18}$$

where “ S ” represents the search space center defined as (15.19).

$$S = \frac{a + b}{2} \tag{15.19}$$

A heuristic optimization method may be used to leap to a better solution than the current best if the jumping probability/rate (j_r) is high enough. The leaping probability is usually between [0, 0.6] and can be assessed as (15.20).

$$j_r = (j_{r,max} - j_{r,min}) - (j_{r,min} - j_{r,max}) \times \frac{fc_{max} - fc}{fc_{max}} \tag{15.20}$$

where $j_{r,min}$ and $j_{r,max}$ are denoted the minimum and maximum jumping probability, respectively. fc_{max} is denoted the maximum number of function calls. “ fc ” is the

number of function calls in the current iteration. In addition, quasi-oppositional points are produced by utilizing the relationships stated in (15.21) by using the leaping rate.

$$x_{i,qop} = \begin{cases} \text{if rand} < j_r \\ S_i + (x_{i,qo} - S_i) \times \text{rand}(0, 1) & \text{if } x_{i,qo} < S_{i1} \\ S_i + (S_i - x_{i,qo}) \times \text{rand}(0, 1) & \text{Or else} \end{cases} \quad (15.21)$$

15.2.4 QSSA Optimization of the Proposed Controller

The QSSA was proven its superiority in high-convergence speed and accuracy over SSA [30]. Integral squared error (ISE) has shown outstanding performance as an optimization index in the literature [23, 33, 34]. Thus, the ISE criterion is used in this paper to optimize the FOPI controller parameters. The voltage amplitude and current errors e_{vodq} and e_{idq} are measured to be used for calculation for objective function $F(x)$ is expressed as (15.22).

$$\text{Minimize } F(x) = \int_0^{T_s} [(e_{ovdq})^2 + (e_{idq})^2] dt \quad (15.22)$$

where $x = (K_p, K_i, \text{ and } \lambda)$ and T_s is the simulation time. Subject to some constraint expressed as (15.23) should be taken carefully.

$$\left. \begin{aligned} 0.001 &\leq K_p \leq 300; \\ 5 &\leq K_i \leq 1500; \\ 0 &\leq \lambda \leq 1 \end{aligned} \right\} \quad (15.23)$$

The new QSSA optimizer flowchart is shown in Fig. 15.4. QSSA obtains the tuned controller parameters compared with obtained by employing SSA using the respective convergence shown in Fig. 15.5. The MSSA convergence curve was found to have a higher convergence rate and smallest ISE value than SSA. Consequently, the optimized parameters of FOPI controllers in the MG under study are given in Table 15.2.

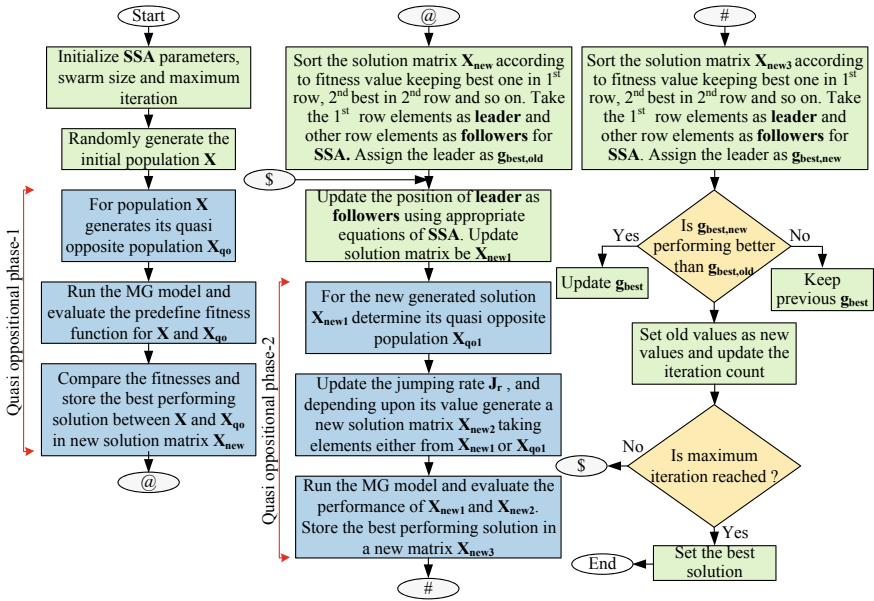


Fig. 15.4 Flowchart of QSSA for proposed control parameters tuned

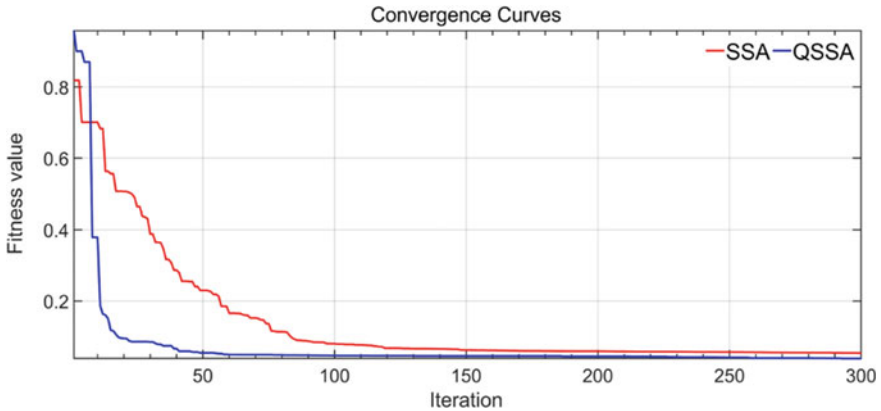


Fig. 15.5 Convergence characteristics of QSSA and SSA techniques

Table 15.2 FOPI controllers parameters

Controller	Symbol	Value
Voltage controller	$K_{vp} + \frac{K_{vi}}{s^{1.5}}$	$0.0056 + \frac{54.1643}{s^{0.4167}}$
Current controller	$K_{cp} + \frac{K_{ci}}{s^{1.5}}$	$169.2437 + \frac{660.5649}{s^{0.6537}}$

15.3 Simulation Results

The performance of the proposed control strategy is tested in this section using MATLAB Simulink in the MG system shown in Fig. 15.1. For analysis, the considered microgrid system parameters and load profile are given in Table 15.1. To show the effectiveness of the proposed QSSA optimized FOPI controller with adaptive droop control, simulation results are compared with droop with inner PI voltage-current controller. Various disturbances, viz. step load variation and momentary faults (i.e., LL-G) which are injected into the MG system in addition to the base load in the MG and observe the power, voltage, and frequency responses.

15.3.1 Step Load Variations on Microgrid

To illustrate the effect of load variations, test loads (Load3 and Load4) are injected into the MG while the base loads (Load1 and Load2) remain connected. A comparison of the conventional controller and the suggested controller simulation results is shown in Figs. 15.5 and 15.6, respectively. The following conclusions may be drawn from these results.

1. The traditional controller causes a divergence in DG voltage from its nominal value when the load is raised in the MG system illustrated in Fig. 15.6a during the Load3 and Load4 which are switch at $t = 2$ s and $t = 4$ s, respectively. On the other hand, the suggested controller rapidly restores the DG voltage to the nominal value illustrated in Fig. 15.7a regardless of load variations in the MG system.
2. Similarly, as demonstrated in Fig. 15.7b, the suggested control method controls the frequency and rate of change of frequency better than traditional ones during the load variations shown in Fig. 15.6b.
3. The active and reactive power fluctuations corresponding to load changes with the traditional controller have a long settling period, as seen in Fig. 15.6c, d. At the same time, it is successfully decreased and smoothed using the suggested controller illustrated in Fig. 15.7c, d.
4. The load current shared by the DG inverters exhibits smooth dynamics and a shorter reaction time for the proposed controller, as illustrated in Fig. 15.7e. While load current response times had a significant effect on the response to load variation for the traditional controller, as shown in Fig. 15.6e.

15.3.2 Momentary Fault (LL-G) on Microgrid System

The test loads (Load3 and Load4) are injected into the MG at $t = 2$ s, while the base loads (Load1 and Load2) are connected to assess the effect of the significant

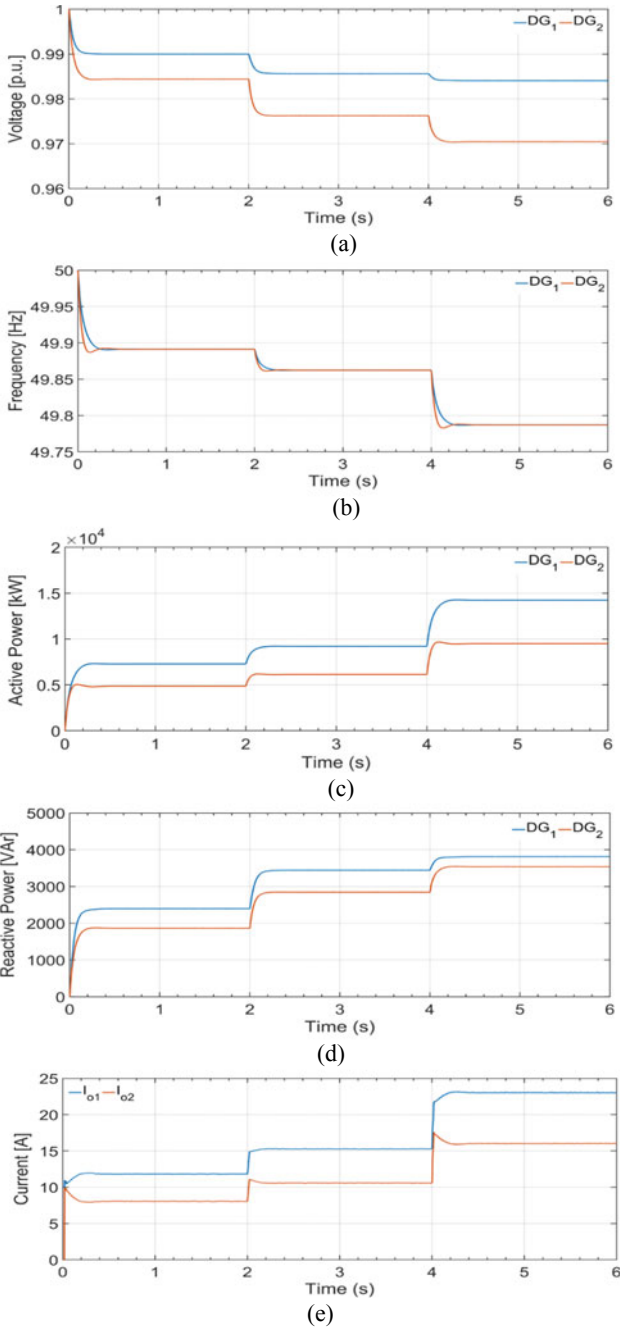
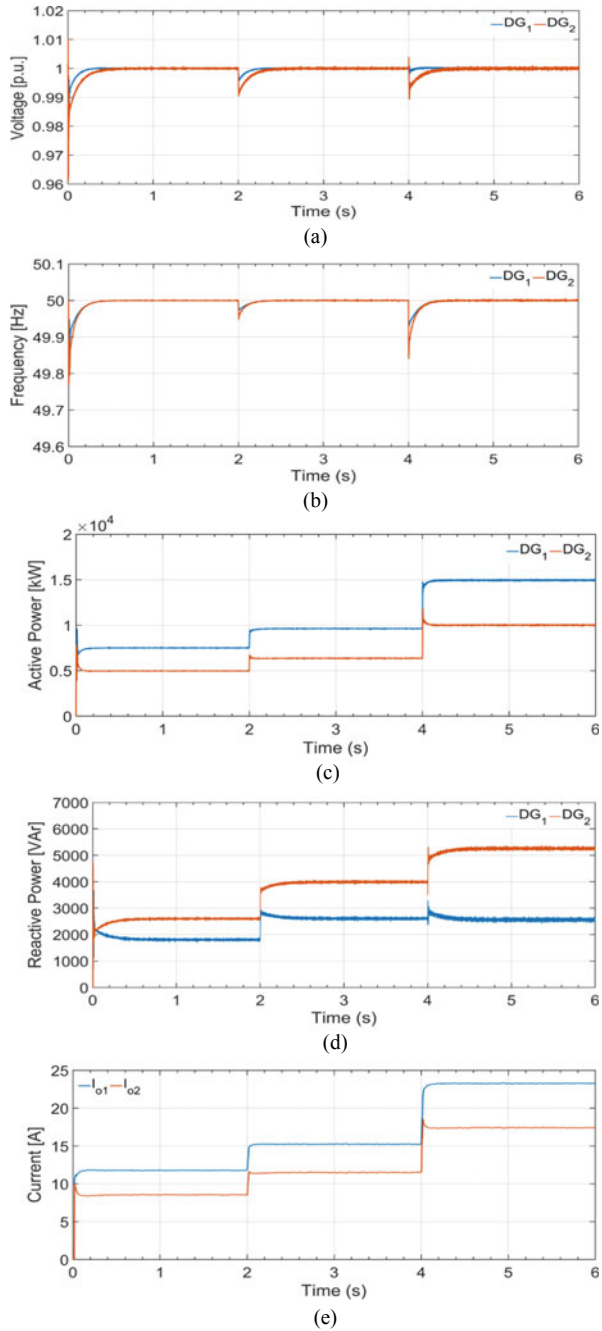


Fig. 15.6 Response of DG inverters with conventional controller for step load variation in microgrid system: **a** voltage, **b** frequency, **c** active power, **d** reactive power, and **e** current

Fig. 15.7 Response of DG inverters with proposed controller for step load variation in MG system: **a** voltage, **b** frequency, **c** active power, **d** reactive power, and **e** current



system disturbance. For the worst-case scenario, a double line to ground (LL-G) fault for 10 cycles at $t = 4$ s is injected into the MG system. A comparison between the traditional controller and our suggested controller is shown in Figs. 15.8 and 15.9. The following conclusions may be drawn from these results.

1. The traditional controller caused a divergence in DG voltage magnitude and frequency from its nominal value when the test loads switched at $t = 2$ s. is illustrated in Fig. 15.8a, b, respectively. On the other hand, the suggested controller rapidly restores the DG voltage magnitude and frequency to the nominal value illustrated in Fig. 15.9a, b, respectively, regardless of load variations in the microgrid system. While LL-G fault trigger at $t = 4$ s. DG voltage and frequency fluctuate for the conventional controller; whereas, the proposed controller effectively controls DG voltage and frequency.
2. The active and reactive power fluctuations corresponding to load changes fault trigger with the traditional controller have a long settling period, as seen in Fig. 15.8c, d, respectively. At the same time, it is successfully decreased and smoothed using the suggested controller illustrated in Fig. 15.9c, d, respectively. The proposed controller appropriately shared the load (3:2) while conventional control was significantly compromised.
3. The load current shared by the DG inverters exhibits smooth dynamics and a shorter reaction time for load variation in the case of the proposed controller, as illustrated in Fig. 15.9e. While load current response times had a significant effect on the response to load variation for the traditional controller, as shown in Fig. 15.8e. While fault was triggered on the PCC of the MG, the proposed controller effectively limits the fault current draw from DG. For the conventional controller, the fault current was effectively high.
4. Hence from Figs. 15.8 and 15.9, it is observed that the proposed controller technique holds a more stable response compared to the conventional approach.

15.4 Conclusion

This article proposes a quasi-oppositional salp swarm algorithm (QSSA)-based FOPI controller with a modified droop controller to enhance MG transient response. The proposed controller regulates the slope ($P - \omega$) and ($Q - V$) droop based on the respective time derivative of DG active and reactive power. This modified droop was provided dampening oscillations of power shared by the DG sources. The FOPI controller dynamically controls the voltage and current controllers to enhance the MG transient response. The gains of the FOPI controller were fine-tuned using the quasi-oppositional salp swarm algorithm (QSSA). The suggested controller impact on the system stability and transient performance is shown using simulation results. The proposed controller performance was compared with convention droop with PI controller in inner loop voltage and current controller of VSC on two DG islanded MG systems. The proposed controller effectively minimizes the power oscillation generated by the DG sources, frequency and voltage magnitude deviation from its

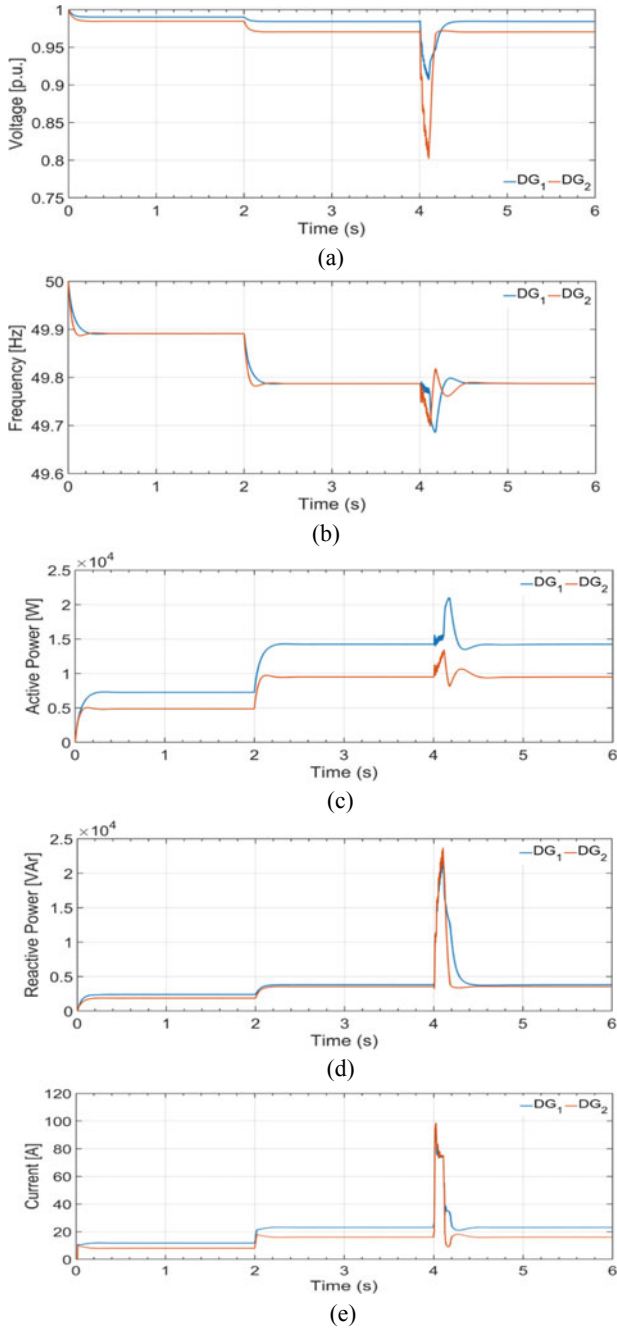


Fig. 15.8 Response of DG inverters with conventional controller for momentary fault (i.e., LL-G) in MG system: **a** voltage, **b** frequency, **c** active power **d** reactive power, and **e** current

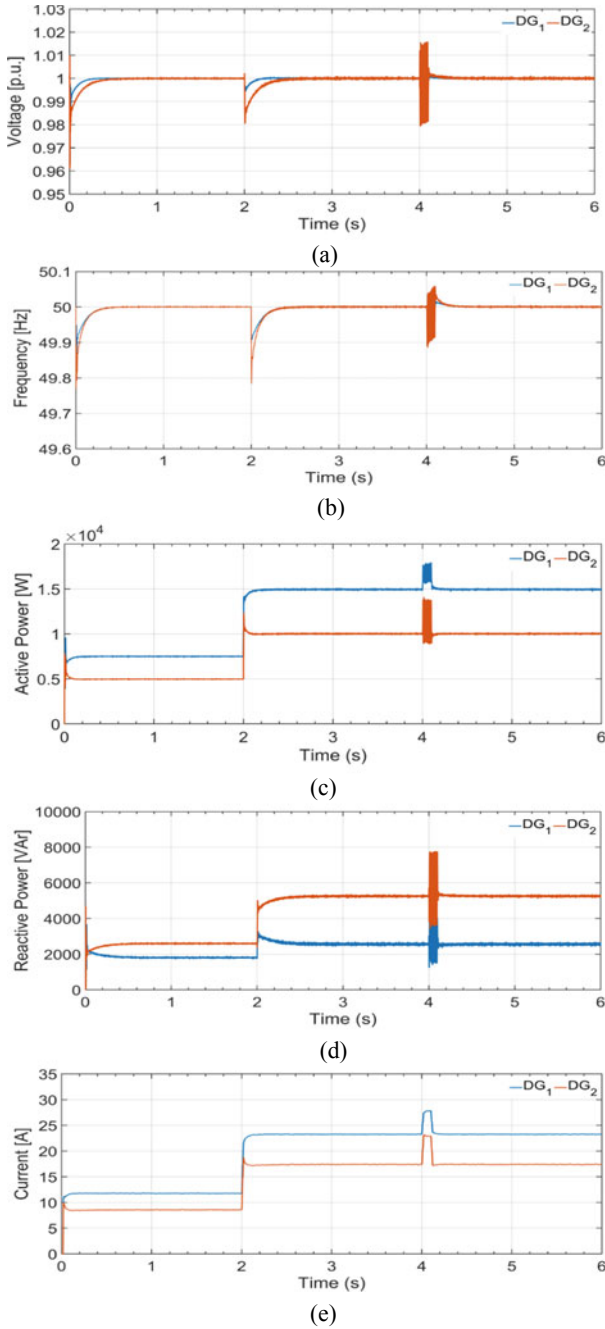


Fig. 15.9 Response of DG inverters with proposed controller for momentary fault (i.e., LL-G) in MG system: **a** voltage, **b** frequency, **c** active power, **d** reactive power, and **e** current

nominal for load demand variation, and sudden abrupt condition (LL-G) fault in the microgrid system than the conventional controller. The steady-state response of the system is not impacted by the suggested controller, which is another advantage.

References

1. Soshinskaya, M., Crijns-Graus, W.H.J., Guerrero, J.M., Vasquez, J.C.: Microgrids: experiences, barriers and success factors. *Renew. Sustain. Energ. Rev.* **40**, 659–672 (2014)
2. Oureilidis, K.O., Demoulias, C.S.: A decentralized impedance-based adaptive droop method for power loss reduction in a converter-dominated islanded microgrid. *Sustain. Energ. Grids Netw.* **5**, 39–49 (2016)
3. Balaguer, I.J., Lei, Q., Yang, S., Supatti, U., Peng, F.Z.: Control for grid-connected and intentional islanding operations of distributed power generation. *IEEE Trans. Industr. Electron.* **58**(1), 147–157 (2010)
4. Ahn, S.-J., Park, J.-W., Chung, I.-Y., Moon, S.-I., Kang, S.-H., Nam, S.-R.: Power-sharing method of multiple distributed generators considering control modes and configurations of a microgrid. *IEEE Trans. Power Deliv.* **25**(3), 2007–2016 (2010)
5. Guerrero, J.M., Chandorkar, M., Lee, T.-L., Loh, P.C.: Advanced control architectures for intelligent microgrids—Part I: decentralized and hierarchical control. *IEEE Trans. Industr. Electron.* **60**(4), 1254–1262 (2012)
6. Guerrero, J.M., Vasquez, J.C., Matas, J., Vicuña, L.G.D., Castilla, M.: Hierarchical control of droop-controlled AC and DC microgrids—a general approach toward standardization. *IEEE Trans. Industr. Electron.* **58**(1), 158–172 (2010)
7. Olivares, D.E., Mehrizi-Sani, A., Etemadi, A.H., Cañizares, C.A., Iravani, R., Kazerani, M., Hajimiragha, A.H., et al.: Trends in microgrid control. *IEEE Trans. Smart Grid* **5**(4), 1905–1919 (2014)
8. Pogaku, N., Prodanovic, M., Green, T.C.: Modeling, analysis and testing of autonomous operation of an inverter-based microgrid. *IEEE Trans. Power Electron.* **22**(2), 613–625 (2007)
9. Barklund, E., Pogaku, N., Prodanovic, M., Hernandez-Aramburo, C., Green, T.C.: Energy management in autonomous microgrid using stability-constrained droop control of inverters. *IEEE Trans. Power Electron.* **23**(5), 2346–2352 (2008)
10. Behera, M.K., Raj, R., Saikia, L.C.: A novel decentralized virtual impedance droop integrating phase locked loop (PLL) control scheme for parallel DG inverter in an islanded microgrid. In: 2020 IEEE 17th India Council International Conference (INDICON), pp. 1–6. IEEE (2020)
11. Yao, W., Chen, M., Matas, J., Guerrero, J.M., Qian, Z.-M.: Design and analysis of the droop control method for parallel inverters considering the impact of the complex impedance on the power sharing. *IEEE Trans. Industr. Electron.* **58**(2), 576–588 (2010)
12. Behera, M.K., Saikia, L.C., Ramoji, S.K., Dekaraja, B., Bhagat, S.K., Babu, N.R.: Voltage and frequency control for DG inverter in low voltage islanded microgrid with improved virtual impedance droop control scheme. In: 2020 IEEE 17th India Council International Conference (INDICON), pp. 1–7. IEEE (2020)
13. He, J., Li, Y.W., Guerrero, J.M., Blaabjerg, F., Vasquez, J.C.: An islanding microgrid power sharing approach using enhanced virtual impedance control scheme. *IEEE Trans. Power Electron.* **28**(11), 5272–5282 (2013)
14. Mahmood, H., Michaelson, D., Jiang, J.: Accurate reactive power sharing in an islanded microgrid using adaptive virtual impedances. *IEEE Trans. Power Electron.* **30**(3), 1605–1617 (2014)
15. Guerrero, J.M., De Vicuna, L.G., Matas, J., Castilla, M., Miret, J.: A wireless controller to enhance dynamic performance of parallel inverters in distributed generation systems. *IEEE Trans. Power Electron.* **19**(5), 1205–1213 (2004)


16. Mohamed, Y.A.-R.I., El-Saadany, E.F.: Adaptive decentralized droop controller to preserve power sharing stability of paralleled inverters in distributed generation microgrids. *IEEE Trans. Power Electron.* **23**(6), 2806–2816 (2008)
17. Khorramabadi, S.S., Bakhshai, A.: Critic-based self-tuning PI structure for active and reactive power control of VSCs in microgrid systems. *IEEE Trans. Smart Grid* **6**(1), 92–103 (2014)
18. Rashad, M., Ashraf, M., Bhatti, A.I., Minhas, D.M.: Mathematical modeling and stability analysis of DC microgrid using SM hysteresis controller. *Int. J. Electr. Power Energ. Syst.* **95**, 507–522 (2018)
19. He, J., Li, Y.W., Xu, D., Liang, X., Liang, B., Wang, C.: Deadbeat weighted average current control with corrective feed-forward compensation for microgrid converters with nonstandard LCL filter. *IEEE Trans. Power Electron.* **32**(4), 2661–2674 (2016)
20. Shan, Y., Hu, J., Liu, M., Zhu, J., Guerrero, J.M.: Model predictive voltage and power control of islanded PV-battery microgrids with washout-filter-based power sharing strategy. *IEEE Trans. Power Electron.* **35**(2), 1227–1238 (2019)
21. Zhang, BiTao, YouGuo Pi (2013) Enhanced robust fractional order proportional-plus-integral controller based on neural network for velocity control of permanent magnet synchronous motor. *ISA Trans.* **52**(4), 510–516 (2013)
22. Pullaguram, D., Mishra, S., Senroy, N., Mukherjee, M.: Design and tuning of robust fractional order controller for autonomous microgrid VSC system. *IEEE Trans. Ind. Appl.* **54**(1), 91–101 (2017)
23. Behera, M.K., Saikia, L.C.: Combined voltage and frequency control for diverse standalone microgrid networks using flexible IDC with novel FOC: a real-time validation. *IETE J. Res.* 1–26 (2021)
24. Zaheeruddin, Singh, K.: Intelligent fractional-order-based centralized frequency controller for microgrid. *IETE J. Res.* 1–15 (2020)
25. Das, D.Ch., Roy, A.K., Sinha, N.: GA based frequency controller for solar thermal–diesel–wind hybrid energy generation/energy storage system. *Int. J. Electr. Power Energ. Syst.* **43**(1), 262–279 (2012)
26. Bevrani, H., Habibi, F., Babahajyani, P., Watanabe, M., Mitani, Y.: Intelligent frequency control in an AC microgrid: online PSO-based fuzzy tuning approach. *IEEE Trans. Smart Grid* **3**(4), 1935–1944 (2012)
27. Hasanien, H.M., Matar, M.: Water cycle algorithm-based optimal control strategy for efficient operation of an autonomous microgrid. *IET Gener. Transm. Distrib.* **12**(21), 5739–5746 (2018)
28. Latif, A., Das, D.C., Barik, A.K., Ranjan, S.: Maiden coordinated load frequency control strategy for ST-AWEC-GEC-BDDG-based independent three-area interconnected microgrid system with the combined effect of diverse energy storage and DC link using BOA-optimised PFOID controller. *IET Renew. Power Gener.* **13**(14), 2634–2646 (2019)
29. Barik, A.K., Das, D.C.: Proficient load-frequency regulation of demand response supported bio-renewable cogeneration based hybrid microgrids with quasi-oppositional selfish-herd optimisation. *IET Gener. Transm. Distrib.* **13**(13), 2889–2898 (2019)
30. Mohapatra, T.K., Dey, A.K., Sahu, B.K.: Employment of quasi oppositional SSA-based two-degree-of-freedom fractional order PID controller for AGC of assorted source of generations. *IET Gener. Transm. Distrib.* **14**(17), 3365–3376 (2020)
31. Mirjalili, S., Gandomi, A.H., Mirjalili, S.Z., Saremi, S., Faris, H., Mirjalili, S.M.: Salp swarm algorithm: a bio-inspired optimizer for engineering design problems. *Advances Eng. Softw.* **114**, 163–191 (2017)
32. Tizhoosh, H.R.: Opposition-based learning: a new scheme for machine intelligence. In: *International Conference on Computational Intelligence for Modelling, Control and Automation and International Conference on Intelligent Agents, Web Technologies and Internet Commerce (CIMCA-IAWTIC'06)*, vol. 1, pp. 695–701. IEEE (2005)
33. Behera, M.K., Saikia, L.C.: A new combined extreme learning machine variable steepest gradient ascent MPPT for PV system based on optimized PI-FOI cascade controller under uniform and partial shading conditions. *Sustain. Energ. Technol. Assess.* **42**, 100859 (2020)

34. Behera, M.K., Saikia, L.C.: An intelligent hybrid GMPPT integrating with accurate PSC detection scheme for PV system using ESSA optimized AWFOPi controller. *Sustain. Energ. Technol. Assess.* **46**, 101233 (2021)

Chapter 16

Conflated Voltage–Frequency Control of Multi-area Multi-source System Using Fuzzy TID Controller and Its Real-Time Validation



Satish Kumar Ramoji , Lalit Chandra Saikia, Biswanath Dekaraja, Manoj Kumar Behera, Sanjeev Kumar Bhagat, Naladi Ram Babu, and Arindita Saha

Abstract This article presents the conflated control pattern of voltage and frequency of the multi-area multi-source interconnected power system by the automatic voltage regulator (AVR) and automatic load frequency control (ALFC) systems. The three-area system has different plants as Area-1 comprises thermal-thermal-electric vehicle (EV fleet), Area-2 comprises thermal-thermal-geothermal, and Area-3 comprises thermal-thermal-wind turbine plant (WTP). As a new attempt for the conflated system, the fuzzy-based tilt-integral-derivative (FTID) controller is being implemented as a secondary controller of ALFC systems and core controller of AVR systems. The optimum controller parameters are achieved using a bio-inspired meta-heuristic algorithm named Harris hawks optimization (HHO) technique. The system performance is evaluated using the performance index called integral square error (ISE) by having 1% perturbation at Area-1. The supremacy of the proposed FTID controller is evaluated by comparing it to the PID and TID controllers using the obtained system dynamic responses and comparing them on the subject of all time-domain indices. The impact of FTID controller in the AVR system is compared to other controllers, and the consequences of the AVR system on the ALFC system are also analyzed. By modifying the generator parameters and changing the system loading conditions, the sensitivity study of the proposed controller reveals that the optimized controller parameters determined under nominal conditions are resilient enough and do not need to be modified. Eventually, the proposed study is investigated using a real-time hardware setup, namely the OPAL-RT OP4510, for real-time corroboration.

S. K. Ramoji (✉) · L. C. Saikia · B. Dekaraja · M. K. Behera · S. K. Bhagat · N. R. Babu · A. Saha
Department of Electrical Engineering, National Institute of Technology Silchar, Silchar, Assam
788010, India
e-mail: satish.ramoji@gmail.com

16.1 Introduction

The ultimate goal of the electric power system is to maintain a continuous balance between the generation of electricity and the uncertainty nature of demand for electricity to ensure the system's stable and safe functioning. By preserving this balance, the frequency and voltage of grid are kept in the permitted limits established by grid rules. In real-time operation, load demand varies regularly, resulting in a relative balance between load and generation that must be adequately maintained. This comparative balance always affects the system frequency and voltage, significantly impacting the overall security of the power system's functioning and control. There are two control loops that can manage the system frequency. The first is the primary loop, which prevents instant frequency changes, and the second is the secondary loop, which is also known as automatic generation control (AGC) or load frequency control (LFC), which is used to reduce frequency deviations and restore the system frequency to its nominal value. While experiencing disturbance due to variations in load demand, AGC uses a linear equation known as area control error (ACE), which monitors deviations and sets them to a null value. In other words, an AGC service is required that assures the stability, security, and cost-effective functioning of the system and provides a unique and comprehensive control form that meets most of the future power system's objectives [1]. The AGC studies are being gradually expanded to include the excitation system, referred to as the ALFC and AVR systems. In general, the AVR system is fast responsive than the ALFC system, owing to the reduced time constant of the excitation mechanism. Although the ALFC and AVR systems operate on different time scales, the AVR system has a substantial influence on ALFC system, while ALFC system has no such influence [2]. Due to a weak coupling impact between the ALFC and AVR systems, only a few researches have been done on this unified pattern, necessitating more research [1, 2].

The AGC studies begin with single area [3, 4], gradually extended to two- or multi-area power system [5] with various conventional plants, for example, single-stage reheat thermal and hydro plants [6–10]. Likewise, the studies are explored with different renewable energy sources such as geothermal plant [11], wind plant [11], dish-Stirling solar thermal plant [12], and solar photovoltaic system [11, 13]. The above studies are confined to AGC or ALFC studies.

Likewise, the AVR circuits are investigated with various controllers and algorithms separately. Many studies of AVR system are explored with classical controllers and fractional order controllers [14, 15].

Introductory studies on conflated ALFC and AVR of one area are initialized with their cross-coupling effects [16, 17] and thermal plants. Progressively, the unified studies are extended to multi-area multi-sourced system with solar thermal plant and diesel generator [18]. The unified studies are also explored with different renewable sources such as wind plant, electric vehicles, gas turbines, dish-Stirling solar thermal plants [19–24], and hydro-thermal plants [24]. Likewise, the combination such as thermal-electric vehicle-wind plant-geothermal plant is not yet analyzed in the coalesced ALFC and AVR pattern. From the thorough literature analysis, it is

conspicuous that many conventional and renewable energy sources are yet to be explored.

To ensure the unified system's efficacy, the ALFC loop must have a robust secondary or supplementary controller, while the AVR loop must have a robust core controller. A number of studies on various types of controllers in a unified ALFC-AVR system are investigated. The controllers for instance IDDF [18], cascaded PIDN-TIDF [19], tilt-integral-derivative with filter [20], two degrees of freedom tilt-integral-derivative [21], F2DOFTID [22], fractional-order proportional-integral-derivative [23], and cascaded fractional-order proportional-derivative with filter to fractional-order proportional-integral-derivative with filter [24] are utilized in both ALFC and AVR structures. There are many fuzzy-logic-based controllers [25–27], and tilt-integral-derivative (TID) [28, 29] controllers are yet to be explored in conflated ALFC and AVR structures. From the literature, it is found that fuzzy-based TID (FTID) controllers are yet to be analyzed in the amalgamated ALFC-AVR system.

Similar to controllers, optimization techniques play an important role in acquiring the paramount values for the controllers, which are relevant for the smooth operation of the power system. Many optimization algorithms such as bacterial foraging optimization [6, 8, 9], sine cosine optimization [11, 12], particle swarm optimization [10], genetic algorithm [16], and lightning search algorithm [18] are successfully implemented in the studies of ALFC and unified ALFC-AVR pattern. In literature, a new optimization technique named as Harris hawks optimization (HHO) [30] is available in the literature, which is utilized in this present work. This HHO technique is derivative-free, fast converging, simple, and highly efficient method. It is generally dependent on chasing pattern and the supporting behavior of the hawks [30].

Based on a thorough review of the literature, it is clear that some objectives, such as:

- (a) To develop a system of three areas such as thermal-thermal-EV in Area-1, thermal-thermal-geothermal plant in Area-2, thermal-thermal-wind plant in Area-3 along with their ALFC and AVR systems.
- (b) To find the best controller among PID, TID, FTID using the HHO algorithm and performance index named integral square error (ISE) for the system developed in (a).
- (c) To achieve the best controller only for the AVR, with the superior controller obtained in (b) and also to investigate the consequence of AVR system on the conflated ALFC-AVR system.
- (d) To analyze the sensitivity of the best controller obtained in (b) by altering the generator parameters and system loading conditions.
- (e) To substantiate the proposed unified system for the real-time analysis using OPAL-RT OP4510 hardware setup.

16.2 Unified Power System Under Study

The proposed unified power system is of three-area multisource under conventional environment. Each area includes its own ALFC and AVR systems. The Area-1 includes thermal-thermal-electric vehicle, Area-2 includes thermal-thermal-geothermal plant, and Area-3 includes thermal-thermal-wind plants which are connected with their respective tie lines. For the pragmatic analysis of the system, thermal plants are considered with pertinent governor dead band, i.e., 0.036 Hz, generator rate constraint, i.e., 0.03 pu MW/min in each area [6]. The capacity ratio of Area-1, 2, and 3 is considered as 1:2:4. Each AGC generator in the area receives an ACE proportional to their participation factor divided by the total of all AGC generators' participation factors. The participation factor of a generator cannot be negative. Hence, the participation factor of each generator in each area is given as $apf_{11} = apf_{12} = apf_{21} = apf_{22} = apf_{31} = apf_{32} = 0.4$, $apf_{13} = apf_{23} = apf_{33} = 0.2$. The transfer function model of the considered unified system is portrayed in Fig. 16.1a. Likewise, the transfer function model of the AVR with cross-coupling coefficients is depicted in Fig. 16.1b.

The study of geo-thermal power plant and wind turbine is considered from [11]. In the proposed unified system, the three controllers such as PID, TID, and FTID are investigated separately. Each controller is used as supplementary controller of ALFC system and core controller of AVR system in every area. The optimization technique named as Harris hawks optimization (HHO) is utilized for achieving the optimal controller parameters, as with the optimized values the augmented system dynamics is achievable. The performance of the proposed unified system is analyzed by the prevailing measuring criterion named as integral squared error (ISE) having 1% of step load perturbation on Area-1, and the objective function of the conflated system is formulated as shown in (16.1):

$$Of_{ISE} = \int_0^T \left\{ (\Delta f_x)^2 + (\Delta P_{tie_{x-y}})^2 + (\Delta V_x)^2 \right\} \quad (16.1)$$

where Of_{ISE} denotes objective function of the conflated system based on ISE performance index, T is the simulation time (100 s considered), the number of area is denoted by x and y , where $x \neq y$. Δf is the frequency deviation, ΔV is the frequency deviation, and ΔP_{tie} is the deviation in tie-line power among the control areas. The codes and simulations of transfer function model of the considered system have been developed in the MATLAB and Simulink platforms.

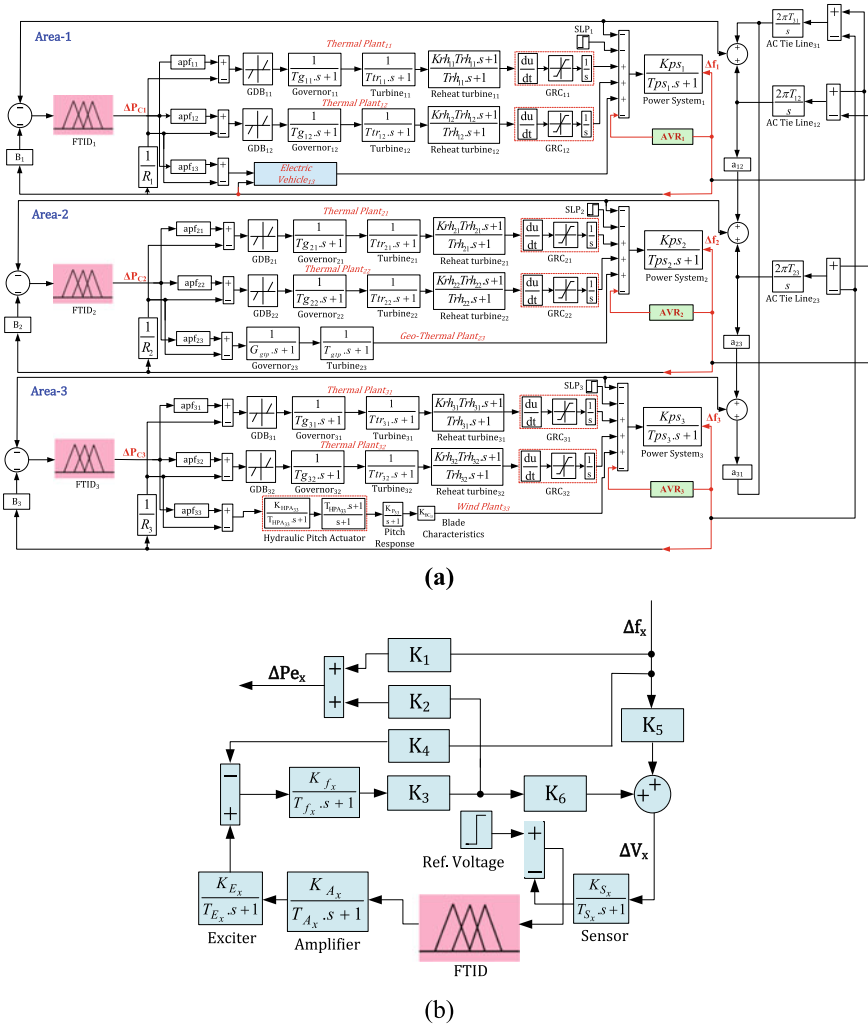


Fig. 16.1 **a** Transfer function model of considered unified system, **b** transfer function model of the AVR system with its cross-coupling coefficients

16.2.1 Modeling of the Cross-Coupling Coefficients Within ALFCs and AVRs

As the frequency of the system is managed by the ALFC system, the voltage is managed by the AVR system in a unified power system. It is noteworthy that the frequency is maintained by governing real power generation, and the voltage is maintained by governing reactive power, both of which are actually achieved by the ALFC and AVR loops, respectively. They can be used separately, but there is a little

coupling effect is present in real-time scenario which is neglected by many studies [20]. The frequency fluctuation varies the real power; as a result, the emf (E_g) as well as terminal voltage of generator varies; then the relation among frequency (speed) and emf is given in (16.2)

$$E_g \propto n \cdot i_{gf} \quad (16.2)$$

where n is the generator rotor speed, i_{gf} is the field current of generator. Likewise, if the generator terminal voltage increases, the error voltage of AVR loop will be less, then the voltage at generator field winding will be less. The fast responsiveness of AVR system confronts the frequency increment which is due to real power increment. Hence, the real power increment impacts the reduction in generator field current so as to voltage constancy [20–22]. It is evident that the real power is influenced by the emf (E_g) and given as shown in (16.3)

$$P_r = \frac{|V_t| |E_g|}{X_{sr}} \sin \delta \quad (16.3)$$

where V_t is terminal voltage, X_{sr} is the synchronous reactance and δ is phase angle difference with in the terminal voltage and the emf of the generator. The terminal voltage of the generator varies as a result of frequency variation, and the AVR loop regulates these variations. Also, because of its relationship to real power, the terminal voltage of the generator influences and controls the frequency of the system. So, the change P_r , V_t , and E_g is given in (16.4)–(16.6)

$$\Delta P_r = K_1 \cdot \Delta \delta + K_2 \cdot \Delta E_g \quad (16.4)$$

$$\Delta V_t = K_5 \cdot \Delta \delta + K_6 \cdot \Delta E_g \quad (16.5)$$

$$\Delta E_g = \frac{K_3 \cdot \Delta E_g}{1 + K_3 \cdot T_{\text{field}} s} - \frac{K_3 \cdot K_4 \cdot \Delta \delta}{1 + K_3 \cdot T_{\text{field}} s} \quad (16.6)$$

where the K_1 , K_2 , K_3 , K_4 , K_5 , and K_6 are the cross-coupling coefficients within ALFC and AVR systems [20–22].

16.2.2 Modeling of Electric Vehicle

The proposed model of EV fleets for studying their unified control provision is presented in this section, and the overall upward and downward principal reserves of a given EV fleet are calculated accordingly. The aggregate model of the EV is

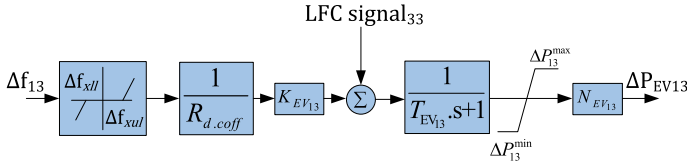


Fig. 16.2 Aggregate model of EV

portrayed in Fig. 16.2. In order to achieve this, first a single EV is modeled, and then an aggregate model is created to represent the entire EV fleets found. The limitations due to distribution network characteristics are ignored here because it is presumed that EVs are directly tied to the transmission system. It is possible for all EVs to abruptly disconnect from the grid, resulting in an unfavorable frequency response. As a result, each EV includes a dead band feature with droop characteristics. The upper (f_{xul}) and lower (f_{xll}) limits of the dead band are set to 10 MHz and -10 MHz, respectively. The aggregate model’s droop coefficient ($R_{d,coff}$) is considered to be the same as conventional units, i.e., 2.4 Hz/p.u. MW. The gain of the EV as K_{EV} and time constant T_{EV} is considered to unity [31]. The maximum and minimum power output and the EV count (N_{EV}) are taken from [31]. For this study, the considered N_{EV} is of 500.

16.3 Fuzzy Logic-Based Tilt-Integral-Derivative (FTID) Controller

In combined voltage and frequency control studies, very few studies are with fuzzy logic control [22]. In frequency control studies, many researchers have used various fuzzy logic control (FLC) strategies in conjunction with integer and fractional-order controllers [26, 27]. From these literatures, it is evident that the FLCs are robust. Some advantages of fuzzy logic controllers are: (i) the ability to incorporate a large number of input signals into FLC system with less complexity [26], (ii) it is possible to simply specify FLC performance in linguistics variables, avoiding the need for sophisticated mathematics, and FLC does not require historical or training data, as is the case for neural networks [26]. FLC is composed of several components, including fuzzification, rule base, fuzzy inference system (FIS), and defuzzification. Fuzzification is the process of converting binary values into fuzzy values by employing a variety of membership functions (MFs) such as triangular, Gaussian, trapezoidal, etc. A basic IF–THEN rule underpins the entire control scheme, and it is the rule that clarifies the entire control scheme. By using the FIS, these rules are translated into fuzzy forms. Here the “center of gravity” defuzzification method is implemented as well as the rule bases are solved using Mamdani FIS. It is desirable to have an equal depiction of both input and output MFs in order to achieve greater computational

efficacy and optimal memory consumption. Due to several advantages, the triangular MFs are highly used [22]. Hence in this study, five membership functions are implemented for both the input and output for instance: Big Negative (BN), Small Negative (SN), Zero (Z), Small Positive (SP), and Big Positive (BP), which is shown in Fig. 16.3. The rule base for the proposed system is charted in Table 16.1 which are considered as inputs, for instance area control error (A) and derivative of area control error (ΔA).

Likewise, the TID controller is also having several advantages [21, 22, 29], such as simple to tune, has a high disturbance rejection ratio, less influenced by changes in plant parameters, and more no. of tuning knobs. In addition, TID has a tilting behavior, which may be detected by studying the transfer function of the TID controller. The TID controller is similar to the PID controller with a difference that the P component of PID controller is multiplied with a tilted component, i.e., $s^{(-1/n)}$. According to merits of both the FLC and TID controllers, the fuzzy-based TID controller is proposed for this study. The structure of FTID controller is shown in Fig. 16.4.

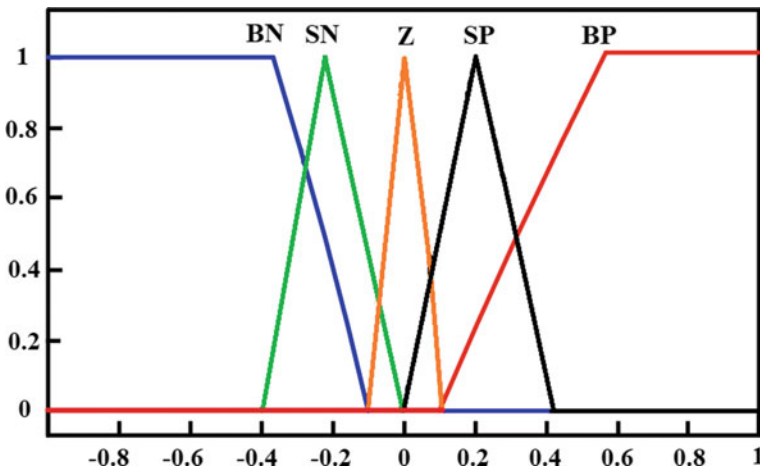


Fig. 16.3 FLC MFs for input and output

Table 16.1 Rule base

A	ΔA				
	BN	SN	Z	SP	BP
BN	BN	BN	BN	SN	Z
SN	BN	BN	SN	Z	SP
Z	BN	SN	Z	SP	BP
SP	SN	Z	SP	BP	BP
BP	Z	SP	BP	BP	BP

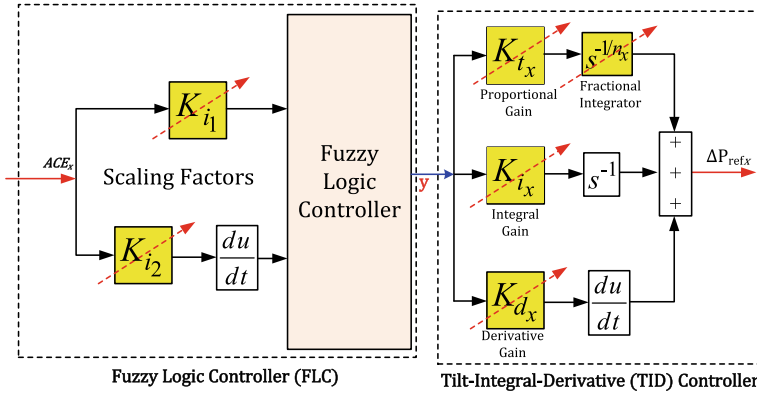


Fig. 16.4 Transfer function model of FTID controller

With the optimization technique, the scaling factors (K_{i1} and K_{i2}) of the FLC and controller parameters of TID such as K_t , K_i , K_d , and n are optimized to accomplish the best values for the efficient operation of the power system. Mathematically, the transfer function of TID controller will be given as

$$G_c(s) = \frac{K_{t_x}}{s^{(1/n_x)}} + \frac{K_{i_x}}{s} + K_{d_x}s \tag{16.7}$$

Likewise, the FLC output is given as

$$\Delta P_{c_x} = y \times G_c(s) \tag{16.8}$$

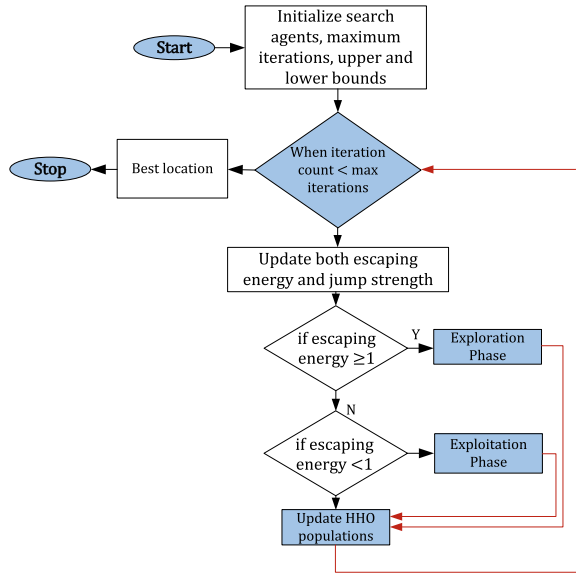
$$\Delta P_{c_x} = y \times \left(G_c(s) = \frac{K_{t_x}}{s^{(1/n_x)}} + \frac{K_{i_x}}{s} + K_{d_x}s \right) \tag{16.9}$$

The controller parameters which are optimized by the optimization algorithm are given as follows:

$$\left. \begin{aligned} K_{t_x}^{\min} &\leq K_{t_x} \leq K_{t_x}^{\max} \\ K_{i_x}^{\min} &\leq K_{i_x} \leq K_{i_x}^{\max} \\ K_{d_x}^{\min} &\leq K_{d_x} \leq K_{d_x}^{\max} \\ n_x^{\min} &\leq n_x \leq n_x^{\max} \end{aligned} \right\}$$

where $K_{t_x}^{\min}, K_{i_x}^{\min}, K_{d_x}^{\min}, n_x^{\min}$ and $K_{t_x}^{\max}, K_{i_x}^{\max}, K_{d_x}^{\max}, n_x^{\max}$ are the minimum and maximum values of K_t, K_i, K_d , and n . The ranges considered for K_t are 0–3, K_i is 0–1, K_d is 0–1, and for n is 0–3.

Fig. 16.5 HHO flowchart



16.4 Harris Hawks Optimization (HHO) Algorithm

The proposed HHO algorithm is a modern swarm-based derivative-free optimization technique that has several active and time-varying phases of exploration and exploitation. The most important component of this approach is the cooperative behavior of diverse pursuit styles, which is referred to as the “surprise pounce” technique. Harris hawks can display a range of team pursuit methods depending on the shifting nature of events and the rabbit’s fleeing moves. When the rabbit is running in zig-zag patterns, they wait and ambush as a group, with other hawks arriving from various directions to add to the confusion. The deliberation of detailed HHO algorithm is referred from [20–22, 30]. The flowchart of the considered HHO technique is shown in Fig. 16.5.

Tunable variables used in this work include population density, maximum iterations, and escape energy, which are all 50, 120, and 0.5 for the HHO technique.

16.5 Simulation Results and Their Outcomes

The system depicted in Fig. 16.1 is considered for further analysis after optimizing the controller values using HHO optimization and the ISE as the performance index, as well as adding 1% SLP to Area-1. Further, the analyses are obtained with nominal loading condition of the system.

16.5.1 System Performance Comparison by Different Controllers

The above described, unified system is investigated with several controllers for instance PID, TID, and fuzzy-based TID or FTID. Each of these controllers serves as secondary controller of ALFC system and core controller of AVR loop in each area at the same time. Similarly, the HHO technique optimizes the controller parameters and other gain values of each controller to the greatest extent possible. The optimum values of each controller are shown in Table 16.2. The system responses are accomplished with these optimal values for each controller, and the results are compared to determine which controller is the best by analyzing the time-domain indices. According to their observations, the FTID controller outperforms all supplementary

Table 16.2 Optimized values of controllers

Controller	Optimized values			
PID	$K_{p1}^* = 0.1568$	$K_{i1}^* = 0.0175$	$K_{d1}^* = 0.5513$	$N_1^* = 58.64$
	$K_{p1a}^* = 0.7716$	$K_{i1a}^* = 0.1249$	$K_{d1a}^* = 0.4882$	$N_{1a}^* = 72.39$
	$K_{p2}^* = 0.7065$	$K_{i2}^* = 0.4435$	$K_{d2}^* = 0.8134$	$N_2^* = 94.16$
	$K_{p2a}^* = 0.8194$	$K_{i2a}^* = 0.6349$	$K_{d2a}^* = 0.7815$	$N_{2a}^* = 64.89$
	$K_{p3}^* = 0.9816$	$K_{i3}^* = 0.3443$	$K_{d3}^* = 0.2337$	$N_3^* = 71.28$
	$K_{p3a}^* = 0.1857$	$K_{i3a}^* = 0.1446$	$K_{d3a}^* = 0.2666$	$N_{3a}^* = 99.54$
TID	$K_{t1}^* = 1.1238$	$K_{i1}^* = 0.5800$	$K_{d1}^* = 0.1912$	$n_1^* = 1.1235$
	$K_{t1a}^* = 0.3965$	$K_{i1a}^* = 0.1260$	$K_{d1a}^* = 0.4261$	$n_{1a}^* = 2.1854$
	$K_{t2}^* = 0.8326$	$K_{i2}^* = 0.1048$	$K_{d2}^* = 0.1032$	$n_2^* = 2.6245$
	$K_{t2a}^* = 0.7661$	$K_{i2a}^* = 0.5264$	$K_{d2a}^* = 0.1134$	$n_{2a}^* = 2.8456$
	$K_{t3}^* = 0.5229$	$K_{i3}^* = 0.2635$ lePara>	$K_{d3}^* = 0.0145$	$n_3^* = 2.5810$
	$K_{t3a}^* = 0.2431$	$K_{i3a}^* = 0.0150$	$K_{d3a}^* = 0.5226$	$n_{3a}^* = 1.3245$
FTID	$K_{i1-1}^* = 1.0305$	$K_{i2-1}^* = 1.0426$	$K_{i1}^* = 1.8546$	$K_{i1}^* = 0.2244$
	$K_{d1}^* = 0.0532$	$n_1^* = 1.0147$	$K_{i1-a}^* = 0.9435$	$K_{i2-a}^* = 0.8912$
	$K_{i1a}^* = 0.0148$	$K_{i1a}^* = 0.1448$	$K_{d1a}^* = 0.4433$	$n_{1a}^* = 2.0124$
	$K_{i1-2}^* = 1.0018$	$K_{i2-2}^* = 1.0024$	$K_{i2}^* = 0.0427$	$K_{i2}^* = 0.4261$
	$K_{d2}^* = 0.4905$	$n_2^* = 2.3106$	$K_{i1-a}^* = 0.3217$	$K_{i2-a}^* = 0.9919$
	$K_{i2a}^* = 0.5117$	$K_{i2a}^* = 0.6221$	$K_{d2a}^* = 0.1335$	$n_{2a}^* = 1.3428$
	$K_{i1-3}^* = 0.6627$	$K_{i2-3}^* = 1.3164$	$K_{i3}^* = 0.0319$	$K_{i3}^* = 0.1300$
	$K_{d3}^* = 0.1445$	$n_3^* = 2.2316$	$K_{i1-a}^* = 0.3975$	$K_{i2-a}^* = 0.0149$
$K_{i3a}^* = 0032$	$K_{i3a}^* = 0.2111$	$K_{d3a}^* = 0.8549$	$n_{3a}^* = 1.8007$	

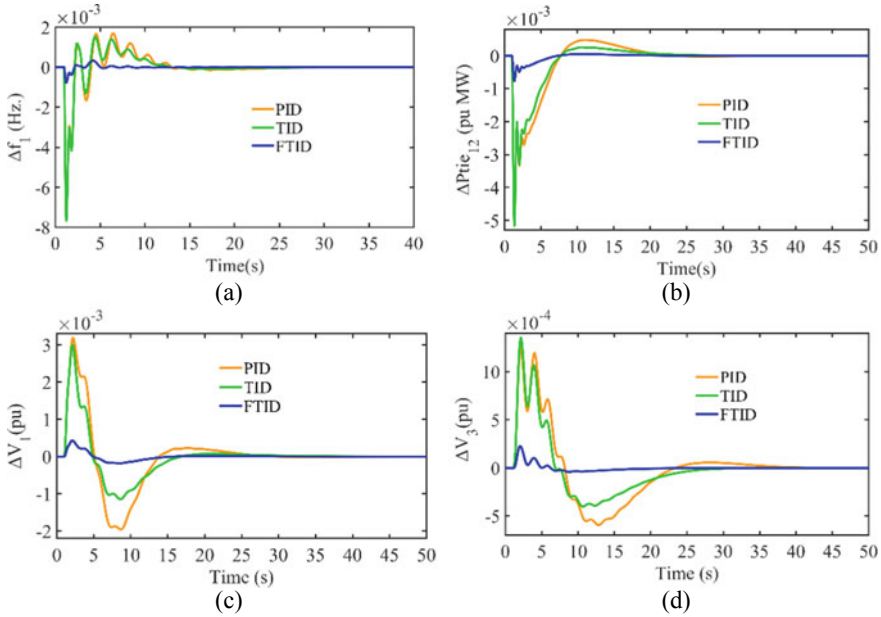


Fig. 16.6 Comparative performance analysis of system **a** Δf of Area-1, **b** ΔP_{tie} among Area-1 and 2, **c** ΔV of Area-1, **d** ΔV of Area-3

controllers on the basis of time-domain indices, i.e., crest overshoot and undershoot, settling time, and oscillation magnitude. The results are shown in Fig. 16.6a–d. Further analyses are being conducted in this regard using the proposed FTID controller.

16.5.2 Study of Different Controllers in AVR and the Effect of AVR on Conflated System

In this study, the behavior of the AVR system is analyzed by varying its core controller, and the impact of AVR system on the conflated ALFC and AVR system is investigated. Therefore, for this analysis, the proposed FTID controller is retained in the ALFC systems of all areas, while the core controllers of the AVRs are investigated by each of the PID, TID, and FTID controllers individually. In each condition, the HHO technique optimizes the controller parameters and other factors. The optimal values are not shown here. The results of the system are achieved and compared using the optimized values. According to the results of the comparison, the AVRs in all areas with the proposed FTID controller outperform the other controllers. The responses are shown in Fig. 16.7a, b. Similarly, the effect of the AVR system is investigated by removing the AVRs from the system under consideration (described in Sect. 16.5).

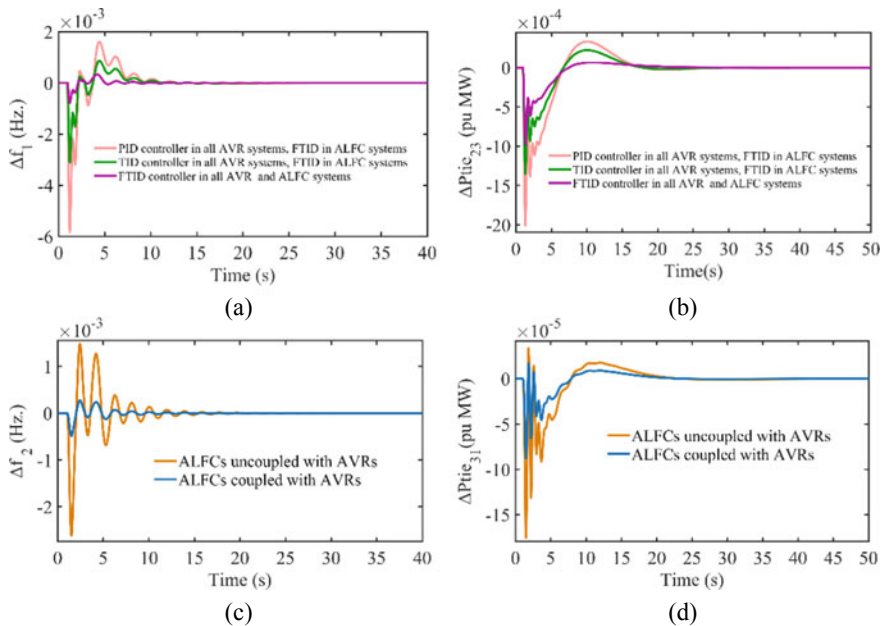


Fig. 16.7 Comparative performance analysis of system **a** Δf at Area-1, **b** ΔP_{tie} among Area-2 and 3, **c** Δf at Area-2, **d** ΔP_{tie} among Area-3 and 1

In this regard, the controller parameters are optimized in both the conditions, i.e., with AVRs in the system and without AVRs in the system. The optimal values of the controllers are accomplished from both scenarios and then compared. From the comparative analysis of the responses, it has been noticed that the system dynamics are significantly improved when the system is equipped with AVRs as opposed to when the system is not equipped with AVRs. The responses are shown in Fig. 16.7c, d.

16.5.3 Sensitivity Study

The sensitivity study of a controller is carried out in order to evaluate the sturdiness or robustness of the controller under various perturbing environments such as parameter variations, changes in system loading, and variations in system nonlinearities. Here the sensitivity is analyzed by varying the generator parameters of the AVR systems and by changing the loading conditions of each area in different ranges. In this regard, the gain and time constant of the AVR generators in all areas are varied by $\pm 20\%$. The controller parameters are optimized by HHO technique in each scenario. The optimized values are not shown here. With the optimal values, the system responses are accomplished and compared. It is clear from the comparative analysis of system

results that controller parameters gained under nominal conditions are sufficiently robust that they do not need to be changed in response to any type of disturbance occurring at generators of AVR systems. The results are shown in Fig. 16.8a, b. Likewise, the loading conditions of each area are also changed such as Area-1 to 20%, Area-2 to 30%, and Area-3 to 40%. As the system loading deviates from its nominal value, the parameters Kps_x , Tps_x , B_x , and D_x deviate from their nominal values. The HHO technique is exploited to optimize the controller parameters in both scenarios. The system's dynamic responses are captured and compared using the controller's optimized parameters, and illustrated in the Fig. 16.8c, d. The responses in both scenarios appear to be nearly identical. According to the results of the comprehensive studies of the responses, it is evident that the optimal controller values achieved under nominal conditions are sufficiently resilient and do not require modification as a result of any type of disturbance.

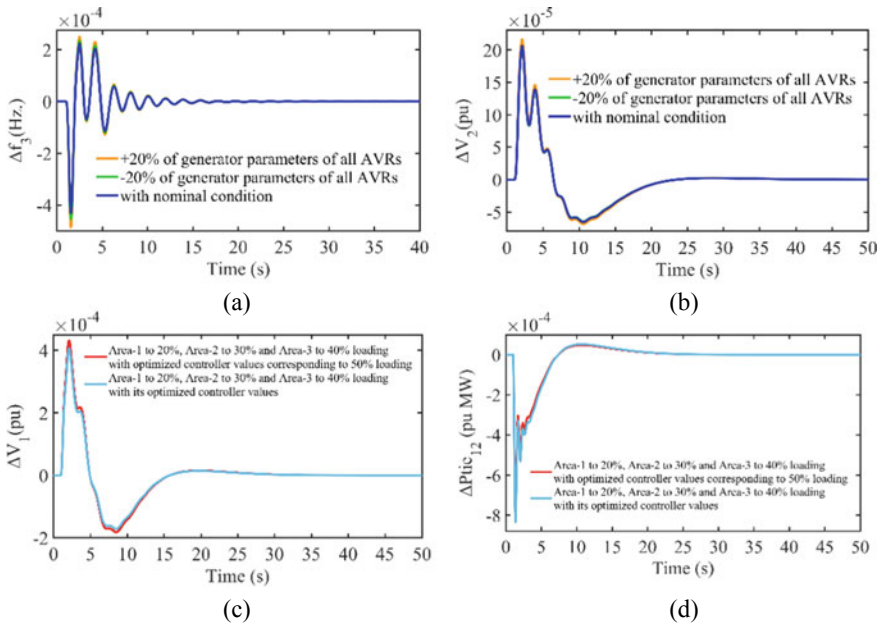


Fig. 16.8 Comparative performance analysis of system **a** Δf at Area-3, **b** ΔV at Area-2, **c** ΔV at Area-1, **d** $\Delta Ptic$ among Area-1 and 2

16.5.4 Study of the Proposed System in OPAL-RT OP 4510 Hardware Setup

In this study, the system performance is analyzed by the OPAL-RT OP 4510 real-time hardware setup for its real-time validation. The real-time digital simulator OPAL-RT OP4510 is powered by Intel Xeon 4-core processors and the Xilinx Kintex-7 FPGA architecture to provide high performance. Because it has the capability of performing real-time parallel computation, the outcomes are similar to those found using typical hardware. The RT LAB software is used to control the OPAL-RT. For this study, the system is also built in RT LAB, which is based on MATLAB and is used for real-time analysis. When using MATLAB, the simulation time is limited to one hundred seconds. Similarly, in RT LAB-based MATLAB, the system results are also accomplished with the same simulation time. The results obtained on the MATLAB platform are exactly equivalent to those acquired on the RT LAB-based MATLAB platform, confirming the validity of the proposed system. Figure 16.9a depicts the laboratory look of the OPAL-RT system, while Fig. 16.9b–d depicts the outputs of the system.

16.6 Conclusion

In this paper, the authors accomplished some effort to exploit the fuzzy-based TID controller in ALFC and AVR systems of a three-area multi-source interconnected power system. The HHO technique is being considered for implementation in order to optimize the controller parameters and other factors. Based on the comparative analysis of system dynamics, it has been discovered that the proposed FTID controller outperforms both the PID and the TID controllers in terms of time-domain indexes. Similarly, the FTID controller in the AVR system outperforms all other controllers in terms of performance. It has also been demonstrated that the effect of the AVR system increases the dynamics of the system. The sensitivity analysis of the system reveals that controller values achieved with nominal conditions are strong enough to deal with any type of disturbances caused by dissimilar loading conditions between each area as well as changes in generator parameters. Finally, the proposed system is validated using the OPAL-RT OP4510 hardware platform for real-time studies.

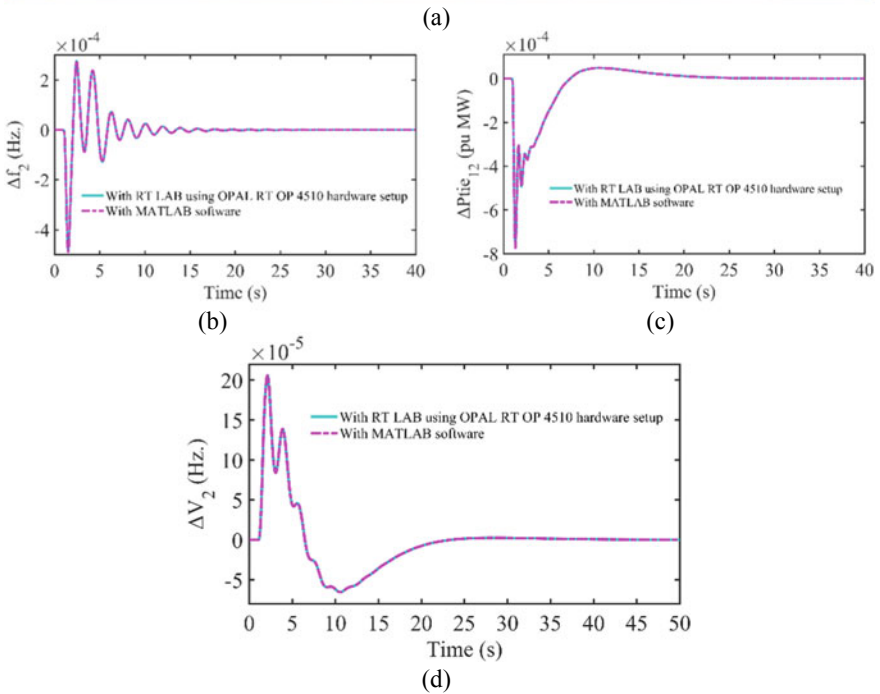
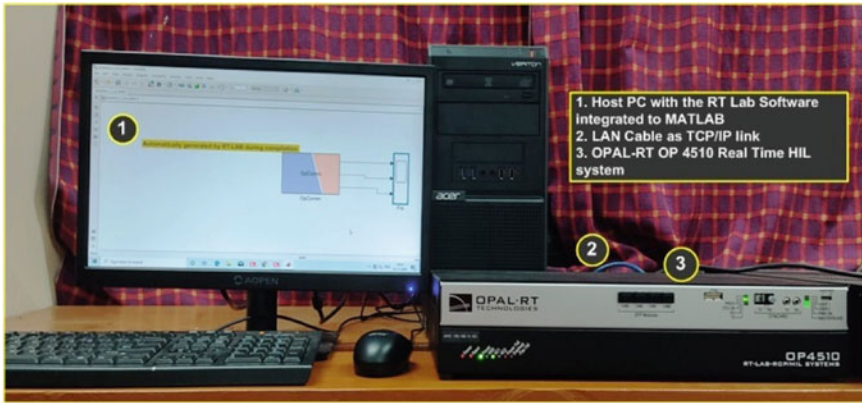


Fig. 16.9 a Laboratory setup of OPAL-RT, comparative performance analysis of system, b Δf at Area-2, c ΔP_{tie} among Area-1 and 2, d ΔV of Area-2

References

1. Bevrani, H.: Robust Power System Frequency Control, 2nd edn. Springer International Publishing, Switzerland (2014)
2. Kwatny, Harry G., Karen Miu-Miller.: Power system dynamics and control, 1st edn. Birkhäuser Basel, New York (2016)

3. Pan, C.T., Liaw, C.M.: An adaptive controller for power system load-frequency control. *IEEE Trans. Power Syst.* **4**(1), 122–128 (1989)
4. Padhan, D.G., Majhi, S.: A new control scheme for PID load frequency controller of single-area and multi-area power systems. *ISA Trans.* **52**(2), 242–251 (2013)
5. Moniya, P., Anand, B.: Automatic generation control with fuzzy logic controller incorporating tandem and cross compound turbine. *J. Ambient. Intell. Humaniz. Comput.* **12**(7), 7071–7083 (2021)
6. Nanda, J., Mishra, S., Saikia, L.C.: Maiden application of bacterial foraging-based optimization technique in multiarea automatic generation control. *IEEE Trans. Power Syst.* **24**(2), 602–609 (2009)
7. Alomoush, M.I.: Load frequency control and automatic generation control using fractional-order controllers. *Electr. Eng.* **91**(7), 357–368 (2010)
8. Saikia, L.C., Sinha, N., Nanda, J.: Maiden application of bacterial foraging based fuzzy IDD controller in AGC of a multi-area hydrothermal system. *Int. J. Electr. Power Energy Syst.* **45**(1), 98–106 (2013)
9. Arya, Y., Kumar, N.: Design and analysis of BFOA-optimized fuzzy PI/PID controller for AGC of multi-area traditional/restructured electrical power systems. *Soft. Comput.* **21**(21), 6435–6452 (2017)
10. Falehi, A.D.: Optimal design of fuzzy-AGC based on PSO & RCGA to improve dynamic stability of interconnected multi area power systems. *Int. J. Autom. Comput.* **17**, 599–609 (2020)
11. Tasnin, W., Saikia, L.C.: Comparative performance of different energy storage devices in AGC of multi-source system including geothermal power plant. *J. Renew. Sustain. Energy* **10**(2), 024101 (2018)
12. Tasnin, W., Saikia, L.C., Raju, M.: Deregulated AGC of multi-area system incorporating dish-Stirling solar thermal and geothermal power plants using fractional order cascade controller. *Int. J. Electr. Power Energy Syst.* **101**, 60–74 (2018)
13. Arya, Y.: AGC of two-area electric power systems using optimized fuzzy PID with filter plus double integral controller. *J. Franklin Inst.* **355**(11), 4583–4617 (2018)
14. Ayas, M.S., Sahin, E.: FOPID controller with fractional filter for an automatic voltage regulator. *Comput. Electr. Eng.* **90**, 106895 (2021)
15. Eltag, K., Zhang, B.: Design robust self-tuning FPIDF controller for AVR system. *Int. J. Control Autom. Syst.* **19**(2), 910–920 (2021)
16. Rakhshani, E., Rouzbehi, K., Sadeh, S.: A new combined model for simulation of mutual effects between LFC and AVR loops. In: 2009 Asia-Pacific Power and Energy Engineering Conference, pp. 1–5. IEEE, Mar 2009
17. Gupta, M., Srivastava, S., Gupta, J.R.P.: A novel controller for model with combined LFC and AVR loops of single area power system. *J. Inst. Eng. (India): Series B* **97**(1), 21–29 (2016)
18. Rajbongshi, R., Saikia, L.C.: Combined control of voltage and frequency of multi-area multisource system incorporating solar thermal power plant using LSA optimised classical controllers. *IET Gener. Transm. Distrib.* **11**(10), 2489–2498 (2017)
19. Ramoji, S.K., Saikia, L.C., Dekaraja, B., Behera, M.K., Bhagat, S.K., Babu, N.R.: Optimal unified frequency and voltage control of multi-area multi-source power system using the cascaded PIDN-TIDF controller. In: 2020 IEEE 17th India Council International Conference (INDICON), pp. 1–6. IEEE, Dec 2020
20. Ramoji, S.K., Saikia, L.C.: Optimal coordinated frequency and voltage control of CCGT-thermal plants with TIDF controller. *IETE J. Res.* 1–18 (2021)
21. Ramoji, S.K., Saikia, L.C.: Utilization of electric vehicles in combined voltage-frequency control of multi-area thermal-combined cycle gas turbine system using two degree of freedom tilt-integral-derivative controller. *Energy Storage* **3**(4), e234 (2021)
22. Ramoji, S.K., Saikia, L.C.: Maiden application of Fuzzy-2DOFTID controller in unified voltage-frequency control of power system. *IETE J. Res.* 1–22 (2021)
23. Ramoji, S.K., Saikia, L.C., Dekaraja, B., Babu, N.R., Bhagat, S.K. and Behera, M.K.: Modeling and simulation of an isolated CCGT and DSTS plant using BWO optimized PI λ D μ controller

- for amalgamated control of voltage and frequency. In: Modeling, simulation and optimization: proceedings of CoMSO 2020, pp. 297–309. Springer Singapore (2021)
24. Dekaraja, B., Saikia, L.C.: Performance of redox flow battery in combined frequency and voltage control of multi-area multi-source system using CFOPDN-FOPIDN controller. *Int. Trans. Elect. Energy Syst.* **31**(3), e12782 (2021)
 25. Golshannavaz, S., Khezri, R., Esmaeeli, M., Siano, P.: A two-stage robust-intelligent controller design for efficient LFC based on Kharitonov theorem and fuzzy logic. *J. Ambient. Intell. Humaniz. Comput.* **9**(5), 1445–1454 (2018)
 26. Arya, Y.: Impact of hydrogen aqua electrolyzer-fuel cell units on automatic generation control of power systems with a new optimal fuzzy TIDF-II controller. *Renew. Energy* **139**, 468–482 (2019)
 27. Arya, Y.: AGC performance enrichment of multi-source hydrothermal gas power systems using new optimized FOPID controller and redox flow batteries. *Energy* **127**, 704–715 (2017)
 28. Lurie, B.J.: National aeronautics and space administration NASA. Three-parameter tunable tilt-integral-derivative (TID) controller. U.S. Patent 5,371,670 (1994)
 29. Guha, D., Roy, P.K., Banerjee, S.: Maiden application of SSA-optimised CC-TID controller for load frequency control of power systems. *IET Gener. Transm. Distrib.* **13**(7), 1110–1120 (2019)
 30. Heidari, A.A., Mirjalili, S., Faris, H., Aljarah, I., Mafarja, M., Chen, H.: Harris hawks optimization: algorithm and applications. *Futur. Gener. Comput. Syst.* **97**, 849–872 (2019)
 31. Debbarma, S., Dutta, A.: Utilizing electric vehicles for LFC in restructured power systems using fractional order controller. *IEEE Trans. Smart Grid* **8**(6), 2554–2564 (2016)